New Methods for Measuring Spectral, Bi-directional Transmission and Reflection using Digital Cameras

by

Nicholas Gayeski

A.B. Physics (2002)
Cornell University

Submitted to the Department of Architecture
in Partial Fulfillment of the Requirements for the Degree of
Master of Science in Building Technology

at the

Massachusetts Institute of Technology

June 2007

Signature of author……………………………………………………………………………
Department of Architecture
May 11, 2007

Certified by………………………………………………………………………………...
Dr. Marilyne Andersen
Assistant Professor of Building Technology
Thesis Supervisor

Accepted by…………………………………………………………………………………
Julian Beinart
Chairman, Committee on Graduate Students
Department of Architecture

Thesis Readers

Dr. Marilyne Andersen
Assistant Professor of Building Technology
Thesis Supervisor
Massachusetts Institute of Technology

Dr. Peter Apian-Bennewitz
Founder
Pab-opto Consulting Services

Dr. Mehlika Inanici
Assistant Professor of Architecture
University of Washington

New Methods for Measuring Spectral, Bi-directional Transmission and Reflection using Digital Cameras

by

Nicholas Gayeski

Submitted to the Department of Architecture
on May 11, 2007 in Partial Fulfillment of the
Requirements for the Degree of Master of Science
in Building Technology

Abstract

Advanced fenestration systems are increasingly being used to distribute solar radiation purposefully in buildings. Distribution of visible light and near infrared radiation can be optimized to enhance daylighting and reduce thermal loads. Light redirecting window systems are one of many innovative fenestration systems available for improving the daylighting and thermal performance of buildings. Many emerging and existing light re-directing systems have both spectrally and angularly selective optical properties. To study these properties, a device that measures the spectral, bi-directional transmission and reflection distribution functions of complex fenestration systems is being developed at the Massachusetts Institute of Technology.

This device, a goniophotometer, will measure photometric and radiometric BT(R)DFs for radiation of 380 to 1700 nanometer wavelengths, encompassing much of the solar spectrum. The device incorporates spectroradiometrically calibrated digital cameras and absorption filters to gather quasi-spectral information about reflection and transmission by complex fenestration systems. It relies on a half-mirrored, aluminum coated acrylic hemi-ellipsoid to project reflected or transmitted light towards a digital camera. The device will be able to characterize BT(R)DFs for a variety of fenestration system materials, assemblies, and building materials.

The goal of this research is to support the development of innovative, spectrally and angularly selective window systems that can improve daylighting and comfort and/or reduce cooling and heating loads in buildings. This thesis focuses on calibrating digital cameras to measure radiances with unknown spectra, developing the hemi-ellipsoid for the new goniophotometer, and developing methods for constructing quasi-spectral BT(R)DFs using this new device. The calibrated cameras also have potential for use in other applications, for example, as radiometers and photometers in rooms with light of known spectra.

Thesis Supervisor: Marilyne Andersen
Title: Assistant Professor of Building Technology

Acknowledgements

I would like to thank my advisor, Dr. Marilyne Andersen, for her continued support and guidance through demanding personal times.

To Dr. Peter Apian-Bennewitz and Dr. Mehlika Inanici, my deepest gratitude for reviewing my work and providing constructive feedback.

Thanks to Courtney Phillips, Eleanor Stokes, and Siân Kleindienst for their collaboration and contributions to the goniophotometer project, especially as it related to camera calibration.

Thanks to Zachary Clifford, Dean Ljubicic, and Timothy Koch for their work on the mechanical and electrical systems and the computer programming supporting this work.

Thanks to Tanury Industries, and especially Ray, Dr. Wang, and President and CEO Michael Akkaoui for their willingness and patience while coating the ellipsoids.

Thanks to all of the professors in the Building Technology Group for sharing their insights and wisdom on this project and other issues.

Finally, thanks to my family, my friends, and Celina for their encouragement of my interests, flexibility with my compromises, and ongoing love and support.

This material is based upon work jointly supported by the Massachusetts Institute of Technology and by the National Science Foundation under Grant No. 0533269.

Contents

List of Figures

Chapter 1

Chapter 2

Chapter 3

Chapter 4

Chapter 5

Chapter 6

List of Tables

Chapter 1

Chapter 5

Chapter 6

1. Introduction

Radiation from the sun has provided light and heat for buildings for centuries. Today, in an age when energy efficiency and conservation, sustainability, and quality of life are high priorities in buildings, optimal use of the sun's light and heat holds new possibilities to meet social challenges. In the last century, major developments in window technologies, such as low-e windows, have led to more intelligent use of solar energy that saves energy and improves comfort. The future will bring more developments. For example, fenestration systems that transmit or reflect different parts of the sun's spectrum to different parts of a building depending on solar angles of incidence could passively adapt to seasonal solar conditions. To enable the development of these emerging technologies, new tools and new information for measuring and assessing their performance will be needed.

This work focuses on new methods for using digital cameras to study such fenestration systems. Devices called goniophotometers are used to study the bi-directional transmission and reflection of solar radiation caused by light-re-directing fenestration systems. Derived from the Greek words gonio, photo and metron meaning angle, light and measure, the word "goniophotometer" describes a device that measures the re-direction of radiation as a function of a few critical parameters. These parameters include the angles of incidence of incoming radiation, the angles of emergence of outgoing radiation, and the wavelength and polarization of radiation. Measuring the wavelength dependent re-direction of light and radiation by complex fenestration systems provides information about how they will perform in the built environment and how they can be designed to optimize performance.

The goniophotometer under development at the Massachusetts Institute of Technology (MIT) will measure quasi-spectral, bi-directional transmission and reflection distribution functions (BT(R)DF) of materials and components used in fenestration systems. The device builds on previous work with existing video-goniophotometers that allow rapid measurement of BT(R)DFs using digital cameras. It also draws from research on the spectroradiometric calibration of digital cameras to measure radiance and luminance of scenes.

1.1 Thesis Structure

The thesis is divided into seven chapters focused on a range of issues including the relevance of complex fenestration systems to buildings, the importance of understanding their spectral, bi-directional optical properties, and new and innovative methods for measuring these properties. Chapter one will discuss the importance and potential for complex fenestration systems in the modern context of building performance, energy use, occupant comfort and aesthetics. It will also discuss recent and future technological advances in fenestration technologies. Chapter two will describe the nature and purpose of goniophotometers and the details of some existing goniophotometers. Chapter three will describe the concept behind the goniophotometer under development at MIT and prior work to develop the device. Chapter four will describe the methods used to develop a half-mirrored hemi-ellipsoid for the device. It will also cover measurement methods to characterize its spectral transmission and reflection properties. Chapter five will describe the methods used to calibrate a charge coupled device (CCD) camera and an Indium Gallium Arsenide (InGaAs) near infrared (NIR) camera as spectroradiometers for measuring radiation of unknown spectra in tandem with appropriate light filters. Chapter six will describe how the output of these cameras can be used to estimate quasi-spectral radiometric BT(R)DFs over a 380 to 1700 nm range, total radiometric BT(R)DFs across that range, and photometric BT(R)DFs. Finally, chapter seven will conclude with a description of the achievements of this research, errors in calibration, and potential applications of the new video-goniophotometer and the calibrated cameras.

1.2 Fenestration in Context

Fenestration systems are a key component of high performance, low energy buildings of the future. They are also a dominant feature in current building designs, many of which are highly glazed. As a result, fenestration systems provide ample opportunities, now and in future buildings, for both conserving energy and using it efficiently to manage lighting and thermal loads. They also provide the opportunity to improve visual and thermal comfort and can even have broad impacts on human health. Furthermore, they present aesthetic and architectural opportunities that impact how people perceive, experience and occupy buildings.

1.2.1 Energy Impacts

Efficient use of sustainable energy in buildings is a critical strategy for addressing global energy and environmental challenges. According to the U.S. Green Building Council, annually buildings account for 68 percent of electricity consumption, 12 percent of fresh water consumption, 88 percent of potable water use, and 40 percent of raw material use. They also generate a third of the municipal solid waste, 30 percent of carbon dioxide emissions, 46 percent of sulfur dioxide emissions, 19 percent of nitrous oxide emissions and 10 percent of fine particulate matter emissions (USGBC 2003). In 2004, building energy consumption accounted for 39 percent of total U.S. energy consumption (USDOE 2006). This is about 39 quadrillion BTUs (quads) of the roughly 100 quads consumed in the U.S. annually (EIA 2005), which accounts for about 23 percent of global annual energy consumption.

Within buildings, lighting, heating and cooling energy accounted for 18, 22, and 11 percent of total building energy consumption respectively. This amounts to about 20 percent of total U.S. energy consumption used only for lighting, heating and cooling buildings and roughly 4.6 percent of global annual energy consumption (USDOE 2006). Lighting, heating and cooling energy are the end-uses most closely linked to fenestration technologies because fenestrations strongly influence thermal loads on buildings as well as light levels within them. According to one study, with lighting, heating and cooling impacts combined fenestration systems account for about 2 quads of the energy consumption of commercial buildings and about 5 quads of energy consumption in residential buildings, or around 7 percent of annual U.S. energy consumption (Carmody et al. 2004).

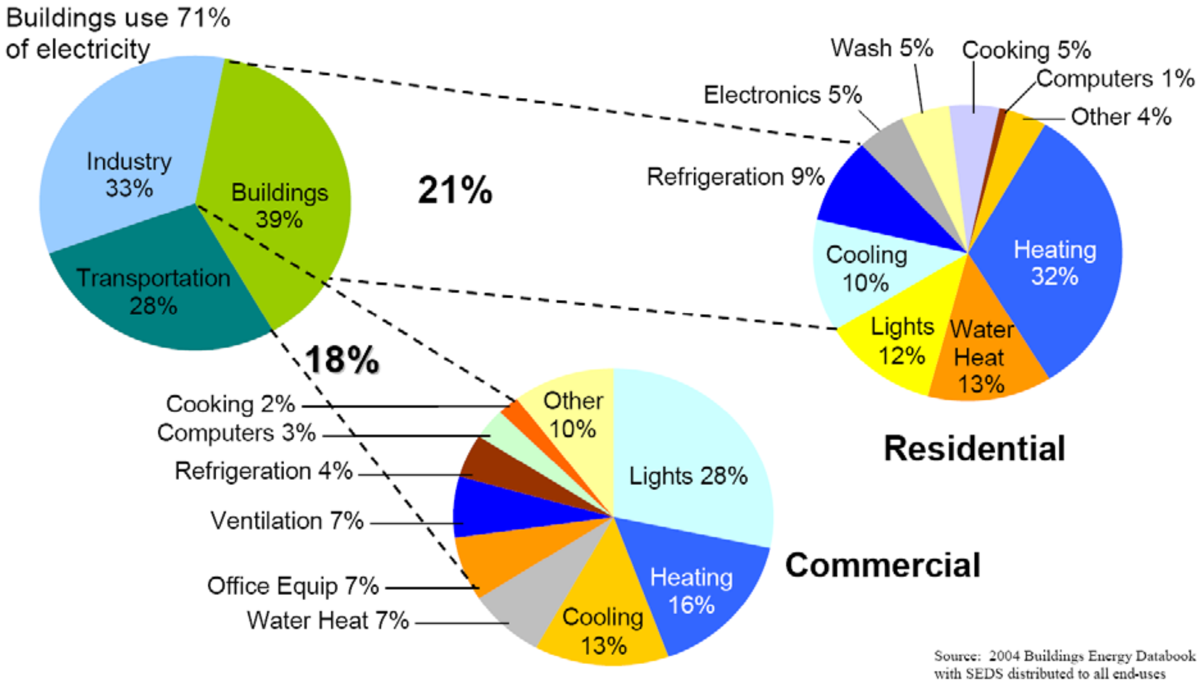

Source: 2004 Buildings Energy Databook with SEDS distributed to all end-uses

Figure 1.1 Building Energy End-Uses in the United States (USDOE 2006)

The potential for complex fenestration systems to reduce fenestration-related energy consumption is great. According to one Lawrence Berkeley National Lab (LBNL) analysis, if one existing fenestration technology, low-emissivity glazings, were deployed throughout the residential building market it was estimated that residential heating and cooling energy consumption attributable to windows would drop by about 41 percent (Arasteh et al. 2003). This amounts to a reduction of the estimated 2.7 quads used annually for residential heating and cooling attributable to windows to 1.6 quads. The study also suggested that “future advanced fenestration products… offer the potential for significantly greater HVAC energy savings than can be achieved with currently available high-performance windows” (Arasteh et al. 2003, p10). They concluded that windows with dynamic optical properties that could change with seasonal or climatic conditions showed the potential for significant savings in HVAC energy in mixed heating and cooling climates and moderate or small savings in purely heating or cooling dominated climates.

Complex fenestration systems can also reduce lighting energy in buildings. In his book*, Dynamic Daylighting Architecture,* Helmut Köster estimates that better use and distribution of daylight could save between 30 and 70 percent of the electrical energy required for artificial lighting (Köster 2004, p 14) assuming that daylighting controls are also used. He estimates that “10 percent of the total electrical energy produced in one day is consumed for artificial lighting in daytime” (Köster 2004, p 13), that is, during the time when complex fenestration could be used to offset those loads. Other estimates suggest that 30 to 60 percent of annual lighting energy could be saved through effective daylighting strategies (Loftness and Harktopf 2002). In terms of magnitude, the “luminous flux in a square meter cross-section of sunlight is enough to adequately light 200 square meters of interior building space” (Selkowitz 1999, p3). However, the details in the implementation of daylighting strategies are often important, both for actual energy savings and user acceptance. It has been suggested, for example, that in a daylit commercial building “the choice of control can make a 30-40% difference to the lighting energy use” (Baker and Steemers 2002).

Within this context, it is clear that advanced fenestration technologies have a significant role to play in reducing the lighting, heating and cooling energy consumption of buildings, and as such have the potential for large scale national and global energy savings.

1.2.2 Daylighting Benefits

Daylighting has many other benefits beyond just energy savings. It has been suggested that daylighting can impact productivity, performance of tasks, visual comfort, circadian rhythms, and retail sales and even have other financial implications. These issues are also often what determine whether daylighting strategies are successful because they dictate whether building occupants are comfortable under daylit conditions and whether owners are happy with the results. On the other hand, many of the links between these factors and daylighting strategies are little understood.

One observation about daylighting is that, psychologically, people tend to prefer views and daylight. (Young and Berry 1979) found that office workers tended to prefer windows because they provided a view. Many surveys have shown that a high percentage of survey respondents will say that they prefer to work under daylit conditions (Boyce et al. 2003b, p26). Although many studies have suggested that surveyed office workers prefer rooms with windows primarily because of view and daylight, other studies have suggested that a negative perception of electric lighting causes a preference for windows. (Cuttle 2002) found that surveyed office workers preferred daylighting primarily because they thought it had less negative impacts on health than electric lighting, not necessarily because they knew of its benefits. At the same time, spaces that are badly daylit can cause glare and discomfort and it has been shown that people will take action to reduce daylighting if it causes discomfort (Boyce et al. 2003b).

Another issue is that daylight can have significant impacts on human health. For example, it has been shown that daylight can have a significant effect on the human circadian system which controls the body's internal clock. Light or radiation "controls the circadian rhythm of hormone secretions and body temperature" with implications for sleep/wake states, alertness, mood, and behavior (Webb 2006). Radiation stimulates retinal ganglion cells that link the eye to the suprachiasmatic nucleus, which controls circadian rhythms (Berson et al. 2002). The higher illuminances usually associated with daylighting, when compared to electric lighting, tend to stimulate the circadian system more effectively. Furthermore, daylight tends to have a better spectrum for stimulating the circadian system than typical artificial lighting due to the spectral sensitivity of the circadian photoreceptors, retinal ganglions (Brainard et al. 2001). On the other hand, those who work at night must work against the natural circadian system. It has been shown that exposure to high illuminances through artificial light at night can cause a phase shift in the circadian rhythm and maintain a more wakeful state at night (Boyce et al. 2003b, p22).

Daylighting has human health impacts beyond circadian rhythms. It has long been known that ultraviolet radiation, such as that present in daylight, can cause tissue damage (Webb 2006). But exposure to ultraviolet radiation can also produce Vitamin D which is necessary for calcium metabolism and a healthy skeleton (Webb 2006). Vitamin D deficiencies have been linked to certain bone disorders and forms of cancer (Boyce et al. 2003b). Daylighting systems may increase human exposure to ultraviolet radiation indoors as compared to artificial lighting if ultraviolet radiation is transmitted by the system, potentially raising both of these issues, although high levels of ultraviolet radiation would likely be required. Lighting conditions can also cause eyestrain, but this is more influenced by an inadequacy in light levels or by extreme contrasts which can be present under both daylit and electrically lit conditions. There are likely to be other human health impacts of daylighting and general lighting conditions that are not yet understood. For example, "people placed under floor lamps with 3500 lux during tests generated the stress hormone adrenaline. After exposing the control group to natural daylight over a 14-day period, the adrenaline levels normalized" (Köster 2004, p365). It is not clear what long term effects on human health these results suggest. In addition, although many of the health effects of daylighting have been investigated generally, specific effects of the spectrum of light on human health and other factors is not well understood (Köster 2004, p380).

Daylighting may also improve productivity and the performance of tasks. Studies have shown that although daylight does not inherently lead to the improved performance of tasks, the use of daylighting has a "greater probability of maximizing visual performance than most forms of electric lighting because it tends to be delivered in large amounts with a spectrum that ensures good color rendering" (Boyce et al. 2003b, p3). One example of how daylighting impacts performance and productivity is the case of schoolchildren in daylit classrooms. One study suggested that students performed slightly better on tests in classrooms that were effectively daylit (HMG 1999a), but a follow up study showed that glare, direct sun penetration, and the inability to control shading and solar conditions can have negative impacts on student performance (HMG 2003). The human health impacts described above can also have major effects on productivity. Sleepiness, mood, and long-term health all have implications for worker productivity, but the direct link between daylighting and productivity as a result of changes to these variables is not very well understood. It has been suggested, for example, that mood impacts the efficiency of decision-making, willingness to collaborate, problem-solving and creativity (Boyce et al. 2003b), but these links are not well-understood, and the subsequent link between them and daylighting is understood even less.

Another interesting aspect of daylighting is its financial impacts. For example, one apparent benefit of daylighting is its effect on retail sales. One study compared sales from retail stores that were conventionally lit with similar stores that employed daylighting through skylights. The daylit spaces had 40 percent higher sales (HMG 1999b). Anecdotal evidence also suggests that rental spaces without windows may have a lower rental value and that daylighting may impact health costs (Boyce et al. 2003b). Another effect of daylighting that may have major financial implications is its impact on the productivity of workers. If daylighting can indeed increase productivity, as has been suggested, the financial return associated with even a small increase in productivity would imply major savings because worker salaries are a significant portion of costs. On the other hand, complex fenestration systems are generally more costly to install than, for example, a simple insulated wall, and thus the costs of daylighting strategies must also be considered.

In summary, the benefits of daylighting are many, but they depend on the effective implementation of daylighting strategies. Daylighting may improve comfort, human health, productivity, the performance of tasks, and have financial implications, but if implemented poorly may have opposite effects, such as causing glare or overheating. A thorough summary of the benefits and potential drawbacks of daylighting can be found in (Boyce et al. 2003b).

1.2.3 Design Opportunities

Creative use of daylight and solar radiation presents many aesthetic and architectural design opportunities. Dynamic changes in the illumination of spaces created by daylighting can, for example, reveal volumes and architectural features or change the perception of texture, color, and the spatial relationships of objects and surfaces. These issues have been discussed in many other sources, such as (Baker and Steemers 2002), (Köster 2004), or (Phillips 2004), and are not covered here. Instead, this section will discuss a few innovative designs using complex fenestration systems with both angularly and spectrally selective properties that are specifically relevant to this research.

There are already many buildings that take advantage of spectral control of light and the use of materials with spectrally dependent properties to create aesthetic and architectural effects with light and color. For example, the Museum for African Art, in Manhattan, by Architect Maya Lin contains a sun-lit space painted in five shades of yellow "each progressively lighter as the eye ascends. This not only emphasizes the stair's outward spiraling form, but also acts as a metaphor for rising, like a bright solar beacon of cultural understanding" (Ojeda and McCown 2004, p12). However, there are not as many examples of buildings that deliberately use complex fenestration systems with spectrally and angularly dependent properties to create architectural effects.

One of these examples is Toshiko Mori's Compound on the Gulf of Mexico in Sarasota, FL which includes a prism shaped skylight, "whose glass surface manages to change color with the time of day, indeed at times replicating the soft blues and pinks of a Gulf of Mexico sunset" (Ojeda and McCown 2004, p181). Prismatic panels have also been used at the Genzyme Building, by Behnisch Architects, in a chandelier to refract light into different colors and enliven the space (Behnisch 2007). In the Dwan Light Sanctuary at the Armand Hammer United World College of the American West, prisms are used to refract light and project spectra onto the white surfaces within the space that move over the day and year with the movements of the sun. The prisms also refract moonlight when the moon is bright. Charles Ross, a co-designer of the space with Virginia Dwan in collaboration with architect Laban Wingert “suggested a space where the movement of the spectrum and the form of the building would act together” (Linton 1999, p171)

These examples of creative use of fenestration systems with both spectrally and angularly depend properties suggest design opportunities for complex fenestration systems that could create dynamic experiences in architecture previously unexplored.

1.3 Fenestration Technologies

The benefits and implications of complex fenestration systems are many and varied, but what are these systems and what technological changes have led to their development? Fenestration technologies have been rapidly evolving over the last 50 years and continue to evolve today. This section will explore a broad range of technological advances in fenestration systems in recent decades, emerging complex fenestration systems that can improve daylighting and thermal performance, and finally complex fenestration systems with specifically designed angularly and spectrally dependent optical properties with potential for application in the built environment.

1.3.1 20th Century Technological Advances

Fenestrations are tasked with addressing many issues as far ranging as acoustics, structural integrity, durability, fire protection, blast resistance, moisture control, airflow, insulation, controlling solar gains, color rendering, glare, view, and illumination (Carmody et al. 2004). Over the last century, technological innovations in fenestrations have addressed of a wide variety of these issues.

For example, technologies such as multi-pane windows, less conductive viscous gas fills and suspended plastic films have improved the insulating properties of windows by increasing their resistance to conductive and convective heat transfer. Improvement in framing technologies, such as insulated vinyl or fiberglass frames have further reduced conductive heat transfer through window assemblies (Frost et al. 1996).

A number of technologies have improved the radiative properties of fenestrations in the visible, NIR, and infrared parts of the spectrum. For example, special inorganic additives have been added to glass that alter their color, adding a tint which changes the amount and spectrum of light passing through it. Tinted windows can reduce heat gain and glare to some extent by reducing the amount of light transmitted and reflecting some of the solar gains, but not as effectively as more recent technologies such as the coatings described below. Surface treatments, such as frit glass, sandblasting and acid etching also alter the reflection and transmission properties of windows, in some cases reflecting some of the incident radiation or diffusely transmitting it (Carmody et al. 2004).

Thin film metal coatings for glazings have greatly enhanced the thermal and optical performance of fenestration systems. Large area, low cost multilayer thin film coatings have been called the “single most important innovation” in fenestration technology (Selkowitz 1999, p2). Various reflective coatings have been widely employed on commercial buildings to reduce heat gains. Low-emissivity (low-e) coatings are highly reflective (not very absorbing and not transmitting) of long-wave infrared radiation that is emitted by objects around room temperature. As a result, they prevent radiative heat transfer of infrared radiation into or out of a building and reduce thermal loads. Spectrally selective low-e, or low-gain low-e coatings also reflect a significant portion of the NIR in solar radiation, significantly reducing solar gains for buildings in cooling dominated climates (Arasteh et al. 2003). One estimate suggests that around 40 percent of the windows sold in the United States today have low-e coatings (Ducker 2000).

Table 1, reproduced from (Watts 2005), shows a comparison of the performance characteristics of tinted films, reflective films and spectrally selective coatings particularly relevant to cooling dominated climates. The data shows that spectrally selective films can provide much higher visible transmission than tinted or reflective windows, while providing similar if not better reductions in solar gains. As such, the luminous efficacy of spectrally selective films, a measure of the amount of useful visible light transmitted relative to solar gains, is high. However, spectrally selective windows are still relatively costly, costing as much as 9 to 12 dollars per square foot compared to 4 to 6 dollars per square foot for reflective films (Watts 2005).

Table 1.1 Comparison of Solar Gain Reducing Glazing Strategies (Watts 2005)

Type	Percent T Daylight	Percent T Solar	Shading Coefficient	Luminous efficacy	Percent reflectance Internal/external
¼” clear glass	89	77	0.96	0.93	7/7
¼” clear tinted	37	64	0.74	0.50	6/6
¼” clear with reflective film	37	44	0.51	0.73	18/28
¼” clear with clear spectrally selective film	70	45	0.51	1.37	8/8

Integrating many of these technological advances into combined systems may have even greater potential for improved building performance. One study estimated that the wide-scale application of “superwindows”, or triple glazed windows with multiple low-e coatings in heating dominated climates as well as spectrally selective windows in cooling dominated climates had the potential to reduce energy consumption by 2.2 quads (Frost et al. 1993).

1.3.2 Complex Fenestration Systems

Although the technological advances described above have greatly changed the types of windows available and their performance, more recent technologies offer even more potential for improved performance, better comfort, and new design opportunities. The term complex fenestration system is used broadly to describe fenestration systems that employ one or more advanced fenestration technologies. A wide variety of emerging technologies, many of which are described here, are used in complex fenestration systems.

One such technology is chromogenic glazings, whose optical properties can be changed based on certain conditions. Photochromic and thermochromic glazings change their optical transmittance in response to illuminance levels and temperature respectively. Gasochromic windows can change transmittance with exposure to diluted hydrogen gas introduced between two panes. The optical properties of electrochromic windows can be changed with an applied voltage. They are made of thin metallic coatings sandwiched between two transparent electrical conductors. When a voltage is applied across the conductors and then removed, the windows can switch states between clear and a “prussian blue” which reduces solar gains and glare (Carmody et al. 2004).

Other electrically powered complex fenestration technologies include liquid crystal device (LCD) and suspended particle device (SPD) windows. LCD windows are translucent in their un-powered state and clear in their powered state. Like LCD windows, SPD windows partially block sunlight in their unpowered states, while they transmit it in their powered state (Carmody et al. 2004).

Refractive, prismatic and holographic optical elements (HOE) which redirect light have also been incorporated into complex fenestration systems. For example, prismatic louvers and glazings have been used to reduce solar gains, redirect and diffuse visible light. Prismatic systems that refract light have existed for many years (Tremblay et al. 1987). “Many patents for prismatic light deflection in the 1980s were turned down due to pre-existing patents, which had been registered in the United States between 1890 and 1910” (Köster 2004, p72). Nevertheless, prismatic elements are finding new applications even today, such as for seasonal shading responsive to sun position (Christoffers 1996). HOEs are only beginning to be applied, but without careful design may create glare and spectral dispersion effects (James and Bahaj 2005a), (James and

Bahaj 2005b). Other refractive elements, such as Fresnel lens', also have applications in the built environment (Tripinagnoststapoulos et al. 2005).

Reflective or deflective elements are also frequently used in complex fenestration systems. For example, diffusely or specularly reflecting blinds and louvers are used to re-direct light up towards the ceiling and deeper into spaces. In the Xilinx Development Center in Longmont, Colorado, designed by Downing Thorpe James with Daylighting Consultant Architectural Energy Corporation, a "mini optical light shelf" made up of reflective louvers with an optimized profile illuminates the ceiling of the building deep into the space, providing diffusely reflected light to working areas (Carmody et al. 2004, p354-356). Some mirrored systems, such as light pipes and anidolics, gather diffuse light and distribute it deep into spaces (Köster 2004). One large scale application of a mirrored system is in the Reichstag in Berlin, Germany renovated by architects Foster and Partners with Lighting Design by Claude Engle. Fixed mirrors occupy a glass dome above the parliament which redirect light down through a skylight illuminating the chambers (Phillips 2004, p72).

Diffusing elements, which scatter incoming light to provide evenly distributed diffuse illumination, are also finding new applications. Honeycomb materials, fabrics, diffusing sunscreens, and translucent insulating materials are often used to provide diffuse illumination, and sometimes insulation as well. Measuring the diffuse scattering by these systems tends "to be difficult to characterize and model properly" (Jonsson et al. 2004).

Other advanced technologies being integrated into complex fenestration systems include highly insulating-translucent aerogel filled glazings, thin-film photovoltaic cells, ceramic rods and even fiber optic cables. In addition, motorized shading and louvers with environmentally responsive control systems are being integrated that increase the possibilities for seasonal and solar adaptations (Carmody et al. 2004).

These many technologies and others are being integrated and refined into new fenestration systems to work together to achieve the many objectives of fenestrations in buildings. For example, laser cut panels and fixed Venetian blinds with a clear glazing were combined in a fenestration seeking to provide view, diffuse illumination and solar control in (Reppel 1998). An interesting summary of a variety of complex fenestration systems and daylighting strategies can be found in many sources, such as (Kischkoweit-Lopin 2002), (CEC 1993), (Köster 2004), and (IEA 2000). Stephen Selkowitz has said that:

> "Advanced glazings will be dynamic elements in facades that are fully integrated into building operations, providing daylighting and natural ventilation, and operated in a manner not only to reduce energy costs but to enhance occupant comfort and performance, and thus maximizing overall value to the building owner. These glazing and façade systems will become essential elements of virtually all 'green buildings', the best of which will reduce energy use by 70% compared to buildings of today." (Selkowitz 1999, p10-11)

Understanding the angular and wavelength dependent properties of these emerging complex fenestration systems will be critical for understanding their performance, design, and integration.

1.3.3 Angularly and Spectrally Selective Fenestrations

Angularly and spectrally selective fenestration refers specifically to complex fenestration systems with optical properties that depend on the surface azimuth and altitude (or zenith) angles of incidence as well as the wavelength of radiation. These systems must be designed and selected to provide dynamic properties appropriate for the building and climate in which they are employed. As a result, understanding the performance of these systems is crucial to their effective implementation.

Köster suggests that "following the various incident angles of light, contingent on the time of day and of the year, is the key to the fundamentals of daylight technology" (Köster 2004, p363). Dynamic control of solar optical properties of fenestrations and the redirection of incident daylight are considered two of "the significant energy-related performance challenges for glazings" (Selkowitz 1999, p2). In addition, it has been said that “directional light control remains the primary optical challenge of glazings” (Selkowitz 1999, p3) and that ‘smart glazings’ with dynamic properties are expected to fill the niche in the U.S. building market left by low acceptance of automated blinds and shades (Selkowitz 1999, p6).

There are many types of angularly and spectrally selective fenestration technologies. Thin film coating technology has advanced such that coatings with angularly selective spectral properties are available. The thin film physics behind how this is achieved is reasonably well-understood (Mbise 1996), (Smith 1997). Spectral, directional control of radiation can also be achieved through compound systems, such as those described in the previous section. Technologies such as HOEs, prisms, reflective elements, optimized geometries and microstructures [Walze et al. 2005] can be integrated into static or dynamic complex fenestration systems that influence the illuminance, irradiance, direction and spectrum of radiation passing through them (Köster 2004, p383-384).

The potential of this kind of system, for example, is to transmit visible light deeply into spaces throughout the year while reflecting NIR during the summer and transmitting it towards thermal mass during the winter. As solar angles change throughout the year, the typical angles of incidence on different facades also change predictably and these systems could be tuned for optimal seasonal performance. One study showed that angularly selective glazings tuned theoretically for optimal optical properties could reduce annual cooling energy loads by 18 percent and annual electricity use by 15 percent *relative to spectrally selective windows*, which are already an improvement over conventional windows, while at the same time providing a better daylight distribution (Sullivan et al. 1998). The study also showed an 11 percent reduction in peak energy loads, which can affect equipment sizing and subsequent operating efficiencies.

The need to account for both daylighting and thermal issues in the development of angularly and spectrally selective glazings and other complex fenestration systems leads to the need to study angularly and wavelength dependent optical properties of fenestration systems across the entire spectrum of solar radiation. The ability to study the way these fenestration systems reflect and transmit solar radiation in different parts of the spectrum will help in characterizing, modeling and analyzing their performance in the built environment as well as in designing new systems. Developing an innovative device to do this quickly, a spectral video-goniophotometer, should help advance the development, understanding, and implementation of advanced spectrally and angularly selective fenestrations.

2. Measuring Spectral, Bi-directional Optical Properties

Measuring the spectral, bi-directional optical properties of fenestration systems is the task of devices generally referred to as goniophotometers. These are devices that can measure the bi-directional transmission and reflection of radiation by objects and materials. Goniospectrometer is a term sometimes used to describe devices that can also measure wavelength dependent properties. Goniophotometers have been widely used to study the optical properties of lamps and luminaires, ground surfaces and ground textures (Andersen and de Boer 2006), and natural materials such as wood (Tsuchikawa et al. 2001). They are increasingly being used for assessing the bi-directional optical properties of fenestration system materials and components (CEC 1993, p4.2). Only very recently have goniophotometers for fenestration systems been developed that measure spectral as well as bi-directional dependence (Breitenbach and Rosenfeld 1998). This chapter will explore the function and utility of goniophotometers, explain many of the goniophotometers used to study complex fenestration systems, and discuss the needs for better measurement of spectral, bi-directional transmission and reflection properties of fenestrations.

2.1 Bi-directional Transmission and Reflection Distribution Functions

Most goniophotometers measure the transmitted or reflected luminance or radiance in a given direction relative to the incident illuminance or irradiance from a given direction onto a sample of interest (Andersen and de Boer 2006). The data measured by goniophotometers can be neatly summarized in a function called a Bi-directional Transmission (or Reflection) Distribution Function (BT(R)DF). BT(R)DFs were first introduced for reflected radiance distributions in (Nicodemus 1970) and (Nicodemus et al. 1977). The Commission Internationale de l'Eclairage defines a BT(R)DF as the ‘‘quotient of the luminance of the medium by the illuminance on the medium’’ (CIE 1977), where the luminance results from reflection or transmission by the material.

Many goniophotometers measure only photometric BT(R)DF, as defined by CIE, which can be described mathematically as follows (Andersen et al. 2001).

$$\text{(2-1)} \quad \mathrm{BT(R)DF}_v(\theta_{t(r)},\varphi_{t(r)},\theta_i,\varphi_i)=\frac{L_v(\theta_{t(r)},\varphi_{t(r)},\theta_i,\varphi_i)}{E_v(\theta_i)}$$

- $(\theta_{t(r)},\varphi_{t(r)})$ are the zenithal and azimuthal angles of emergence of transmitted (or reflected) radiation,
- (θ_i,φ_i) are the angles of incidence of incoming radiation illuminating a sample,
- L_v is the luminance of transmitted (reflected) light, and the subscript v is used to denote photometric quantities, and
- E_v is the illuminance of incoming radiation.

The units of BT(R)DFs are per steradians, or sr^{-1}. The important components of a BTDF are shown in Figure 2.1. Measuring a photometric BTDF relies on knowledge of the angles of incidence of incoming radiation (θ_1,φ_1), the total illuminance on the sample (shown below as L_1*$d\omega_1$*cos θ_1), and measurements of the transmitted (or reflected) luminance L_2 transmitted in the direction (θ_2, φ_2). The BT(R)DF can be calculated for all known angles using the equation above.

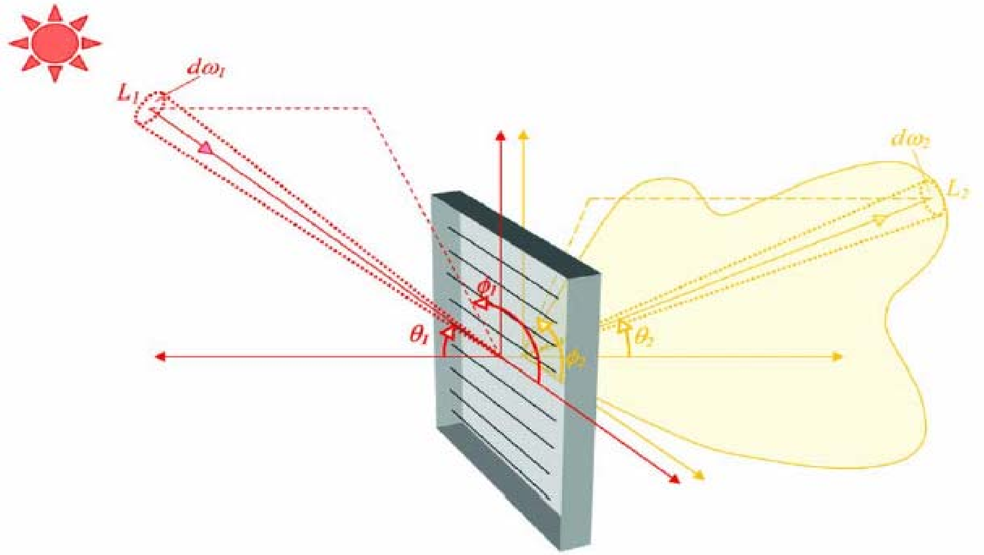

Figure 2.1 The components of a BTDF. L_1*$d\omega_1$*cos θ_1 is the incident illuminance from direction (θ_1, φ_1) and L_2 is the transmitted luminance in direction (θ_2, φ_2) (Andersen and Scartezzini 2005)

The concept of BT(R)DFs in radiometric units could be defined as the quotient of the spectral radiance from a sample by the spectral irradiance of the sample. In general, spectral BT(R)DFs are then dependent on two angles of incidence, two angles of reflection, wavelength and the polarization of source radiation (Ward 1992). Mathematically, these BT(R)DFs can be described as follows:

$$\text{(2-2)} \quad \mathrm{BT(R)DF}_e(\theta_{t(r)},\varphi_{t(r)},\theta_i,\varphi_i,\sigma,\lambda) = \frac{L_e(\theta_{t(r)},\varphi_{t(r)},\theta_i,\varphi_i,\sigma,\lambda)}{E_e(\theta_i,\sigma,\lambda)}$$

- $(\theta_{t(r)},\varphi_{t(r)})$ are the zenithal and azimuthal angles of emergence of transmitted (or reflected) radiation,
- (θ_i,φ_i) are the angles of incidence of incoming radiation on a sample,
- σ,λ are the polarization and wavelength of radiation,
- $L_e(\theta_{t(r)},\varphi_{t(r)},\theta_i,\varphi_i,\sigma,\lambda)$ is the spectral, bi-directional radiance of emerging radiation and the subscript e is used to denote radiometric quantities, and
- $E_e(\theta_i,\sigma,\lambda)$ is the spectral, directional irradiance of incoming radiation.

These spectral BT(R)DFs tell you the amount of irradiation that gets redirected as a spectral radiance into a particular direction as a function of wavelength and polarization. For convenience in this thesis, we assume that radiation impinging on the sample is unpolarized and ignore the dependence on polarization. This is reasonable because radiation from the sun incident on fenestration systems generally consists of randomly polarized light. The goniophotometer developed here will use a radiation source emitting randomly polarized light, like solar radiation, and will thus measure the net BT(R)DF for the sum of randomly polarized radiation.

One could also define radiometric BT(R)DFs as the quotient of the total radiance from a sample across a finite wavelength interval to the total irradiance on the sample across that same interval. This definition of radiometric BT(R)DF will be referred to as a quasi-spectral radiometric BT(R)DF. The full wavelength-dependent BT(R)DF is entirely independent of the source of radiation, and is a property of the material or system being studied, whereas the quasi-spectral BT(R)DF defined above depends on the radiation source, and may be different across a given wavelength interval depending on the spectral irradiation of the sample. This quasi-spectral BT(R)DF concept can also be extended to photometric BT(R)DFs, which are then defined as the total luminance from a sample across a finite wavelength interval to the total illuminance on the sample across that same interval. The photometric BT(R)DFs defined by CIE over the full spectrum are the limiting case of quasi-spectral photometric BT(R)DFs, where the wavelength interval includes all wavelengths relevant to photometric quantities.

Any photometric or radiometric BT(R)DF that is integrated over many wavelengths, i.e. quasi-spectral BT(R)DFs including those integrated over the entire spectrum, are limited to describing the transmission or reflection properties of a material to radiation with a particular spectrum. This limitation is due to the fact that, without knowing the true spectral, bi-directional transmission or reflection properties of a sample, as summarized in a spectral radiometric BT(R)DF, one will not know whether over some part of the spectrum, the sample will transmit or reflect more or less radiation from different light sources with different spectra due to its spectral transmission or reflection properties. For example, an extreme case of a sample that transmits only radiation above 550 nm will be found to have a finite photometric BT(R)DF in any given direction when illuminated with sunlight. The same sample, when illuminated with light containing only bluish light, between 380 and 480 nm for example, would be found to transmit *no* radiation in any given direction and thus the BT(R)DF would be zero in all directions! This illustrates a limitation of *all* existing goniophotometers that do not measure wavelength dependent BT(R)DFs. They only measure BT(R)DFs valid for radiation with relative spectra equal, or at least similar to the radiation used for measurements. The errors between the total BT(R)DF measured using the light source for each goniophotometer and the total BT(R)DF for a particular source, such as solar radiation, must then be considered when using the BT(R)DFs in applications.

Most existing goniophotometers only measure total photometric BT(R)DFs, with the limitations described above. There are at least two that have the ability to measure spectral radiometric BT(R)DFs across various wavelength intervals (Andersen and de Boer 2006). These devices will be described further in section 2.3. The new quasi-spectral video-goniophotometer under development at MIT will have the ability to estimate total and quasi-spectral photometric BT(R)DF as well as total and quasi-spectral radiometric BT(R)DFs from 380 to 1700 nm and over wavelength sub-intervals defined by eight filters used in the device, as described in Chapters 3 through 6.

2.2 The Utility of BT(R)DFs

The value of knowing the BT(R)DFs of complex fenestration systems is in the enhanced ability to characterize, analyze and predict their performance in the built environment. BT(R)DFs may also provide insights into possible designs for new fenestration technologies. It has been suggested that detailed knowledge of the optical properties of complex fenestrations are needed "to optimize the use and design of advanced fenestration systems, and thus efficiently control solar gain and daylighting through windows" (Andersen et al. 2005b).

BT(R)DFs may be useful to architects, designers, lighting consultants and engineers in selecting fenestration systems for the built environment (Andersen and de Boer 2006). Visualization of the angular distribution of light emerging from fenestration systems at different times of the day and year, and additional information about the distribution of NIR may provide more intuitive information about the performance of complex fenestration systems. Better communication of this information could, in turn, help increase the integration of these systems and thus improve daylighting and thermal performance.

BT(R)DFs have already proven to be useful to designers, engineers, consultants and researchers seeking to visualize and simulate the performance of complex fenestration systems. Lighting and energy simulation tools such as Radiance, Delight and Window 5 (used by Energy Plus) can model detailed performance of fenestration systems when provided with BT(R)DF data (Andersen and de Boer 2006), (Reinhart and Herkel 2000), (Mitanchey et al. 2002), (de Boer 2006). However, frequently BT(R)DFs for fenestrations and materials are not available for simulations. Often, this results in simulations with simplified assumptions about the performance of materials and fenestration systems. The development of goniophotometers with the capability of measuring spectral or quasi-spectral BT(R)DFs, such as the one presented here, can enable the creation of material libraries with detailed BT(R)DF data for simulating their performance in the built environment (Inanici 2007).

2.3 Goniophotometers

Today, there are a variety of goniophotometers used to study complex fenestration systems by measuring photometric and/or radiometric BT(R)DFs. Goniophotometers generally employ one of two principles for measuring BT(R)DFs, a scanning approach or a video-projection approach. The scanning approach consists of scanning the hemisphere of transmitted or reflected radiation from a sample with a detector to measure the luminance or radiance in a finite number of directions. The scanning approach can also be applied to radiation transmitted or reflected from a sample that is projected onto a surface. The projected radiation is then scanned to measure transmitted or reflected radiation or luminance. The video-projection approach consists of taking an image of a projection of the hemisphere of transmitted or reflected radiation, or at least a part thereof, using a calibrated digital camera from which luminance or radiance can be determined in all directions (Andersen and de Boer 2006).

Each approach has its advantages and disadvantages. Scanning goniophotometers tend to take a longer time to measure BT(R)DFs because they require numerous measurements for each angle of incidence. For example, if transmitted or reflected luminance was measured at 1 degree increments in altitude and azimuth, a scanning goniophotometer would require 360 times 90, or 32,400 measurements for one incidence angle. In (CEC 1993) it was estimated that to study the radiometric BT(R)DFs of a sample across 50 nm spectral bands from 350 to 750 nm (8 bands) at 1 degree increments in incidence and transmission or reflection angles, it would require $(360 \times 90 \times 8)^2$ or 6.72×10^4 measurements for all incidence and transmission or reflection directions. Clearly, this is unrealistic and in reality scanning goniophotometers measure discrete BT(R)DFs for on the order of one or two hundred directions. Because discrete data points around the hemisphere are measured, depending on the angular resolution at which measurements are taken some features of BT(R)DFs may be lost (Andersen and de Boer 2006).

Video-projection goniophotometers have the advantage that for each angle of incidence only one measurement is necessary to measure transmitted or reflected luminance. This is a result of projecting the light or radiation onto a sensor array that effectively measures the full hemisphere, or at least a large portion thereof, at one time. Compared to scanning goniophotometers with a 1 degree resolution in altitude and azimuth, 32,400 measurements are reduced to 1 for each angle of incidence. On the other hand, if the same resolution is required for the angles of incidence and spectral bands are studied such as those described above, a projection goniophotometer would still require (360 x 90 x 8) or 259,200 measurements to characterize the quasi-spectral BT(R)DF.

Again, this is unrealistic, but it illustrates an important difference between the types of goniophotometers. If the number of angles of incidence and transmission or reflection at which BT(R)DF measurements are desired is defined by N, scanning goniophotometers require on the order of N^2 measurements whereas video-projection goniophotometers require on the order of N. If many spectral bands are to be studied, defined by M, a scanning approach would require $(MN)^2$ measurements whereas a video-projection approach would only require MN. On the other hand, if spectral information can be gathered at once in the scanning process, such as with a spectrometer, the measurements required for scanning goniophotometers are reduced back to N^2, whereas if a ‘video-spectrometer’ type detector is not available for the video-projection approach, MN measurements are still required.

As a typical example, consider that if 145 angular directions are of interest in incidence directions and 1 degree solid unit of angle resolution is required in emerging direction, ignoring spectral analysis, a scanning approach would require 52,200 measurements whereas a video-projection approach would require only 145.

In addition to a reduced number of measurements, video-projection goniophotometers avoid the problem of discrete measurements. This is because the full hemisphere of transmitted or reflected radiation is projected onto an array of sensors inside the digital camera, thus greatly reducing the possibility of missing fine angular resolution features within BT(R)DFs. The limitation in angular resolution is then delineated only by the angular resolution of the imaging system, which depends on the optics of the camera used and the size of the sensors, such as silicon chips, within the sensor array.

In addition to time and sampling issues, there is an issue of the interchangeability of detectors in order to measure a range of spectral properties in goniophotometers. For example, scanning goniophotometers have the advantage that the detector used to scan the hemisphere can be easily changed. Silicon detectors, Indium Gallium Arsenide (InGaAs) detectors, thermopiles, spectrometers and other devices can be used to measure optical properties within the ultraviolet, visible, NIR and infrared parts of the spectrum. Video-projection goniophotometers are less flexible, mainly because there are not generally digital cameras available with all of these types of sensors integrated into a sensor array. Video-projection goniophotometers have the spectroradiometric limitations of the cameras used. Charge coupled device (CCD) cameras have been used in previous video-projection goniophotometers, and the quasi-spectral video-goniophotometer described here will explore the potential of an InGaAs NIR digital camera as well.

There are many practical issues in all goniophotometers having to do with such problems as the obstruction of light at various angles of incidence or the size of samples allowed by the sample holder. A thorough investigation of many goniophotometers for complex fenestration systems can be found in (Andersen and de Boer 2006) or

(Andersen 2004). The remainder of this section will describe certain aspects of existing scanning and video-projection goniophotometers relevant to this research.

2.3.1 Scanning Goniophotometers

A typical scanning goniophotometer consists of a light source, a sample, and a detector which can be repositioned in some combination such that radiation reflected or transmitted in different directions by the sample can be measured by the detector for different angles of incidence of incoming radiation. The detector typically measures total luminance or radiance over a certain wavelength interval to which it is sensitive. In some devices the detector can measure spectral radiance across that interval.

The first fenestration system scanning goniophotometer was built during the 1980s at the Lawrence Berkeley National Lab (LBNL). This device was used to predict the performance of multi-layer fenestration systems (Papamichael et al. 1988). A similar device was designed at the Fraunhofer Institute for Solar Energy (ISE) (Apian-Bennewitz 1994), but included many improved features such as adjustability for varying sample sizes and adaptively refined angular resolution (Apian-Bennewitz and von der Hardt 1998) to capture high resolution BT(R)DF features. A schematic of the ISE device is shown in Figure 2.2.

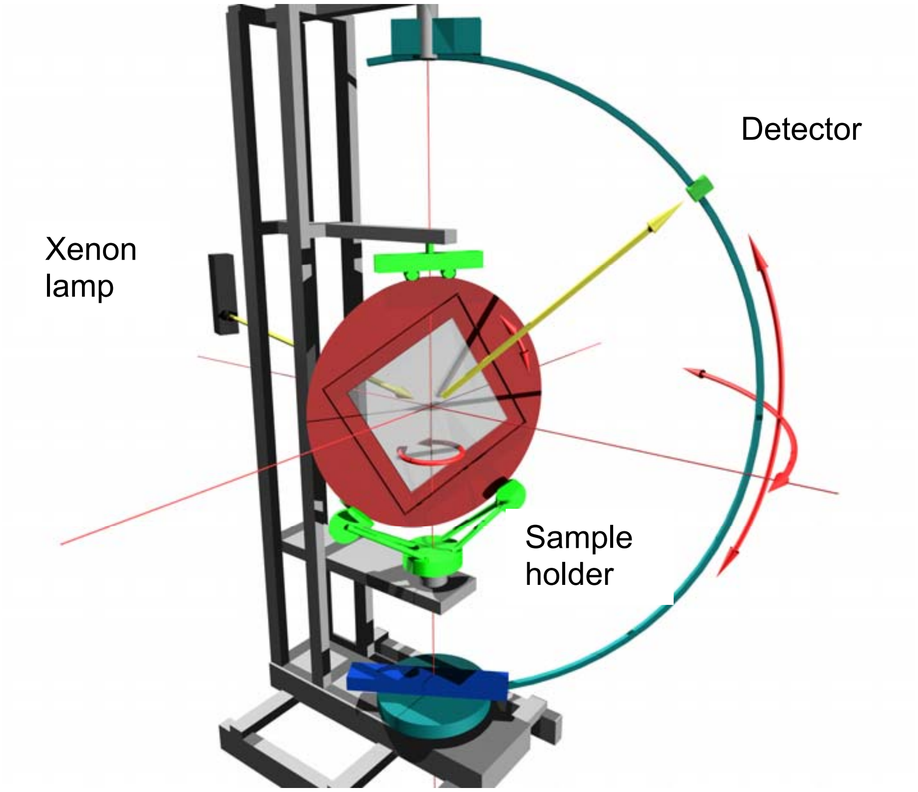

Figure 2.2 ISE scanning goniophotometer schematic (Apian-Bennewitz 1998)

Additional scanning goniophotometers have been built at the University of Technology Sydney (UTS), the Berlin University of Technology (TUB) and TNO Building and Construction Research, Delft (TNO) (Smith 1999), (Aydinli 1996), (Andersen 2004). These devices follow similar principles to both the ISE and LBNL goniophotometers. There are other scanning goniophotometers, such as a goniophotometer at MIT described in (Ngan et al. 2005), that are used for other applications such as computer graphics.

There are two additional scanning goniophotometers of note. The first is another device designed by Apian-Bennewitz (Apian-Bennewitz 2007) at the pab^{TM} optical consultancy located in Freiburg, Germany. This device is shown in Figure 2.3. This device is notable because it is compact, transportable, and, in a way, modular. It is modular in that the detector and light source can be treated as an interchangeable component.

This feature enables measurement for different kinds of light across different parts of the radiation spectrum. Different lamps with different spectra can be used to study radiation of different types. Different detectors, such as silicon detectors, pyroelectric detectors, and thermopiles can be used to measure radiometric, photometric, or even infrared BT(R)DFs (Apian-Bennewitz 2007).

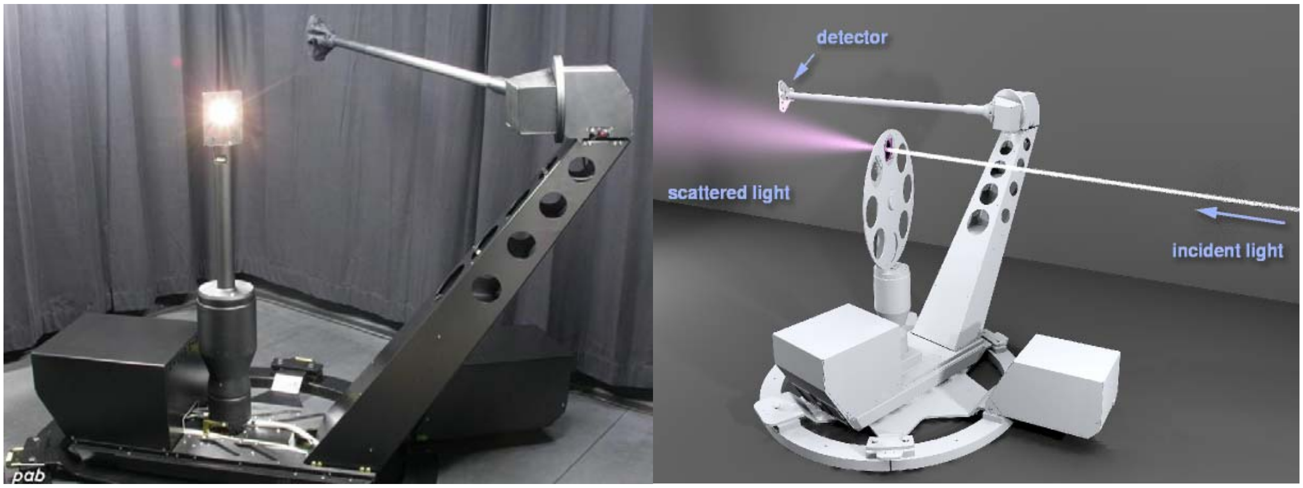

Figure 2.3 pab-opto goniophotometer and schematic (Apian-Bennewitz 2007)

The other scanning goniophotometer of note, particularly for this research, is a goniospectrometer developed at Cardiff University and now at the Technical University of Denmark (TDU) shown in Figure 2.4. Especially innovative about this device is a light collection system made of parabolic mirrors which focuses light into a fiber optical cable which then feeds two scanning spectrometers. Calibrated silicon and InGaAs detectors are used to measure the spectral radiance of transmitted light. A diffraction grating sweeps through each detector’s range of sensitivity, about 300 to 1100 nm for the silicon detector and 900 to 2100 nm for the InGaAs detector to measure spectral radiance with a spectral resolution of about 5 nm (Breitenbach et al 2001).

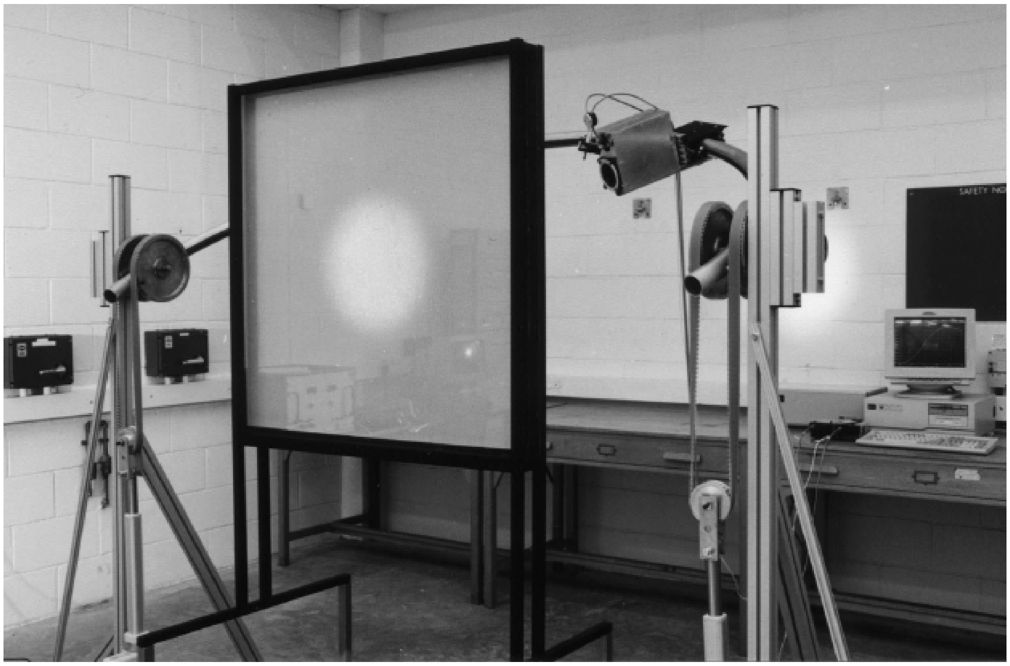

Figure 2.4 DTU/Cardiff goniospectrometer (Breitenbach et al. 2001)

2.3.2 Video-Projection Goniophotometers

The video-projection approach to goniophotometric measurement is a much different strategy for measuring BT(R)DFs than the scanning approach, which presents different opportunities and challenges. Video-projection goniophotometers typically project the full hemisphere of radiation transmitted or reflected by the sample, or a large fraction thereof, onto a digital camera using diffusely or specularly reflecting surfaces. In doing so, the calibrated digital camera can measure luminances in every direction over an entire hemisphere of transmission or reflection in one or a few image(s).

There are three existing video-projection goniophotometers relevant to this paper (Andersen and de Boer 2006). All three measure the luminance of transmitted or reflected light using a calibrated digital CCD camera. Two of the devices, one developed at LBNL by (Ward 1992) and the other at the University of Rennes 1 (Deniel 2002) were developed primarily for computer graphics applications to make better, faster or more photo-realistic renderings.

The device developed by Ward at LBNL projects light onto a digital camera using a half-mirrored, acrylic hemi-sphere as shown in Figure 2.5. Light is then recorded by a CCD camera and pixel locations are mapped to reflection angles from the sample through a spatial calibration. The initial concept was to use a half-mirrored hemi-ellipsoid, which is the inspiration for the projection principle used for the MIT goniophotometer. This first device also inspired the video-projection goniophotometer at the University of Rennes 1, and another device at the Solar Energy and Building Physics Laboratory at the Swiss Federal Institute of Technology (EPFL).

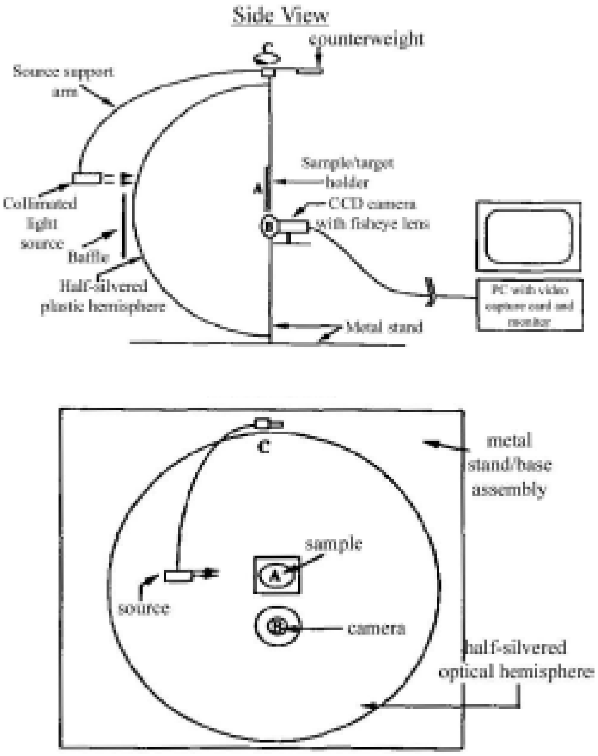

Figure 2.5 LBNL video-projection goniophotometer (Ward 1993)

Figure 2.6 EPFL video-projection goniophotometer (Andersen et al. 2005a)

The EPFL projection goniophotometer, shown in Figure 2.6, uses a diffusely reflecting white screen that can be moved to six different positions and projects light onto a calibrated CCD camera mounted with a wide angle lens and a photopic filter. A schematic of the device is shown in Figure 2.7. The spectral sensitivity of the CCD camera used in the EPFL device has been modified, based on a spectral sensitivity calibration and the selection of

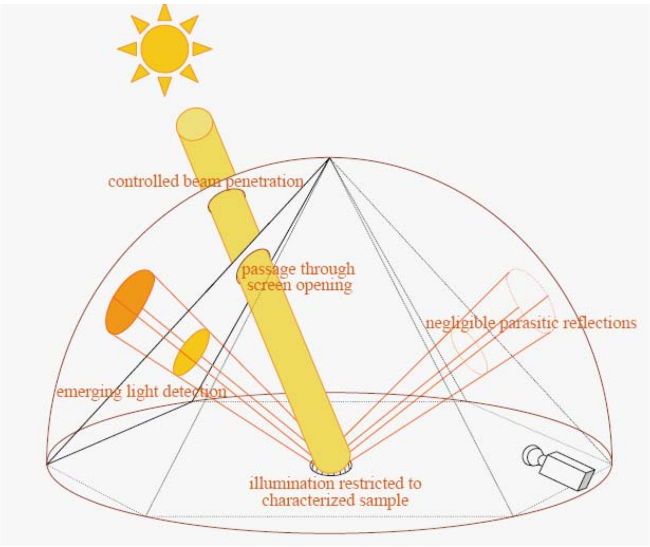

Figure 2.7 EPFL goniophotometer schematic (Andersen et al. 2005a)

absorption filters, to closely mimic the photopic response of the human eye (Andersen et al. 2001). This important modification enables the device to accurately measure the luminance of light sources regardless of whether the spectrum is known. The digital output of the camera is then correlated to luminance levels for use in calculating photometric BT(R)DFs. Although the camera can accurately measure luminances of unknown spectra, the device still has the limitations of all goniophotometers that measure wavelength integrated quantities, as described above. These include that if the sample being studied has wavelength-dependent properties, the photometric BT(R)DFs measured are limited to describing the sample's photometric reflection and transmission to light with a spectrum the same or similar to that used for experiments.

2.4 Recent Innovations

The goniophotometers described above represent the state of the art in existing goniophotometers for analyzing complex fenestration systems. Innovations in these devices over the past 25 years have ranged from expanding the types and sizes of fenestration systems that can be analyzed, to increasing the speed and resolution for which measurements can be taken, to expanding the wavelengths over which analyses can be performed.

The ability to measure radiometric BT(R)DFs across a 300 to 2200 nm wavelength interval are important innovations presented by (Apian-Bennewitz 2007) and (Breitenbach and Rosenfeld 1998). The implementation of a video-projection based approach took an important step in improving angular resolution and drastically reducing the number of measurements necessary for each angle of incidence (Ward 1992), (Deniel 2002), (Andersen 2004). The newest scanning goniophotometer (Apian-Bennewitz 2007) provides the important innovation of changeable light sources and detector types for analysis of many radiation spectra over various spectral bands. Many of the existing goniophotometers are undergoing upgrades to improve the scanning method, detector type and changeability, as well as better light sources (Andersen and de Boer 2006).

The innovations of all these devices can be summarized into four categories, the speed and resolution with which measurements are taken, the spectral range over which measurements can be taken, the relative spectra for which measurements are relevant or can be measured, and the types of output the devices can provide. The device being developed at MIT seeks to advance three of these four innovations. Because it is a video-projection goniophotometer, the speed and angular resolution of the device is expected to be superior, or at least comparable, to existing video-projection goniophotometers. In addition, spectroradiometrically calibrated CCD and InGaAs digital cameras will be used to extend the spectral range of the device to 380 to 1700 nm. The use of filters with the spectroradiometrically calibrated cameras will also increase the types of BT(R)DFs capable of being measured.

3. A Spectral, Video-Goniophotometer

3.1 Design Concept

As previously described, the new goniophotometer being developed at MIT will merge the speed and continuous coverage of video-projection goniophotometers and some of the spectral analysis capabilities of certain scanning goniophotometers. Like a typical video-projection goniophotometer, it makes use of a light source, a rotating sample holder, a projecting device, and a CCD digital camera. Unlike a typical projection goniophotometer, filters are used to sample the spectrum of the light source to isolate wavelength intervals and an InGaAs digital camera is used to extend its range into the NIR. In addition, the projection method uses a custom made, half-mirrored hemi-ellipsoid to reflect light emerging from a sample onto a digital camera mounted with a fish eye lens. A diagram of the device is shown in Figure 3.1.

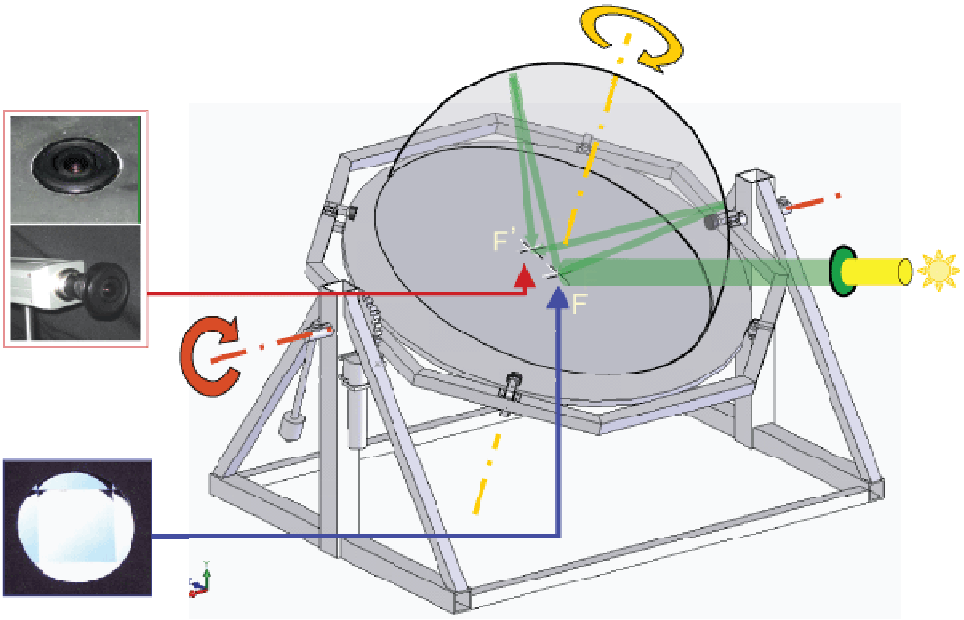

Figure 3.1 MIT spectral video-goniophotometer schematic

Instead of measuring only photometric BT(R)DF like previous video-projection goniophotometers, the device will be able to measure photometric BT(R)DF as well as quasi-spectral radiometric BT(R)DF. These quasi-spectral capabilities will include radiometric BT(R)DF across a 380 to 1700 nm wavelength interval and radiometric BT(R)DF across wavelength sub-intervals defined by the absorption filters described in Chapter 5. Although it will not provide the full spectral radiometric BT(R)DF possible with such devices as the DTU goniophotometer, it will provide useful spectral information much more rapidly. This is achieved through spectroradiometric calibration of a charge coupled device (CCD) and an Indium Gallium Arsenide (InGaAs) NIR digital camera used in conjunction with absorption filters as described in Chapter 5.

For each angle of incidence investigated, images will be taken with the CCD camera using eight filter combinations to isolate eight different wavelength intervals at a few integration times. Images will be taken with the InGaAs camera for only one wavelength interval (its full range) at a few integration times. The total time necessary for image acquisition and filter positioning at one angle of incidence and one band is likely to be around 5 seconds, depending on the final speed of the filter wheel. An additional 5 seconds is expected for positioning the table between each angle of incidence. With these assumptions, one angle of incidence will require 50 seconds. If 145 angles are studied, adding an additional 2 minutes for changing the digital cameras, a full analysis is likely to take around 2 hours. This is much faster than all the existing scanning goniophotometers and about four times as fast as the fastest video-projection goniophotometer (Andersen and de Boer 2006).

The light source is sampled using combined long pass and short pass filters to isolate wavelength intervals. For transmission measurements, the filtered radiation directly illuminates a sample mounted on a rotating table with two degrees of rotational freedom (Andersen et al. 2005c). In reflection mode, radiation must pass through the hemi-ellipsoid to illuminate a sample from the top. The sample is located at one focal point of the hemi-ellipsoid. Radiation is then re-directed by the sample through transmission or reflection. A portion of this re-directed light is specularly reflected off of the half-mirrored hemi-ellipsoid towards the other focal point of the hemi-ellipsoid, where the fish eye lens and digital camera are located. The radiance viewed by the camera is then recorded in a series of images, taken at different integration times, to capture the full range of radiances and luminances re-directed by the sample for each wavelength interval.

Once images have been recorded by the camera for each wavelength interval, the images can be processed to calculate quasi-spectral BT(R)DFs for the sample. Using the spectroradiometric calibration described in Chapter 5 of this thesis, the digital output of the camera can be used to estimate the radiance viewed by the camera from each direction for each wavelength interval. Re-scaling this radiance to account for the known spectral reflectivity of the ellipsoid, the radiance emerging from the sample in each direction can be estimated. Finally, knowing the irradiance on the sample, accounting for the spectral transmissivity of the filters and the ellipsoid, the radiance emerging from the sample in every direction can be compared to the irradiance of the sample for each filter combination, which correspond to different wavelength intervals. This provides an estimate of the radiometric BT(R)DF of the sample to the filtered radiation over each interval. These BT(R)DFs can then be used to estimate the average BT(R)DF of the sample to the unfiltered spectrum across smaller, non-overlapping wavebands within each wavelength interval defined by the filters (which overlap). These smaller wavebands are explained in Chapter 6 and correspond to sub-intervals within each filter’s wavelength interval where the transmitted radiation is above a threshold and the sensitivity of the camera channel being used is reasonably constant.

From these average BT(R)DFs across non-overlapping wavebands, a quasi-spectral BT(R)DF can be constructed across the full wavelength range to which the cameras are sensitive, 380 to 1700 nm. From these quasi-spectral BT(R)DFs, the total (i.e. not quasi-spectral) radiometric and photometric BT(R)DFs from 380 to 1700 nm can be calculated for a given spectrum, such as the solar spectrum.

So long as the spectrum of the lamp used for experiments has a similar relative spectrum to that of the solar spectrum and the digital cameras can accurately measure the radiance of the filtered radiation, the estimated average radiometric BT(R)DF across each wavelength interval will be accurate. If the radiance of unknown spectra can indeed be measured accurately over large wavelength intervals using the digital cameras, passband filters can be used that are larger than narrow passband filters to enable faster analysis. The details of measuring radiances with the digital cameras and estimating quasi-spectral and total BT(R)DFs will be explained in Chapters 5 and 6. The remainder of this chapter will describe specific components of the spectral, video goniophotometer.

3.2 Components

3.2.1 Rotating Sample Holder

Figure 3.2 Rotating Sample Holder and Hemi-Ellipsoid

A rotating table with two degrees of rotational freedom is used to hold fenestration system samples and the half-mirrored hemi-ellipsoid. A diagram of the table and a picture with the hemi-ellipsoid mounted are shown in Figure 3.2. The rotating table and motors were designed and constructed by Dean Ljubicic, and the motors, electronics and controls were designed or refined by Courtney Phillips/Browne (Browne 2006), Siân Kleindienst, Zachary Clifford, Timothy Koch, Roselin Osser, and Steve Banzaert.

Two separate motors control the altitude and azimuth angles of the table, which are used to set the zenithal and azimuthal angles of incidence for light on a sample. The table also includes a camera mount, a port for the digital cameras and a mechanism for mounting samples. The sample is mounted at one focal point of the hemi-ellipsoid and the fish eye lens of the camera is located at the other focal point. A full description of the design and construction of the rotating table can be found in (Ljubicic 2005). There are a limited number of incidence angles that cannot be recorded without rotating the sample itself due to the camera obstructing the light beam.

3.2.2 Light Source, Filter Wheel and Beam Shaper

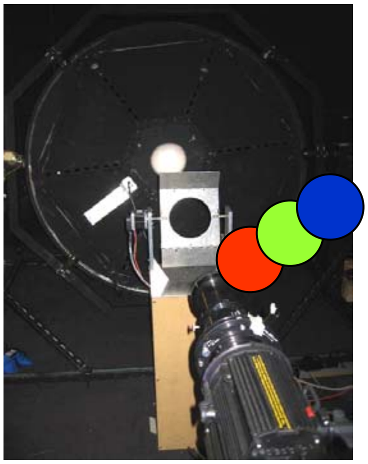

Figure 3.3 Light Source, Beam Shaper and Color Glass Filters

The light source for the goniophotometer is a 400W Dedolight HMI lamp chosen for its relative spectrum, which is similar to sunlight, and its collimation (Browne 2006). The light is positioned perpendicularly to the sample with the table in the vertical position. A beam shaper is used to ensure a fixed spot size for different angles of incidence on the sample. The beam shaper rotates to the same angle as the rotating table, limiting the edges of the spot in the vertical direction. A filter wheel, still under development (Koch 2007), will cycle through combinations of Schott Color glass longpass and shortpass filters to sample the Dedolight spectrum. The specific filters chosen will be explained in chapter 5. The arrangement of the light source, beam shaper and filters (represented by colored circles) is shown in Figure 3.3.

3.2.3 Half-Mirrored, Hemi-Ellipsoid

The hemi-ellipsoid is an extruded acrylic shell coated with a thin film of aluminum. American Tooling and Engineering, Inc. made the aluminum tool used for forming the ellipsoid, and Spartech PDC extruded melted acrylic sheets over the tool.

Courtney Phillips designed and managed the production of the acrylic hemi-ellipsoids. The final dimensions of the hemi-ellipsoid are shown in Figure 3.4 (Browne 2006). Six hemi-ellipsoids were produced and the one with the least deformities was chosen for the goniophotometer. To create a half-mirror, the hemi-ellipsoids were coated with a thin film of aluminum, as described in Chapter 4.

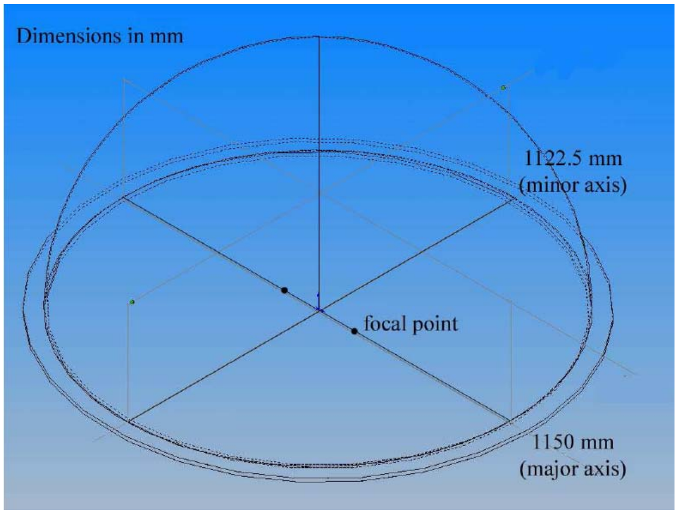

Figure 3.4 Final ellipsoid dimensions (Browne 2006)

3.2.4 Digital Cameras

Two digital cameras were selected for the spectral video-goniophotometer, a charge coupled device (CCD) camera covering the visible range and the beginning of the NIR, and an Indium Gallium Arsenide (InGaAs) camera covering a range of 900 to 1700 nm in the NIR. These two cameras were selected to span the wavelengths over which the spectral power distribution of solar radiation is most significant. Initially, Vidicon tube and Lead Sulfide cameras were investigated to capture a wavelength range extending up to 2200 nm in the NIR, including a greater portion of the solar spectrum. However, these cameras were found to provide an unreliable relationship between output and the radiance viewed by the camera. The output changed significantly as the camera heated up, and residual spots after

Figure 3.5 SU320 NIR camera and Kappa color CCD camera

pixels were saturated lasted many minutes. These factors made it impossible to use the output of the camera as a way to estimate the radiance of a scene. Instead, semiconductor array cameras were selected for both the visible and the NIR.

The silicon chip CCD camera is a Kappa DX20 color CCD camera, shown in Figure 3.5. The InGaAs camera, a Sensors Unlimited SU320 1.7RT camera, is also shown. A Fujinon FE185C057HA high resolution fisheye lens is used with both cameras. The NIR filter has been removed from the CCD camera to capture wavelengths between 780 and 945 nm. A photopic V(λ) filter could be applied to the fisheye lens in order to measure photometric BT(R)DFs, similar to other applications in which digital cameras are used to measure luminance, such as (Bellia et al. 2002). However, the goal of this device is to also measure the radiometric BT(R)DFs across the solar spectrum, as well as its spectral dependence, while still providing reasonably accurate photometric BT(R)DF. Rather than using V(λ) filters on the camera lens, absorption filters are then used to sample incident light into wavelength intervals over which the cameras output can still measure total radiance across the interval reliably. This method will be explained in detail in Chapter 5.

3.2.5 Image Acquisition and Processing

The components described above are the primary parts of the spectral video-goniophotometer. However, there are many computer controls necessary for capturing, communicating, and processing images that are critical elements of the device. A Visual Basic script is used as an interface to the user and to control the rotating table. Another script is used to command the CCD camera. Currently, the NIR camera is controlled using a National Instruments (IMAQ) interface, but control of the NIR camera will ultimately be integrated into the goniophotometer interface. This includes control of the integration time for the NIR camera which is currently controlled manually with a dial. Once images have been captured by one of the cameras, they will be exported to Matlab® for image analysis, BT(R)DF calculation and visualization. The program will then provide saved data and visualized BT(R)DFs to the user.

4. Developing the Hemi-Ellipsoid

Of the components described above, the hemi-ellipsoid deserves special attention due to its importance in imaging and the possibility that it may change the spectrum of transmitted or reflected radiation. Coating the hemi-ellipsoid and developing methods for measuring its spectral properties are thus critical steps in the development of the goniophotometer. This chapter will describe the coating process, the procedures followed to measure spectral transmission, reflection and absorption at different locations on the ellipsoid, and their results.

4.1 Coating Methods and Simulations

Figure 4.1 Tanury PVD vacuum chamber (Tanury 2007)

Six hemi-ellipsoids were made of extruded acrylic coated with a thin-film of aluminum. The six hemi-ellipsoids were coated at Tanury Industries using a cathodic arc evaporation physical vapor deposition (PVD) process in the vacuum chamber shown in Figure 4.1. This process allows deposition of metals on low temperature substrates, such as acrylic, which would melt at higher temperatures. A low voltage, high current arc was struck on an aluminum target creating a jet of ionized, vaporized aluminum in a vacuum (Richter et al. 1998), (Vyskocil et al. 1992). This deposited a very thin layer of aluminum on the acrylic hemi-ellipsoid. The hemi-ellipsoids with greater deformities were used as test cases to experiment with coating methodologies, such as the position of the hemi-ellipsoid, the vacuum strength and arc power.

The hemi-ellipsoids were mounted, one at a time, in a vacuum chamber and coated with aluminum as they rotated within the chamber. They were mounted flat in the chamber, such that their edges were perpendicular to the target. In this position, the edges of the hemi-ellipsoids had greater exposure to the jet of ionized aluminum from the target and received a thicker coating. However, compared to alternative set-ups, such as mounting the hemi-ellipsoids on their side, this presented a coating method with the most predictable variation in thin-film thickness. It was expected that the thickness would vary primarily with zenith along the hemi-ellipsoid, and less with azimuth.

The following procedures were followed for the first attempt at creating a semi-transparent hemi-ellipsoid. The hemi-ellipsoid was mounted flat in the chamber, sealed in, and the chamber was evacuated to a 1.2E-5 torr vacuum overnight. The hemi-ellipsoid was then coated for 16 minutes, until it was visibly semi-transparent, at a power of 5.5 kW. Following this process, transmission through the hemi-ellipsoid for a small set of wavelengths was estimated using a red laser pointer and an illuminance meter. This was considered a reasonable surrogate for measuring the complete spectral properties of the ellipsoid due to the gradually changing spectral properties of typical aluminum coatings and the unavailability of more sophisticated tools at the PVD facility. The results of these measurements, showing the transmission coefficients of the hemi-ellipsoid to the laser point light as a function of zenith angle on the hemi-ellipsoid, are shown in Figure 4.2, including measured points and a parabolic fit to the data.

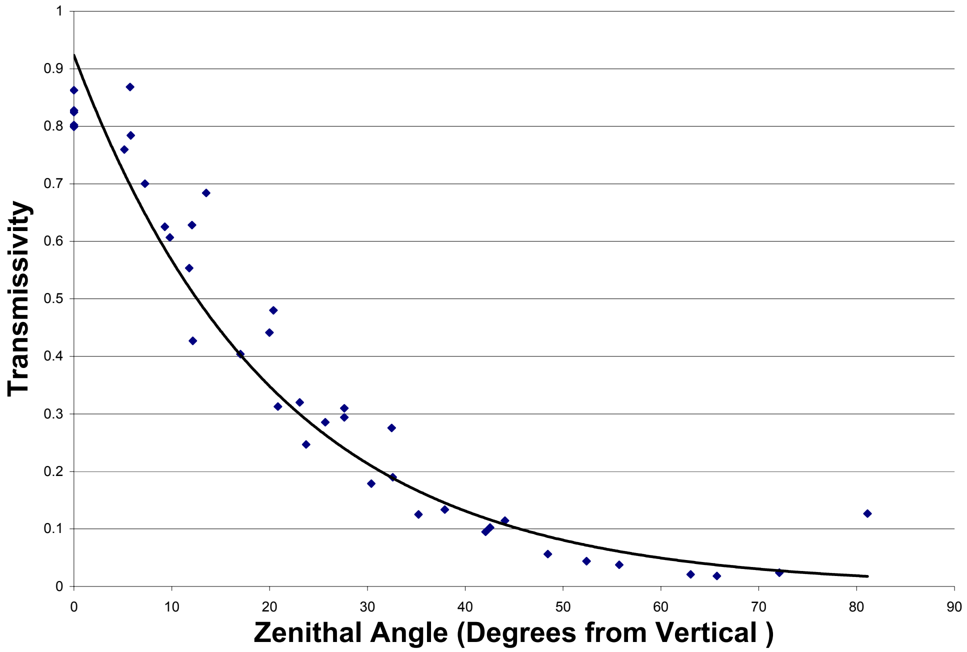

Figure 4.2 Transmissivity versus zenith angle for first semi-transparent hemi-ellipsoid (measurements at many azimuths)

The results show that the variation of transmissivity with zenith angle is very dramatic approaching the apex of this hemi-ellipsoid. For the next attempt, a higher vacuum was created by evacuating the chamber for two nights in an effort to increase the throw of the vaporized aluminum from the target over the top of the hemi-ellipsoid. A 9.3E-6 torr vacuum was achieved and the power was kept at about 5.5 kW, but the coating time was reduced to five minutes because the coating became visibly more opaque much faster. The results of the second coating attempt are shown in Figure 4.3, again with measured points and a parabolic fit.

The second coating did achieve a more uniform transmissivity as a function of zenith angle. This variation would be easier to account for during the goniophotometer's measurement process than the first coating, both because of the gradual variation with zenith angle and the similarity between different azimuth angles. A third coating was attempted at the same power and a similar vacuum pressure of 8.9E-6 torr, but with a shorter coating time. To estimate the length of time necessary for coating it was assumed that the decrease in the transmissivity of the coating varied directly with coating time. Figure 4.4 shows the results of scaling the measured data points for the five minute coating to predict the results of a three minute coating, assuming that the change in transmissivity is directly proportional to the ratio of coating times, or three fifths.

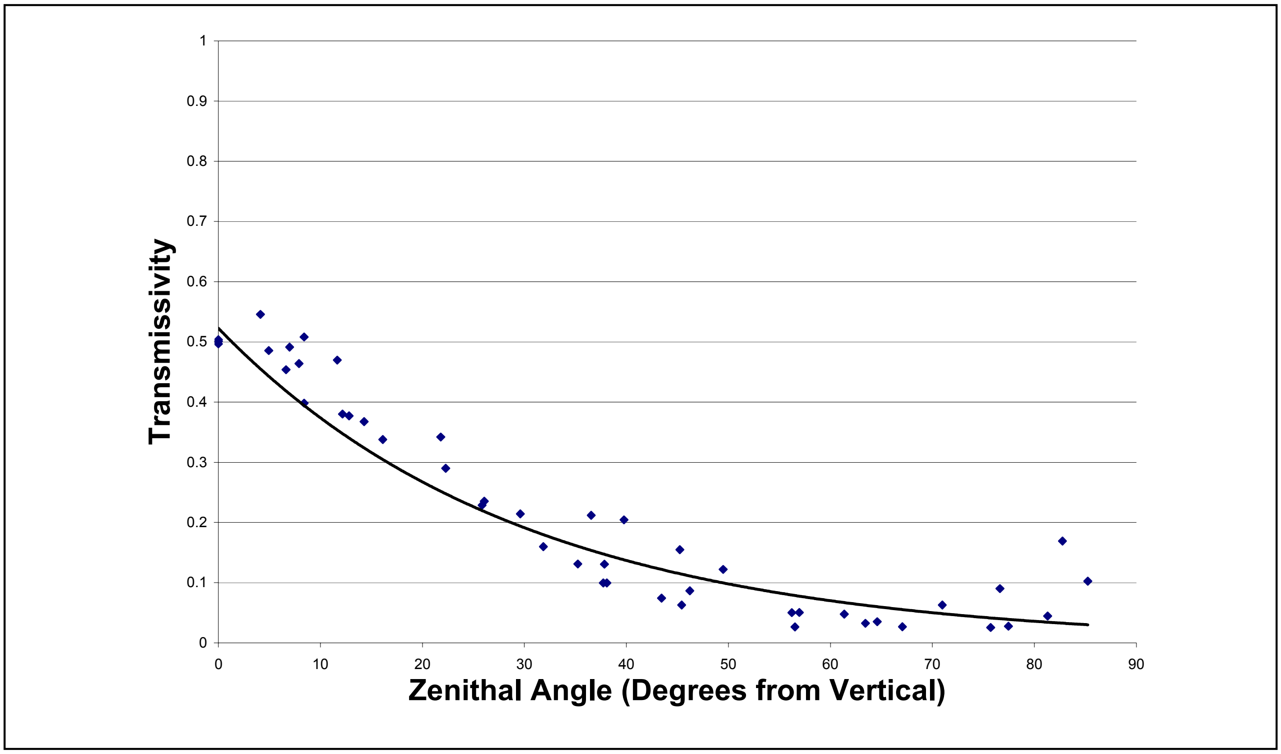

Figure 4.3 Transmissivity versus zenith angle for second semi-transparent hemi-ellipsoid (measurements taken at many azimuths)

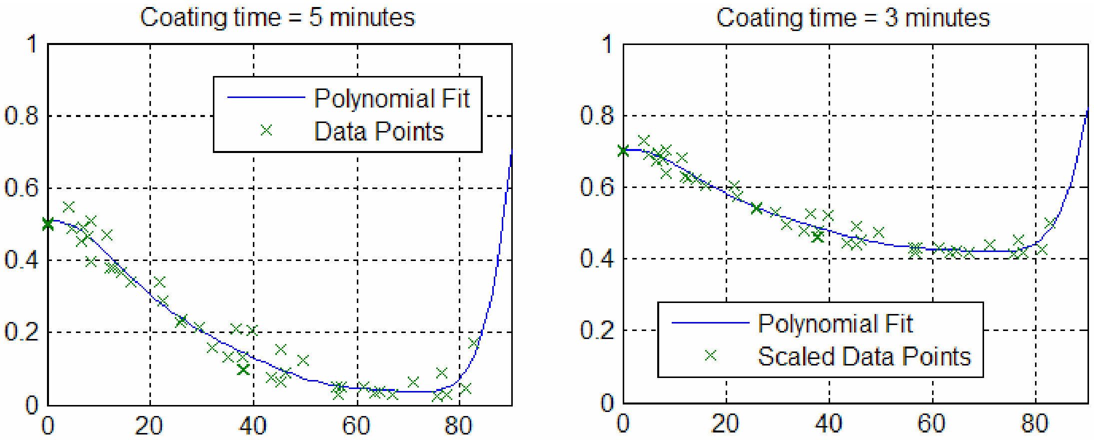

Figure 4.4 Measured data vs predicted data assuming a direct relationship between the decrease in transmissivity and coating time

Using this prediction, the third coating was performed with a target coating time of three minutes. However, during the coating process the hemi-ellipsoid seemed more opaque than optimally desired, similar to the previous five minute coat. As a result, the decision was made to stop the third coat at two minutes and forty seconds.

The results of the third coating attempt are shown in Figure 4.5. The results show that along a few azimuths the transmission of the laser light through the hemi-ellipsoid varied with zenith angle similarly to that predicted, except for greater transmissivity near the apex. However, along one side of the hemi-ellipsoid, the coating was not as thick. This is probably the influence of a short coating time relative to the rotation speed of the ellipsoid within the chamber, which, although not known precisely was on the order of one rotation per thirty seconds.

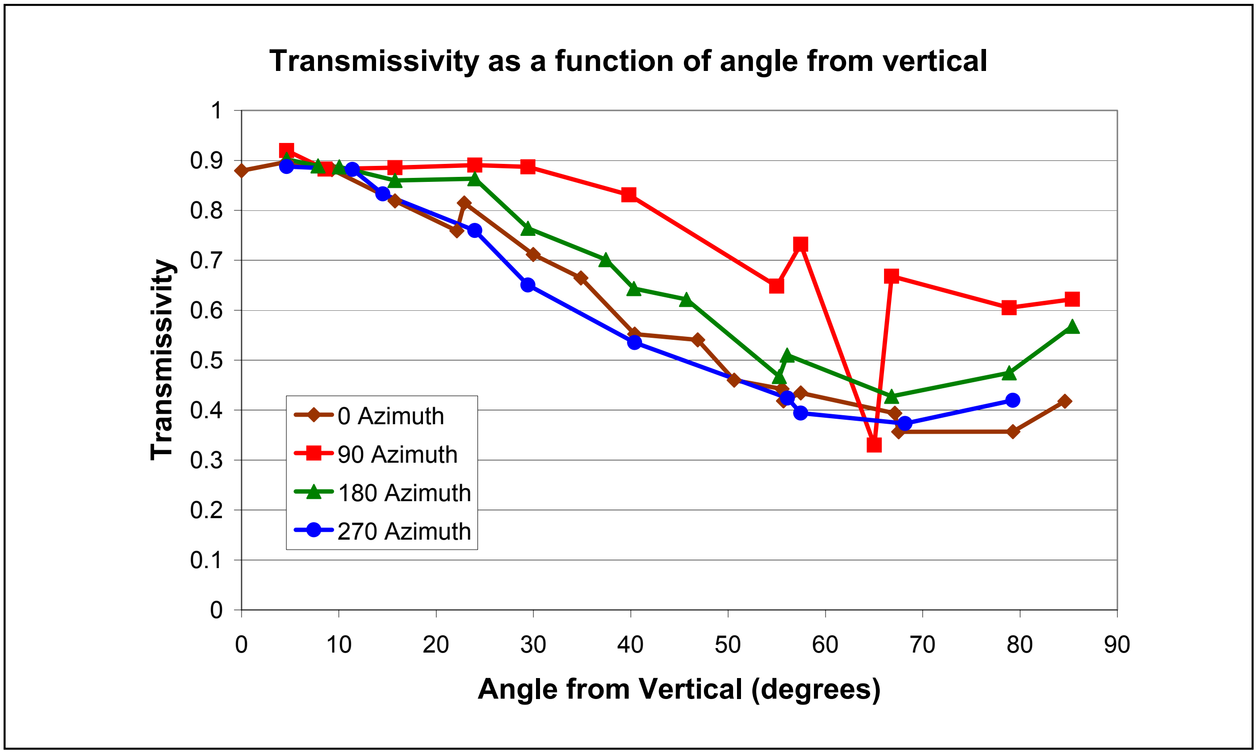

Figure 4.5 Transmissivity versus zenith angle for third semi-transparent hemi-ellipsoid (measurements taken at many azimuths)

Among the available semi-transparent hemi-ellipsoids, the second coating presented above was chosen due to its predictable zenithal and azimuthal variations and reasonable semi-transparency for zenithal angles below about 60 degrees. It will be shown later that in order to create a semi-transparent hemi-ellipsoid with similar reflection and transmission coefficients to maximize transmission and reflection, the second coating is a reasonable compromise because of the high absorptivity of thin-film aluminum coatings. A thin film coating of aluminum with around 50 percent transmission for the laser pointer would have a very low reflection coefficient. A coating that was 50 percent transmissive and 50 percent reflective, or close to it, could not have been achieved with a thin film of aluminum on acrylic (see section 4.3).

The remaining three of the six hemi-ellipsoids were used to test completely reflective coatings and coatings in other orientations. All of these coatings were not viable for the goniophotometer in reflection mode due to highly non-uniform coatings, opaque coatings, or “poisoned” coatings for which trace gases in the chamber altered the color of the aluminum thin film. In retrospect, other assumptions could have been made about the variation of transmissivity with coating time based on the deposition rate of the thin film, if it could have been determined, but these methods were not realized at the time of the coating.

4.2 Measuring Spectral Transmission and Reflection

Once the coatings were completed, the semi-transparent hemi-ellipsoids were transported back to the lab for testing. Because the goniophotometer will ultimately measure quasi-spectral BT(R)DFs, it is necessary to account for the spectral transmission and reflection through or off of the hemi-ellipsoid when calculating the change in spectrum caused by a fenestration system sample. This requires detailed knowledge of spectral transmission and reflection properties of the hemi-ellipsoid across the 380 to 1700 nm range.

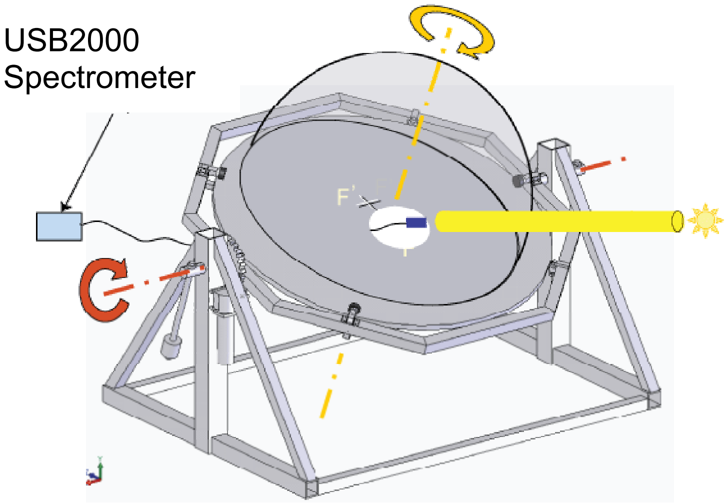

Figure 4.6 Transmissivity measurement set-up

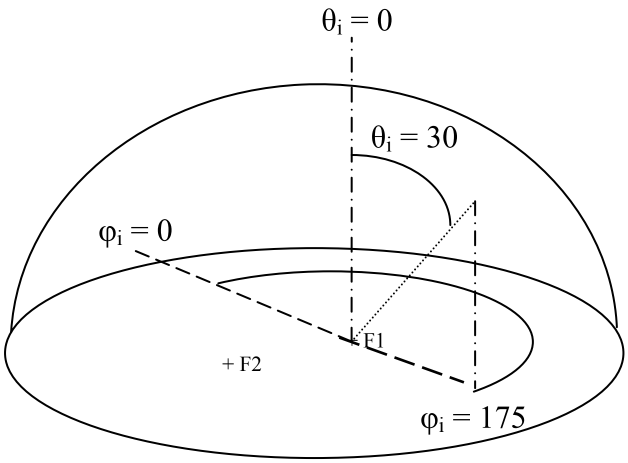

Figure 4.7 Sample-oriented (or table-oriented) coordinate system

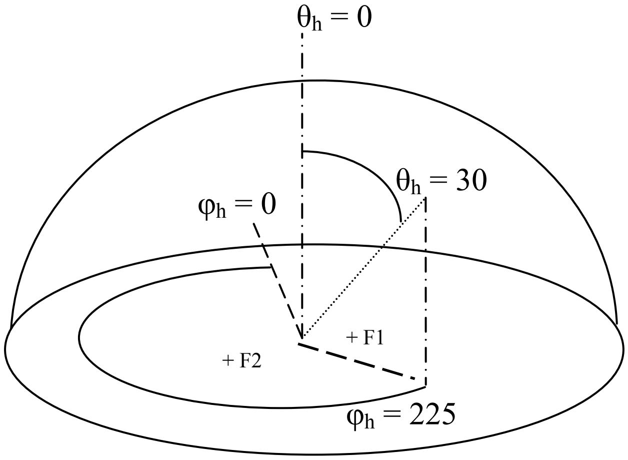

Figure 4.8 Ellipsoid-oriented coordinate system

In order to measure spectral transmission coefficients across the 380 to 900 nm range, an Ocean Optics USB2000 spectrometer was used to compare the spectrum of the HMI lamp with and without passing through the ellipsoid. A schematic of the setup for the transmission measurement experiment is shown in Figure 4.6.

Measurements were taken for two different coordinate systems. One set of measurements was taken for coordinates determined by movements of the rotating table, which correspond to angles of incidence on a sample, as shown in Figure 4.7. Another set of measurements were taken for coordinates determined by the geometry of the hemi-ellipsoid, where the zero zenith is at the apex of the hemi-ellipsoid and the zero azimuth is on a semi-minor axis, shown in Figure 4.8. These two coordinate systems were chosen so that measurements were available that either directly corresponded to incidence angles on a sample (Figure 4.7), or were independent of the table and sample positioning (Figure 4.8) so that if changes to the table coordinate system occurred (e.g. if the azimuth or altitude positioning changed due to modifications to its controls or errors in motor positioning) the properties of the hemi-ellipsoid would still be known in a independent coordinate system.

The following procedures were followed for transmission measurements in the sample-oriented coordinate system. The spectrometer was fixed in place through the sample holder port facing the HMI lamp. First, the spectrum of the HMI lamp was measured before fixing the hemi-ellipsoid on the table. Next, the hemi-ellipsoid was fixed in place and the spectrum of the HMI lamp, after passing through the hemi-ellipsoid, was measured for many angles of incidence to fenestration samples.

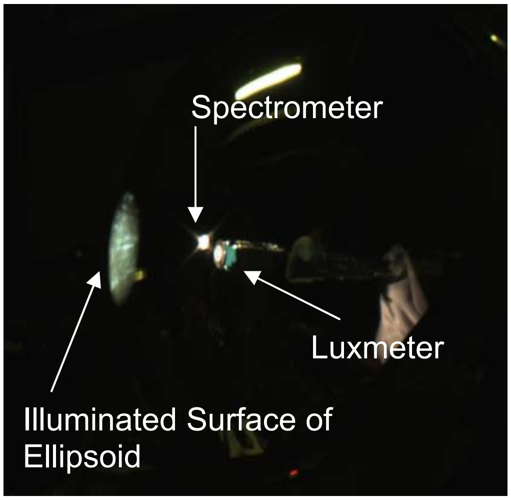

Figure 4.9 Typical transmission measurement

Measurements were taken at zenith angles 0 through 80 by ten degree increments and 85, and azimuth angles 0 to 315 by 45 degree increments. A picture of the experiment is shown in Figure 4.9. The instruments in the center are the end of the spectrometer fiber optic cable and an illuminance meter, which was used to check the consistency of the spectrometer measurements. The spot to the left of the picture is the edge of the hemi-ellipsoid. The HMI lamp is not shown. The results of the spectral transmission measurements for zenith angles 30 and 50 are shown in Figures 4.10 and 4.11.

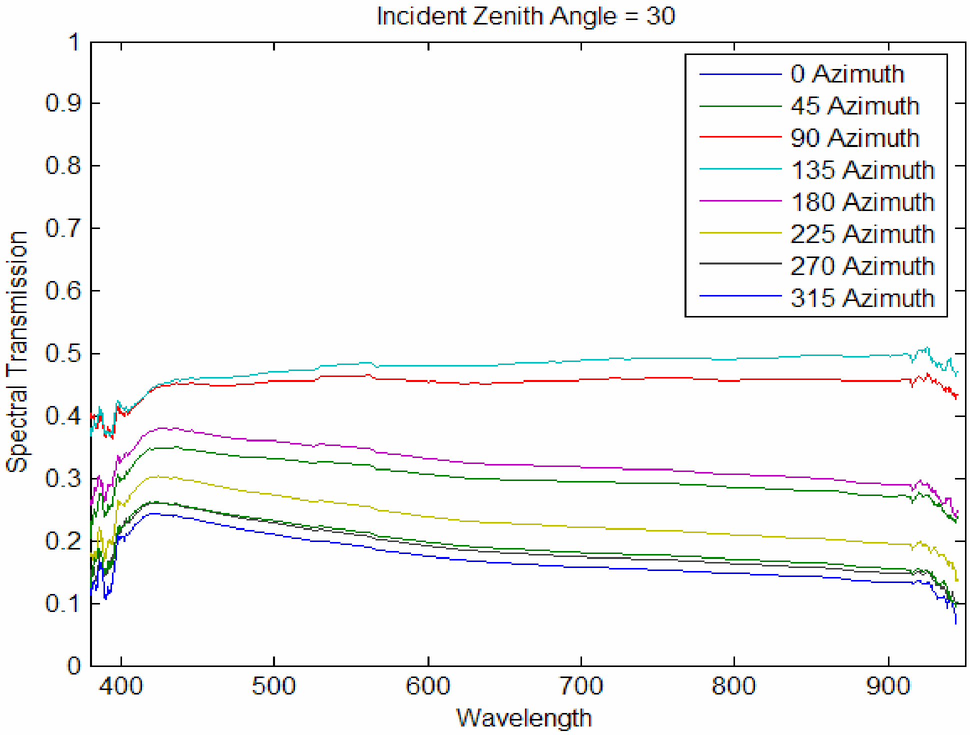

Figure 4.10 Spectral transmission by the ellipsoid for a zenith angle of incidence of 30 degrees from 380 to 950 nm

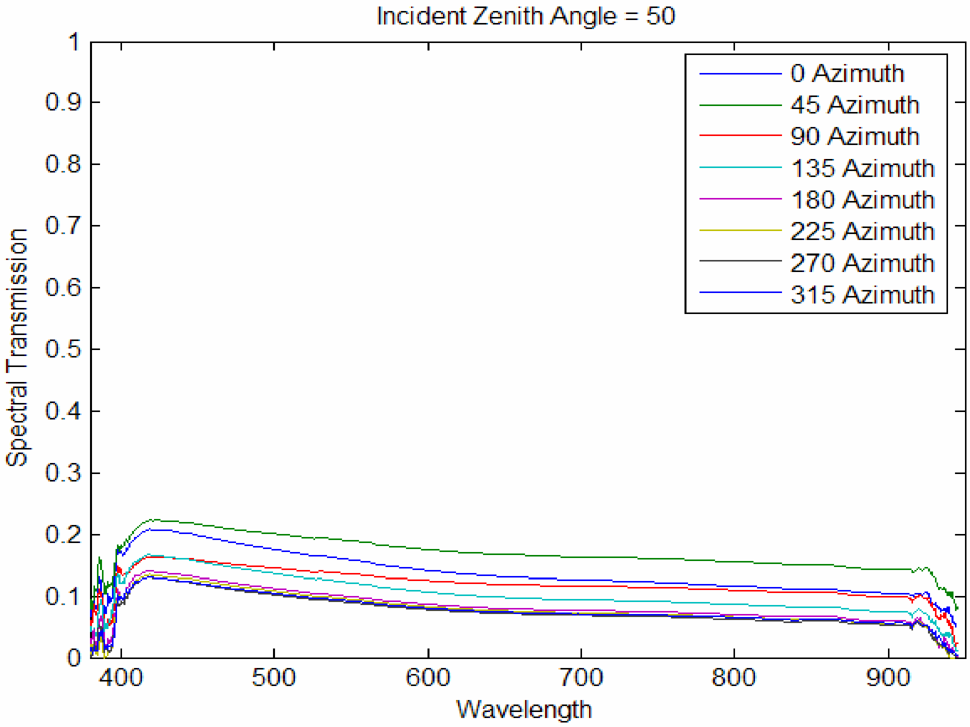

Figure 4.11 Spectral transmission by the ellipsoid for a zenith angle of incidence of 50 degrees from 380 to 950 nm

The results show that for low zenithal angles of incidence, spectral transmission by the hemi-ellipsoid can vary greatly with azimuth angle. On the other hand, the spectral transmission does not vary much by azimuth for high zenithal angles. The results also show that, as expected, for lower zenith angles, where light passes closer to the apex of the hemi-ellipsoid, transmission through the ellipsoid is greater overall.

Reflection measurements were also taken in the sample-oriented coordinate system. In this case, the HMI lamp was positioned through the sample holder port, and the spectrometer was positioned through the camera port pointing towards the reflected beam. A picture of this setup is shown in Figure 4.12.

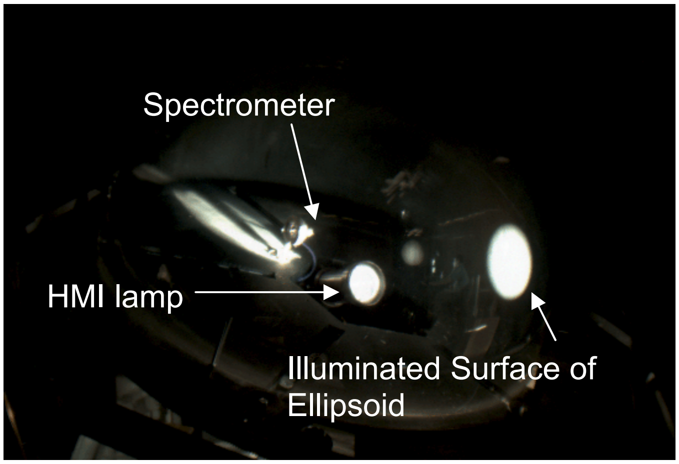

Figure 4.12 Reflection measurement set-up

It was difficult to measure a baseline spectrum for reflection measurements. In theory, the spectral irradiance of the HMI lamp could be measured for each position by removing the hemi-ellipsoid and moving the spectrometer to the position corresponding to the same distance in front of the beam as that traveled by the reflected beam. However, this measurement technique is not reliable because spectrometer measurements depend so much on the orientation of the spectrometer. Instead, the spectrum of the HMI lamp was measured at a distance equal to the average total distance from the HMI lamp to the ellipsoid and then to the spectrometer once with precise orientation of the spectrometer. This measurement was used as the comparison to the spectrum of the beam reflected off of the hemi-ellipsoid. In addition, it was difficult to ensure that the angle of acceptance to the spectrometer remained the same for all measurements and that the spectrometer readings were not influenced by re-positioning at each azimuth and zenith angle. As a result, the magnitude of the reflection coefficients are considered to be slightly inaccurate, but the shape of the

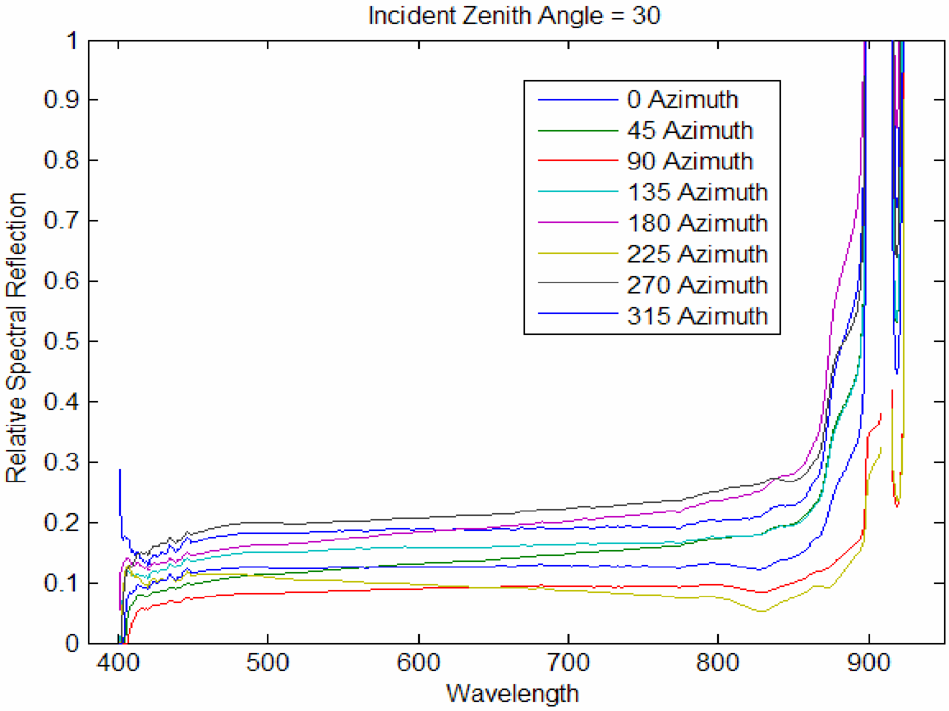

Figure 4.13 Relative spectral reflection for zenithal angle of incidence of 30 degrees for 380 to 950 nm

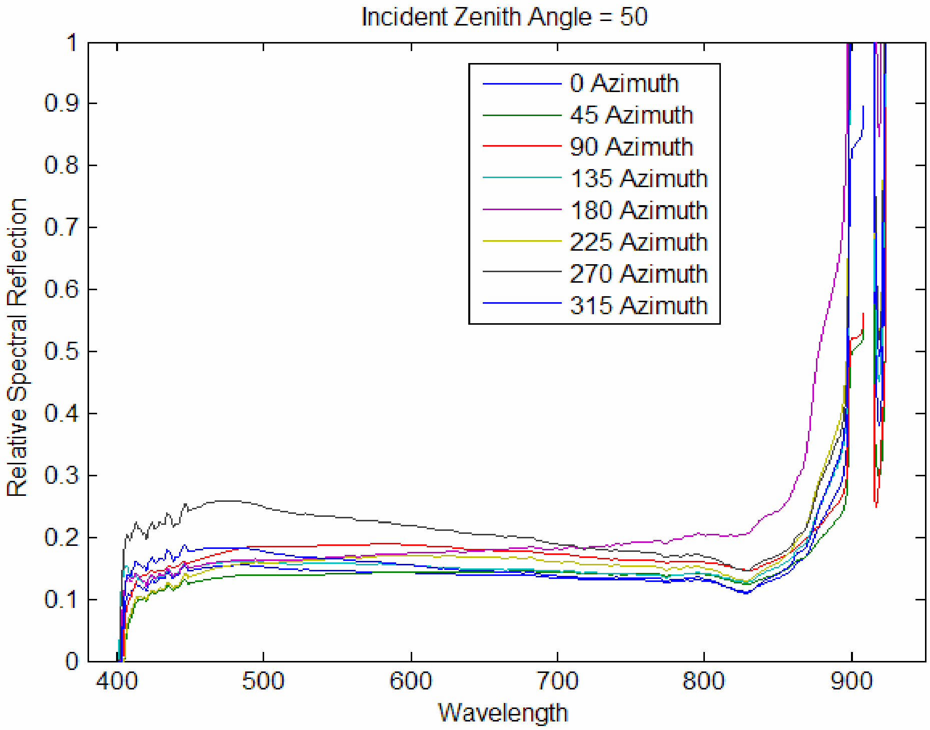

Figure 4.14 Relative spectral reflection for zenithal Angle of incidence of 50 degrees for 380 to 950 nm

spectral reflection coefficients relative to each other are considered accurate. The results for the 30 and 50 degree zenithal angles of incidence are shown in Figures 4.13 and 4.14.

The reflection measurements results, although not reliable in magnitude, show that the spectral reflection coefficients are relatively flat. The behavior at the edges is considered non-physical, but rather an artifact of low spectral irradiances in the part of the spectrum below 400 nm and above 850 nm to which the spectrometer was marginally sensitive.

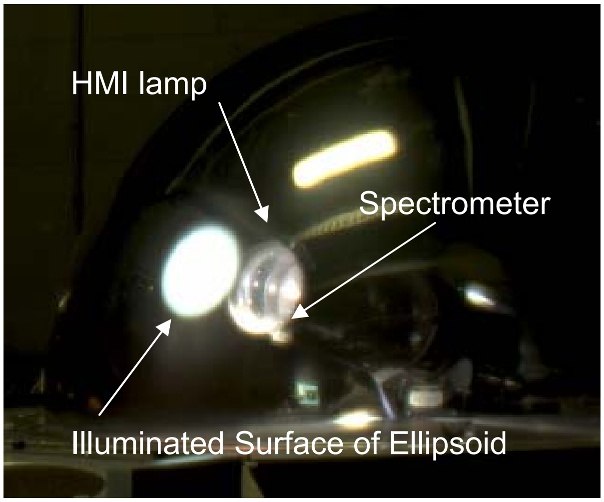

Figure 4.15 New reflection measurement set-up

A similar series of measurements were also taken in the ellipsoid-oriented coordinate system for both transmission and reflection. Transmission measurements were taken by centering the hemi-ellipsoid on the rotating table and taking transmission measurements exactly as previously described but in this new position, using the apex and a semi-minor axis of the ellipsoid as zenith and azimuth references. Reflection measurements were also taken in this coordinate system by positioning the Dedolight very close to the inside surface of the hemi-ellipsoid and measuring spectra immediately after the light is reflected from the surface. The setup for these reflection measurements is shown in Figure 4.15.

The results of these experiments for zenithal angles fixed to the hemi-ellipsoid of 10 and 80 degrees are shown in Figure 4.16. Again, the spectral behavior towards each end of the spectrum is considered to be an artifact of the low spectral irradiance in that part of the spectrum, and thus poor readings by the spectrometer, and not real properties of the hemi-ellipsoid.

The methods developed here provide spectral transmission coefficients and approximate spectral reflection coefficients of the hemi-ellipsoid across a 400 nm to about 900 nm interval It will be assumed that the trends continue to 380 nm. These coefficients were measured in two coordinate systems. A sample-oriented coordinate system will ultimately be used for goniophotometer experiments, however measurements will have to be repeated because the hemi-ellipsoid will be modified as described in section 4.5. It is useful to know the coefficients in the ellipsoid-oriented coordinate system because they are independent of any other component of the goniophotometer. Because the spectral transmission and reflection properties of the ellipsoid vary gradually with azimuth and altitude, interpolation will be used to estimate the spectral properties between the zenith and azimuth angles for which these properties are measured.

Additional information is necessary to determine the precise magnitude of the spectral reflection coefficients because the spectral irradiance to which reflected radiation was compared did not have the exact magnitude of the true non-reflected beam because, for reasons described above.   Therefore, the final step in measuring the hemi-ellipsoid's spectral reflection coefficients across the 380 to 900 nm range is to fix the absolute position of the approximate spectral reflection curves using a relation between transmission and reflection coefficients derived in the next section.

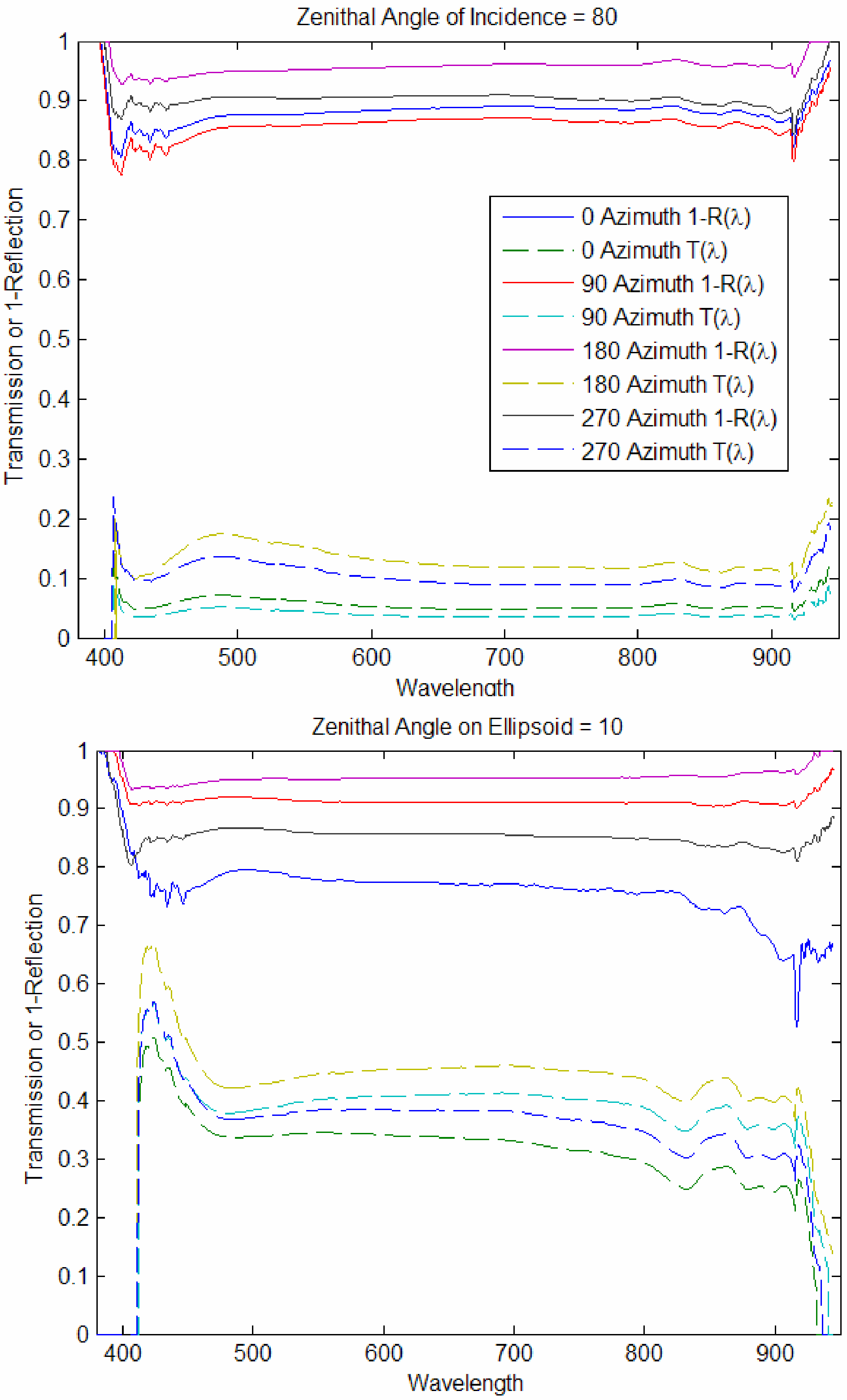

Figure 4.16 Spectral transmission and reflection at hemi-ellipsoid coordinates for two zenith angles

4.3 Relating Reflection to Transmission

Although the magnitude of the spectral reflection coefficients presented in section 4.2 are considered inaccurate, as described above, the *shape* of these curves is assumed to be correct. Additional measurements were conducted to scale the spectral reflection curves measured above to their true magnitude. To achieve this, the precise reflection, transmission and absorption coefficients were measured at a few wavelengths and many points on the hemi-ellipsoid. These measured points were then used to fix the magnitude of the spectral reflection curves.

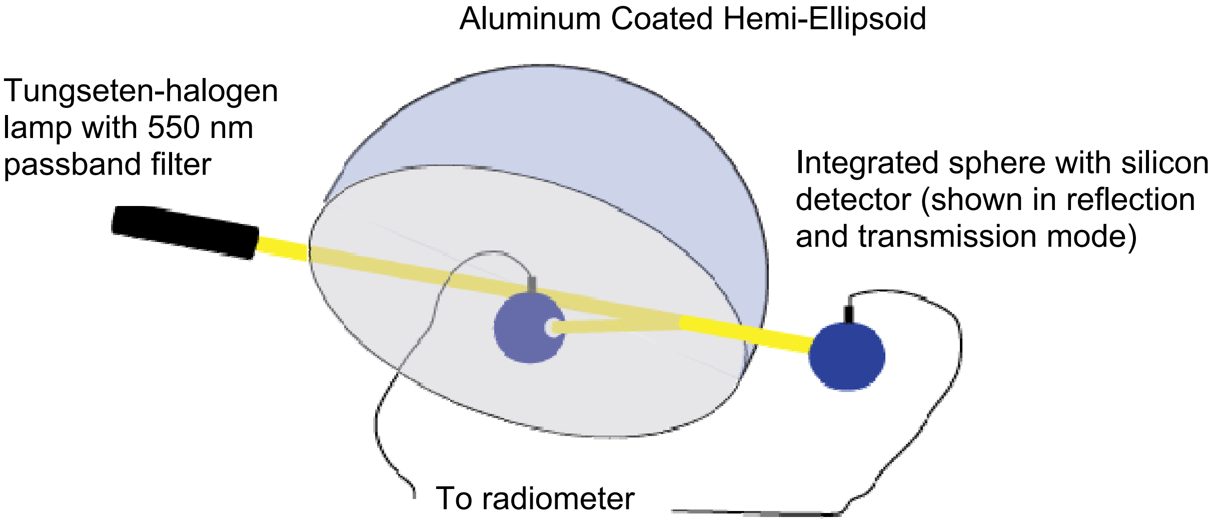

Figure 4.17 Experimental set-up for transmission, reflection, and absorption measurements for 550 nm light

The experiment was conducted with a Labsphere integrating sphere calibrated to measure total radiant flux for monochromatic beams from 375 to 1100 nm at 25 nm increments. A tungsten-halogen lamp with a 550 nm narrow passband filter was placed inside the hemi-ellipsoid and reflected off of its surface. The beam was incident slightly off-normal incidence to the surface of the hemi-ellipsoid so that the reflected beam could be measured without obstructing the incident beam. The integrating sphere was used to measure the total flux in the 550 nm beam in three scenarios: reflected off of the inside of the hemi-ellipsoid, transmitted through the ellipsoid, and without the hemi-ellipsoid. Through these measurements, the reflected, transmitted and baseline radiant flux are known and can be used to calculate the transmission, reflection and absorption coefficients of the hemi-ellipsoid at various zenith and azimuth angles for 550 nm monochromatic radiation.

The setup for these experiments is shown in Figure 4.17. Figure 4.18 shows the measured transmission, reflection and absorption coefficients of the hemi-ellipsoid to 550 nm light along the 180 and 0 degree azimuth angles defined by coordinates relative

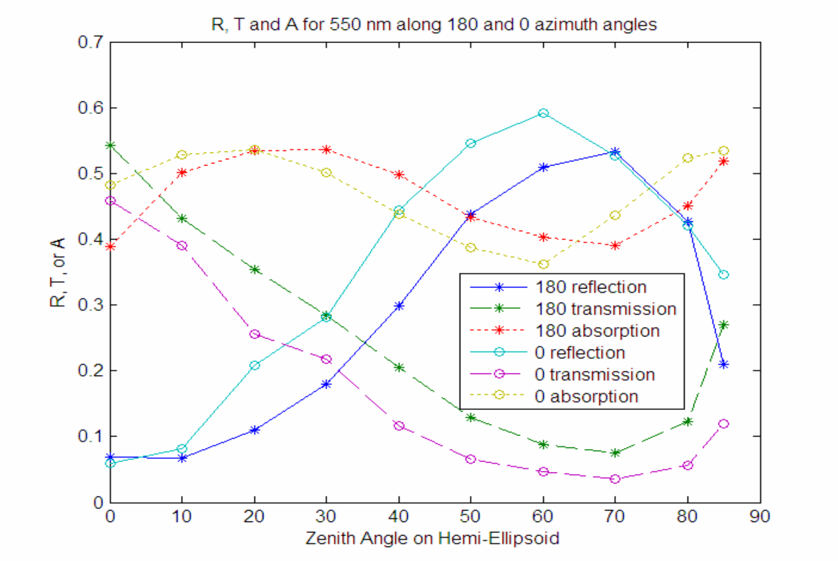

Figure 4.18 Reflection, transmission and absorption coefficents for 550 nm along 0 and 180 degree azimuths

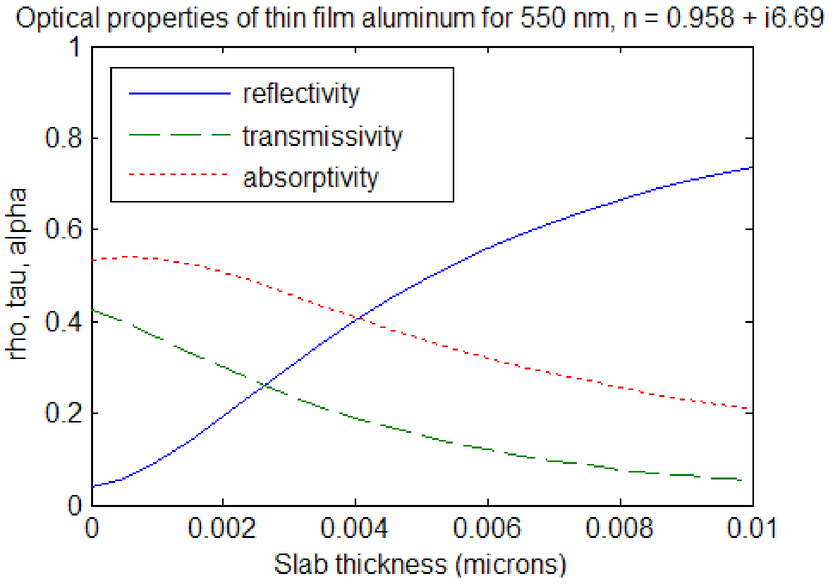

Figure 4.19 Theoretical reflection, transmission and absorption coefficients at 550 nm for a thin film of aluminum

to the hemi-ellipsoid.

The results show that the trend in the measured reflection, transmission and absorption coefficients along each azimuth correspond to an increasing aluminum thin film thickness moving from low zenithal angles to high zenithal angles, as expected. The theoretical coefficients for a thin film of aluminum on a slab of acrylic are shown in Figure 4.19. The thin film model employed to calculate these coefficients as a function of film thickness can be found in (Modest 1993). The complex index of refraction used for aluminum can be found in (Palik 1997) and is also available at (BYU 2007). The index of refraction of acrylic was assumed to be n=1.5.

The theoretical results show that the relationship between reflection, transmission and absorption coefficients measured for the hemi-ellipsoid agree with what is expected from theory, except at the very edges of the hemi-ellipsoid. Note that the film thickness does not increase linearly with zenith and that the exact complex index of refraction of the aluminum is not known. Despite these uncertainties, the theory and measured results show that there is a predictable relationship between reflection, transmission and absorption and a functional relation between them can be determined using experimental data.

Plotting the reflection coefficients against transmission coefficients for 550 nm light for all measured data points leads to a simple curve relating reflection to transmission as shown in Figure 4.20. The outliers from the curve are points along the 0 degree azimuth at the very edges of the hemi-ellipsoid, that is, for zenith angles of 70 degrees or higher. Additional points measured at 70, 80 and 85 degree zenith angles for other azimuths are also plotted to show that the relationship holds for most points on the hemi-ellipsoid except for the few outliers along the 0 degree azimuth. A smaller set of points were measured for lower zenith angles because little deviation from the curve was found in the points measured. A parabolic fit of the measured data points is shown in Figure 4.20 (labeled “predicted curve”) and can be used to calculate reflection coefficients as a function of transmission for a 550 nm wavelength. This measured fit of the data is used instead of trying to deduce the latent variables of film thickness and aluminum index of refraction at every point on the hemi-ellipsoid.

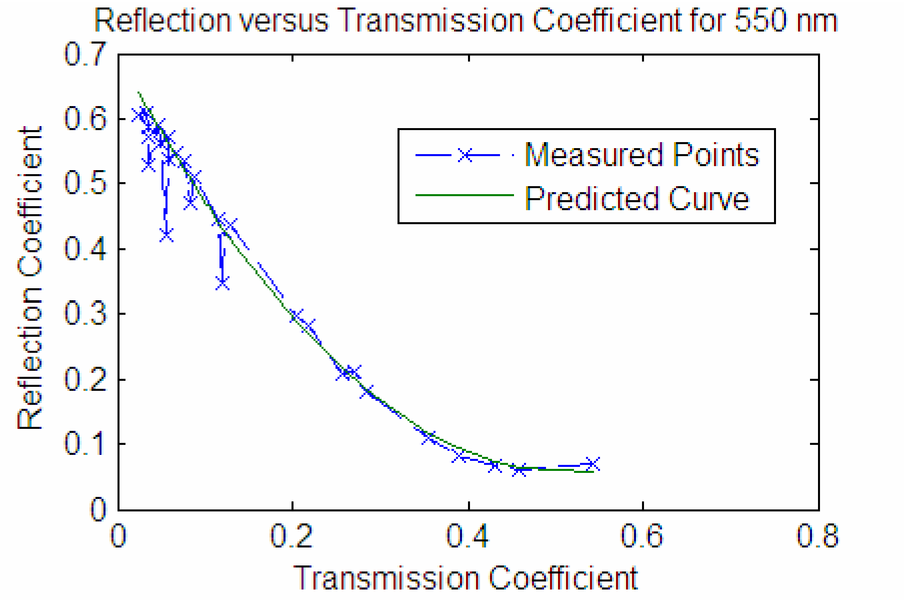

Figure 4.20 Reflection vs transmission coefficients at 550 nm

The relationship found above can then be used to fix the approximate spectral reflection curves found in section 4.2. The magnitude of the 550 nm reflection point had to be calculated from the measured transmission coefficient at 550 nm based on the relationship between reflection and transmission shown above. Because the shape of the curves are assumed to be correct, the spectral reflection coefficients for other wavelengths were simply shifted with the 550 nm point to find the true spectral reflection coefficients across the 380 to 900 nm range.

A sample of the effect of rescaling the measured spectral reflection curves based on this relationship is shown in Figure 4.21 on the following page. One minus the original, measured spectral reflection coefficients are shown as the solid curves on the top graph, and one minus the rescaled spectral reflection coefficients are shown on the bottom graph. The spectral transmission coefficients are shown for both cases.

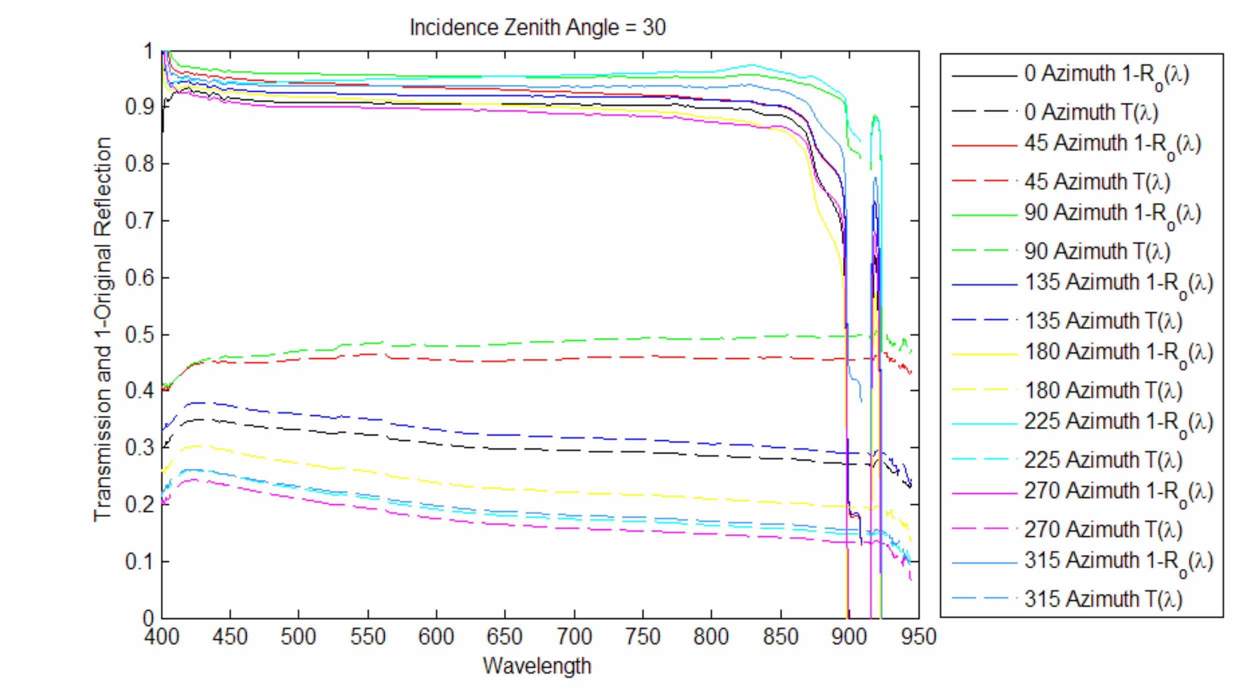

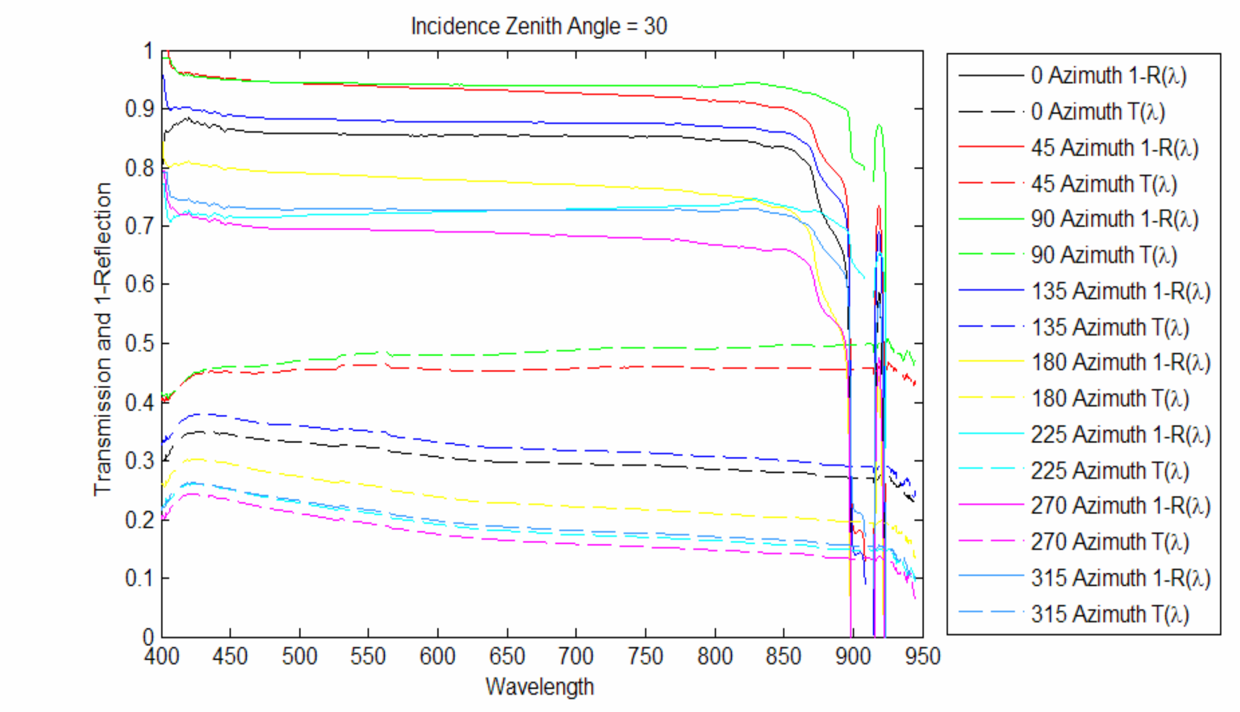

Figure 4.21 Spectral transmission coefficients and one minus the original (o) measured spectral reflection coefficients (top). Same compared to one minus the *rescaled* spectral reflection coefficients (bottom). Note that the difference in the curves gives the spectral absorption coefficients.

4.4 Spectral Properties from 900 to 1700 nm

Although the procedures developed above provide detailed information about the spectral transmission and reflection properties of the hemi-ellipsoid over the 380 to roughly 900 nm range, they do not provide information about its properties from 900 to 1700 nm because the spectrometer is insensitive to these wavelengths. According to theory, the spectral transmission and reflection coefficients for a thin film of aluminum on acrylic are given by the curves shown in Figure 4.22. These curves are again based on the wavelength dependent complex index of refraction published in (Palik 1997) and an acrylic index of refraction of n=1.5.

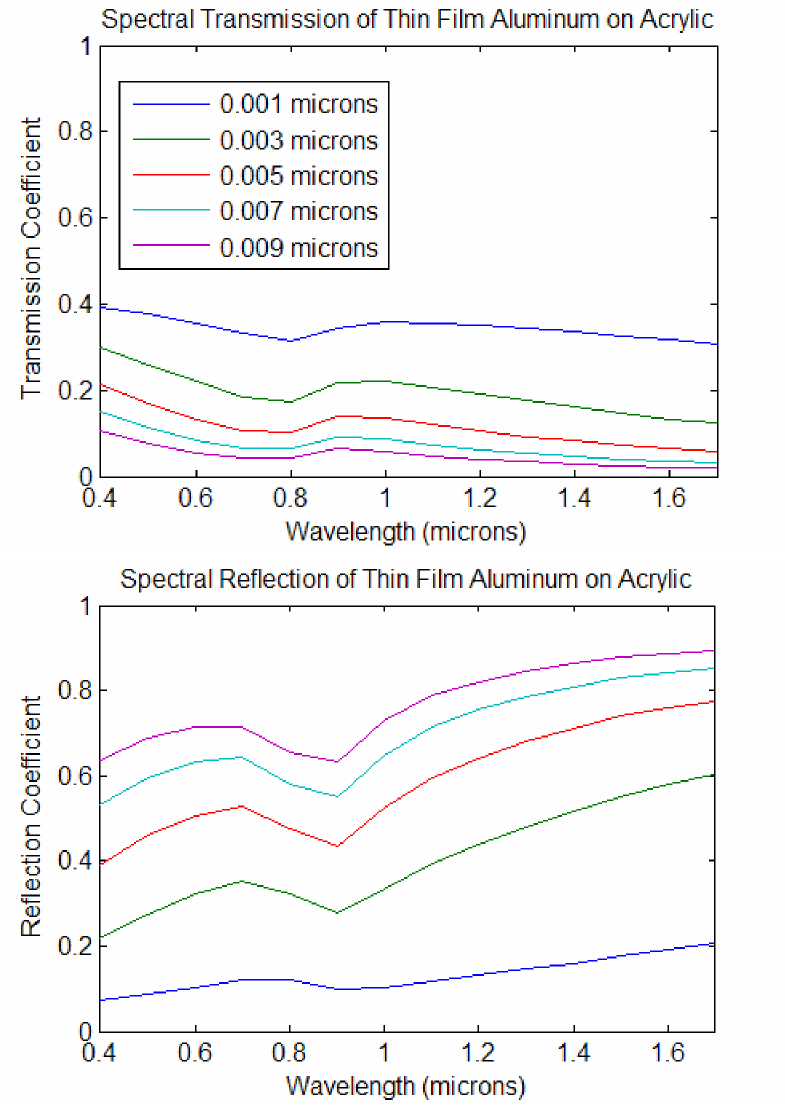

Figure 4.22 Theoretical spectral reflection and transmission of a thin film of aluminum on acrylic

The theoretical curves show a dip in the spectral transmission coefficients around 800 nm and in the spectral reflection coefficients around 800 to 850 nm. These dips, where the properties of aluminum should cause greater absorption, were not observed in experiments for the coating on the hemi-ellipsoid. Beyond these points the trend in theoretical reflection and transmission continues through the NIR. Using these observations, it can be assumed that the trends in spectral transmission and reflection measured up to 900 nm continue through the NIR. The only equipment currently available to measure spectral properties in the NIR is the Labsphere integrating sphere, the calibrated radiometer and an indium gallium arsenide detector. Although it would be possible to measure the reflection, transmission and absorption coefficients for every 25 nm from 900 to 1700 nm using the monochromator and integrating sphere, this would require 7200 measurements to cover the ten zenith and eight azimuth angles used for spectral measurements in the 380 to 900 nm range. It would also require a difficult experimental set up with a tungsten-halogen lamp and monochromator assembly located inside the hemi-ellipsoid.

Rather than perform all of these measurements, a few measurements across the 900 to 1700 nm waveband will be taken for a few zenith and azimuth angles. These will be used to test whether the trends observed across the 380 to 900 nm range do indeed extend into the NIR as generally expected from theory. These experiments will be part of future work on the goniophotometer.

4.5 Required Modifications to the Hemi-Ellipsoid

Although the methods for measuring spectral transmission and reflection of the hemi-ellipsoid have been developed here, the existing measurements will not be used for actual measurements of fenestration samples using the goniophotometer. As mentioned earlier, modifications to the hemi-ellipsoid must be made that will change the referential between locations on the surface of the hemi-ellipsoid and angles of incidence to a fenestration sample.

By testing the way in which light emerging from one focal point of the hemi-ellipsoid was reflected towards the other focal point, it was determined that the hemi-ellipsoid was slightly too tall. This is likely a result of extruding the hemi-ellipsoid too far beyond the precise hemi-ellipsoidal mold used to form it. The true focal plane of the hemi-ellipsoid must be found through an additional set of experiments. Once the correct focal plane has been determined, the hemi-ellipsoid will be trimmed along its edge. Testing will show whether this modification provides the correct alignment of the focal points of the hemi-ellipsoid, and thus the sample and camera ports on the rotating table. These tests and modifications will be part of future work on the goniophotometer.

As a result of these modifications, the spectral transmission and reflection coefficients of the hemi-ellipsoid must be referenced to a new coordinate system that is shifted towards the apex of the hemi-ellipsoid. The measurements conducted in the ellipsoid-oriented coordinate system could, theoretically be converted into this new coordinate system, but it will likely be simpler and more accurate to re-measure the spectral transmission and reflection coefficients in the new coordinate system directly. The best procedure for re-measuring spectral transmission and reflection coefficients is to measure them in a sample-oriented coordinate system (assuming the table positioning controls have been finalized) for the modified hemi-ellipsoid, i.e. where the table movements determine the zenith and azimuth angles, as described in section 4.2. The relationship between reflection and transmission coefficients at 550 nm can still be used to fix the magnitude of the new measured spectral reflection curves as described in section 4.3. Repeating the measurements will also provide the opportunity to simultaneously measure the hemi-ellipsoids properties in the NIR with an NIR spectrometer.

5. Camera Calibrations

5.1 Camera Calibration Goals

The digital cameras are the most critical component of the goniophotometer. They are the components through which radiances and luminances of transmitted or reflected radiation will be measured, and then used to estimate quasi-spectral BT(R)DFs. They were selected for their sensitivity to visible and NIR radiation to enable analysis across a 380 to 1700 nm wavelength interval, spanning most wavelengths over which solar radiation is significant. The cameras serve as multi-point radiometers, measuring the radiances of a full hemisphere of light emerging from a sample in one image. In order to use the cameras' digital output as a measure of radiance or luminance re-directed by a fenestration system, spectroradiometric and spatial calibrations must be conducted to relate digital output at each pixel in the camera image to the radiance of the beam in a given direction emerging from a sample. Additional factors to account for include the minimum angular resolution of each camera and a vignetting correction to account for light drop off near the edges of the image. This chapter describes the procedures for and results of these camera calibrations.

5.2 CCD Camera Calibrations

5.2.1 Camera Settings

The first step in calibrating the Kappa DX20 color CCD camera was to fix the digital and mechanical parameters of the camera such that the digital output would not be altered by a simple change in the camera's settings. A non-linear gamma of 0.5 was chosen to enable better differentiation of low luminance features in a single image. Other gammas could also have been chosen, but this gamma was selected to maintain a low digital level of noise while still providing the benefits of low luminance differentiation. For a gamma of 0.5, or 50 as defined by the camera settings, a 12 bit threshold of 1200 was chosen to maintain the 8 bit digital background noise below 10 pixel values, as shown in Figure 5.1.

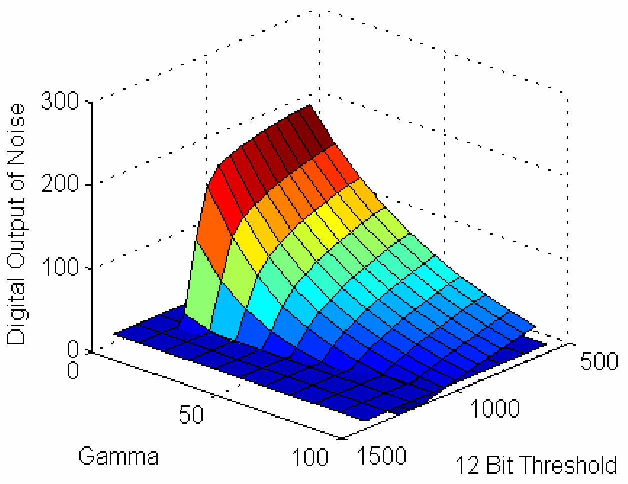

Figure 5.1 CCD noise level vs gamma and 12 bit threshold

The fisheye lens was fixed to an f number of f/4 to provide a large enough aperture for sufficient light to enter for low luminance levels while maintaining a reasonable depth of field. Ultimately, the pixels will be averaged over user selected solid units of angle, and the focus of images will be less important. The only camera setting that can vary is the integration time. The integration time, which can range from microseconds to minutes, is varied to capture images of less or more radiance or luminance.

5.2.2 Vignetting Correction

Vignetting is the term for light falloff near the edges of the image (Inanici 2006) caused by obstructions to light entering the camera at the edges of a scene due to the apertures of the optical system. In this case, vignetting is significant in part because a fish eye lens is used. In order to measure and account for the effect of vignetting, an experiment was performed wherein pictures were taken of a spot of constant irradiance on a Spectralon coated diffusing reflectance standard created with a Labsphere KI-120 tungsten-halogen lamp. Pictures were taken with the camera lens at a fixed distance from the spot in a fixed location, but rotated from 0 degrees, or normal, to 90 degrees. Because the camera is mounted with a fish eye lens, it can still view the spot at 90 degrees, but some of the light entering the camera is blocked due to vignetting.

Table 5.1 Vignetting Correction Factors

Angle from Normal	Factor
0	1.000
10	1.000
20	1.000
30	1.000
40	1.000
50	0.998
60	0.987
70	0.968
80	0.949
90	0.910

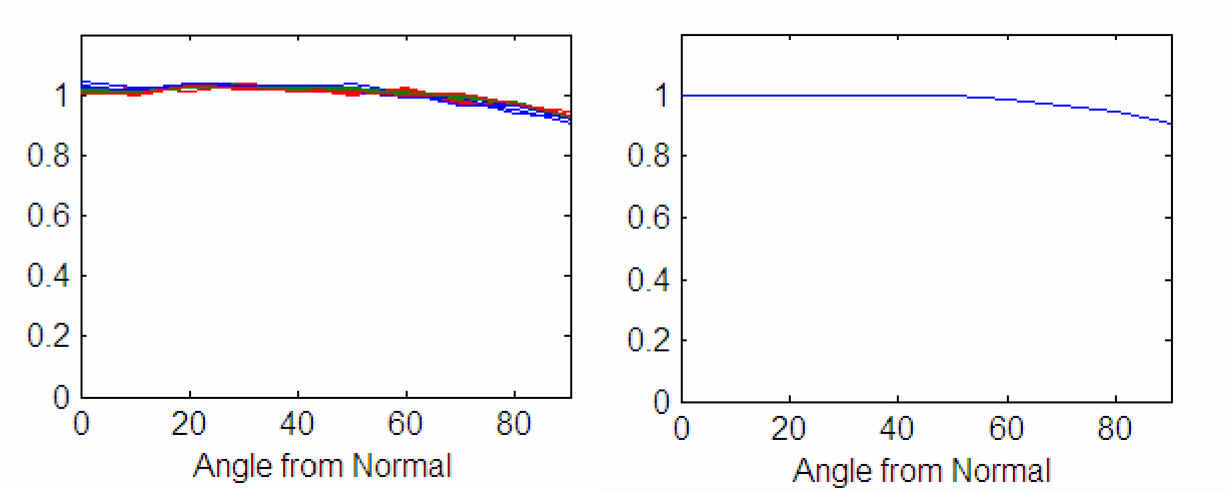

Figure 5.2 Light drop-off, or vignetting, with zenith angle relative to fisheye lens

The average pixel value over the spot was recorded at each position for each channel, R, G and B for a few different spots. By comparing the average pixel value at each angle to that for the normal direction, the magnitude of the light falloff toward the edge of the image can be determined. The results of all of the experiments are shown in Figure 5.2.

The falloff for each channel for each experiment is shown on the left. The average falloff is shown on the right. Although the correction factor for light falloff between 0 and 40 degrees was not exactly one, it was close enough that a value of one could be assumed until light falloff began in earnest near the edges of the image.

To apply the vignetting correction factors, the digital output of the camera should be divided by the vignetting correction factor based on the angle from the normal from which light arrived. This angle can be correlated to pixel location on the image, as will be explained in section 5.2.4. The resulting digital level will be an effective digital output that can be used with the results of the spectroradiometric calibration, presented in section 5.2.5 to estimate radiance.

5.2.3 Angular Resolution

The angular resolution of the camera determines the point at which a spot with a given radiance will not be imaged over a full sensor area, and the digital output of the corresponding pixel will be lower than expected for the scene radiance. To account for this effect, a series of pictures were taken of a green spot with the camera at increasing distances from the spot. The Labsphere tungsten-halogen lamp with a 550 nm passband filter was used to create a spot on a Spectralon coated diffusing reflectance standard. The spot diameter was 1.25 inches. Pictures were taken with the Kappa DX20 color CCD camera every centimeter from 15 to 85 cm away from the spot. The results of the experiment are shown in Figure 5.3. The figures show the pixel values over the spot for camera positions at 20, 45, 65 and 70 cm away. The color scale ranges from 60 to 80 in pixel values and only the G channel is shown.

One can observe the disappearance of the highest pixel levels (shown in red) in the 70 cm spot, indicating a decrease in digital levels unrelated to scene radiance. For camera positions greater than 65 cm away the maximum pixel value recorded by the camera began to decrease despite the constant radiance from the spot. At 65 cm away, the spot occupied slightly less than 0.0017 steradians of solid angle from the perspective of the camera.

The conclusion from this experiment is that radiances viewed by the camera varying over less than 0.0017 steradians will not generate the expected digital output based on the spectroradiometric calibration described in section 5.2.5. The digital output will be lower and the radiance will be under-predicted. This places a lower bound on the angular resolution of the BT(R)DFs measured by the goniophotometer, and BT(R)DF patches should be averaged over solid units of angle at least greater than 0.0017 steradians in order to accurately convert digital output to scene radiance. It is expected that typical averaging will occur over much larger solid units of angle.

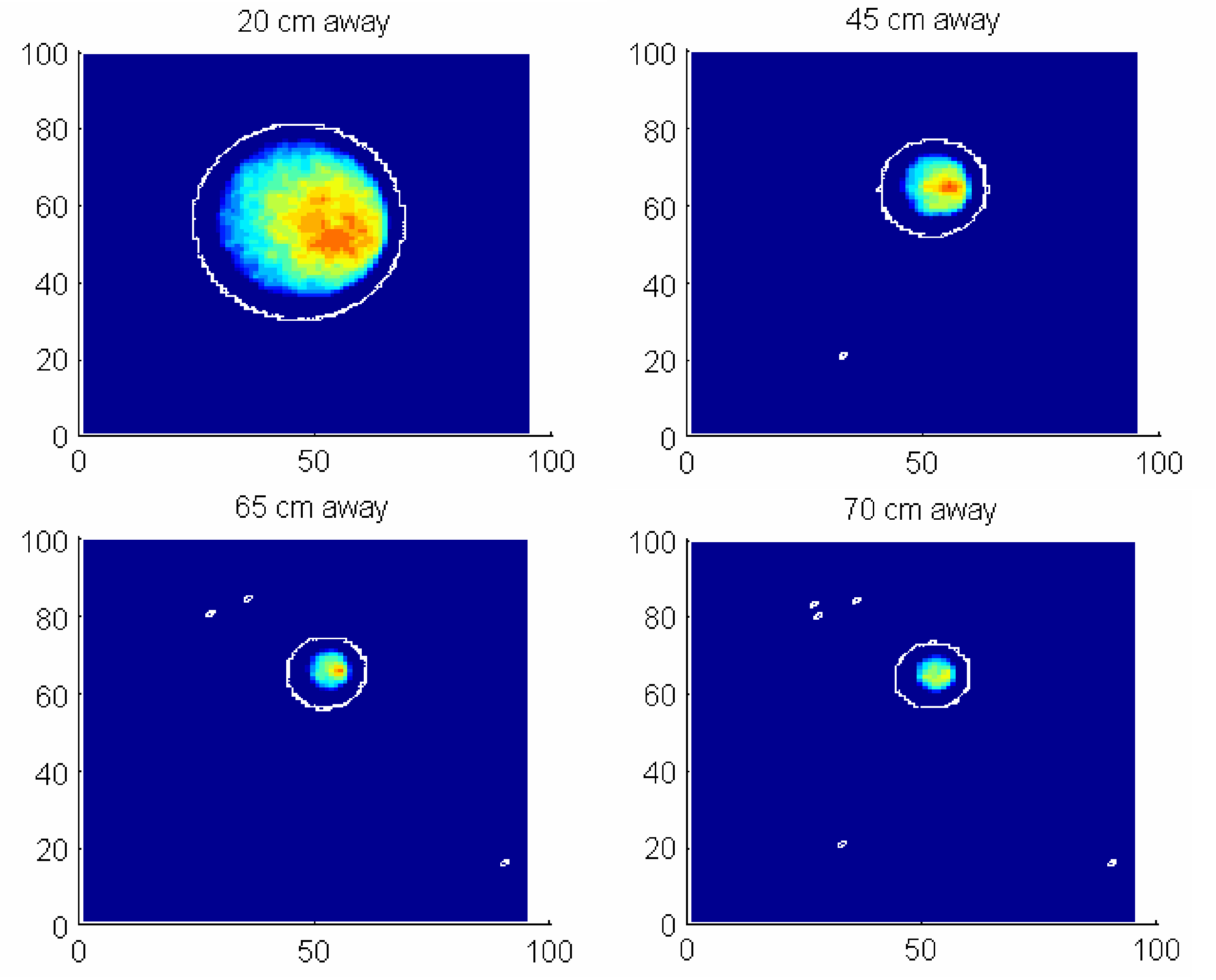

Figure 5.3 G pixel values recorded by the camera for a spot of constant radiance at a camera distance of 20, 45, 65 and 75 cm

5.2.4 Spatial Calibration

A spatial calibration relating pixel locations within the image to the angles from which light entered the camera was performed. This calibration will ultimately provide a relationship between pixel locations in an image and the polar angles of emergence from a fenestration system sample, as shown in Figure 5.4.

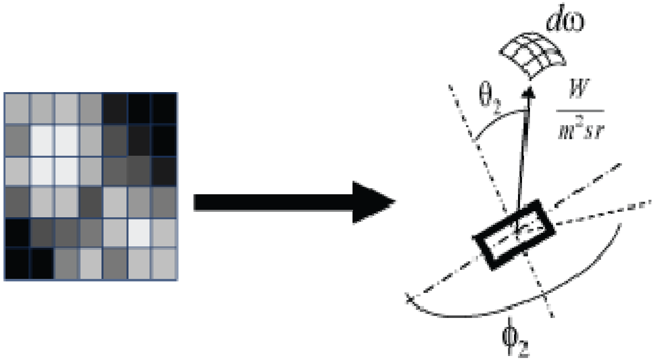

Figure 5.4 Relating pixel locations to angles of emergence from a fenestration sample

The first step is to locate the optical center, or the principal point, of the camera. The principal point is the point on the image that is at the base of a line perpendicular to the camera lens (Clarke 1998). For a camera with a fish eye lens, straight lines through the principal point will appear straight on the image, whereas other straight lines will show curvature. To locate the principal point of the CCD camera, the plumb line method was used (Browne et al. 1971). Pictures were taken of a piece of foam board colored with straight black lines positioned perpendicularly to the CCD camera. Many images were taken moving the foam board laterally to the camera and positioning the plumb lines vertically and horizontally as shown in Figure 5.5. Using this method, pixel location (549, 620) in the 1380 x 1028 size image was found to be the principal point of the camera.

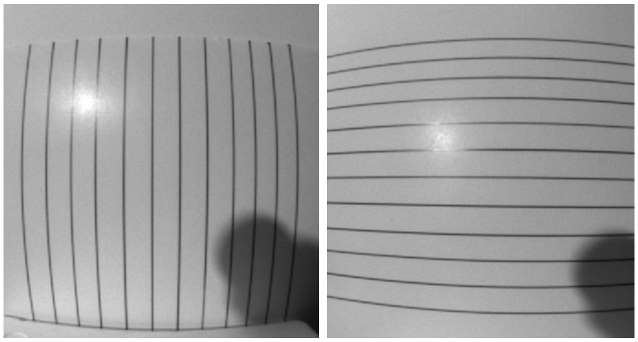

Figure 5.5 Plumb-line method for locating the principal point

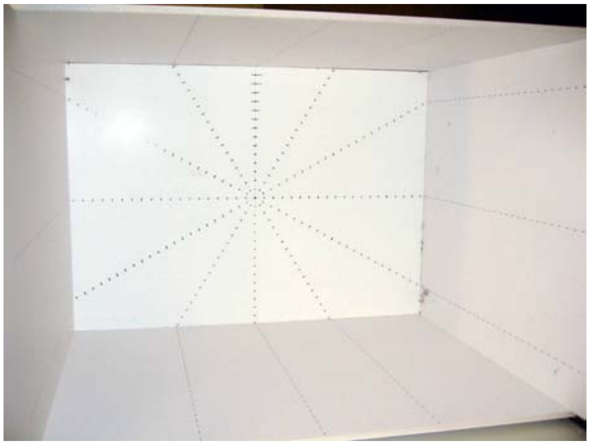

Figure 5.6 Box with spatial calibration grid

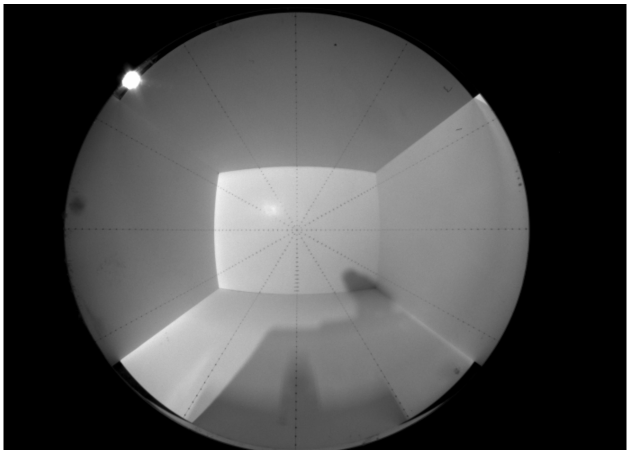

Figure 5.7 Centered image of calibration grid through fish eye lens

Once the principal point of the camera was found, a box with grid of points at known zenithal and azimuthal angles was used to determine the relationship between angles impinging on the camera and pixel locations.

The spatial calibration box is shown in Figure 5.6. The box was positioned such that the back of the box was perpendicular to the camera at a known distance from the camera. The lines on the box are drawn at every 30 degrees from 0 to 360. Points were drawn along each azimuth one inch apart from which zenithal angles could be calculated knowing the geometry of the box and its relationship to the camera. With the center of the box imaged at the principal point of the camera, these azimuths appear as straight lines traversing the camera image, as shown in Figure 5.7. From these images, it can be seen that azimuth angles can be calculated from the image using a coordinate system with the principal point at its center.

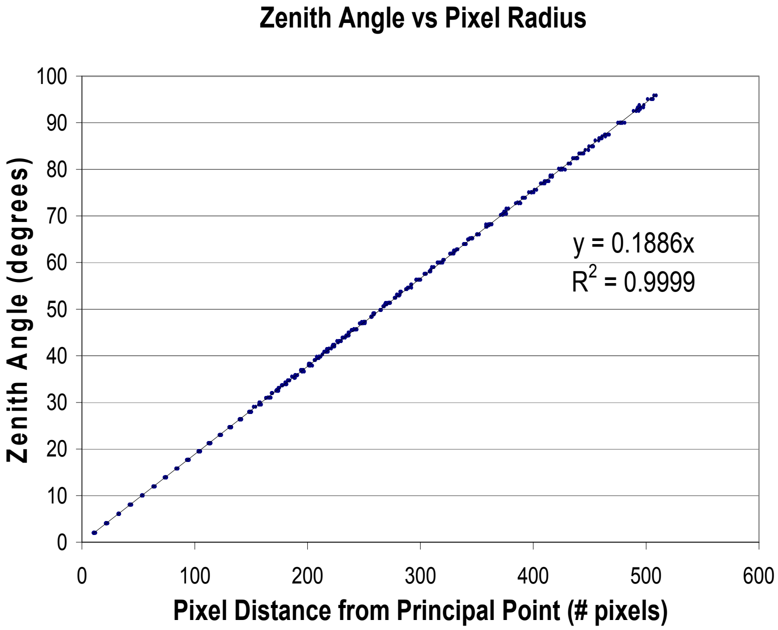

Figure 5.8 Relationship between pixel location in image and zenith angle

The azimuth from which light entered the camera can be calculated in the usual way, defining a desired direction as the 0 azimuth. This direction will be determined once the goniophotometer set up is complete. The zenithal direction from which light impinging on a pixel entered the camera can be determined by the pixel's distance, in image coordinates, from the principal point. The relationship between pixel distance from the principal point and the zenithal angle of the grid point imaged at that pixel is shown in Figure 5.8. The measured linear relationship between pixel radius (measured from the principal point) and the zenithal angle of incident light is similar to that found for other fisheye lens systems (Voss and Chapin 2004), (Schwalbe 2005). The standard error in the linear regression was about 1.26 percent. A coefficient of 0.1886 degrees per pixel relates zenith angle to the pixel location relative to the principal point.

Although this calibration determines the directions from which light entered the camera system based on pixel locations, it does not provide information about the direction from which light emerged from the fenestration system being studied. Theoretically, the relationship between the angles at which light approached the camera after reflection from the hemi-ellipsoid and the angles from which light emerged from a sample can be calculated. This is because the sample is positioned at one focal point of the hemi-ellipsoid and the camera is positioned at the other.

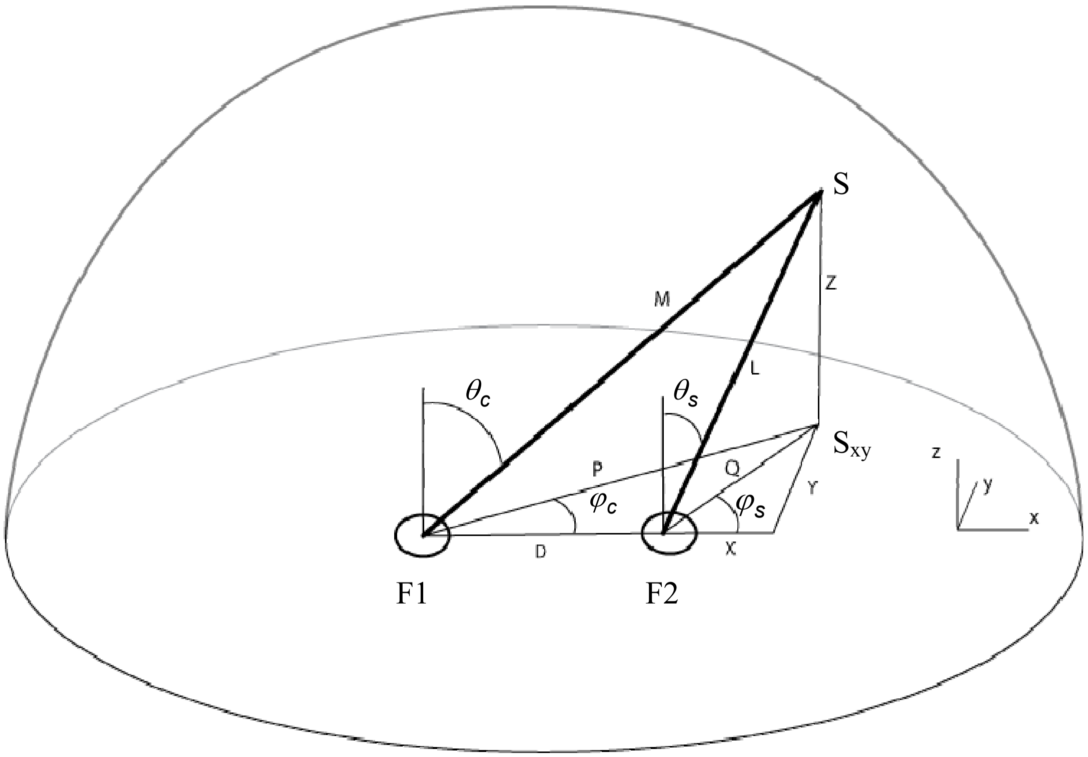

Figure 5.9 Ellipsoid geometry used to convert camera angles into emerging sample angles

A diagram of the geometry and quantities necessary for relating the angles entering the camera at focal point F1 to angles emerging from a sample at focal point F2 are shown in Figure 5.9. The separation between the focal points is given by D. Not shown are the semi-major and semi-minor axes of the hemi-ellipsoid, which are defined as quantities A and B. A is the longer, semi-major axis running through either of the focal points. The semi-minor axes, B, are equal in the y and z directions. These are known properties of the ellipsoid.

The angles entering the camera, which were shown to correlate to pixel locations, are given by zenith angle and azimuth angle (θ_c, φ_c). The angles of emergence from the sample are given by (θ_s, φ_s). M and L are each lines from the focal points to the surface of the hemi-ellipsoid. From the definition of an ellipse it is known that M+L = 2A. Z is a line in the z-direction which projects point S on the hemi-ellipsoid to point S_{xy} in the xy plane at the base of the hemi-ellipsoid. P and Q are the projections of M and L onto the xy plane. The first relations to observe are given by simple trigonometry:

(5-1) $\sin(\theta_c) = \frac{P}{M}$ (5-2) $\cos(\varphi_c) = \frac{D+X}{P}$ (5-3) $\sin(\theta_s) = \frac{Q}{L}$ (5-4) $\cos(\varphi_s) = \frac{X}{Q}$

Equations (5-1) and (5-2) can be used in equation (5-4) to find the zenith angle of emergence from the sample in terms of M, Q, the known camera angles and the focal point separation. The definition of a hemi-ellipsoid, that is the relation M+L=2A, can be used to convert equation (5-3) into a function of M and Q. The results are shown as equations (5-5):

(5-5a) $$\cos(\varphi_s) = \frac{M\sin(\theta_c)\cos(\varphi_c) - D}{Q}$$

(5-5b) $$\sin(\theta_s) = \frac{Q}{2A - M}$$

M can be found using the equation for an ellipse in a coordinate system with the origin at focal point F1 of the ellipse, such that the distance from the origin to the point on the ellipse is given by M. The equation for this ellipse in this coordinate system is give by:

(5-6) $$\frac{\left(x + \frac{D}{2}\right)^2}{A^2} + \frac{y^2 + z^2}{B^2} = \frac{\left(M\sin(\theta_c)\cos(\varphi_c) + \frac{D}{2}\right)^2}{A^2} + \frac{M^2\sin^2(\theta_c)\sin^2(\varphi_c) + \cos^2(\theta_c)}{B^2} = 1$$

This can be rewritten as a quadratic equation for M as follows:

(5-7) $$M^2\left[\frac{\sin^2(\theta_c)\cos^2(\varphi_c)}{A^2} + \frac{\sin^2(\theta_c)\sin^2(\varphi_c) + \cos^2(\theta_c)}{B^2}\right] + M\left[\frac{D\sin(\theta_c)\cos(\varphi_c)}{A^2}\right] + \left[\frac{D^2}{4A^2} - 1\right] = 0$$

This equation can be solved for M using the quadratic formula. Q can be found in terms of the known camera angles, the focal point separation D, and M as follows:

(5-8) $$Q^2 = X^2 + Y^2 = (M\sin(\theta_c)\cos(\varphi_c) - D)^2 + (M\sin(\theta_c)\sin(\varphi_c))^2$$

After simplification, this leads to:

(5-9) $$Q^2 = M^2\sin^2(\theta_c) + D^2 - 2MD\sin(\theta_c)\cos(\varphi_c)$$

At this step, knowing the distances M and Q, the properties of the ellipsoid A, B and D, and the incoming camera angles (θ_c, φ_c), the emerging angles from the sample can be calculated using equations (5-5), which are applicable regardless of which camera is being used. Thus, the theoretical relationship between (θ_c, φ_c) and (θ_s, φ_s) provides a link between the pixel locations on the image and the emerging angles from a fenestration system sample. One caveat is that these relations assume the half-mirrored hemi-ellipsoid is optically perfect. Once modifications to the hemi-ellipsoid have been made to correct the location of the focal plane, these relations between pixel locations and emerging angles from the second focal point, or system sample, will be verified experimentally and corrected as necessary to account for hemi-ellipsoid deformities.

Additionally, each pixel will not be used as a data point for BT(R)DFs. Pixels will be averaged over certain solid units of angle selected by the user. Pixels will be averaged primarily for two reasons. First, the angular resolution provided by the digital cameras are more than required for BT(R)DF assessment of fenestration systems and would lead to an unnecessary volume of data. Second, because a finite area of a fenestration sample is illuminated there is the possibility that an individual pixel receives radiation from a larger set of angular directions than that determined by its own angular resolution. This cone of angular acceptance will be measured experimentally once the hemi-ellipsoid has been modified and will provide more information about the true angular resolution of the goniophotometer. Averaging at less than this angular resolution would not be meaningful.

Two averaging methods have been considered. One is a typical approach dividing the hemi-sphere of emerging angles into a grid defined by increments in azimuth and zenith angles, dθ and dφ. This method has been used before (Andersen 2004) with success. However, this method leads to larger solid units of angle near the horizon of the hemi-sphere and smaller solid units of angle near the apex. The desire to average over constant solid units of angle throughout the hemisphere motivated the need for a second possible averaging method.

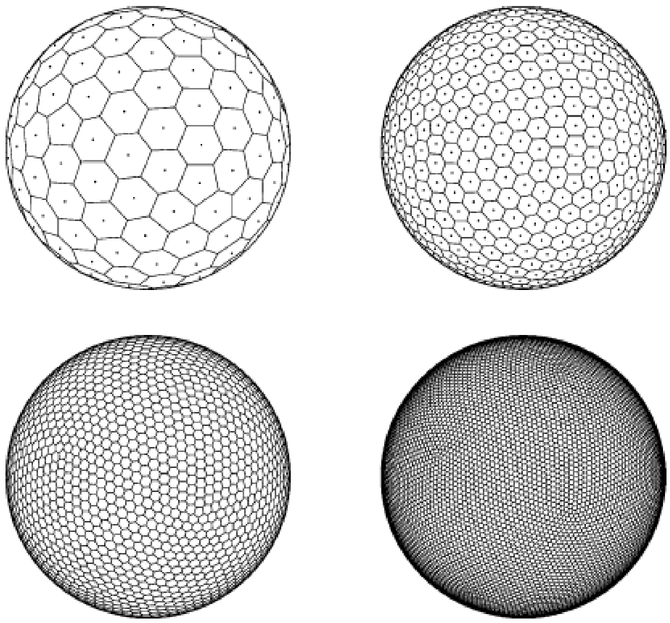

Figure 5.10 Examples of CCVTs (Du et al. 2003 p3951)

The second averaging method considered is one in which the hemi-sphere is divided into equal solid units of angle chosen by the user. This can be achieved by tiling the unit hemi-sphere with a regular hexagonal grid, or a spherical hexagonal tessellation. These can be constructed from a triangular grid of equilateral triangles, or from the Voronoi cells for a triangular grid of evenly spaced points similar to the approach taken in (Apian-Bennewitz and von der Hardt 1998). These spherical-hexagonal tilings are part of a set of Voronoi tilings of a sphere known as constrained centroidal Voronoi tessellations (CCVT). It has been shown that it is "topologically impossible" to tile a sphere completely with congruent spherical hexagons (Du et al. 2003 p3951), and each spherical hexagonal tiling will include 12 pentagons. For large grid tilings, this is an acceptable non-uniformity in angular averaging. A few examples of CCVTs that tile a sphere with hexagons are shown in Figure 5.10.

If the area of the hexagons are small compared to the surface area of the unit circle, 4π, then the area of the hexagon is approximately the area of the hexagon in a plane. If the spacing between points on the edge of the hexagon is given by s, then the area of the hexagon is simply $\left[3\sqrt{3}/2\right]s^2$. Since this is along a unit sphere, the area is also the solid unit of angle subtended by the hexagon, because $\Delta\Omega = A / 1^2$. The side length s on the unit sphere is equivalent to a unit of angle $\Delta\theta$ along a great circle of the sphere. If the apex of the hemisphere is chosen as the center of the first hexagon, this angle $\Delta\theta$ provides a zenith angle which can be used to locate each successive ring of hexagons until the edge of the hemisphere has been reached. Pixels within the image will be aggregated based on their locations within these hexagonal grids that define equal solid units of angle.

The trade-offs between each averaging method have not yet been fully explored. The constant zenithal and azimuthal increment method leads to averaging over larger solid units of angle near the edges of the hemi-sphere than at the top. The averaging method over solid units of angle overcomes this issue, however it leads to averaging over fewer pixels near the edge of the image and more pixels near the center of the image. It is not yet clear whether averaging over a non-uniform number of pixels or averaging over non-uniform solid units of angle presents the best method.

Predefined angular averaging resolutions, either in solid units of angle or zenithal and azimuthal increments, will be provided as options for the user to limit the possible angular resolution chosen. These will be constrained based on the angular resolutions calibrations. The computer codes for both averaging methods have not yet been finalized.

5.2.5 Spectroradiometric Response

A critical calibration for the goniophotometer is relating the digital output of the camera to radiances emerging from a fenestration system sample. This was achieved through spectroradiometric calibration of the digital cameras. Spectroradiometric calibration consists of measuring the camera's digital response to known radiances of monochromatic radiation. The output of a digital camera for a given pixel at a given wavelength is related to the spectral exposure, in units of energy, of the sensor area correlating to that pixel. The spectral exposure is dependent on the number of photons of a given wavelength impinging on the detector area, which are in turn related to the radiance of the scene viewed by the camera (Holst 1998). In its most simple form, the spectral exposure, $H(\lambda)$ is related to scene spectral radiance by:

$$H(\lambda) = k\frac{L_e(\lambda)}{N^2}t_{int} \tag{5-10}$$

where *k* is a constant depending on the optical and geometric properties of the imaging system, *N* is the aperture number, t_{int} is the integration time and $L_e(\lambda)$ is spectral radiance (Martinez-Verdu et al. 1999). In this application, the f-number of the lens is fixed at f/4, and thus the N in the equation (5-10) can be included in the constant of proportionality. Furthermore, the digital output for a pixel is physically related to its spectral exposure and can be thought of as a function of the scene radiance, such that:

$$\text{(5-11)} \qquad NDL_{R,G,B}(\lambda) = DL_{R,G,B} / 2^8 = f(H(\lambda))$$

where $NDL_{R,G,B}$ and $DL_{R,G,B}$ are the Normalized Digital Level and Digital Level of the R,G, or B channel.

To study the relationship between spectral exposure and the NDL response of the camera, the camera output was measured against known monochromatic radiances and integration times. The constant of proportionality relating radiance to spectral exposure, k, was not measured. Instead, the relationship between NDL and the product $L_e(\lambda)$ t_{int} was measured directly. $L_e(\lambda)$ t_{in} is a measure of the energy per unit area per steradian viewed by the camera. It is directly related to the real spectral exposure of the sensor area and will be referred to as $h(\lambda)$, because it is not strictly the spectral exposure at the CCD sensor array. To verify the reciprocity relationship for digital cameras, the monochromatic radiance and integration time were both varied to show that the digital output of the cameras was related only to the product of the two, that is, to $h(\lambda)$ (Martinez-Verdu et al. 1999).

The Labsphere KI-120 Illuminator tungsten-halogen lamp, a Spectral Products CM110 monochromator, and a ~99 percent reflective Labsphere Spectralon coated diffusing, reflectance standard were used to create monochromatic radiances for viewing by the camera as shown in Figure 5.11. The Kappa DX20 color CCD camera was mounted with a Fujinon FE185C057HA high resolution fisheye lens and the NIR filter was removed. Pictures were taken at many integration times, from about one millisecond to many seconds to cover a full range of exposures from below the camera's threshold to above saturation for each wavelength.

The 8-bit digital output of the camera was averaged over the pixels viewing a monochromatic spot on the reflectance standard. The radiance viewed by the camera was estimated by measuring the irradiance of the diffusing reflectance standard and calculating the radiance reflected towards the camera based on the wavelength dependent reflection coefficients of the reflectance standard provided by Labsphere. Two methods were used to measure irradiance. First, an Ocean Optics USB2000 spectrometer was used to measure the irradiance of the reflectance standard. A Labsphere integrating sphere was then used to repeat the experiments for more accurate irradiance measurements to confirm and refine the results of the spectrometer experiments, as well as to gather more accurate data for the absolute spectral responsivity calibration, described in section 5.2.6. These experiments were conducted with monochromatic beams at every 50 nm from 450 nm to 950 nm.

Figure 5.12 shows the typical S-shaped relationship between NDL and h(λ) for the R, G and B channels measured through these experiments. The shape of these response curves was observed to be the same for each channel and all wavelengths. That is, for a given channel and wavelength, the ratio of one spectral exposure to another corresponds to a certain ratio of NDLs. These ratios are the same for different channels and different wavelengths.

To state it in another way, if the spectral exposure for any channel and any wavelength is divided by the spectral

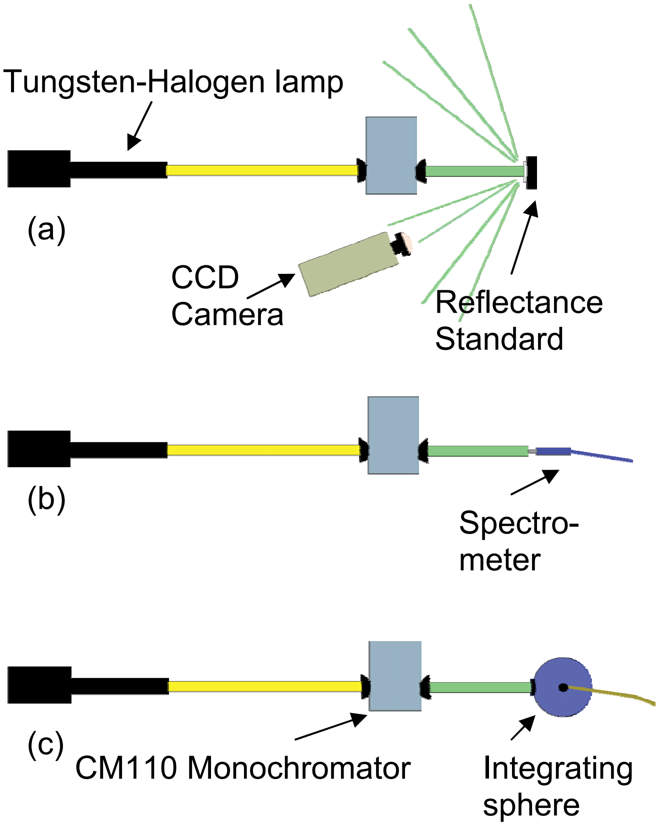

Figure 5.11 Spectroradiometric calibration set-up
(a) Images taken with CCD camera
(b) monochromatic irradiance measured with spectrometer
(c) Monochromatic irradiance measured with integrating sphere

exposure that leads to a selected NDL for that channel and wavelength, such as NDL = 0.3, the shape of the camera's response, given by NDL versus normalized exposure, is the same for any channel at any wavelength. Figure 5.13 shows all of the points for NDL versus the normalized spectral exposures, h(λ)/$h^{0.3}_{R,G,B}(\lambda)$ for all channels and wavelengths. The spectral exposures h(λ) have been divided by the exposure resulting in NDL = 0.3 (hence named $h^{0.3}_{R,G,B}(\lambda)$). NDLs above about 0.8 will be discarded to avoid saturation of each channel, which occurs above this level, and NDLs below about 0.05 will also be discarded to avoid the threshold of the camera's response. NDLs beyond these thresholds will not be used to measure radiances.

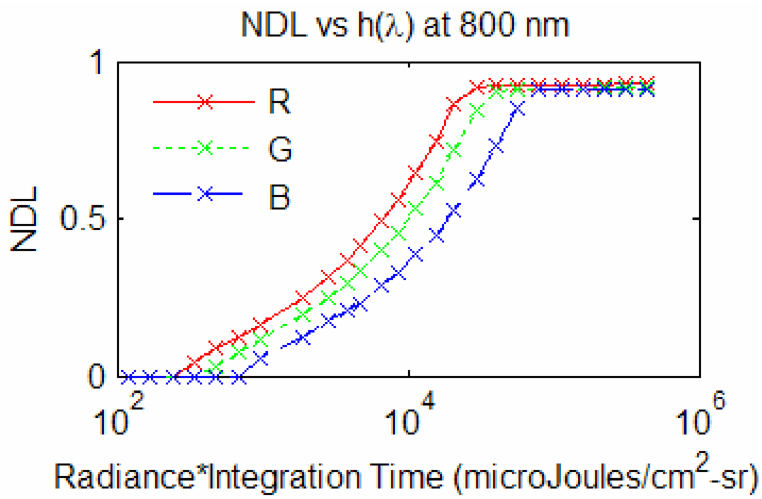

Figure. 5.12 R, G and B response to 800 nm radiation

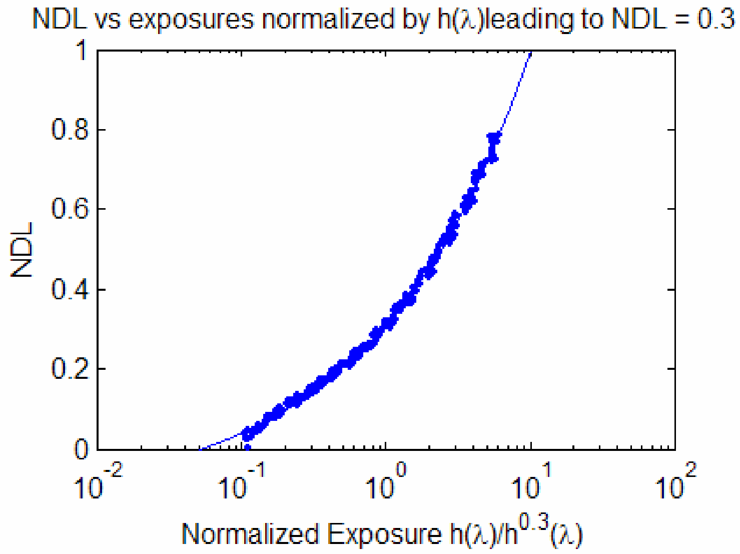

Figure 5.13 Normalized response for R, G and B channels to many wavelengths fit with a logistic dose response function

The response above, and the response of CCD camera's generally, is best approximated by certain functions, including logistic dose response, sigmoid, asymmetric sigmoid, Gaussian cumulative, and Weibull cumulative functions (Martinez-Verdu et al. 1999). A logistic dose response function was found to fit the Kappa DX20 response curve best over the range of NDL = 0.05 to 0.8. This curve is the solid line in

Figure 5.13. All of the spectral sensitivity properties of the camera are contained in the wavelength dependent normalization factor, $h^{0.3}{}_{R,G,B}$ (λ), for each channel. The logistic dose response curve for the camera was found to be:

$$NDL_{R,G,B} = a + \frac{b}{1 + \left(\frac{h(\lambda)/h^{0.3}_{R,G,B}(\lambda)}{c} \right)^{d}} \tag{5-12}$$

with a = -0.13254, b = 363.51, c = 1.4468e7 and d = - 0.40717. Again, this result is only for the Kappa DX20 CCD camera mounted with the Fujinon fisheye lens and disregarding saturation and threshold points. Equation (5-12) can be inverted to solve for the spectral exposure corresponding to a given digital output as follows:

$$h(\lambda) = h^{0.3}_{R,G,B}(\lambda) \times c \left(\frac{b}{(NDL_{R,G,B} - a)} - 1 \right)^{1/d} \tag{5-13}$$

This equation suggests that if the spectral exposures that lead to a given digital output are known, given by $h^{0.3}{}_{R,G,B}$ (λ), then the actual spectral exposure of a pixel can be calculated from the digital output of the pixel. Because h (λ) = L_e(λ) t_{in}, monochromatic radiance can also be calculated from the digital output of the camera if $h^{0.3}{}_{R,G,B}$ (λ) is known, as can be seen by substituting the radiance and integration time for the spectral exposure, yielding:

$$L_e(\lambda) = \frac{h^{0.3}_{R,G,B}(\lambda)}{t_{int}} \times c \left(\frac{b}{(NDL_{R,G,B} - a)} - 1 \right)^{1/d} \tag{5-14}$$

5.2.6 Spectral Sensitivity

The spectral sensitivity of the camera is a measure of the relative response of the camera to different wavelengths of radiation. For color CCD cameras there are 3 channels, R, G and B, each with their own spectral sensitivity. The B channel is more sensitive to bluish light, such as 400 to 500 nm, the G channel is more sensitive to greenish light, such as 500 to 570 nm, and the R channel is more sensitive to reddish light, such as above 600 nm. The spectroradiometric calibration described above provides a measure of the spectral sensitivity of each channel in the normalization spectral exposures, represented by $h^{0.3}_{R,G,B}$ (λ), which lead to the same digital response for each wavelength. This is a measure of the total energy for each wavelength incident on a pixel that leads to the same digital response. In the spectroradiometric calibration above, $h^{0.3}_{R,G,B}$ (λ) was measured every 25 nm, but the spectral sensitivity of the camera is desired to a 5 nm spectral resolution. This resolution is desired to achieve accurate measurements of spectra as explained in (ASTM 2001).

The normalization spectral exposures $h^{0.3}_{R,G,B}$ (λ) at 5 nm intervals from 380 to 945 nm were calculated from experiments using the same setup shown in Figure 5.11. Images of the monochromatic radiances were taken at the same integration time for each wavelength. Only the Ocean Optics spectrometer was used to measure the spectral irradiance of the reflectance standard because the integrating sphere is only calibrated to measure monochromatic flux through its port for every 25 nm from 400 to 1100 nm. The monochromatic radiance viewed by the camera was calculated based on the measured irradiance and the reflectance standard's spectral reflection coefficients.

Through the inverted logistic dose response function given by equation (5-13) and (5-14), the normalized spectral exposures, $h^{0.3}_{R,G,B}$ (λ), can be calculated from the real digital output of the camera, the normalization digital level, NDL = 0.3, and the measured spectral exposure, or radiance multiplied by integration time. This relation is given by:

$$\text{(5-15)} \qquad \frac{h^{0.3}_{R,G,B}(\lambda)}{h_{\text{Measured}}(\lambda)} = \frac{h^{0.3}_{R,G,B}(\lambda)\times c\left(\dfrac{b}{(0.3-a)}-1\right)^{1/d}}{h^{0.3}_{R,G,B}(\lambda)\times c\left(\dfrac{b}{((\text{NDL}_{R,G,B,\text{Measured}})-a)}-1\right)^{1/d}}$$

Where all quantities are known except $h^{0.3}_{R,G,B}$ (λ). This method was used rather than trying to measure $h^{0.3}_{R,G,B}$ (λ) directly because that would have required modifying the irradiance of the reflectance standard or the integration time until a digital output of exactly NDL = 0.3 was achieved for every wavelength. In practice, it was difficult to achieve the same digital output for every wavelength exactly, and the approach above was considered more accurate.

Using this method, $h^{0.3}_{R,G,B}$ (λ) was calculated for each channel for every 5 nm from 380 to 945 nm. The inverse of these normalized spectral exposures give the absolute spectral responsivity (ASR) of each channel, that is, how responsive each channel is to a given wavelength of radiation (Brown et al. 2001),. The ASR can be written $r_{R,G,B}(\lambda) = 1/h^{0.3}_{R,G,B}$ (λ), where the subscripts denote a different ASR for each channel. It has the units of digital output per unit energy per unit area per solid unit of angle, or NDL/(μJ/cm^2–sr).

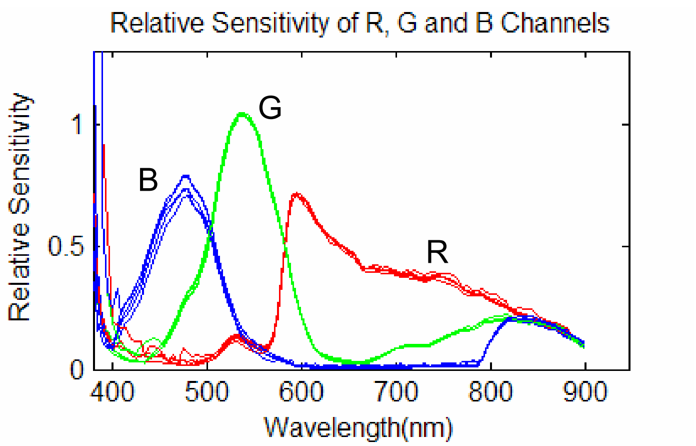

Figure 5.14 Relative sensitivity of R,G,and B for all experiments with fixed relationship between R, G and B

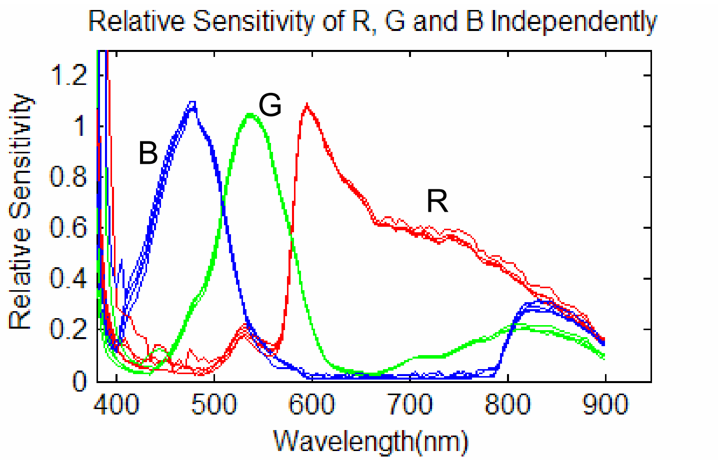

Figure 5.15 Relative sensitivity of R,G,and B for all experiments with R, G and B scaled independently

The experiments and calculations described above were performed many times to achieve accurate measurements of each channels' ASR. The initial results, in terms of relative sensitivity, are shown in Figure 5.14. In Figure 5.14 the relative sensitivities of each channel for all experiments are plotted with the relative magnitude of each channels ASR held fixed as measured. In Figure 5.15, the relative sensitivities of each channel are plotted independently of each other. Five different data sets are plotted. Some data sets were not used due to saturation or underexposure at certain wavelengths.

The relative sensitivity is shown, rather than the ASR, because it was determined that the irradiance measurements from the spectrometer were highly dependent on the positioning of the spectrometer, yielding ASR curves that were shifted significantly from experiment to experiment. The relative sensitivities measured by this method, however, are seen to be similar for all experiments. Figure 5.14 seems to suggest that there is some discrepancy in the measurements of the B channels ASR, but looking at Figure 5.15 it can be seen that the results for each channel plotted separately, that is when the ratio between channel sensitivities is not held fixed, are self-consistent. This means that for some experiments the ratio of the G channel's sensitivity overall to the B channel's sensivity overall was found to be slightly higher or lower than in other experiments, but that the relative spectral sensitivity of each channel was always similar.

In addition to the data shown, experiments were conducted to refine the relative sensitivity curves below 400 nm and above 900 nm. A Xenon lamp was used instead of the tungsten halogen lamp to measure the relative sensitivity of each channel below 400 nm. For measurements above 900 nm, higher integration times than those typically used for the visible region had to be used to measure relative sensitivities. The results of these experiments were then added to the measurements shown in Figures 5.14 and 5.15 to span the full 380 to 945 nm range. The relative sensitivity curves from each of the experiments were then averaged to determine a single average relative sensitivity for each channel.

Because the spectrometer-measured irradiances were determined to be unreliable for absolute measurements, the integrating sphere measurements described in the previous section, 5.2.5, were used to scale the relative sensitivity of each channel to an appropriate magnitude, thereby determining the ASR of each channel. The relative sensitivity of each channel was positioned relative to the integrating sphere

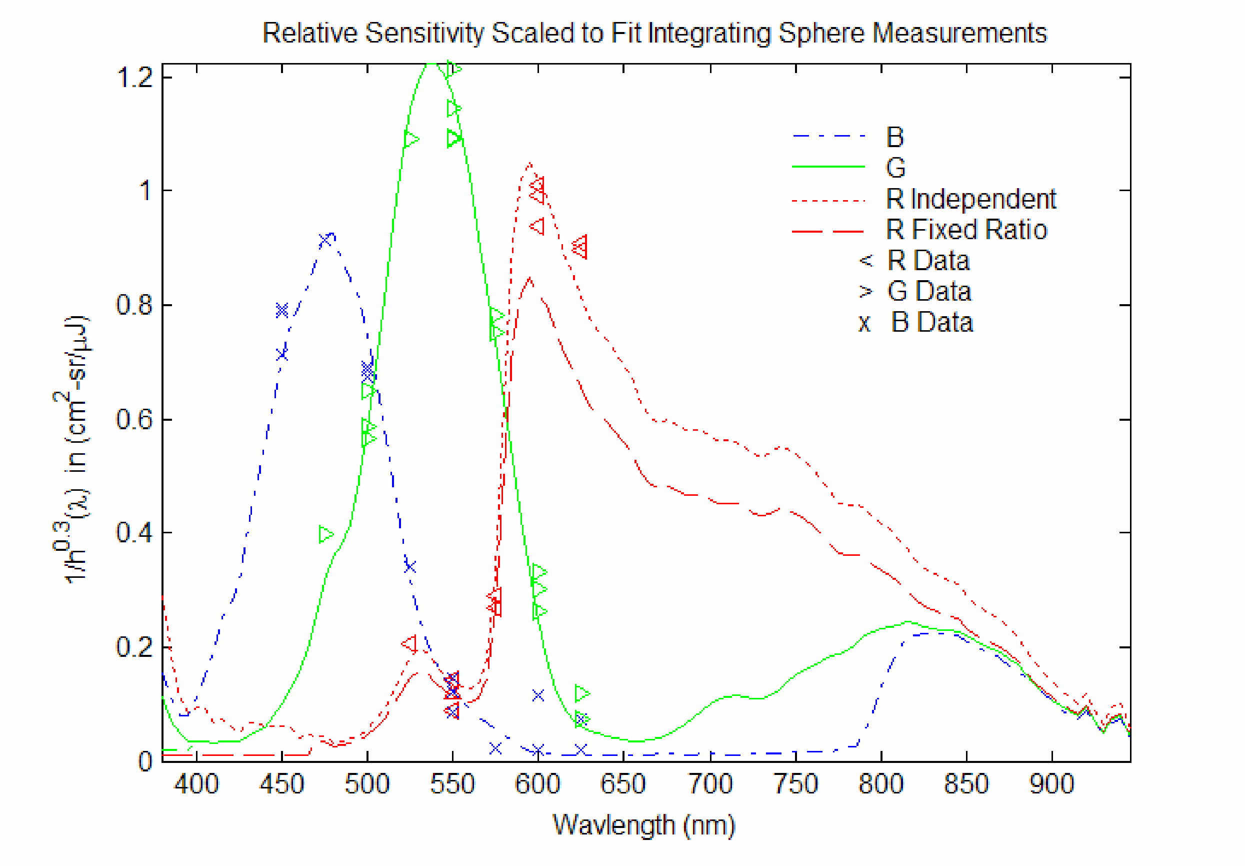

Figure 5.16 ASR curves of each channel determined by scaling each channel's relative sensitivity to the corresponding integrating sphere measurements.

Two scalings of the R channel are shown. R Independent, for which the relative sensitivity of the R channel is scaled independently of G and B, and R Fixed Ratio, for which the sensitivity of R relative to G and B is kept as measured in the relative sensitivity calibration

measurements such that the sum of the square of the differences between the scaled ASRs and the integrating sphere data points was minimized. The resulting curves are the true ASRs of each channel as shown in Figure 5.16.

Figure 5.16 shows two different scalings for each of the channels ASR curves. One scaling in which all channels are scaled to fit the integrating sphere measurements together, with their measured relationships to each other held constant, and another scaling in which they are scaled independently of each other. For the G and B channels, the choice of scaling for the relative sensitivity curve does not make a difference in the determination of the channel's ASR. However, it can be seen that the R channel has a higher ASR curve if it is scaled independently of the other channels.

This can be explained by a discrepancy between the integrating sphere measurements of irradiance above 600 nm and the spectrometers measurements of irradiance above 600 nm. At about 600 nm, the sensitivity of the silicon detector used for the integrating sphere measurements begins to drop. Above about 650 nm, the detector's output for the brightest monochromatic spots generated with the monochromator is comparable to its lowest possible reading. That is, the detector can measure no less than 1 microwatt and the monochromatic spots provide only a few microwatts flux through the integrating sphere's port. Approaching 650 nm, it is suspected that the accuracy of the detectors output is effected by a sloping detector sensitivity and the radiance calculated from the integrating sphere's output is incorrect. At the same time, the 600 to 650 nm range in which the measurements disagree is well within, in fact in the center of, the spectrometer range of highest efficiency.

For these reasons, the spectrometer measurements are used, given by "R Fixed Ratio" in Figure 5.16, to determine the ASR curve of the R channel relative to the G and B channels by maintaining the relative relationship between R channel's sensitivity and the G and B channel's sensitivity. Essentially, only integrating sphere data points below 600 nm were used to scale the relative sensitivities to determine the ASRs. This is accomplished by scaling the R channel with the G and B channels in the ratios determined by the ratios of their relative sensitivities.

One confirmation that the spectrometer measurements are more appropriate to use is that above 850 nm the R, G and B channels have been observed to give the same digital output for any monochromatic radiance. The ASR calculated for the R channel from integrating sphere measurements contradicts this observation, while the spectrometer determined ASR maintains it, as can be seen by the convergence of the ASRs in that region in Figure 5.16.

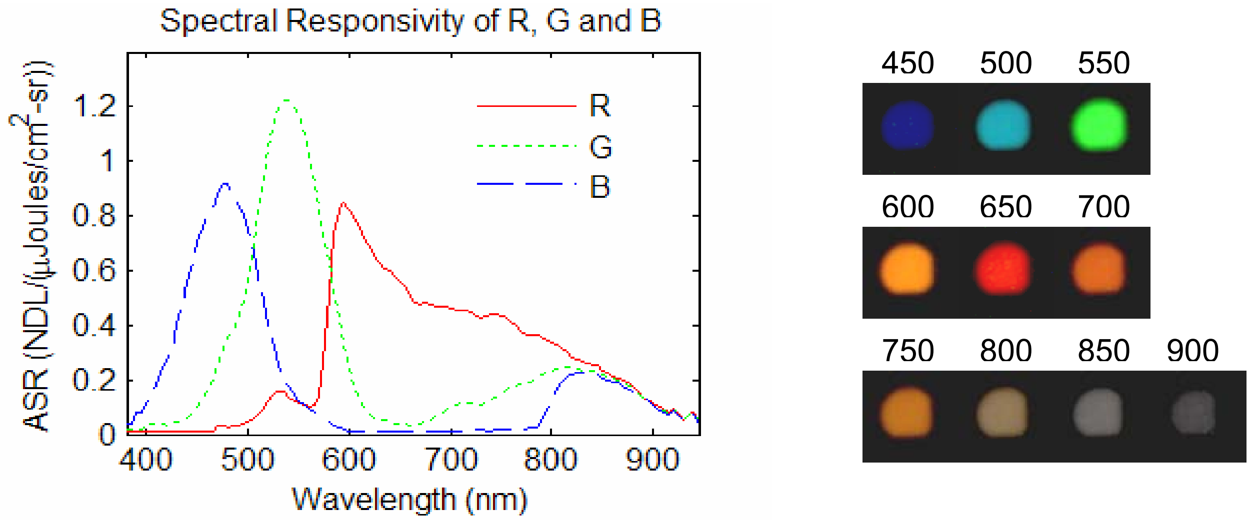

Figure 5.17 Final ASR for R, G, and B and monochromatic spots

Another feature to observe in Figure 5.16 is the decision to crop the R channels ASR curve below 475 nm. This was done because the erratic behavior observed in the 380 to 475 nm range for the R channels ASR is known not to represent the channels true responsivity, but is rather an error generated by the methodology for calculating the normalized spectral exposures, $h^{0.3}_{R,G,B}(\lambda)$. Because the R channels output is so low in this range, errors occur when calculating the normalized spectral exposures. The same behavior can be observed for the G channel below 400 nm and the B channel below about 390 nm (even when the Xenon lamp was used). For this reason, the ASRs for these channels were cropped over intervals in which they are known to be insensitive rather than use the errant, calculated normalized spectral exposures.

Figure 5.17 shows the final, cropped and appropriately scaled ASR curves for each channel. It should also be noted that the B channel's ASR below 390 nm has been assumed to drop, rather than rise as shown in Figure 5.16, to fit the trend in its sensitivity. This decision was made because, even with the Xenon lamp, useful images of monochromatic radiances below 390 nm were difficult to achieve because of the lamps low output in this region, and the calculated ASRs based on these images were subject to similar errors caused by very low channel sensitivities.

The result of this spectral sensitivity calibration is an ASR curve for the R, G and B channels given by $r_{R,G,B}(\lambda) = 1/h^{0.3}{}_{R,G,B}(\lambda)$ for 5 nm wavelength intervals spanning 380 to 945 nm. This can also be written in discrete form, since discrete 5 nm wavelength intervals are used, as $r_{R,G,B,\Delta\lambda} = 1/h^{0.3}{}_{R,G,B,\Delta\lambda}$. Equation (5-14) can also be written in discrete form to relate the digital output of each channel, when viewing a 5 nm-wide monochromatic beam, to the total radiance in that 5 nm interval, given by:

$$L_{e,\Delta\lambda} = \frac{h^{0.3}_{R,G,B,\Delta\lambda}}{t_{int}} \times c\left(\frac{b}{(NDL_{R,G,B} - a)} - 1\right)^{1/d} \tag{5-16}$$

Theoretically, if narrow passband filters were used to isolate wavelengths of radiation viewed by the camera into 5 nm bands, the camera could measure the radiance in each of these beams exactly (to within the calibration errors discussed in the next section). However, 5 nm wide box-like filters are not available. Furthermore, it would require 113 filters to span the full 380 to 945 nm range with 5 nm filters.

If one desires to accurately measure radiances using the digital output of the camera without numerous, 5 nm wide filters, another approach is required. The approach is to filter the radiation viewed by the camera over larger wavelength intervals. The wavelength intervals must be selected so that the digital output can still be accurately converted into radiances. This process and its resulting accuracy will be explained in section 5.2.8. First, however, it is important to understand the camera's response to polychromatic radiation, rather than just the monochromatic radiances discussed in this and previous sections.

5.2.7 Response to Polychromatic Radiation

To understand the camera's response to polychromatic radiances, first we will investigate the expected response of the camera from theory, and then compare this to the measured response of the camera from experiments.

Theoretically, the digital output of the camera stimulated by polychromatic radiation should be related to the total, not spectral, exposure of its sensor array as explained in (Brown et al. 2001). The total exposure of a pixel is given by the integral of its spectral exposures weighted by that channels ASR, $r_{R,G,B}(\lambda) = 1/h^{0.3}{}_{R,G,B}(\lambda)$. The digital output of the channel is a function of this total exposure, given by:

(5-17) $$NDL_{R,G,B} = f\left(\int r_{R,G,B}(\lambda)h(\lambda)d\lambda\right)$$

Since the spectral exposure we use here is simply given by radiance multiplied by integration time, this can be re-written as:

(5-18) $$NDL_{R,G,B} = f\left(\int r_{R,G,B}(\lambda)L_e(\lambda)t_{int}d\lambda\right)$$

Or in discrete form:

(5-19) $$NDL_{R,G,B} = f\left(\sum_{380-945} r_{R,G,B,\Delta\lambda}L_{e,\Delta\lambda}t_{int}\right)$$

Where $L_{e,\Delta\lambda}$ is the total radiance over a wavelength interval $\Delta\lambda$ and the sum occurs over all wavelength intervals to which the camera is sensitive, since the camera is not sensitive to radiances outside of this range. If the total radiance of the beam across the range to which the camera is sensitive is given by:

(5-20) $$L_{e,beam,380-945} = \sum_{380-945} p_{\Delta\lambda}L_{e,beam,380-945}$$

So that:

(5-21) $$L_{e,\Delta\lambda} = p_{\Delta\lambda}L_{e,beam,380-945}$$

in equation (5-16) and $p_{\Delta\lambda}$ is the fraction of the total radiance from 380 to 945 nm in a wavelength interval $\Delta\lambda$, then equation (5-19) can be re-written in as:

(5-22) $$NDL_{R,G,B} = f\left(L_{e,beam,380-945}t_{int}\sum_{380-945} r_{R,G,B,\Delta\lambda}p_{\Delta\lambda}\right)$$

This says that the absolute responsivity of the camera to a polychromatic beam is simply a weighted sum of the ASRs, where the weights are determined by the relative spectra of the beam, given by $p_{\Delta\lambda,}$ across the wavelength interval to which the camera is sensitive. For the Kappa CCD camera this region is 380 to 945 nm. For this work, the spectra must be aggregated into discrete 5 nm intervals because this is the resolution with which the discretized absolute spectral responsivities, $r_{R,G,B,\Delta\lambda,}$ were measured. The

$r_{\Delta\lambda}$'s in equation (5-22) are different for each channel and given by $1/h^{0.3}_{R,G,B,\Delta\lambda}$, and so equation (5-22) can be re-written as:

$$\text{(5-23)} \qquad NDL_{R,G,B} = f\left(L_{e,beam,380-945} t_{int} \sum_{380-945} \frac{p_{\Delta\lambda}}{h^{0.3}_{R,G,B,\Delta\lambda}} \right)$$

Because the non-linear response of the camera has the same shape for all channels and all wavelengths, it is reasonable to assume that the function relating NDL and radiance for a polychromatic beam is the same as that for a monochromatic beam, shown in equation (5-12). This suggests that the functional form of equation (5-23) is given by:

$$\text{(5-24)} \qquad NDL_{R,G,B} = a + \frac{b}{1 + \left(\frac{(L_{e,beam,380-945} t_{int}) / h^{0.3}_{R,G,B,beam}}{c} \right)^{d}}$$

which has the same form as equation (5-23) except that the functional form has been defined, and (5-12) except that the absolute spectral responsivity has been replaced by a polychromatic responsivity given by the weighted sum of absolute spectral responsivities, or:

$$\text{(5-25)} \qquad \frac{1}{h^{0.3}_{R,G,B,beam}} = \sum_{380-945} \frac{p_{\Delta\lambda}}{h^{0.3}_{R,G,B,\Delta\lambda}}$$

This can be thought of as the total (not spectral) absolute responsivity of each channel to a polychromatic beam with the relative spectrum given by equation (5-21).

This leads to a final equation relating the camera's digital output for polychromatic radiation to the total radiance in that beam across the wavelength range to which the camera is sensitive, 380 to 945 nm. This is given by:

$$\text{(5-26)} \qquad L_{e,beam,380-945} = \frac{h^{0.3}_{R,G,B,beam}}{t_{int}} \times c\left(\frac{b}{(NDL_{R,G,B} - a)} - 1 \right)^{1/d}$$

where the absolute responsivity of R, G and B to the beam, $1/h^{0.3}_{R,G,B,beam}$, is given by equation (5-25).

The theory thus suggests that if the relative spectrum of polychromatic radiation viewed by the camera is known, then equation (5-26) can be used to convert the digital output of the camera into the total radiance of the polychromatic beam the camera is viewing. The CCD camera can then be used as a multi-point radiance or luminance meter for polychromatic beams of known relative spectra across the 380 to 945 waveband. In controlled situations, such as a room with spectrally neutral surfaces and daylight, sunlight or electric light of known spectra, quick light distribution assessments can be made at locations of interest in the room for a large field of view.

The theory developed above has been confirmed by the experiments explained below. To verify that the camera predicts the total radiance of polychromatic radiation accurately, as described by equation (5-26), images of polychromatic and monochromatic beams with known spectral radiances were taken and the relationship was verified.

First, a polychromatic beam made up of two monochromatic beams was imaged. The experimental setup for this procedure consisted of two monochromatic sources irradiating the Labsphere reflectance standard simultaneously, and separately. The Labsphere tungsten-halogen lamp was equipped with 450, 500 or 550 nm narrow passband filters and the 400W HMI lamp was filtered by the monochromator to 450, 500 or 550 nm radiances. The spectral irradiance of the standard for each beam was measured separately using the Labsphere integrating sphere and the corresponding radiance was calculated using the spectral reflection coefficients of the reflectance standard. Images of the standard were then taken irradiated by each beam separately and both beams together at different integration times. A schematic of the experimental setup is shown in Figure 5.18.

The results, comparing the measured exposure (radiance times integration time) versus NDL to the predicted exposure versus NDL from the polychromatic logistic dose response, equation (5-24), are shown in Figure 5.19. The plotted points are the camera's NDL plotted against the measured spectral exposure using the integrating sphere for each scenario, where 500 and 550 designate the separate measurements and "Com" designates both beams simultaneously. The lines are the predicted response curves of the camera based on the spectral sensitivity calibration and polychromatic response formulations using equation (5-24). The results show that the measured response curves match the predicted response curves very closely for wavelengths to which the camera is sufficiently sensitive. The R channel, on the other hand, could not be used to predict the radiance in 500 nm, 550 nm, or mixed 500 and 550 nm beams. On the other hand, the G and B channel could predict the spectral exposures to within less than 5 percent typically, or at worst 10 percent near the slopes in their sensitivities, such as at 450 nm.

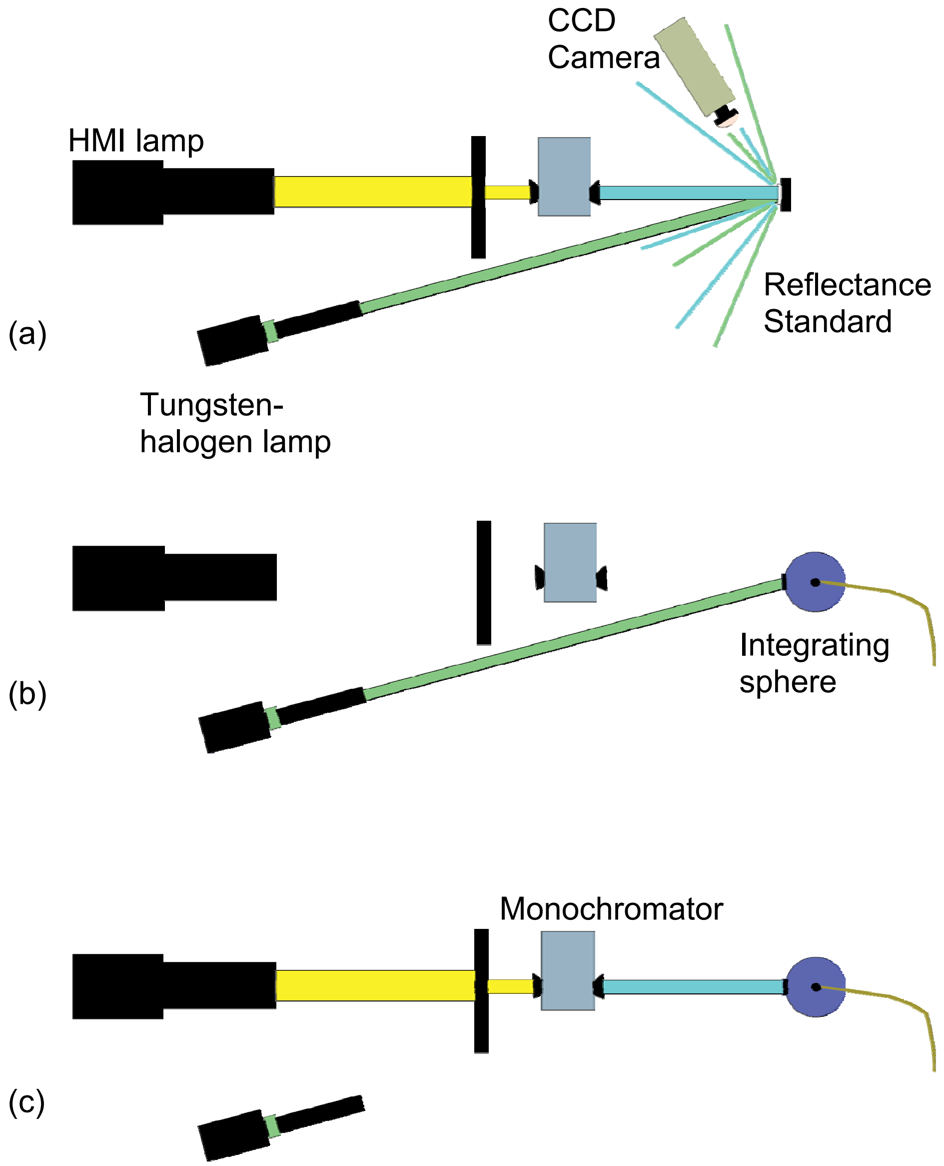

Figure 5.18 Schematic of two beam polychromatic response experiment
(a) Camera viewing polychromatic radiance generated by 500 and 550 nm beams irradiating a reflectance standard
(b) Measuring the irradiance of the reflectance standard from the 550 nm beam using the integrating sphere and
(c) the same for the 500 nm beam

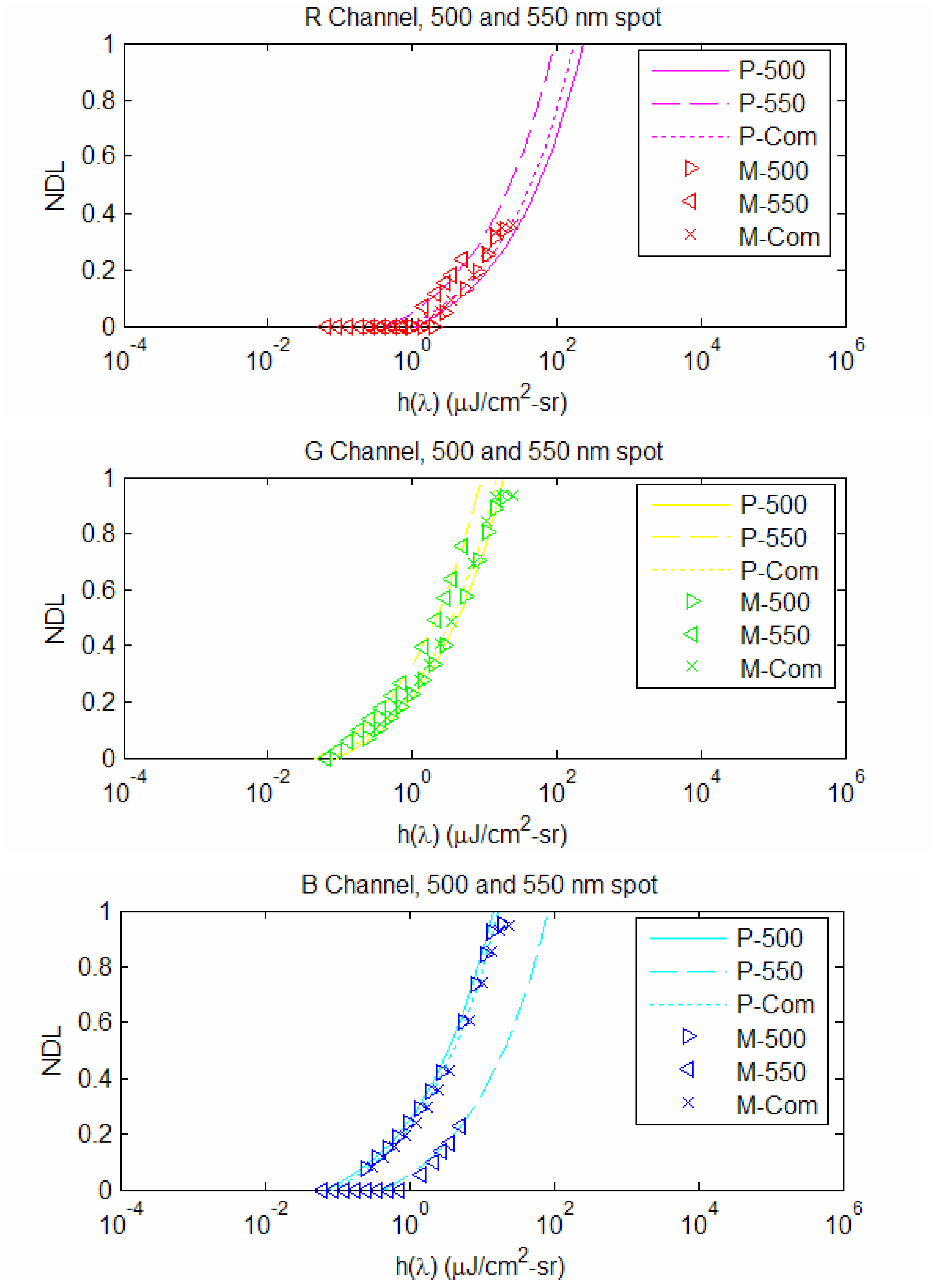

Figure 5.19. Predicted exposures from R, G, and B channels compared to measured exposures

To extend these results to general polychromatic beams and to quantify the typical expected errors, a series of pictures were taken with the Kappa CCD camera of spots on the diffusing reflectance standard with a few different known spectra. The spectral irradiance of the beam incident on the reflectance standard was measured using the spectrometer and integrated over 380 to 945 nm to calculate the total radiance seen by the camera across that interval. Using the relative spectrum, the digital output of each channel was used to estimate the total radiance of the beam across that interval. Figures 5.20 and 5.21 show the NDL of each channel plotted against the measured exposure to a variety of beams from 380 to 945 nm and the predicted exposures for those same NDL. The relative spectrum for each of the spots studied is also shown. All available filters were used to produce the variety of polychromatic and monochromatic radiances, only some of which are shown in Figures 5.20 and 5.21.

The measured and predicted exposures are seen to follow the same response curves very closely. This excludes points near saturation, at NDL ~ 0.9, and on certain channels for spots where the channel is highly insensitive to the relative spectrum of radiances emerging from the spot. Again, the R channel predicts the response curve to 450 nm light very poorly. This is because the sensitivity of the R channel is negligible for that wavelength, as evident in its ASR curve shown in Figure 5.17. No channel can be expected to reliably predict radiances where its sensitivity is too low. This will be accounted for during the BT(R)DF measurement process by not using channels that are too insensitive to predict radiances over certain wavebands, as described in Chapter 6. In addition, it can be seen that after one channel has saturated, the response of the other channels no longer follows the predicted response curves. This can easily be avoided by never predicting radiances with pixels for which any channel is saturated. Neighboring pixels should also be discarded to avoid adjacency effects.

Over the set of validation spots, some of which are shown in Figures 5.20 and 5.21, excluding saturation points and insensitive channels, the average error for estimating radiance for each channel was found to be 8.9 percent for R, 4.3 percent for G, and 5.2 percent for B. These calibration errors are a good estimate of the total errors in modeling the non-linear response of the camera, the spectral sensitivity calibration and the polychromatic response formulation combined.

Although these errors may be accepted and the existing ASRs used for experiments with the goniophotometer, further work may be performed to improve on these errors by adjusting the ASRs shown in Figure 5.17 if, for example, a given channel is consistently over-estimating or under-estimating spectral exposure. This work would focus on using the results of the validation experiments to modify the R channel's ASR curve to better agree with the viewed validation radiances. This modification is justified due to the uncertainties in the determination of the R channel's ASR due to the conflict between integrating sphere and spectrometer predicted R channel ASRs. These refinements may be made as part of future work on the goniophotometer.

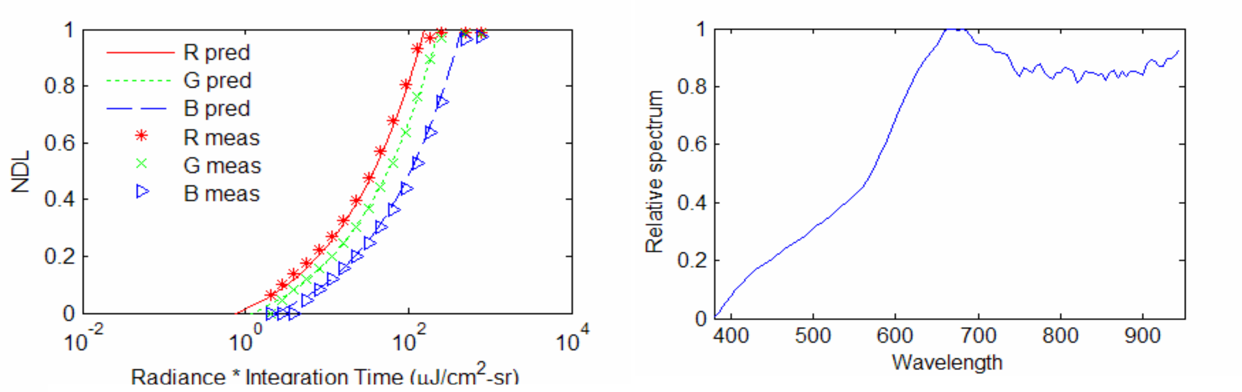

(a) Camera response to raw tungsten-halogen lamp

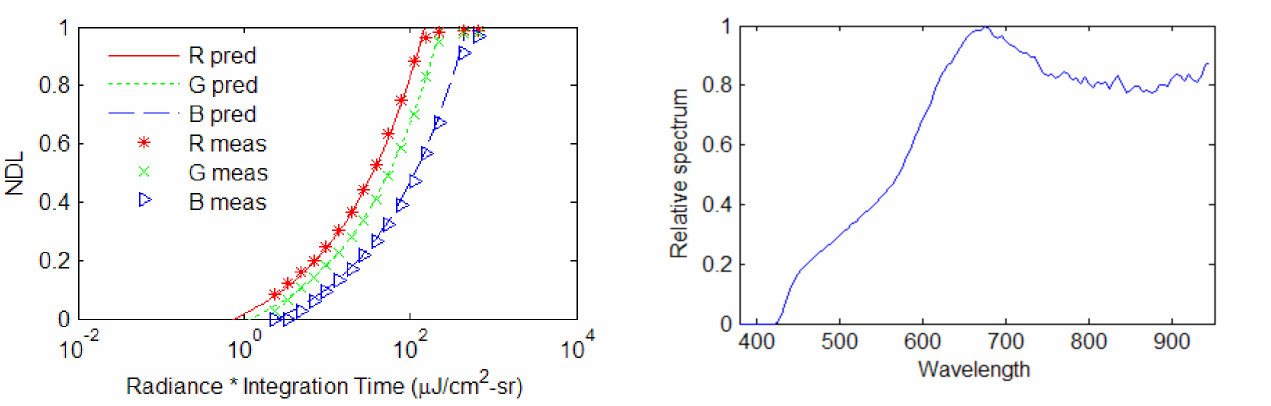

(b) Camera response to tungsten-halogen lamp with 450 nm long pass filter

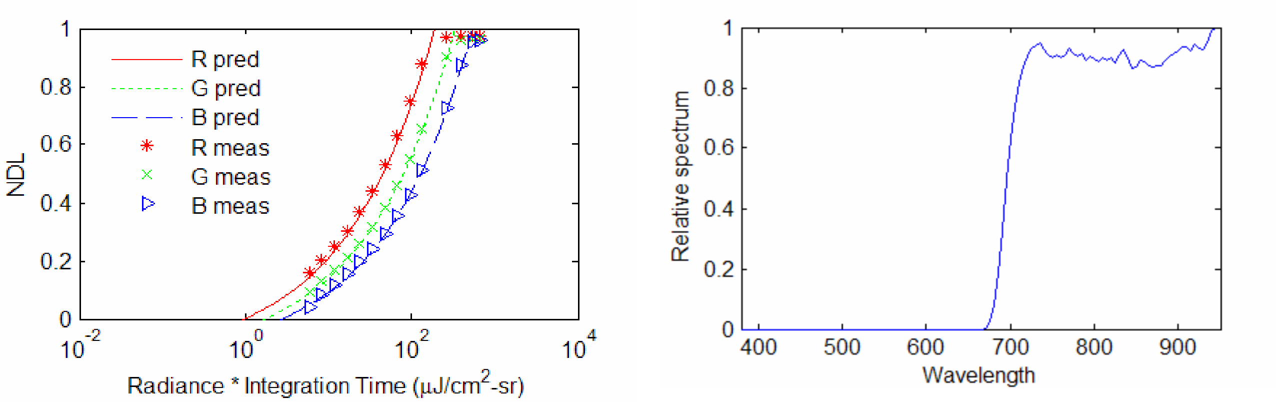

(c) Camera response to tungsten-halogen lamp with 695 nm long pass filter

Figure 5.20 Measured versus predicted response curves for polychromatic validation spectra

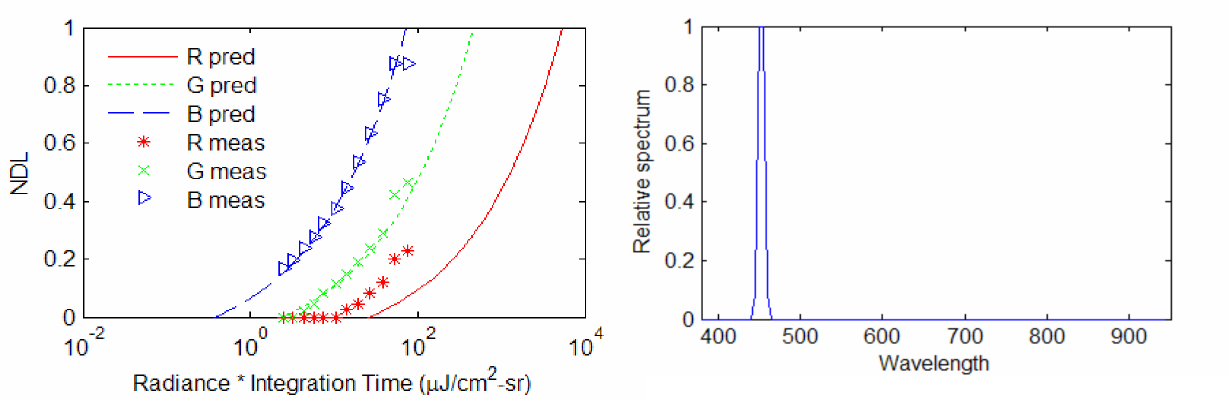

(a) Camera response to tungsten halogen lamp with 450 nm passband filter

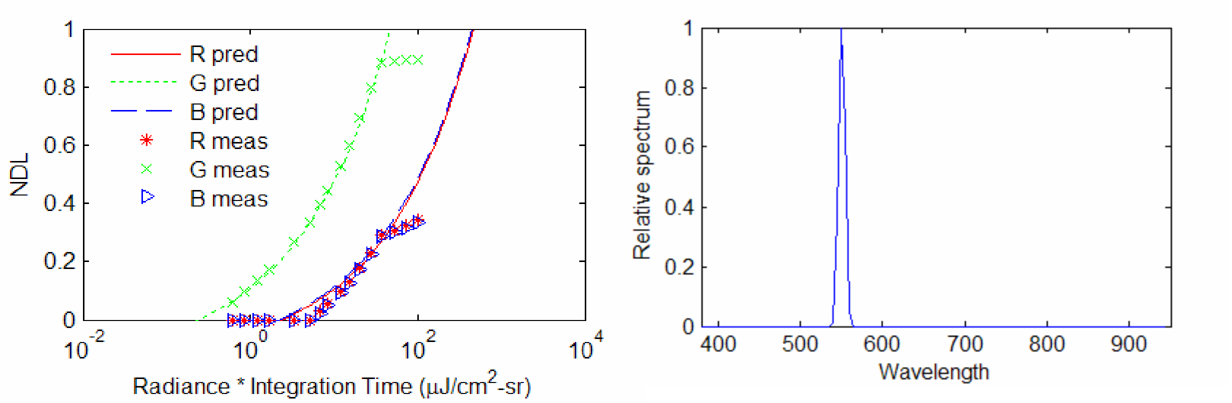

(b) Camera response to tungsten halogen lamp with 550 nm passband filter

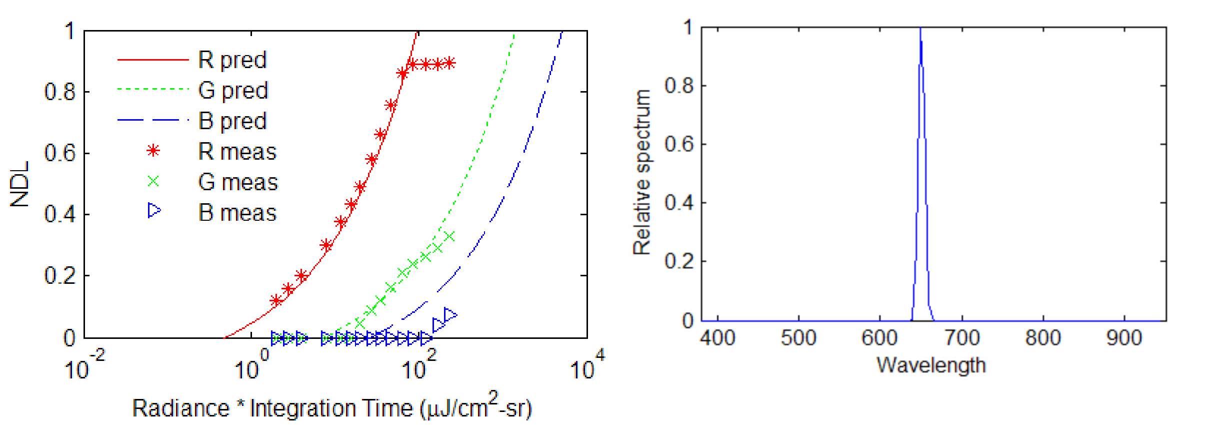

(c) Camera response to tungsten halogen lamp with 650 nm passband filter

Figure 5.21 Measured versus predicted response curves for three monochromatic validation spectra

5.2.8 Measuring Radiances with Unknown Spectra

Measuring the radiance of beams with known relative spectra can be useful in many instances, such as measuring the BT(R)DFs of spectrally neutral fenestration systems or in studying radiance and luminance distribution in spaces where spectra are known. However, in order to study fenestrations with unknown, spectral BT(R)DF, it is important to be able to use the camera as a radiance and luminance meter even when the spectrum is unknown.

Spectrally selective materials will change the relative spectrum of reflected or transmitted light, and thus change the absolute responsivity of the camera to the reflected or transmitted beam from that for a neutral sample, for which the relative spectrum is unchanged and known. The easiest conceptual way to address this issue is to use narrow passband filters to sample the spectrum and thus avoid the need to measure polychromatic beams, but such ideal, box-like filter either don't exist or are prohibitively expensive. In addition, it would slow down the measurement process by necessitating many pictures for all of the filters. A different method has been developed to accurately measure the net radiometric or photometric transmission or reflection by a sample across wavelength intervals of interest, divided into segments of the visible and NIR.

The approach is to break up the spectrum into wavelength intervals over which the camera can still accurately measure total radiance across that interval. This is done by choosing filters which span wavelength intervals over which the camera's sensitivity is reasonably flat. The analysis presented here focuses on the camera's ability to accurately measure radiances across such intervals, and not the goniophotometer's ability to estimate quasi-spectral BT(R)DF, which will be discussed in Chapter 6.

As mentioned, ideally, box-like filters could sample the spectrum over intervals defined by each channel's spectral sensitivity. These could be defined so that if the camera's average sensitivity over the interval was used to predict a monochromatic radiance, the measured monochromatic radiance would differ from the true monochromatic radiance by no more than a defined value, such as 20 percent. For an error of at most 20 percent in measuring any monochromatic radiance over any interval, 31 box-like filters from 380 to 945 nm would be required, with some bands as large as 725 to 810 nm and many as small as 5 nm, as shown in Figure 5.22. For this analysis, channel ASRs below 10 percent of the maximum ASR were assumed to be poor predictors of radiance (based on the validation experiments described above) and channels were discarded over regions with such low responsivities.

The 20 percent error would only occur for monochromatic radiances where the true sensitivity for that wavelength differed most from the average sensitivity to all wavelengths across the interval. Conversely, if the camera viewed monochromatic radiation for which its ASR *was* the average ASR within the band, there would be no additional errors due to the filtering method.

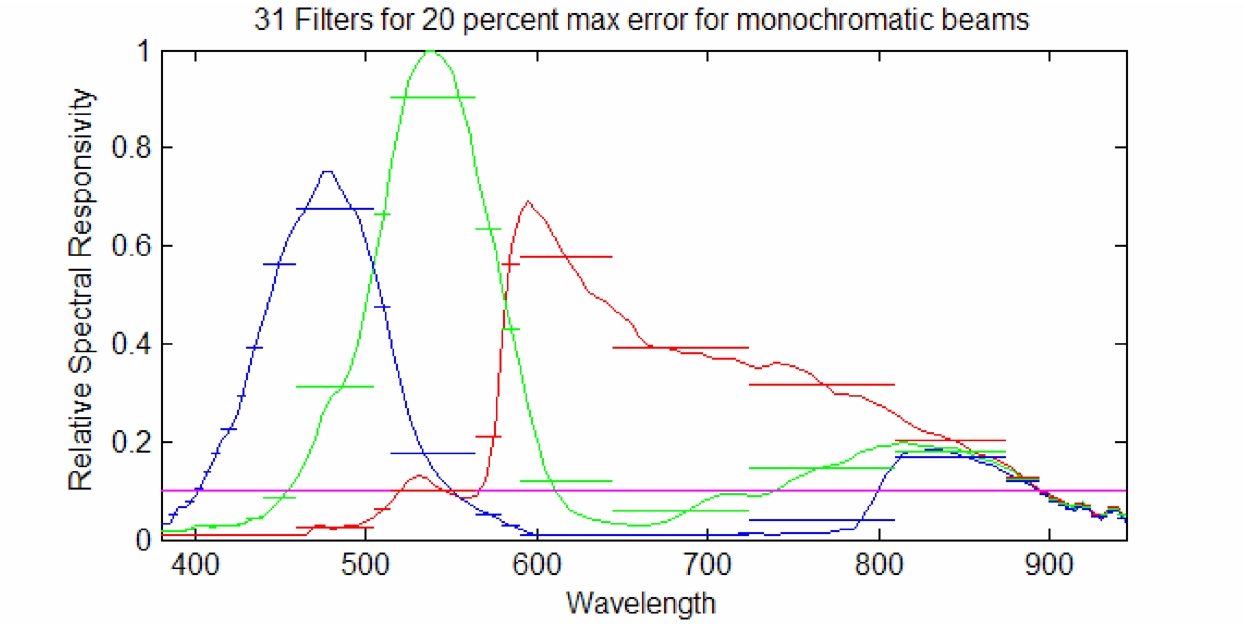

Figure 5.22 Example of box-like filter method. Flat lines represent average spectral responsivity within each band. The discontinuities in the step functions are the boundaries between each theoretical band.

With this theoretical box-like filter method, polychromatic beams with flatter relative spectra across each wavelength interval could be predicted much more accurately than monochromatic beams at arbitrary locations within each interval. For example, if the spectral radiance were constant across an interval, the total radiance would be predicted precisely, in theory, neglecting calibration errors in the ASR curves themselves. If the spectral radiance varied only slightly across the interval, such as 0 to 30 percent from the mean across the interval, the errors would be much smaller than the 20 percent error achievable for the worst case monochromatic beam, generally less than 5 to 10 percent depending on the band.

Although this theoretical, box-like filter approach has promising implications for its ability to measure radiances of unknown spectra, real filters are not available or affordable at arbitrary cutoffs with ideal box-like features. In addition, the constraints dictated by accurately measuring monochromatic radiances, discussed in the previous two paragraphs, are too stringent for the fenestration systems likely to be studied.

Simulations of the cameras predicted radiance for real unknown spectra were performed to study the potential for accurate radiance measurements using *real* filters that span larger wavelength intervals with non box-like transitions. The total radiance across each wavelength interval calculated from the simulated digital output was compared to the true radiance across the interval. Simulations were performed with all possible combinations of Schott short, long and band pass filters listed in the Schott Glass Filter Catalog (Schott 2007). Schott Color Glass Filters were chosen because they provided affordable filters with reasonably sharp transitions from absorbing to transmitting over wavelengths that could isolate flatter sections of each channel's ASR curves.

The filter combinations that led to the best predicted radiance and luminance from the camera across each filter set's wavelength interval for a variety of unknown spectra were chosen for use with the CCD camera. These simulations are described in greater detail in Section 6.5 as part of the quasi-spectral BT(R)DF estimation methods, but the details of the simulations will not be presented here.

The optimal filters determined by the simulations are shown in Table 5.2. The spectral transmission coefficients of these filter combinations from 380 to 945 nm are shown in Figure 5.23, and the resulting filtered HMI spectra are shown in Figure 5.24. These filters span larger wavelength intervals where either the R, G, or B channel have gradually changing ASR and span smaller wavelength intervals where the channel ASR have greater slopes. There are also more filters for wavelengths at which the photopic response curve has the greatest slope.

Table 5.2 Filter Specifications

APPROXIMATE λ INTERVAL	SCHOTT COLOR GLASS FILTERS AND THICKNESSES
1) 380-500 nm	GG400 (1 mm), BG25 (2 mm),BG39 (1mm)
2) 450-590 nm	GG455 (2 mm), BG7 (2 mm)
3) 480-590 nm	GG495 (2 mm), BG 7 (2 mm)
4) 500-650 nm	OG530 (2 mm), BG42 (2 mm)
5) 550-640 nm	OG570 (2 mm), BG39 (2 mm)
6) 570-690 nm	OG590 (2 mm), BG40 (2 mm)
7) 650-850 nm	RG665 (2 mm), KG1 (2 mm)
8) 800-945 nm	RG830 (2 mm)

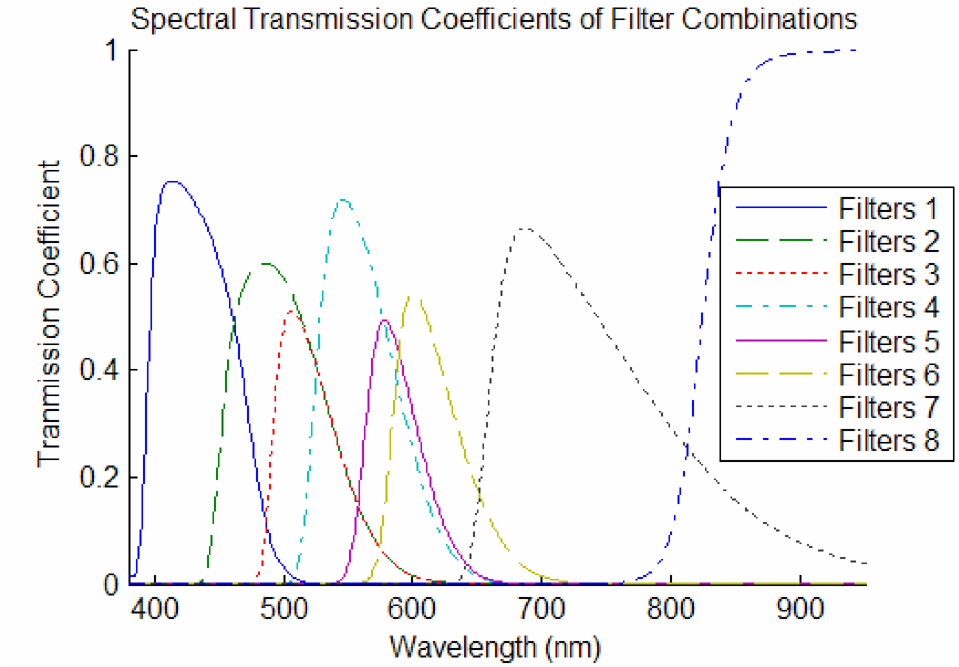

Figure 5.23 Spectral transmission coefficients of filter combinations

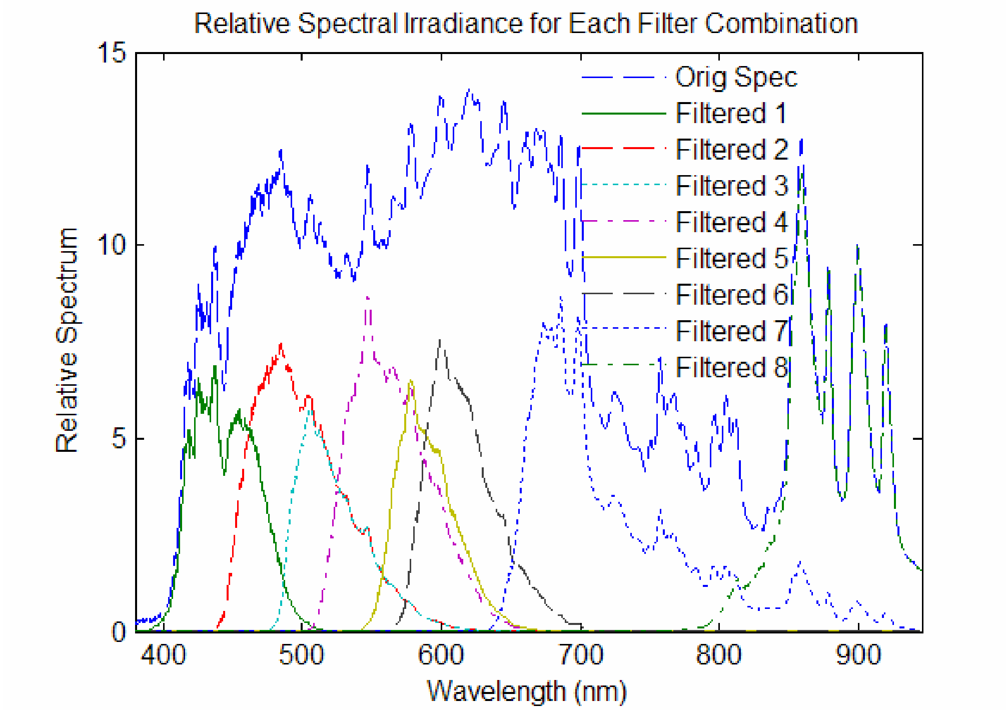

Figure 5.24 Original spectra of the HMI lamp and filtered spectra

It will be shown that these filter sets lead to reasonably accurate estimates of radiance and luminance across the wavelength intervals they span for spectra that have been altered from an assumed spectrum within certain constraints. That is, constraints were defined on how much a known spectrum viewed by the camera can be altered while still enabling radiance and luminance estimation across each filter set's wavelength interval to a defined level of accuracy. This was done by first assuming the CCD camera is viewing radiances with the relative spectrum determined by the filter combinations described above and the HMI lamp. Then, these spectra were altered systematically to determine how and how much the spectrum within each interval could be altered without introducing unacceptable errors in estimated radiance and luminance.

As mentioned, first we assume that the camera is viewing the spectrum of one of the filtered HMI spectra shown above. The camera's absolute responsivity to any of these spectra is given by:

(5-27) $$\left[\frac{1}{h^{0.3}_{R,G,B,\mathrm{filter}}}\right] = \sum_{\mathrm{filter}} \frac{p_{\Delta\lambda,\mathrm{SpectraCamera}}}{h^{0.3}_{R,G,B,\Delta\lambda}}$$

(5-28) $$p_{\Delta\lambda,\mathrm{SpectraCamera}} = \frac{p_{\Delta\lambda,\mathrm{HMI}}\tau_{\Delta\lambda,\mathrm{Filter}}}{\sum_{\mathrm{filter}} p_{\Delta\lambda,\mathrm{HMI}}\tau_{\Delta\lambda,\mathrm{Filter}}}$$

That is, it is once again a weighted sum of the ASRs, where the weights are given by the relative spectra of the filtered HMI spectrum, given by $p_{\Delta\lambda,\mathrm{HMI}}\tau_{\Delta\lambda,\mathrm{Filter}}$, for that filter set. The summation index "filter" is used to denote the sum over all 5 nm intervals $\Delta\lambda$ across the total wavelength interval spanned by the filter set, as shown in Table 5.2 and Figure 5.24. The radiance contribution from all other wavelengths within 380 to 945 nm is negligible.

The next step is to alter the relative spectrum viewed by the camera from this assumed spectrum by a defined amount. This is similar to assuming that a sample has wavelength dependent transmission or reflection properties over the filter interval and will thus alter the relative spectrum of the light viewed by the camera, but within certain constraints. The alterations considered before, for measuring monochromatic radiances with the box-like filter method, would in effect be comparable to reflection or transmission from samples that reflect or transmit only one wavelength. This is a highly improbable spectral property for the fenestration systems that will be studied.

The spectrum viewed by the camera for each filter set was altered systematically by assuming that it was modified by a sample with linearly increasing or decreasing spectral transmission or reflection coefficients by a defined amount over a defined wavelength interval. For example, for the first filter set, one alteration of the filtered HMI spectrum investigated was for a spectral transmission coefficient that varied from 0.7 to 0.3 over 50 nm from 400 to 450 nm. Figure 5.25 shows the way in which the spectrum viewed by the camera was altered systematically for each filter combination. The solid

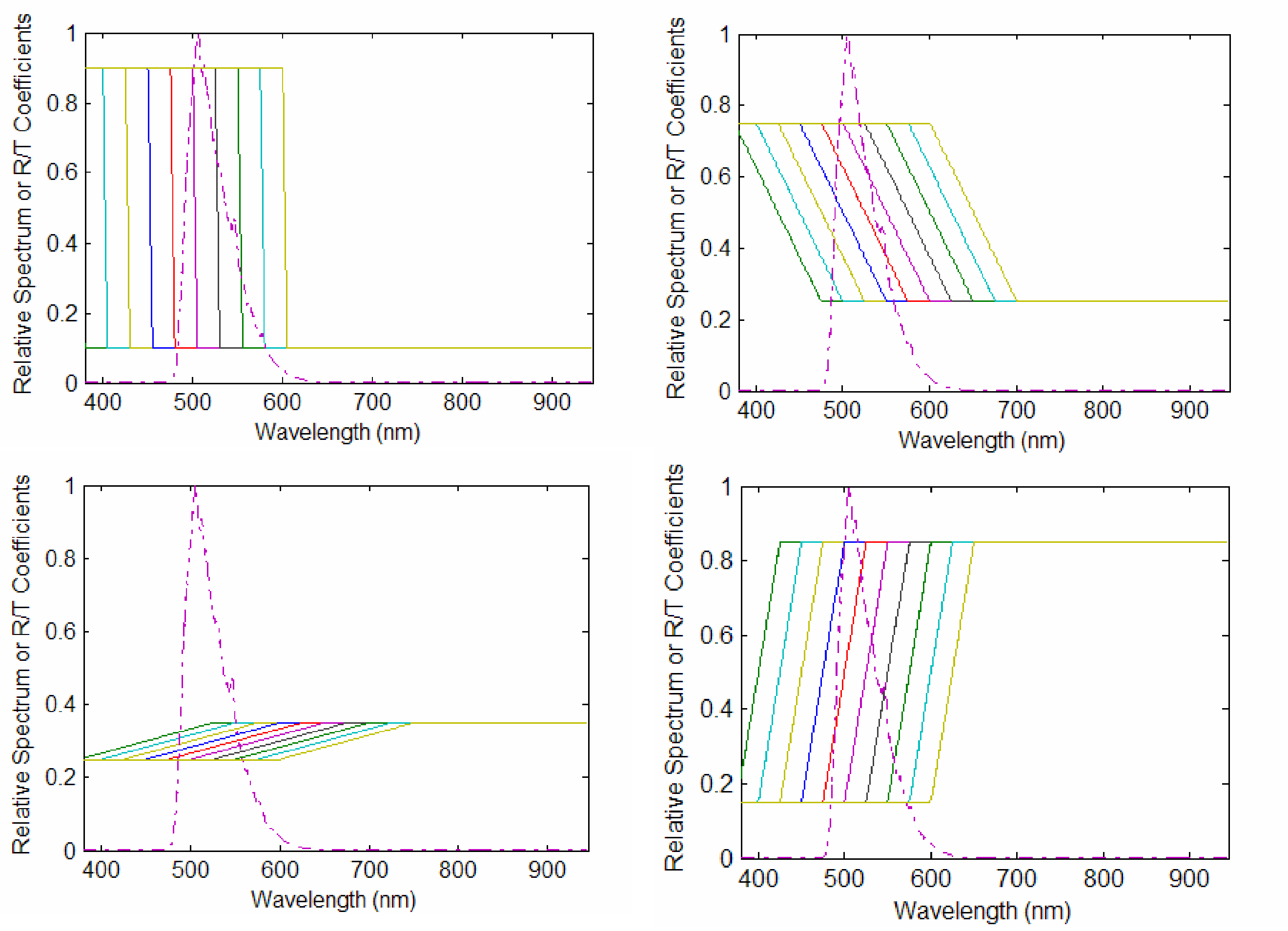

Figure 5.25 Hypothetical transmission coefficients used to alter filtered HMI spectra to calculate errors in using the original relative spectra to calculate channel responsivity and estimate total radiance or luminance for each filter combination, despite the alterations to the known relative spectra resulting in an unknown spectra

lines show the spectral transmission (or reflection) coefficients of a theoretical material which alters the filtered HMI spectrum, which is shown as the dotted line. For now, the effects of the hemi-ellipsoid are ignored because this will be covered as part of the goniophotometer's ability to measure quasi-spectral BT(R)DFs in Chapter 6, rather than the camera's ability to measure radiances and luminances, which is covered here.

As shown in Figure 5.25, many different types of alterations were considered. The following parameters were varied: the wavelength interval over which alterations to the relative spectrum occurred and the magnitude of the change in relative spectrum. Higher errors in radiance estimation can be expected for alterations to spectra that significantly reduce the total radiance over a wavelength interval, such as that cause by a very lowly transmitting sample.

Using this method of systematically altering the spectrum viewed by the camera, the errors introduced by using the camera to estimate the radiance of unknown spectra for each filter set can be calculated. Note that *some* knowledge of the spectrum is assumed, that is, the spectrum viewed by the camera is assumed to be altered from an expected spectrum (the filtered HMI spectrum). Each channel's responsivity to the expected spectrum, given by equations (5-25) and (5-26), is used to calculate radiance. Again, this is like assuming that the spectral transmission coefficients across the filter's wavelength interval are constant, but only in order to calculate the camera's responsivity. Then, the error between the radiance calculated using this responsivity is compared to the true radiance of the altered spectrum.

The results of this error analysis provide limits on how much a spectrum can be altered within each wavelength interval spanned by the filter sets such that the camera can still measure radiance or luminance accurately when assuming the relative spectrum of radiation has not changed (even though it has) to calculate channel responsivity This is the approach that will be used to measure radiances and luminances of unknown spectra with the cameras within each filter set. Alterations to the spectrum were defined that introduce errors in radiance estimation by no more than about 10 percent, roughly, and errors in luminance estimation by no more than 20 percent, roughly, for each filter set. These defined errors are not exactly achieved for the worst case scenario for each filter set. Sometimes the errors are a little higher. It should also be noted that typically for these changes the errors are much *lower* than the error introduced by the worst positioning of the change within the wavelength interval.

For example, for the first filter set, as shown in Figure 5.26, the relative spectrum viewed by the camera can be altered by 35 percent over a 50 nm interval without introducing errors in radiance estimation greater than 10 percent and luminance

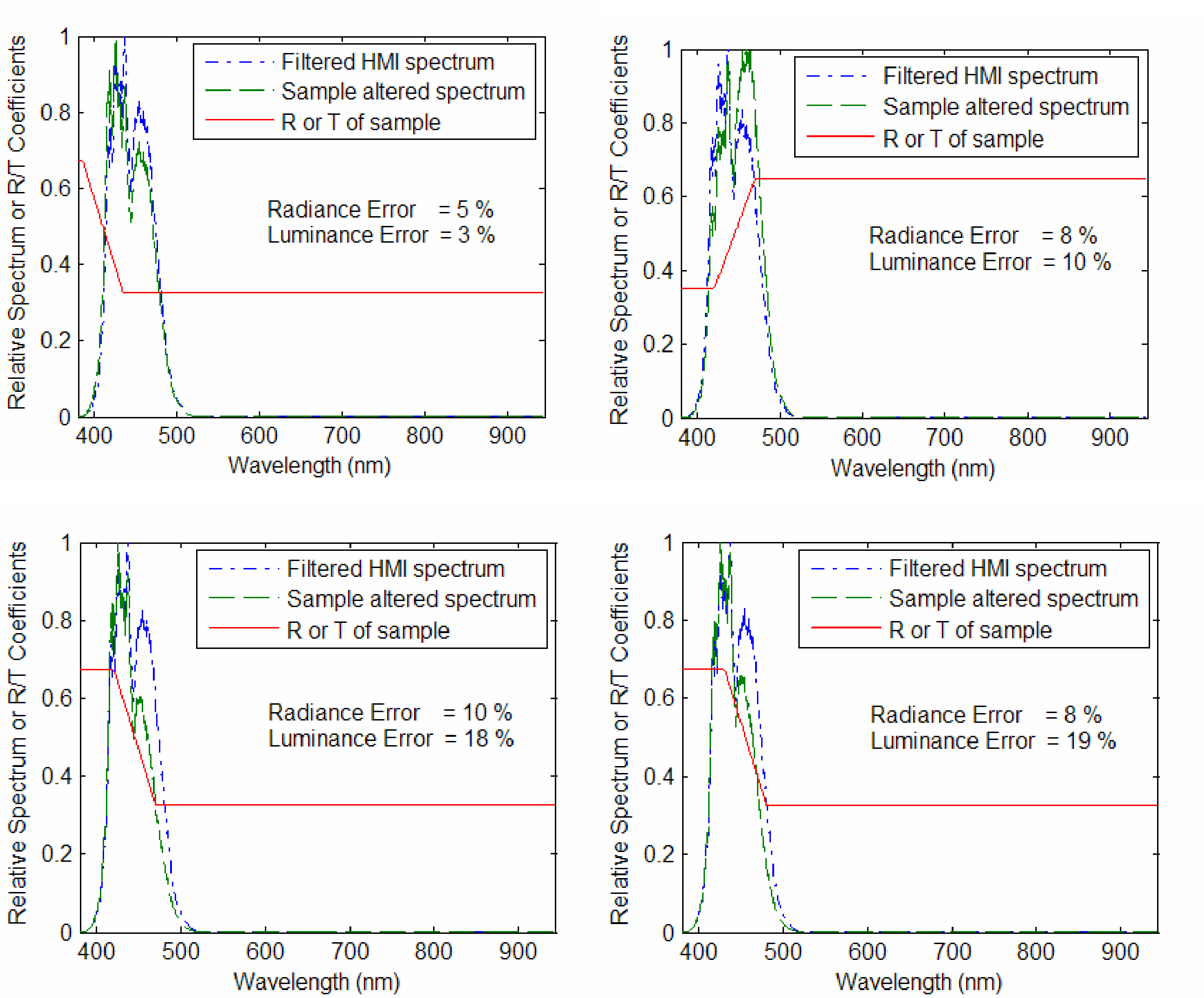

Figure 5.26 Maximum errors in radiance or luminance estimation using filter set 1 resulting from a 35 percent variation in sample reflection or transmission coefficients across a 50 nm interval

estimation errors greater than 20 percent. This is like saying that the spectral reflection or transmission coefficients of a sample can vary by 35 percent over a 50 nm interval within filter set one's wavelength span without introducing errors in radiance more than 10 percent or luminance by 20 percent in the worst case.

These are the worst errors introduced by such a variation, meaning that the slope of the alteration (downwards) and the position of the change (from 415 to 465 nm) are those which cause the most error, as shown on the bottom of Figure 5.26. Any variations over larger intervals, for smaller changes to the spectrum, for the same change positioned at any other wavelength within the interval, or for a change that slopes in the other direction, will lead to less error as shown in the top of Figure 5.26 for a two cases.

Luminance errors for spectral alterations near the edge of the wavelength interval, like that in the bottom left of Figure 5.26, are greater because the edge of the interval is close to where the V(λ) curve begins to rise, and thus errors in relative spectra become more significant to luminance estimation.

A similar analysis was performed for all of the filter combinations to calculate the maximum allowable variation in sample spectral transmission or reflection coefficients over each filter set's wavelength interval for which the camera can still provide accurate radiance or luminance measurements to within a defined degree of error. Table 5.3 shows the maximum allowable spectrum alterations, or transmission or reflection coefficient properties, by the magnitude of the change in spectral properties (Percent Change in R or T) over a wavelength interval (Variation Interval) located anywhere within the wavelength interval spanned by each filter set.

Graphs of the variations in spectra, under the constraints in Table 5.3, that lead to the maximum radiance errors and maximum luminance errors within each filter set's wavelength interval are shown in Figures 5.27 through 5.28 respectively. These graphs show the expected spectrum the camera is assumed to have viewed (that for a sample neutral across the interval), the altered spectrum that the camera *actually* viewed (that for a sample *not* neutral across the interval), and the transmission or reflection coefficients that would cause this alteration (neglecting the effects of the hemi-ellipsoid, which will be minor due to its generally flat spectral properties).

Table 5.3 Constraints on spectral transmission and reflection coefficients within filter wavelength intervals

Parameter/Filter Set	**F1**	**F2**	**F3**	**F4**	**F5**	**F6**	**F7**	**F8**
Filter Start Wavelength(nm)	380	450	480	500	550	570	650	800
Filter End Wavelength(nm)	500	590	590	650	640	690	850	945
Variation interval (nm)	50	100	50	50	50	50	100	100
Percent Change in R or T	35	30	50	35	30	50	30	50
Max Rad. Error	10	9	9	13	13	6	5.5	13
Max Lum. Error	19	24	9	9	7	21	30	N/A

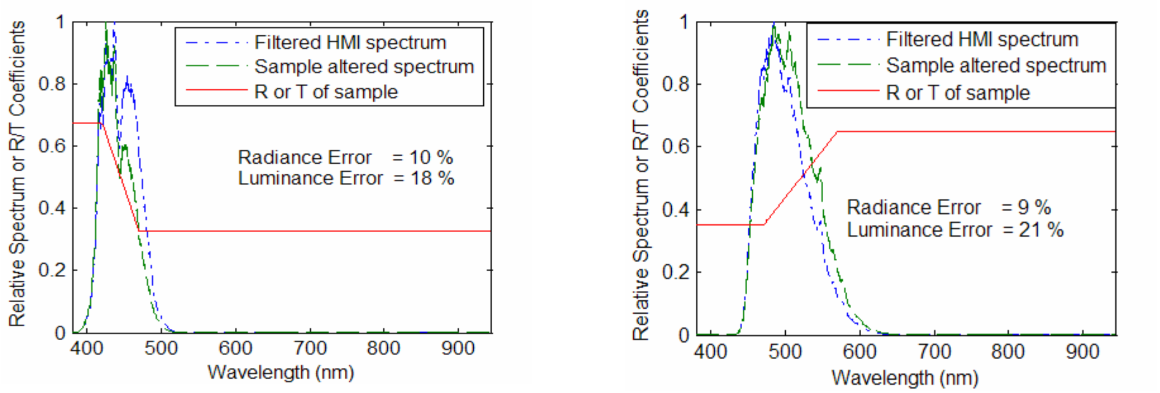

(a) Filter Set 1, 380-500 nm (b) Filter Set 2, 450-590 nm

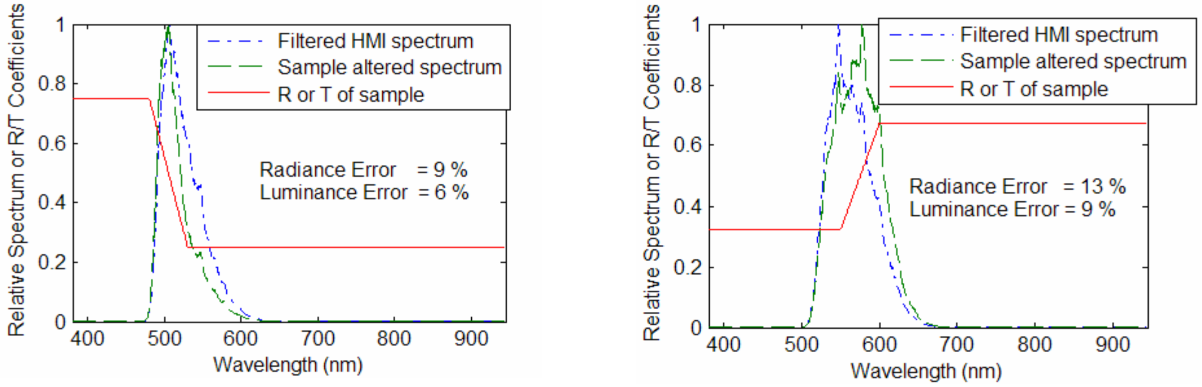

(c) Filter Set 3, 480-590 nm (d) Filter Set 4, 500-650 nm

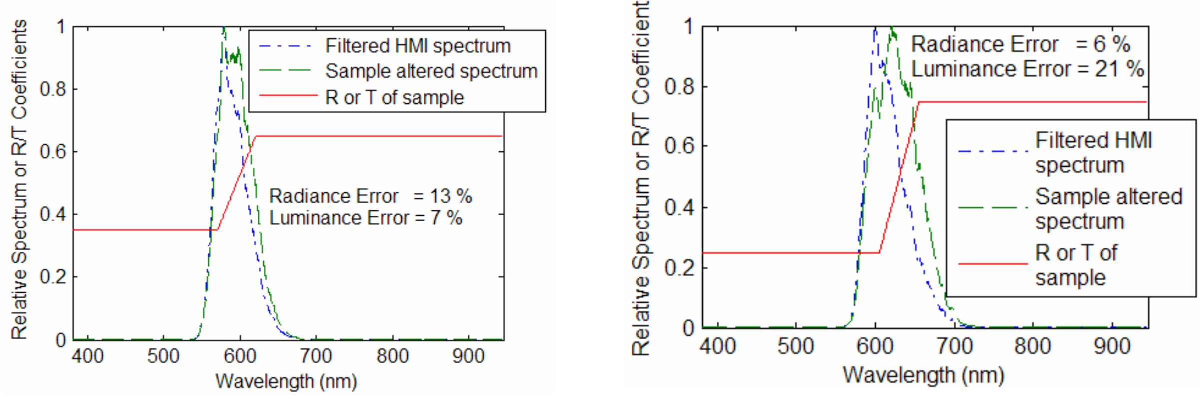

(e) Filter Set 5, 550-640 nm (f) Filter Set 6, 570-690 nm

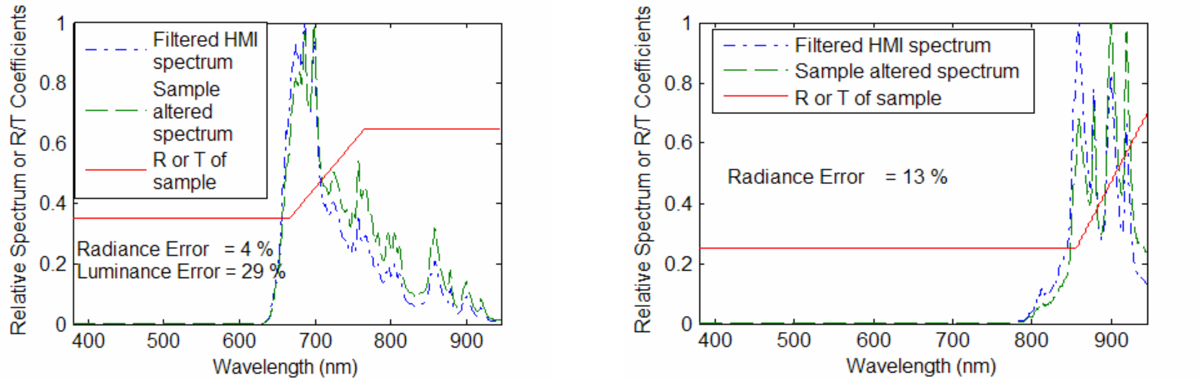

(g) Filter Set 7, 650-850+ nm (h) Filter Set 8, 800-945 nm

Figure 5.27 Hypothetical alterations in spectra leading to maximum errors in radiance estimation for each filter set under constraints defined in Table 5.3

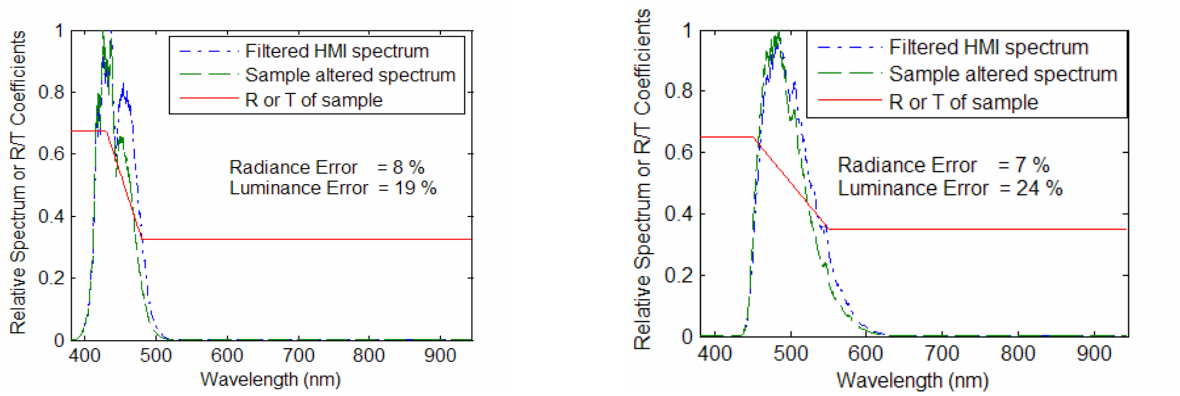

(a) Filter Set 1, 380-500 nm

(b) Filter Set 2, 450-590 nm

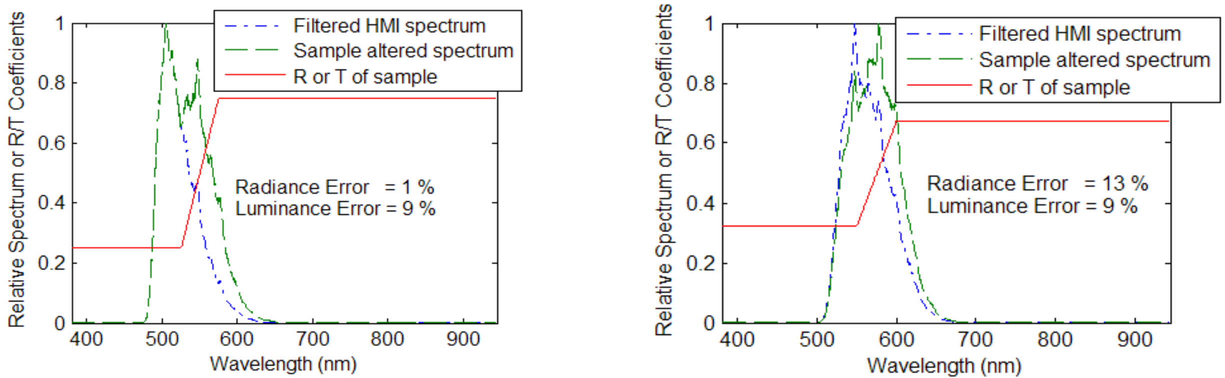

(c) Filter Set 3, 480-590 nm

(d) Filter Set 4, 500-650 nm

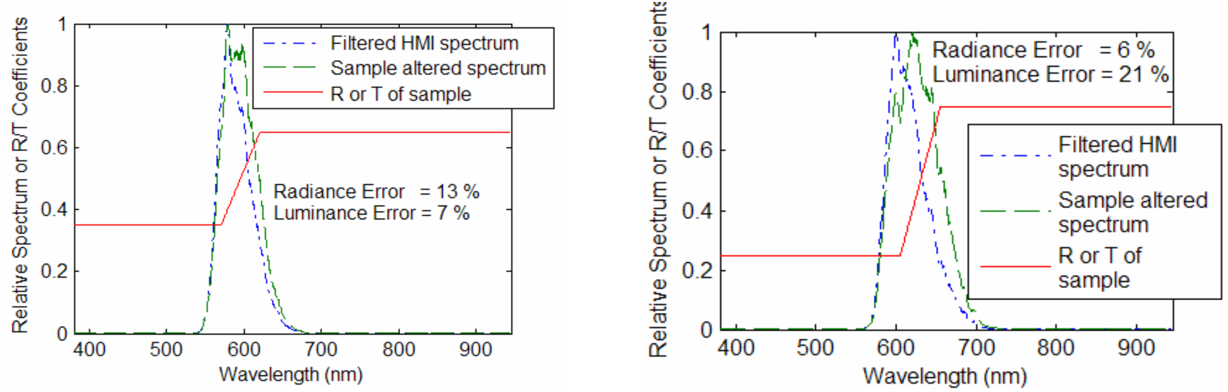

(b) Filter Set 5, 550-640 nm

(f) Filter Set 6, 570-690 nm

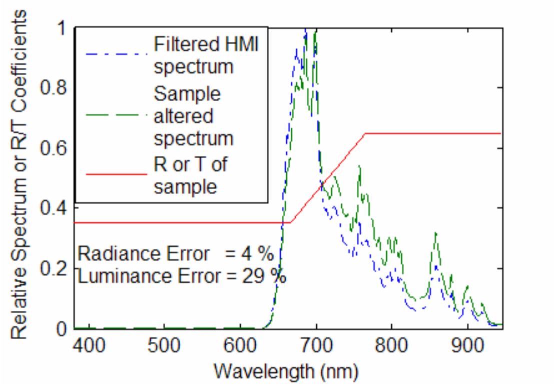

(g) Filter Set 7, 650-850 nm

Figure 5.28 Hypothetical alterations in spectra leading to maximum errors in luminance estimation for each filter set under constraints defined in Table 5.3

This systematic analysis of the possible changes to the spectrum viewed by the camera for the HMI lamp sampled with each filter sets provides an estimate of the constraints on the spectrally selective samples that the camera will be able to analyze with reasonable accuracy.

The errors resulting from alterations in spectra presented above are *in addition* to calibration errors described in section 5.2.7. Again, this analysis neglects the effects of reflection off of or transmission through the hemi-ellipsoid, which will be accounted for in Chapter 6.

The fact that the errors in radiance or luminance estimation over each filter interval depend on how spectrally selective a sample is over that interval and where within the interval its wavelength dependent optical properties change poses a difficult problem for the goniophotometer. The analysis above is meant to provide a summary of the hypothetical types of wavelength dependencies that can reasonably be studied, however, without knowing something about how spectrally selective a sample is beforehand, it will be difficult to determine the exact accuracy of the radiance or luminance estimates determined using each filter combination.

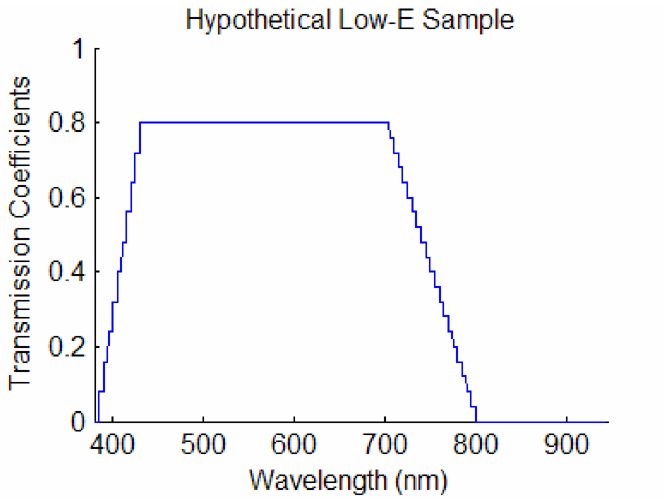

Figure 5.29 Transmission Coefficients of Hypothetical Low-E Sample

On the other hand, most fenestration systems do not have the types of spectral properties that cause the worst errors found in this analysis. Across the visible region, most fenestration systems are close to neutral, and could thus be measured to a very high degree of accuracy, as will be demonstrated in Chapter 6. In the low wavelength visible region, or in the ultraviolet, there may be samples with sharply rising spectral transmissivities. At the same time, approaching the NIR some samples with spectrally selective low-e coatings may show sharply falling spectral transmissivities.

Still, the additional errors caused by the filtering method for this type of sample would be far less significant than the maximum errors described above. For example, a hypothetical fenestration with spectral transmission coefficients shown in Figure 5.29 would result in radiance estimation errors of 5 percent for filter set one, negligible errors for filter sets two through six, 10 percent error for filter set seven, and very high errors for filter set eight, but only because there is little to no radiance in that range. The additional errors in luminance estimation would be insignificant because the sample is essentially neutral across the wavelengths for which photometric quantities are most important.

A more detailed analysis of the *typical* errors in radiance and luminance estimation using this method, and also errors in quasi-spectral BT(R)DF estimation using methods developed in Chapter 6, are presented in section 6.5. This section deals only with the accuracy of the CCD camera in estimating the radiance or luminance of spectra altered, within certain constraints, from an expected spectra for theoretically possible wavelength dependent optical properties, which may not be common in real fenestration systems.

Chapter 6 will first explain how the radiance estimates from the camera's can be used to calculate the average bi-directional transmission or reflection coefficients across defined bands within each filter's wavelength interval. Section 6.5 will the present analysis of the actual *expected* errors in using the goniophotometer for total radiance across the 380 to 1700 nm range, total luminance and BT(R)DF estimation for *real* fenestration systems using their *actual* optical properties. The errors in calculating these properties for typical fenestration samples will be shown to be generally much lower than the radiance and luminance errors presented in this section.

5.3 InGaAs Camera Calibrations

Many of the same procedures used to calibrate the CCD camera were also performed to calibrate the Sensors Unlimited SU320 1.7RT NIR camera. The images from the NIR camera were captured through an NI-PCI1422 Image Acquisition Board. The settings for the camera response were set to linear, corresponding to a gamma of one. The image size for the 320 by 240 array had to be cropped to 320 by 238 in order to grab frames stably. The digital level of noise was found to be about 0.16 NDL for the 12-bit camera. Many of the pixels in the used NIR camera are permanently saturated or defective; about one to two percent of the total pixels. These pixels will not be included in the BT(R)DF measurement process.

5.3.1 Vignetting Correction

A similar vignetting correction experiment as that described for the CCD camera in section 5.2.2 was also performed with the NIR camera. The SU320 1.7RT camera with the Fujinon fish eye lens was rotated from normal to perpendicular viewing the same scene and the drop off in pixel levels with zenithal angle was observed. The diffusing reflectance standard was not used due to the low angular resolution of the camera and

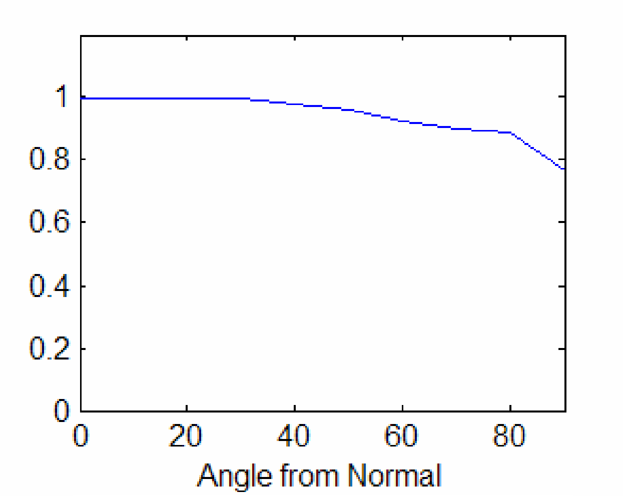

Figure 5.30 Light drop off with zenith angle relative to fish eye for NIR camera

Table 5.4. NIR Vignetting Correction Factors

Angle from Normal	Factor
0	1.000
10	1.000
20	1.000
30	1.000
40	0.981
50	0.962
60	0.924
70	0.899
80	0.888
90	0.769

the need for a spot occupying a larger solid unit of angle. Instead, a non-diffusely reflecting piece of white foam board was used to reflect light from the HMI lamp. Images were taken with the camera in the same position relative to the reflected light so that the camera remained at the same location within the angular distribution of light reflected off of the foam board. The camera was then rotated at this position from normal to perpendicular relative to the spot, just like the procedure for the CCD camera. The resulting drop off in pixel values with zenith angle is shown in Figure 5.30. The vignetting correction factors for the NIR camera are shown in Table 5.4. The digital output of the NIR camera should be divided by these factors prior to calculating radiance from its output.

5.3.2 Angular Resolution

Like the angular resolution experiment for the CCD camera described in section 5.2.3, pictures were taken at further and further distances away until a decrease in the digital output of the camera was observed for a spot with the same radiance. Like the NIR vignetting correction experiment, a piece of white foam board was used so that the initial spot occupied a large enough solid unit of angle relative to the camera so that this experiment could be performed. The spot imaged was 9.25 inches in diameter. When instead the reflectance

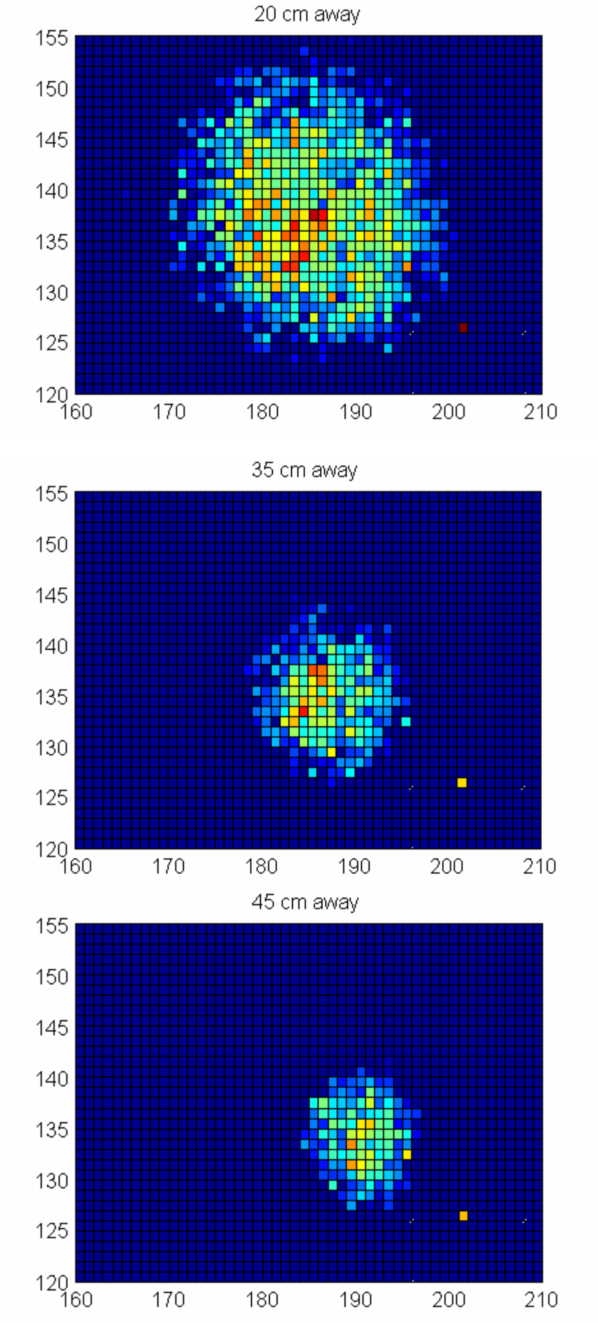

Figure 5.31 Angular Resolution of NIR camera

standard was used, which is 1.25 inches in diameter, the occupied solid unit of angle was already below the angular resolution threshold of the NIR camera for distances that did not obstruct the light beam, and pixel values were already showing reduced values due to the angular resolution of the camera.

The distance at which the decrease in pixel values begins and the size of the spot viewed define the angular resolution of the NIR camera. The NIR camera's average digital output over the spot remained constant until the spot occupied a solid unit of angle less than about 0.25 steradians, corresponding to the 45 cm away graph in Figure 5.31, which shows the NDLs in the NIR image on a 0.65 to 0.8 scale. This places a lower bound on the angular resolution of the NIR camera and the ability of the goniophotometer to resolve features of BT(R)DFs over the NIR.

5.3.3 Spatial Calibration

The same calibration box used to calibrate the CCD camera was used for the NIR camera. However, due to the lower angular resolution of the NIR camera larger calibration points spaced at 3 inches apart were added to the spatial calibration grid along each azimuth. The marker used to draw the calibration grid for the CCD camera was not absorptive to NIR, and thus small, black cardboard pieces that absorbed NIR were fixed along each azimuth. A series of pictures were taken as shown in Figure 5.32.

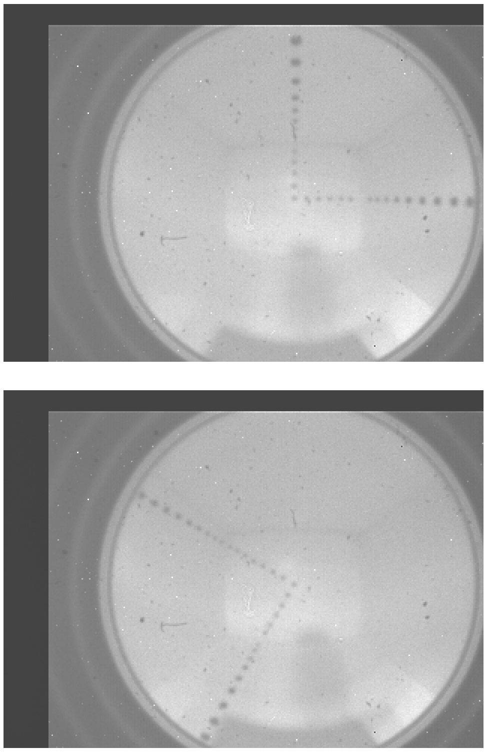

Figure 5.32 NIR camera spatial calibration pictures

The principal point of the NIR camera image was found to be pixel location (193,129). This is far from the center of the sensor array, but in agreement with the unexplained black edges shown in Figure 5.32 found in the images captured by the PCI 1422 framegrabber. Like the CCD camera, the azimuth angle can be calculated in the usual way using a coordinate system where the principal point of the camera defines the center of the coordinate system. The relationship between zenithal angle and pixel distance from the principal point is shown in Figure 5.33. The standard error in the linear regression was 0.5 percent. A coefficient of about 0.7995 degrees per pixel relates zenith angle to the pixel location relative to the principal point.

The same relationships between angles incoming to the camera and angles emerging from the sample derived for the CCD spatial calibration apply here, after pixel locations have been converted into incoming angular directions. The same averaging methods will also be applied over larger solid units of angle.

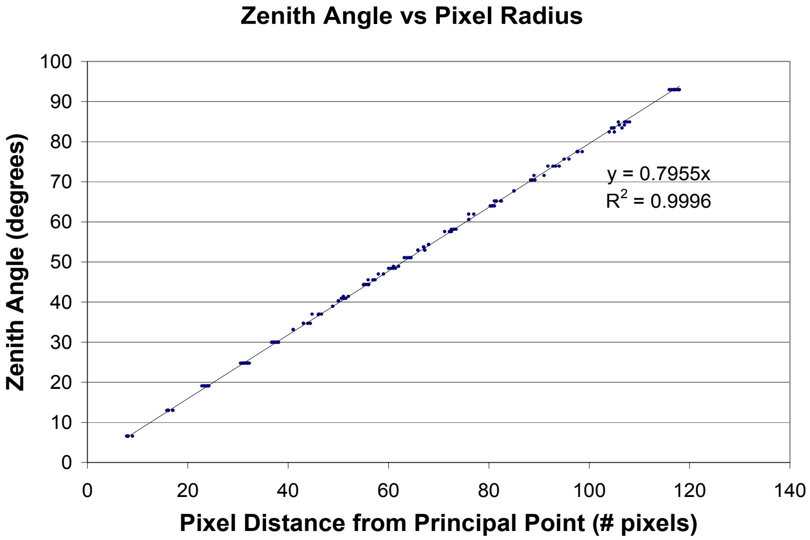

Figure 5.33. Relationship between pixel location and zenith angle for NIR camera

5.3.4 Spectroradiometric Response

The shape of the digital response relative to the spectroradiometric stimuli for the NIR camera was also measured to correlate scene radiance and digital response. The NIR camera was too insensitive to register monochromatic spots on the reflectance standard generated using the Spectral Products CM110 monochromator. Therefore, a different experimental setup was used to measure the spectroradiometric response of the NIR camera than that used for the CCD camera. First the shape of the spectroradiometric response was measured using polychromatic beams, then the absolute spectroradiometric response was measured using a 1480 nm beam.

For polychromatic beam measurements, a Labsphere tungsten-halogen lamp was used to illuminate the Spectralon coated diffusing reflectance standard. Pictures of the spot were taken at all possible integration times, 0.068, 0.136, 0.272, 0.544, 1.088, 2.177, 4.354, and 8.231 milliseconds. The diffusing reflectance standard was then replaced with the Labsphere integrating sphere mounted with an InGaAs detector. Knowing the integration times for the NIR camera, the flux through the integrating sphere could be used to calculate a quantity proportional to the spectral exposure of the camera, $h^*_{NIR}(\lambda)$ = Flux x Integration Time. While this is not the same as the $h(\lambda)$ used for the spectroradiometric calibration of the CCD camera, which included the scene radiance, nor the true spectral exposure of the sensor array, it is proportional to both of these quantities. This surrogate exposure had to be used because the diffusing reflectance standard created monochromatic radiances too dim to be viewed by the NIR camera.

The digital output of the camera was measured against this quantity, $h^*_{NIR}(\lambda)$ and the results are shown in Figure 5.34. The same functions used to determine the best fit for the CCD camera's response were fit to the NIR camera data, like in (Martinez-Verdu et al. 1999). A Gaussian Cumulative function was found to fit the data best, of the form:

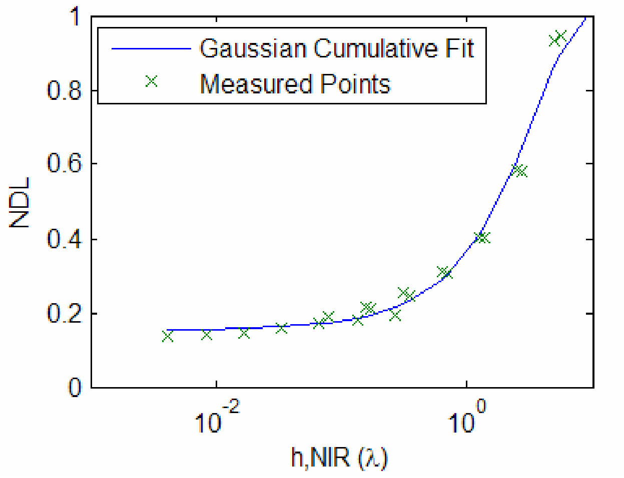

Figure 5.34 NIR camera response curve

(5-29) $$NDL_{NIR} = a + \frac{b}{2}\left[1 + \mathrm{erf}\left(\frac{h^*_{NIR}(\lambda)/h^{*0.3}_{NIR}(\lambda) - c}{d\sqrt{2}}\right)\right]$$

where a = -3.9619, b = 5.0124, c = -5.3157 and d = 5.7771 and erf is the error function.

After finding the shape of the camera's spectroradiometric response, the absolute response to a 1480 nm monochromatic beam was measured. A Labsphere tungsten-halogen lamp was used with the 1480 nm narrow passband filter to create a monochromatic spot on the reflectance standard. This spot was bright enough for the camera to see because a passband filter rather than the monochromator was used. Pictures of the spot were taken with the NIR camera, again at all possible integration times. The irradiance of the reflectance standard was then measured using the Labsphere integrating sphere mounted with an InGaAs detector. The radiance of the spot viewed by the camera was then calculated from this measured irradiance.

The NIR camera output for this 1480 nm spot was very low, despite being the highest radiance achievable with the current equipment. However, the measured spectroradiometric response curve fits the data well, ignoring one data point at the highest integration time, apparent in Figure 5.35. This integration time, however, has actually shown the same deviation in expected output for other spots, that is, a drop rather than a rise in output. It was hence assumed that this point was not representative of the response of the camera at a higher integration time, but rather that there may be a problem with the integration time settings of the camera and that the highest integration time should not be used.

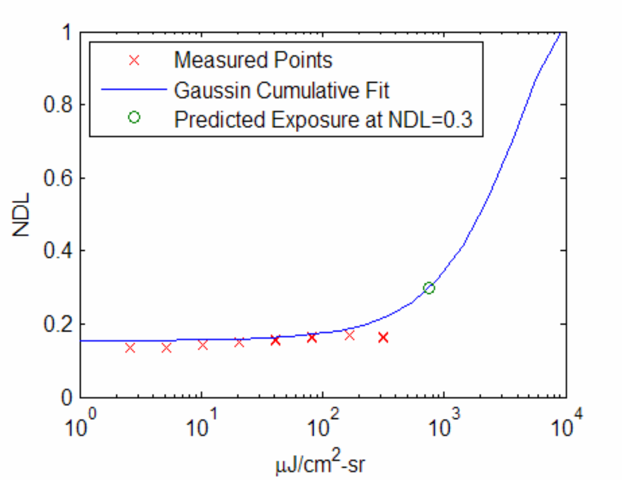

Figure 5.35 Absolute spectral responsivity of NIR camera to 1480 nm radiation

Using the fitted curve shown in Figure 5.35, the spectral exposure $h_{NIR}(\lambda) = L_e(\lambda)*t_{int}$, or radiance multiplied by integration time, leading to a given digital output can be calculated. For example, for monochromatic radiation of 1480 nm, a spectral exposure of $h_{NIR}^{0.3}(1480) = 0.758$ mJ/cm^2-sr would lead to a digital output of NDL=0.3, represented as the circular data point in Figure 5.35. By inverting the Gaussian Cumulative function, a relationship between digital output and a monochromatic radiance at 1480 nm viewed by the camera can be found, given by:

(5-30) $$L_e(1480) = \frac{h_{NIR}^{0.3}(1480)}{t_{int}} \times \left[c + d\sqrt{2} \times \text{erfinv}\left[\frac{2}{b}(NDL_{NIR} - a) - 1 \right] \right]$$

where erfinv is the inverse error function. To generalize this relationship for all wavelengths between 900 and 1700 nm, the spectral exposure $h^{0.3}{}_{NIR}$ (1480) will be used to find the absolute spectral responsivity, $r_{NIR}(\lambda) = 1/h^{0.3}{}_{NIR}(\lambda)$, of the camera based on the relative sensitivity curves. This will be explained in section 5.3.5. Because the data gathered is limited to only a 1480 nm calibration point, further calibration will be necessary to confirm these calibrations when a NIR spectrometer is available for polychromatic calibration, or if higher monochromatic irradiances can be achieved with new equipment, such as additional narrow passband filters.

5.3.5 Spectral Sensitivity

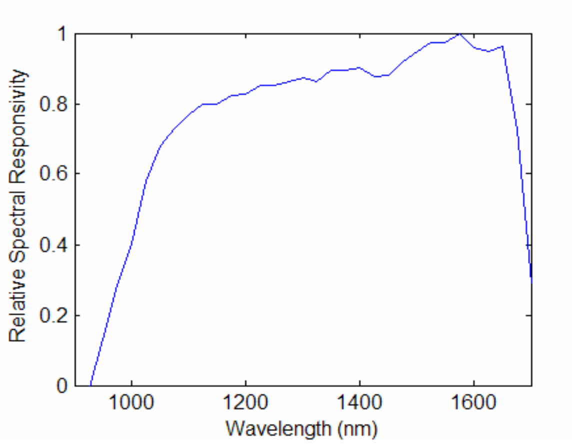

Figure 5.36 Measured relative spectral responsivity of SU320-1.7RT

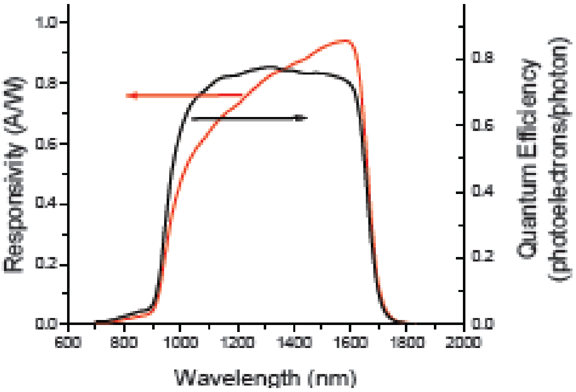

Figure 5.37. Published spectral responsivity of SU320M 1.7RT

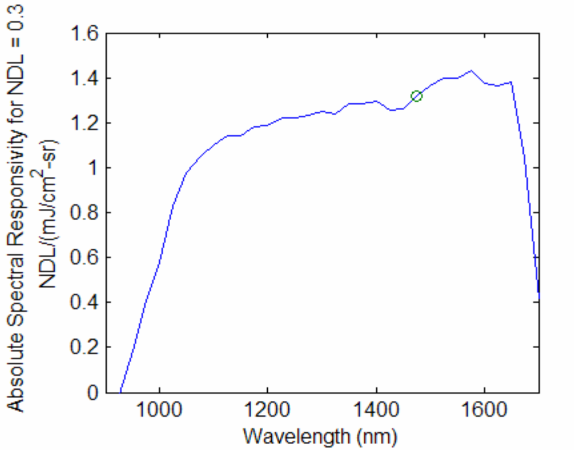

Figure 5.38. Absolute spectral responsivity (ASR) of SU320-1.7RT

A different approach was used to measure the spectral sensitivity of the NIR camera than that taken for the CCD camera. Because spots with high enough radiance could not be created using the monochromator and the diffusely reflecting standard, the output of the monochromator was viewed directly. This is similar to the approach used in (Bellia et al. 2002). First, images were taken of monochromatic beams exiting the monochromator every 25 nm from 900 to 1700 nm. Longpass filters were used to filter all but the first order peaks of the monochromator. Next, the camera was replaced with a Labsphere integrating sphere mounted with an InGaAs detector and the radiant flux of the beam exiting the port was measured with a calibrated radiometer. Although the angular distribution and thus the true radiance viewed by the camera were not known, it was assumed that the angular distribution of light exiting the monochromator did not change as wavelengths were changed. Using this assumption, the radiant flux of the beam exiting the monochromator was used as a surrogate for radiances, since only relative radiances are important to the relative sensitivity calibration.

To determine the relative spectral sensitivity of the camera, the measured effective spectral exposure $h^*_{NIR}(\lambda)$, flux times integration time, was rescaled by the ratio of effective spectral exposures leading to a normalization NDL, 0.3, and the actual NDL output of the camera determined through the Gaussian Cumulative relationship derived above. In this way, the effective spectral exposures leading to the same digital output for all the wavelengths can be compared and the action spectrum of the camera can be determined, as was done for the CCD camera channels. The inverse of these exposures gives the relative spectral responsivity of the NIR camera as shown in Figure 5.36. The published responsivity of SU320M 1.7RT, the successor to the SU320, is shown in Figure 5.37. Comparing the two figures, the measured responsivity of the camera agrees well with the published responsivity for a similar InGaAs camera.

The absolute response of the camera to 1480 nm radiances and the relative spectral responsivity were then used to determine the ASR of the NIR camera. Whereas for the CCD camera many wavelengths were used to fix the relative spectral responsivity curve, the 1480 nm data point is the only point available to determine the ASR of the NIR camera. The spectral exposure leading to NDL= 0.3 was found to be $h_{NIR}{}^{0.3}(1480)$ = 0.758 mJ/cm^2-sr as explained in the previous section. This leads to an absolute spectral responsivity of $r_{NIR}(1480) = 1/h^{0.3}{}_{NIR}(1480) = 1/0.758$ NDL/(mJ/cm^2–sr). This point can be used to fix the location of the relative spectral responsivity curve, as shown in Figure 5.38, which leads to the ASR function, $r_{NIR}(\lambda) = 1/h^{0.3}{}_{NIR}(\lambda)$. This ASR can be used to convert the digital output of the camera to the scene radiance viewed by the camera for monochromatic light between 900 and 1700 nm through the relation:

$$L_e(\lambda) = \frac{h_{NIR}^{0.3}(\lambda)}{t_{int}} \times \left[c + d\sqrt{2} \times \mathrm{erfinv}\left[\frac{2}{b}(NDL_{NIR} - a) - 1 \right] \right] \tag{5-31}$$

As mentioned before, this relation will be verified with additional data points as part of future work on the goniophotometer.

5.3.6 Response to Polychromatic Radiation

Currently, the response of the NIR camera to polychromatic radiation in the NIR cannot be validated because an NIR spectrometer is not available for experiments. However, a reasonable assumption that seems to be supported by the shape of the camera's response to polychromatic beams is that, like the CCD camera, the digital response of the NIR camera to polychromatic radiation is a function of the total exposure (Brown et al. 2001):

(5-32) $$\mathrm{NDL}_{\mathrm{NIR}} = f\left(\int r_{\mathrm{NIR}}(\lambda) h(\lambda) d\lambda\right)$$

and that the relative shape of the response is the same as it was for monochromatic radiation, i.e. it is the Gaussian Cumulative function given by equation (5-29). Over discrete 25 nm bands from 900 to 1700 nm, this can be rewritten using the Gaussian Cumulative response function as:

(5-33) $$\mathrm{NDL}_{\mathrm{NIR}} = a + \frac{b}{2}\left[1 + \mathrm{erf}\left(\frac{\sum_{\Delta\lambda}(L_{e\Delta\lambda} \times t_{\mathrm{int}}) / h^{0.3}_{\mathrm{NIR},\Delta\lambda} - c}{d\sqrt{2}}\right)\right]$$

Calculating the camera's responsivity to a polychromatic beam, this can be rewritten:

(5-34) $$\mathrm{NDL}_{\mathrm{NIR}} = a + \frac{b}{2}\left[1 + \mathrm{erf}\left(\frac{L_{e,\mathrm{beam},900-1700} \times t_{\mathrm{int}} / h^{0.3}_{\mathrm{NIR,beam}} - c}{d\sqrt{2}}\right)\right]$$

where, $\frac{1}{h^{0.3}_{\mathrm{NIR,beam}}} = \sum_{\Delta\lambda} \frac{p_{\Delta\lambda}}{h^{0.3}_{\mathrm{NIR},\Delta\lambda}}$ is the responsivity of the camera to the polychromatic beam, $L_{e,\mathrm{beam},900-1700} = \sum_{900-1700} p_{\Delta\lambda} L_{e,\mathrm{beam},900-1700}$ is the total radiance of the beam, and $p_{\Delta\lambda}$ is the fraction of the total radiance from 900 to 1700 nm located in each 25 nm wavelength interval. This is a parallel formulation to that described in section 5.2.7. From equations (5-33) and (5-34) , a formula for converting the camera's digital output into radiance for polychromatic radiation of known relative spectra can be found:

(5-35) $$L_{e,\mathrm{beam}} = \frac{h^{0.3}_{\mathrm{NIR,beam}}}{t_{\mathrm{int}}} \times \left[c + d\sqrt{2} \times \mathrm{erfinv}\left[\frac{2}{b}(\mathrm{NDL}_{\mathrm{NIR}} - a) - 1\right]\right]$$

This relationship and the assumptions from which it was derived will be validated once an NIR spectrometer is available. The result relies primarily on the assumption that the responsivity of the camera to polychromatic radiation can be calculated as a weighted sum of its responsivities to monochromatic radiation, just like the CCD camera. This assumption is likely to be true and will be verified when the right equipment is available.

5.3.7 Measuring Radiances with Unknown Spectra

The first approach considered for measuring the radiance of unknown spectra within the NIR region was again to filter radiation with box-like filters over intervals in which the spectral sensitivity of the NIR camera was flat. Eight box-like filters could be selected with which the radiance of any monochromatic beam could be measured to within 20 percent error using the theoretical box-like filter intervals shown in Figure 5.39. Like the CCD camera, smaller intervals are necessary where the NIR camera's responsivity curve is changing rapidly, such as from 900 to about 1100 nm. However, where the camera's ASR curve is flat, such as from 1125 to 1675 nm, one wideband filter, spanning a larger wavelength interval could be used to measure monochromatic radiances to within 20 percent. This is because the ASR curve varies over this region by no more than 20 percent. However, as before, idealized box-like filters over these intervals are not reasily available or affordable. As a result, a different strategy is employed.

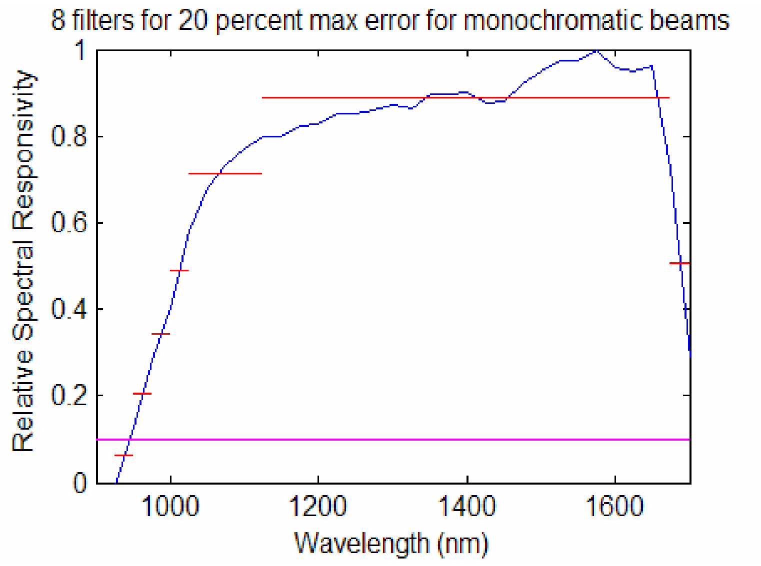

Figure 5.39 Hypothetical box-like filters for 20 percent maximum error in mon9chromatic radiance estimation across NIR

Because the NIR camera's ASR curve is so flat over most of the NIR range, it may be possible to do without filters when using the InGaAs camera to measure radiance across the 900 to 1700 nm range. To determine how accurately these measurements can be made, an analysis similar to that performed for the CCD camera in section 5.2.8 was also performed for the NIR camera. The goal was to determine how much the spectrum within the 900 to 1700 nm range can be altered from an assumed spectrum that is used to convert camera output into radiance estimates without introducing unacceptable errors. The real spectrum of the HMI lamp in the NIR region has not yet been measured, because an appropriate NIR spectrometer is not yet available. Because what matters primarily are alterations in the assumed spectrum, it was considered reasonable to use a surrogate spectrum for the HMI lamp in the NIR that slopes downward from 900 to 1700 nm, which agrees with the general trends of published NIR spectra for HMI lamps. This analysis will be performed again once the spectrum of the HMI lamp can be measured in the NIR.

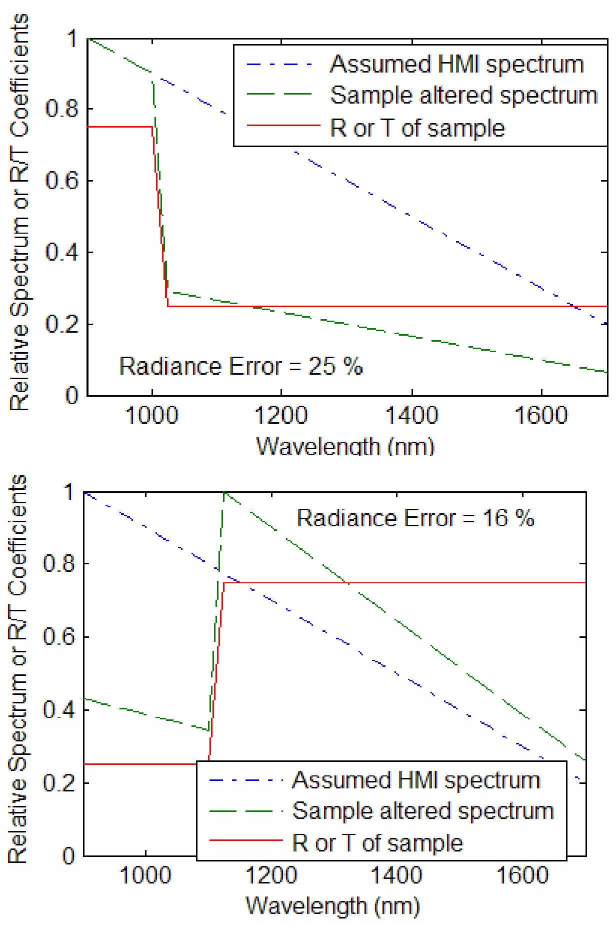

Figure 5.40 Worst radiance estimate errors for 50 percent change in spectral T/R over 25 nm

The results of this analysis are shown in Figures 5.40 through 5.44. Figure 5.40 shows that a 50 percent drop in transmission or reflection coefficients over a 25 nm can lead to at worst 25 percent error in radiance estimation, if that drop occurs in the region where the ASR of the NIR camera is changing rapidly, i.e. between 900 and 1100 nm. It also shows that the same change but a jump rather than a drop leads to lower error in radiance estimation. This difference in error between these two cases demonstrates how samples that cause a concentration in spectral power in the 900 to 1100 nm region will introduce the most error in radiance estimation when assuming a sample is neutral across the 900 to 1700 nm region to calculate the camera's responsivity.

Alterations in spectra that occur due to spectral transmission or reflection coefficients which vary over larger intervals cause less error. For example, a 50 percent drop in spectral transmission or reflection coefficients over 300 nm across the 900 to 1200 nm region causes an error in radiance estimation of 20 percent, as shown in Figure 5.41. Even more gradual changes, such as the same change over 800 nm, or the full interval, cause even less error, 11 percent or less for the assumed HMI spectrum analyzed, as shown in Figure 5.42.

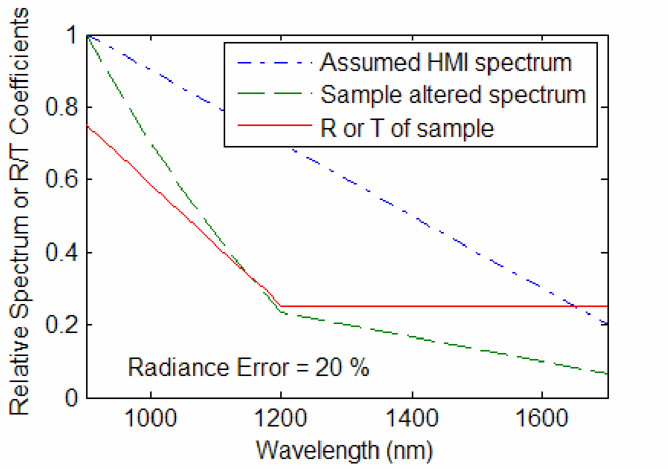

Figure 5.41 Worst radiance estimate error for 50 percent change in R/T over 300 nm

In order to estimate the errors for the worst case scenario, it was assumed that a sample with spectral reflection or transmission coefficients that changed significantly over the 900 to 1100 nm and 1600 to 1700 nm region were being studied. Changes over the

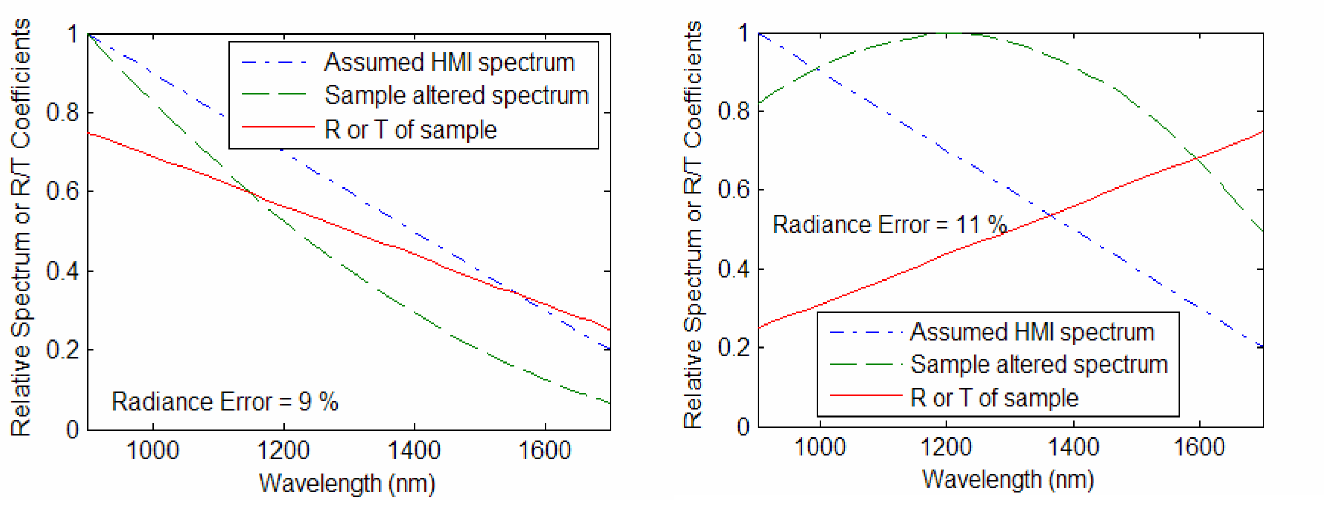

Figure 5.42 Radiance estimate errors for 50 percent change in R/T over full interval

1100 to 1600 nm region will have less impact because the camera's sensitivity over this region is much more flat. The results confirm that samples that concentrate radiation over wavelengths where the camera's sensitivity is changing rapidly can cause significant errors, as high as 34 percent as is shown on the left in Figure 5.43. On the other hand, a sample that reduces the radiation over those wavelengths causes less error, as is shown on the right. This analysis is for a sample with assumed spectral transmission or reflection coefficients that drop or rise by 70 percent over the 900 to 1100 nm and 1600 to 1700 nm regions.

Conversely, samples with spectral reflection or transmission coefficients that change

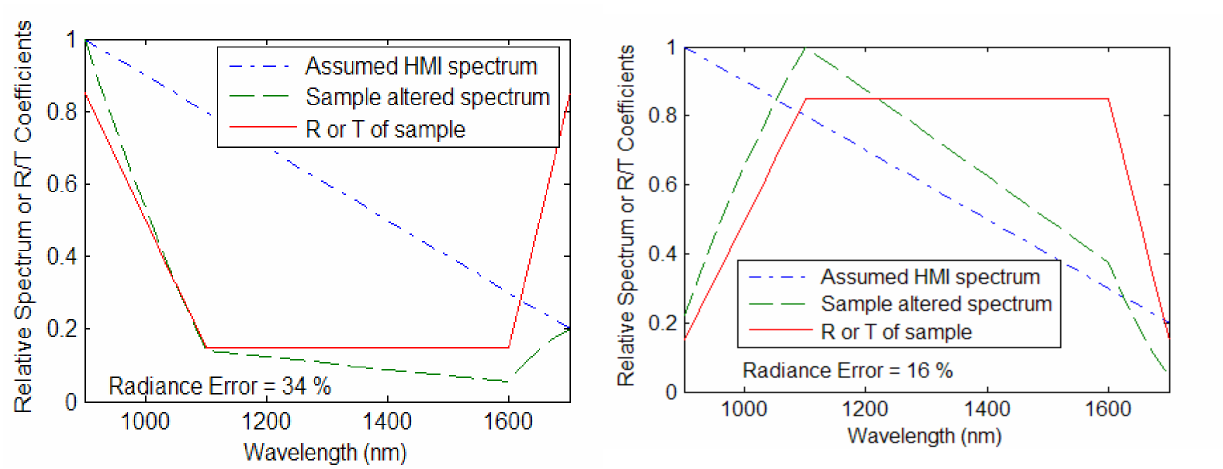

Figure 5.43 Radiance estimate errors for samples with spectral properties varying in the 900 to 1100 and 1600 to 1700 nm regions.

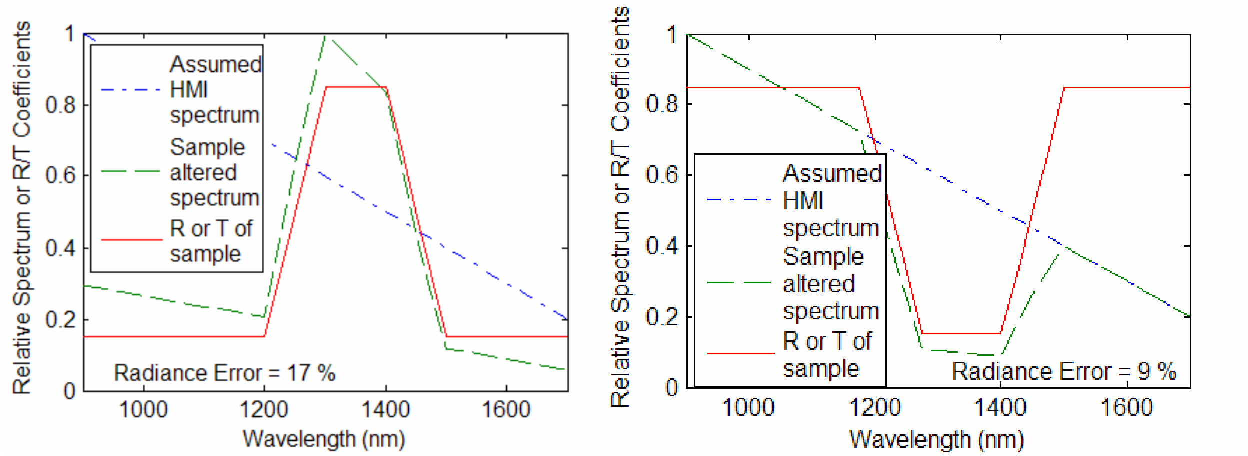

Figure 5.44 Radiance estimate errors for samples with spectral properties varying most in the 1100 to 1600 nm region

significantly only within the 1100 to 1600 nm waveband will cause far less additional error, as low as ten percent, even when the changes are as much as 70 percent over 100 nm intervals as shown in Figure 5.44.

Because the true NIR spectrum of the HMI lamp is not yet known, it is difficult to generalize the errors introduced by radiance estimation methods for the NIR camera due to samples with spectrally dependent properties within the NIR. The errors depend on the spectral properties of the sample as well as the real spectrum of the HMI lamp over the 900 to 1700 nm. These errors will be studied more thoroughly once the spectral properties of the HMI lamp, the hemi-ellipsoid, and any potential filters that might be used are better known within the NIR. The analysis presented here is meant to provide some information about how much an expected spectrum viewed by the NIR camera can be altered without introducing significant errors in the radiance estimated from its digital output.

5.4 Calibrations Summary

The camera calibrations and filter selections described above enable total radiance and luminance estimation of filtered HMI radiation entering each camera at every pixel in the camera. CCD camera settings were chosen to minimize noise and enhance the camera's ability to distinguish low luminance levels. The NIR camera settings were chosen to enable stable frame capture and minimize noise.

The vignetting correction factors for each camera provide a correction for the decrease in pixel values near the edge of each image due to vignetting. The pixel values should be divided by the vignetting factors corresponding to each zenith angle of emergence, which are related to pixel locations in the image.

The minimum angular resolution of each camera was measured to provide a minimum angular resolution threshold over which radiance or luminance estimates should be aggregated. The minimum angular resolution of the CCD camera was found to be about 0.0017 steradians and the NIR camera's was found to be about 0.25 steradians, a very high and a very low angular resolution respectively. Spatial calibrations that relate pixel locations in each camera's image to angular directions emerging from a fenestration system sample were also performed. This provides a conversion between known image information to directional information about radiation transmitted or reflected by a sample.

Spectroradiometric calibrations were performed that relate pixel values to monochromatic radiances from a given direction for each camera. Then, the ASR of each camera was calculated and the response of the camera to polychromatic beams was formulated. This information allows the conversion of the digital output of each camera into a radiance seen by each pixel if the relative spectrum of the polychromatic beam is known. In order to convert the digital output of the camera into radiances for unknown spectra, filters are used to sample the spectra over wavelength intervals in which total radiance across the interval can be accurately measured to within a desired error . This can be done for samples with spectral properties that obey the non-neutral constraints defined in sections 5.2.8 and 5.3.7.

Once the additional error estimations and calibrations for the NIR camera are performed and the spatial calibration is confirmed for the modified hemi-ellipsoid, these calibrations will allow users to convert the digital output at each pixel of each camera to a total radiance emerging from a sample for a given filter set in a direction from the sample that corresponds to that pixel's location. As will be explained in the next chapter, this information and knowledge about the irradiance of the sample enables the estimation of a banded, or quasi-spectral BT(R)DF across the 380 to 1700 nm range.

6. Measuring Quasi-Spectral BT(R)DFs

6.1 Overview of the Process

The ultimate goal of the device is to be able to measure four quantities:

- the average radiometric BT(R)DF of samples for solar radiation across sub-intervals within the 380 to 1700 nm range,
- the average photometric BT(R)DF of samples for solar radiation across sub-intervals within the 380 to 1700 nm range,
- the total radiometric BT(R)DF of samples for solar radiation across the full 380 to 1700 nm interval, and
- total photometric BT(R)DF of samples for solar radiation.

Chapter 6 will describe the complete process by which this occurs, and at which stage of this process each of the calibrations described in Chapter 5 are applied. The two most critical steps in this process are to calculate the irradiance and illuminance of the sample at given angles of incidence and to calculate the radiance or luminance in every reflected or transmitted direction based on the digital output of the camera for each filter set.

In order to calculate the irradiance of the sample, first the spectral exitance of the HMI lamp must be known. Then, the spectral exitance upon passing through the filters for each filter set can be calculated knowing the spectral transmission coefficients of the filter combinations. After passing through the filters, the radiation either irradiates the sample directly, in transmission mode, or passes through the hemi-ellipsoid, in reflection mode. If the radiation is passing through the hemi-ellipsoid, the spectral transmission coefficients of the hemi-ellipsoid at that location, i.e. for that angle of incidence, must be used to calculate the new spectrum of irradiation on the sample. The location at which light passes through the hemi-ellipsoid depends on both the zenithal and azimuthal angles of incidence, as explained in Chapter 4. Finally, the spectral irradiance of the sample can be calculated by multiplying this spectral irradiance by the cosine of the zenithal angle of incidence. This provides the denominator for equation (6-1), below, for the BT(R)DF over the wavelength interval spanned by the filter set.

Next, the digital output of the camera must be used to estimate the radiance and luminance emerging from the sample in every direction for each filter set. As explained in Chapter 5, the digital output of each of the camera's can be converted into radiances over each filter set's wavelength interval as long as the spectral properties of the sample being studied obey the constraints described in sections 5.2.8 and 5.3.7, allowing radiance measurements for non-neutral samples. For samples that are known to be neutral, radiances can be measured over a 380 to 945 nm and a 900 to 1700 nm directly because the relative spectrum of radiation is unaltered and thus the true responsivities of the cameras are known. Using an assumed relative spectrum, these radiances can be divided by the spectral reflection coefficients of the hemi-ellipsoid at a location depending on the angles of reflection or transmission from the sample to find the radiance emerging from the sample.

Since the pixel locations on the image have been related to angular directions emerging from the sample, the pixel location correlates to a location on the hemi-ellipsoid. The spectral reflection coefficients for this location are used to calculate the total radiance for a filter set emerging from the sample in every direction corresponding to all of the pixels. These radiances can then be averaged over a user-selected solid unit of angle, in steradians, which corresponds to averaging over pixels, to calculate the average radiance in a finite number of angular directions. This provides the numerator in equation (6-1), below, for the BT(R)DF over the wavelength interval spanned by the filter set.

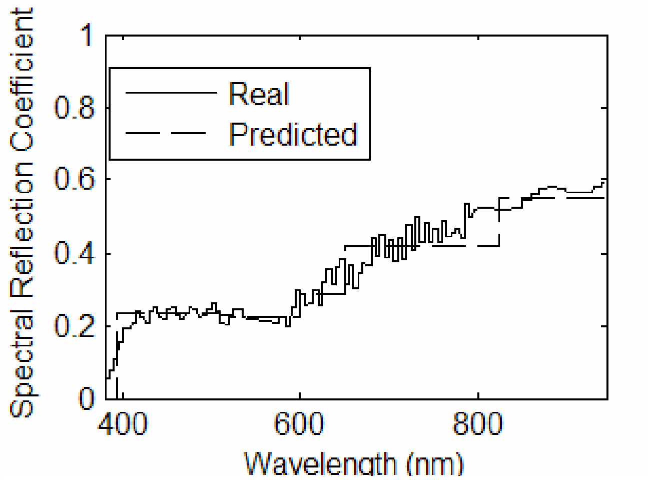

Figure 6.1 Typical predicted quasi-spectral BT(R)DF for one angular direction

Dividing the numerator and denominator provides the BT(R)DF for each filter set as a function of transmission or reflection zenith and azimuth angles and incidence zenith and azimuth angles for each of the filter sets. That is, they provide average BT(R)DFs of the sample to the filtered radiation for each filter set. The quasi-spectral BT(R)DF across the full 380 to 1700 nm range can be estimated by combining the BT(R)DFs for each filter set into a step-like quasi-spectral BT(R)DF. The measured filter set BT(R)DFs are assumed to represent the average BT(R)DF of the sample to the unfiltered spectrum of the HMI lamp over non-overlapping, finite wavebands. A sample quasi-spectral BT(R)DF for one direction is shown in Figure 6.1.

This quasi-spectral BT(R)DF can then be used to calculate the total BT(R)DF across the full 380 to 1700 nm interval for solar radiation, which has a similar enough spectrum to that incident on fenestration samples from the HMI lamp that a reasonable estimate of the total radiance transmitted or reflected can be achieved. This will be demonstrated in section 6.5. The total photometric BT(R)DF can also be calculated for solar radiation using the quasi-spectral BT(R)DF. The finer spectral resolution in the visible region allows photometric BT(R)DF to also be calculated to within a reasonable error, as described in section 6.5. The remainder of this chapter will describe each of the steps in the process to estimate quasi-spectral BT(R)DFs in greater detail.

6.2 Estimating BT(R)DFs for Each Filter Set

The first quantity of interest is the average radiometric BT(R)DF of a sample to the filtered HMI radiation across each of the wavelength intervals defined in Chapter 5, corresponding to each filter set. This radiometric BT(R)DF for each filter set can be defined by the equation:

$$\text{(6-1)} \quad BT(R)DF_{e,\text{filterset}}(\theta_i,\varphi_i,\theta_{t(r)},\varphi_{t(r)}) = \frac{L_{e,\text{sample,filterset}}(\theta_i,\varphi_i,\theta_{t(r)},\varphi_{t(r)})}{E_{e,\text{sample,filterset}}(\theta_i,\varphi_i)}$$

This equation will be referred to as the “filter set radiometric BT(R)DF”. In this equation, $L_{e,\text{sample,filterset}}(\theta_i,\varphi_i,\theta_{t(r)},\varphi_{t(r)})$ is the total radiance from the sample in every transmitted or reflected direction $(\theta_{t(r)},\varphi_{t(r)})$ for incidence angles (θ_i,φ_i) for each of the filter sets in Table 5.2. No filter is used for the NIR camera. $E_{e,\text{sample,filterset}}(\theta_i,\varphi_i)$ is the total irradiance of the sample for incidence angles (θ_i,φ_i) for that filter set. The subscript “filterset” in all equations will be used to indicate total quantities over the full wavelength interval defined by each filter set. In order to calculate these filter set BT(R)DFs, the radiance from the sample in every direction and the irradiance of the sample for any given incidence direction must be determined for each filter set. This can be achieved using the calibrations developed in Chapters 4 and 5, and is described below.

First, the irradiance of the sample can be calculated for each set of incidence angles chosen by the user from the known spectral power distribution of the HMI lamp, the known filter transmission coefficients, and the known hemi-ellipsoid transmission coefficients as a function of angle of incidence. For reflection measurements, the spectral irradiance of the sample is simply given by the following equation;

$$\text{(6-2)} \quad E_{e,\text{sample,filterset}}(\theta_i,\varphi_i,\lambda) = E_{e,\text{HMI}}(\lambda) \times \tau_{\text{filterset}}(\lambda) \times \tau_{\text{Hemi-Ellipsoid}}(\theta_i,\varphi_i,\lambda) \times \cos(\theta_i)$$

where $E_{e,HMI}(\lambda)$ is the known spectral exitance of the HMI lamp, $\tau_{filterset}(\lambda)$ are the known spectral transmission coefficients of the filter combinations, $\tau_{Hemi-Ellipsoid}(\theta_i,\varphi_i,\lambda)$ are the known spectral transmission coefficients of the hemi-ellipsoid for incidence angles (θ_i,φ_i), and $\cos(\theta_i)$ accounts for the effect of off-normal irradiation. This value can be discretized to an appropriate wavelength interval based on the resolution with which each wavelength dependent property is known. In this case, the wavelength dependence of the filters is the limiting factor, which is known over 1 nm intervals. The spectral irradiance of samples for transmission measurements is similar, except that the transmission coefficients of the hemi-ellipsoid are excluded from equation (6-2). Since the radiances predicted by the camera are not true spectral radiances, but rather total radiances across the wavelength interval defined by each filter set, the spectral irradiance of the sample is integrated to calculate the total incident irradiance for that filter set using the equation:

$$(6\text{-}3)\quad E_{e,sample,filterset}(\theta_i) = \int E_{e,sample,filterset}(\theta_i,\lambda)d\lambda$$

The next step is to calculate the bi-directional radiance distribution $L_{e,sample,filterset}(\theta_i,\varphi_i,\theta_{t(r)},\varphi_{t(r)})$ of radiation emerging from a sample for a given filter set. This is done using the calibrated cameras. The process for calculating radiances from the digital output of only the CCD camera is explained here. The NIR camera will follow a similar process, except that the Gaussian Cumulative function defines the relationship between digital output and radiance.

Knowing the spectral properties of the filters and all elements of the goniophotometer, the absolute responsivity of the camera at each pixel for every angle of incidence for a filter set is given by the following equation:

$$(6\text{-}4)\quad \left[\frac{1}{h^{0.3}_{R,G,B,filterset}}\right](\theta_i,\varphi_i,\theta_{t(r)},\varphi_{t(r)}) = \sum_{filter\,interval} \frac{a_{\Delta\lambda,filterset}(\theta_i,\varphi_i,\theta_{t(r)},\varphi_{t(r)})}{h^{0.3}_{R,G,B,\Delta\lambda}}$$

Where $a_{\Delta\lambda,\text{filterset}}(\theta_i,\varphi_i,\theta_{t(r)},\varphi_{t(r)})$ is the relative spectrum of the light viewed by the camera for a given filter set and the summation occurs over the wavelength interval defined by each filter set, denoted by "filter interval". This is simply a restatement of the result found in Chapter 5 that the absolute responsivity of a given pixel is simply a weighted sum of the absolute spectral responsivities, where the weights are given by the relative spectrum of the radiation being viewed.

Equation (6-4) demonstrates that, for a general spectrally and angularly selective sample, the camera's responsivity is different at every pixel location depending on the relative spectrum of transmitted or reflected light that enters the camera at the angles corresponding to that pixel location. This relative spectrum depends on the spectral properties of each element of the goniophotometer and the sample being studied. The pixel to which this responsivity applies is defined by the spatial calibration that relates the transmission angles (θ_t,φ_t) to pixel locations (x,y). The relative spectrum $a_{\Delta\lambda,\text{filterset}}(\theta_i,\varphi_i,\theta_t,\varphi_t)$, discretized over 5 nm wavebands Δλ, can be written as a function of the goniophotometer properties and the sample properties as follows. For transmission:

(6-5)

$$a_{\Delta\lambda,\text{filterset}}(\theta_i,\varphi_i,\theta_t,\varphi_t)=\frac{p_{\Delta\lambda,\text{HMI}}\times BS(d)\times\tau_{\Delta\lambda,\text{filterset}}\times\tau_{\Delta\lambda,\text{sample}}(\theta_i,\varphi_i,\theta_t,\varphi_t)\times\rho_{\Delta\lambda,\text{Ellipsoid}}(\theta_{t(r)},\varphi_{t(r)})}{\sum\limits_{\text{filter interval}}p_{\Delta\lambda,\text{HMI}}\times BS(d)\times\tau_{\Delta\lambda,\text{filterset}}\times\tau_{\Delta\lambda,\text{sample}}(\theta_i,\varphi_i,\theta_t,\varphi_t)\times\rho_{\Delta\lambda,\text{Ellipsoid}}(\theta_{t(r)},\varphi_{t(r)})}$$

For reflection:

(6-6)

$$a_{\Delta\lambda,\text{filterset}}(\theta_i,\varphi_i,\theta_r,\varphi_r)=\ldots$$

$$\ldots=\frac{p_{\Delta\lambda,\text{HMI}}\times BS(d)\times\tau_{\Delta\lambda,\text{Filterset}}\times\tau_{\Delta\lambda,\text{Ellipsoid}}(\theta_i,\varphi_i)\times\rho_{\Delta\lambda,\text{sample}}(\theta_i,\varphi_i,\theta_r,\varphi_r)\times\rho_{\Delta\lambda,\text{Ellipsoid}}(\theta_{t(r)},\varphi_{t(r)})}{\sum\limits_{\text{filter interval}}p_{\Delta\lambda,\text{HMI}}\times BS(d)\times\tau_{\Delta\lambda,\text{Filterset}}\times\tau_{\Delta\lambda,\text{Ellipsoid}}(\theta_i,\varphi_i)\times\rho_{\Delta\lambda,\text{sample}}(\theta_i,\varphi_i,\theta_r,\varphi_r)\times\rho_{\Delta\lambda,\text{Ellipsoid}}(\theta_{t(r)},\varphi_{t(r)})}$$

- $p_{\Delta\lambda,\text{HMI}}$ is the fraction of the HMI lamp's spectral exitance in wavelength interval Δλ,
- BS(d) is the beam spread, as a function of distance, of the HMI lamp on its way to the sample (which has not yet been adequately measured),

- $\tau_{\Delta\lambda,\text{filterset}}$ are the spectral transmission coefficients of the filter set,
- $\tau_{\Delta\lambda,\text{Ellipsoid}}(\theta_i,\varphi_i)$ are the spectral transmission coefficients of the hemi-ellipsoid for incidence angles (θ_i,φ_i)
- $\rho_{\Delta\lambda,\text{Ellipsoid}}(\theta_{t(r)},\varphi_{t(r)})$ are the spectral reflection coefficients of the hemi-ellipsoid for transmission or reflection angles $(\theta_{t(r)},\varphi_{t(r)})$, and are the same for both transmission or reflection, and
- $\tau_{\Delta\lambda,\text{sample}}(\theta_i,\varphi_i,\theta_t,\varphi_t)$ and $\rho_{\Delta\lambda,\text{sample}}(\theta_i,\varphi_i,\theta_{r,}\varphi_r)$ are the unknown bi-directional spectral transmission and reflection coefficients of the sample being studied.

Because the bi-directional spectral transmission and reflection coefficients of the sample are unknown, an assumption must be made about the spectral properties of the sample over the wavelength interval spanned by each filter set in order to estimate the responsivity of the camera, and thus convert digital output to a radiance estimate. The assumption, as described in chapter 5, is that the sample is neutral across the filter set's wavelength interval (but only across that interval), which leads to a relative spectrum of:

$$(6\text{-}7)\quad a_{\Delta\lambda,\text{filterset,neutral}}(\theta_i,\varphi_i,\theta_t,\varphi_t)=\frac{p_{\Delta\lambda,\text{HMI}}\times\tau_{\Delta\lambda,\text{filterset}}\times\rho_{\Delta\lambda,\text{Ellipsoid}}(\theta_{t(r)},\varphi_{t(r)})}{\sum\limits_{\text{filter interval}}p_{\Delta\lambda,\text{HMI}}\times\tau_{\Delta\lambda,\text{filterset}}\times\rho_{\Delta\lambda,\text{Ellipsoid}}(\theta_{t(r)},\varphi_{t(r)})}$$

for transmission and a similar one for reflection. This assumption of "filter set neutral" sample properties introduces additional error into radiance estimates, but filters were chosen that minimize errors in total radiance estimates across the filter interval to at most 13 percent and generally less than 10 percent for constrained spectrally dependent properties summarized in Table 5.3 and section 5.3.7. This assumption also allows the definition of the responsivity of the camera to samples neutral across the filter interval as a function of pixel location and incidence angle as follows:

$$\left[\frac{1}{h^{0.3}_{R,G,B,\text{filterset}}}\right]_{\text{neutral}}(\theta_i,\varphi_i,x(\theta_{t(r)},\varphi_{t(r)}),y(\theta_{t(r)},\varphi_{t(r)}))=\ldots$$

(6-8)
$$\ldots=\sum_{\text{filter interval}}\frac{a_{\Delta\lambda,\text{filterset},\text{neutral}}(\theta_i,\varphi_i,x(\theta_{t(r)},\varphi_{t(r)}),y(\theta_{t(r)},\varphi_{t(r)}))}{h^{0.3}_{R,G,B,\Delta\lambda}}$$

where the reflection or transmission angles have been replaced by image coordinates $(x,y)=(x(\theta_{t(r)},\varphi_{t(r)}),y(\theta_{t(r)},\varphi_{t(r)}))$ which are given through the spatial calibrations. This responsivity will be referred to as the “filter neutral responsivity”. Using this responsivity, the transmitted or reflected radiance off of a sample can be predicted using the relation:

$$L_{e,\text{sample},\text{filterset}}(\theta_i,\varphi_i,\theta_{t(r)}(x,y),\varphi_{t(r)}(x,y))=\ldots$$

(6-9)
$$\ldots=\frac{\left[h^{0.3}_{R,G,B,\text{filterset}}(\theta_i,\varphi_i,x,y)\right]_{\text{neutral}}}{t_{\text{int}}}\times c\left(\frac{b}{(NDL_{R,G,B}(x,y)/VC(x,y)-a)}-1\right)^{1/d}$$

Where:

- $L_{e,\text{sample},\text{filterset}}(\theta_i,\varphi_i,\theta_{t(r)}(x,y),\varphi_{t(r)}(x,y))$ is the total radiance estimated by each channel for the filtered HMI radiation for incidence angles (θ_i,φ_i) in direction $(\theta_{t(r)},\varphi_{t(r)})$, which is related to pixel location (x,y),
- $\left[1/h^{0.3}_{R,G,B,\text{filterset}}(\theta_i,\varphi_i,x,y)\right]_{\text{neutral}}$ is the filter neutral responsivity given by equation (6-8),
- t_{int} is the integration time at which the image was taken,
- $NDL_{R,G,B}(x,y)$ is the normalized digital output of channel R, G or B at pixel location (x,y)

- $VC(x,y)$ is the vignetting correction factor for pixel location (x,y) which depends on $\theta_{t(r)} = \theta_{t(r)}(x,y)$, and
- a, b, c and d are the coefficients of the logistic dose response function found in section 5.2.4.

This provides an estimate of the total radiance transmitted or reflected in every direction by a sample for a given filter set, $L_{e,sample,filterset}(\theta_i, \varphi_i, \theta_{t(r)}, \varphi_{t(r)})$, which is the numerator of the filter set BT(R)DF equation (6-1). The two important errors in this estimation are the spectroradiometric calibration errors, which were found to be about 5 percent for the G and B channels and 9 percent for the R channel, and the radiance estimation method errors caused by the filter neutral assumption, which were found to be lower than at most 13 percent for allowable samples and which reduce to 0 percent for samples that *are* neutral across the filter set's wavelength interval. The errors in the NIR radiance estimation will be further analyzed as part of future work.

Once the directionally dependent total irradiance of the sample, $E_{e,sample,filterset}(\theta_i, \varphi_i)$, and the bi-directionally dependent total radiance from the sample, $L_{e,sample,filterset}(\theta_i, \varphi_i, \theta_{t(r)}, \varphi_{t(r)})$ have been calculated as described above for each filter set, they can be averaged using one of the methods described in 5.2.4 over solid units of angle for a selected angular resolution. Then, the filter set radiometric BT(R)DFs can be easily be found, again, through equation (6-1), by dividing the total radiance for all incident and emerging directions by the irradiance for each incidence direction for each filter set.

A photometric BT(R)DF can also be found for each filter set. This is done by again using the filter neutral assumption, which results in the assumption that the relative spectrum of the filtered radiation is not changed. The radiance calculated by the camera and the irradiance on the sample can then be easily converted into a luminance and an illuminance using the luminous efficacy of the relative spectrum of the filtered radiation. The resulting luminances and illuminance can be divided to find the filter set photometric BT(R)DF similarly to the radiometric BT(R)DF in equation (6-1), using the the equation:

(6-10) $$\mathrm{BT(R)DF}_{v,\mathrm{filterset}}(\theta_i,\varphi_i,\theta_{t(r)},\varphi_{t(r)}) = \frac{L_{v,\mathrm{sample},\mathrm{filterset}}(\theta_i,\varphi_i,\theta_{t(r)},\varphi_{t(r)})}{E_{v,\mathrm{sample},\mathrm{filterset}}(\theta_i,\varphi_i)}$$

6.3 Combining Filter Set BT(R)DFs to Estimate Quasi-Spectral BT(R)DF

At this point in the process the average BT(R)DFs of the sample to the filtered HMI spectrum for each filter set have been estimated, or the filter set radiometric and photometric BT(R)DFs. The ultimate goal, however, is to develop an estimate of continuous quasi-spectral BT(R)DFs across the full 380 to 1700 nm interval. This can be achieved by combining all of the filter set's BT(R)DFs across the spectrum into one step-like, banded BT(R)DF such as that shown in Figure 6.1. However, some of the filters overlap, as shown in Figure 6.2, and there arises an issue of which filter set to use to estimate transmission or reflection by the sample over the overlapping sub-band(s).

The NIR band is not shown, but it spans the full length of the 900 to 1700 nm range, because no filters are planned for the NIR, and it overlaps the last CCD camera filter

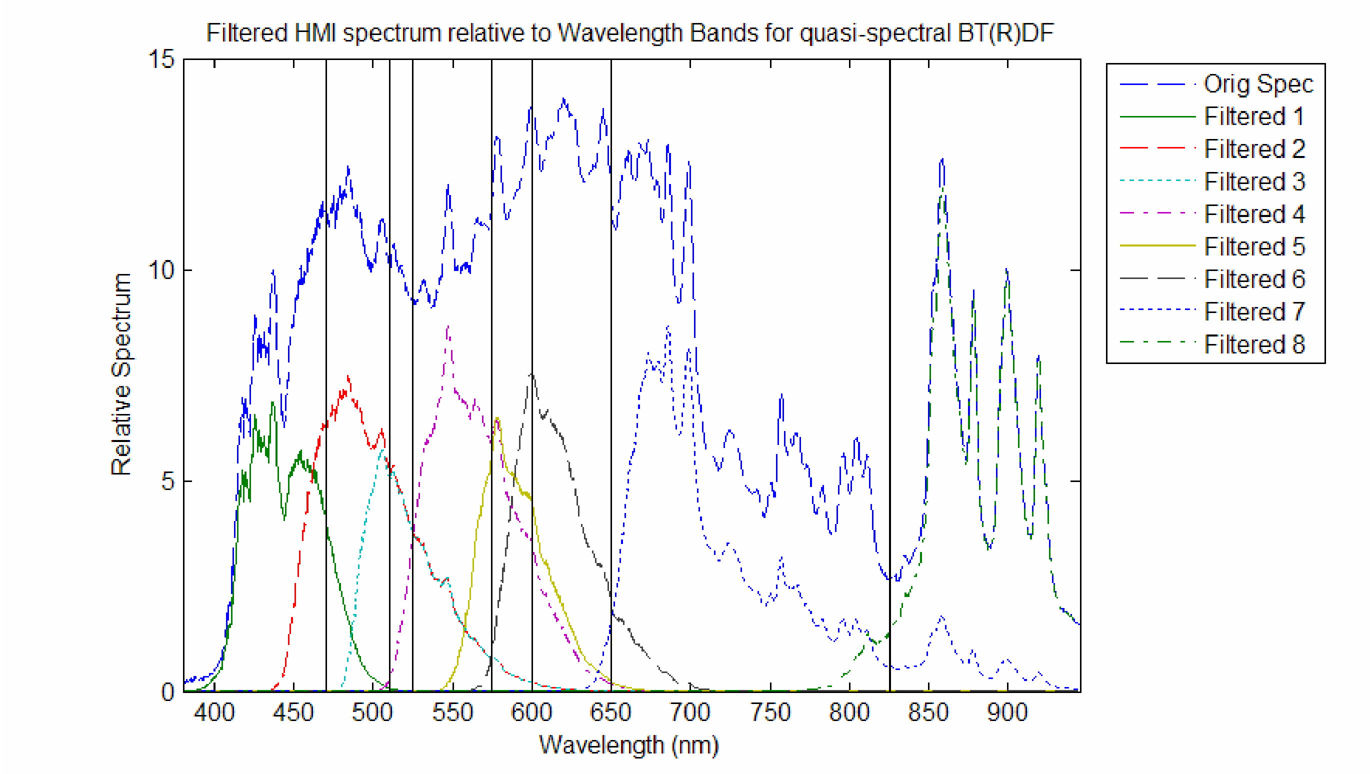

Figure 6.2 CCD filter sets and the locations of the wavelength boundaries selected for using filter set BT(R)DFs to estimated sample BT(R)DF across defined wavebands

set. This choice was made due to the uniformity of the NIR camera's ASR, but may be reconsidered if future experiments show the need for greater accuracy in the NIR.

Two factors determine which filter set BT(R)DF to use over a waveband, the wavelength interval for the filter set (as defined by a radiance threshold) and the shape of the ASR curve for the most useful channel over the wavelength interval of the filter set (i.e. how flat the ASR curves are over what interval). First, the best channel is chosen for radiance estimation for a given filter set. The B channel is used for filter sets one and two, The G channel is used for filter sets three, four and five, and the R channel is used for filter sets six, seven and eight. The one grayscale channel for the NIR camera is used for the NIR. These choices are based on the ASR curves of each channel, including the NIR. The channel that has the most constant ASR over the wavelength interval for a given filter set and which is sensitive enough to all wavelengths within that interval is chosen for radiance estimation.

The next step is to determine the wavebands over which each filter set BT(R)DF should be used to estimate average transmission or reflection coefficients. The wavebands chosen for quasi-spectral BT(R)DF estimation were initially based on each filter set's wavelength interval relative to the CCD camera's ASR curves for each channel, as shown in Figure 6.3. The filter set spanning the smallest wavelength interval should be used first over any waveband. Also, filter sets clearly cannot be used to estimate reflection or transmission coefficients over intervals for which they transmit no radiation. Furthermore, a given channel should not be used in combination with a certain filter set to estimate reflection or transmission coefficients over a waveband where the channel is not sensitive. Finally, radiance estimates are most accurate over intervals where the ASR curves are flat.

For example, within the visible region, filter sets three and five are used to estimate coefficients over a small waveband in which all three CCD channel ASRs are varying dramatically, as shown in Figure 6.3. Therefore, the bands for which those filter sets

Table 6.1 Filter set wavelength intervals compared to *wavebands* used for quasi-spectral BT(R)DF estimation

Filter set	Filter set wavelength interval (nm)	Waveband for BT(R)DF estimation with filter set (nm)
1	380 – 500	380 – 470
2	450 – 590	470 – 510
3	480 – 590	510 – 525
4	500 – 650	525 – 575
5	550 – 640	575 – 600
6	570 – 690	600 – 650
7	650 – 850	650 – 825
8	800 – 945	825 – 945
NIR	900-1700	945 – 1700

are used are very small, 510 to 525 nm for filter set three and 575 to 600 nm for filter set five.

These types of constraints helped determine the wavebands over which each filter set BT(R)DF should be used to estimate the average BT(R)DF of the sample to unfiltered radiation over non-overlapping intervals. The wavebands applied to which each filter set BT(R)DF were refined based on simulations of the cameras output, in which the predicted total radiance and luminance over the full 380 to 945 nm range was calculated based on the simulated output of the camera. The wavebands were adjusted so that the error between the predicted total radiance and luminance across 380 to 945 nm for the quasi-spectral BT(R)DF estimated for the choice of wavebands and the real total radiance across 380 to 945 nm was minimized. These simulations were performed for a variety of real materials, and will be described further in section 6.5. The wavebands selected relative to their corresponding filter sets are shown in Table 6.1.

Filter set one is used for quasi-spectral BT(R)DF estimation over the 380 to 470 nm waveband, filter set two is used from 470 to 510 nm, filter set three is used from 510 to 525 nm, filter set four is used from 525 to 575 nm, filter set five is used from 575 to 600 nm, filter set six is used from 600 to 650 nm, filter set seven is used from 650 to 825 nm, and filter set eight is used from 825 to 945 nm. The NIR camera, without filters, will be used to estimate BT(R)DFs over the 945 to 1700 nm range. For each of these wavebands, the coefficients of the filter set BT(R)DF are used as the coefficients of the quasi-spectral BT(R)DF of the sample over that waveband. This can be summarized, for both radiometric and photometric quantities, by the equation:

(6-11) $$\mathrm{BT(R)DF}_{e(v),\mathrm{band}}(\theta_i,\varphi_i,\theta_{t(r)},\varphi_{t(r)}) = \mathrm{BT(R)DF}_{e(v),\mathrm{filterset}}(\theta_i,\varphi_i,\theta_{t(r)},\varphi_{t(r)})$$

For example, the average BT(R)DF from 380 to 470 nm for unfiltered radiation in a given direction is estimated to be the same as the filter set BT(R)DF for filter set one, which is the sample's average BT(R)DF to radiation filtered by filter set one. Filter set one transmits partially across a 380 to 500 nm interval but most significantly between about 380 and 470 or 480 nm, depending on the definition of a radiance threshold for the filter set. For filter set one, this could be written:

(6-12)

$$\mathrm{BT(R)DF}_{e(v),380-470}(\theta_i,\varphi_i,\theta_{t(r)},\varphi_{t(r)}) = \mathrm{BT(R)DF}_{e(v),\mathrm{filterset},1}(\theta_i,\varphi_i,\theta_{t(r)},\varphi_{t(r)})$$

Since both radiometric and photometric filter set BT(R)DFs are available, both radiometric and photometric BT(R)DFs can be estimated for each waveband. Together, the wavebands span the full 380 to 1700 nm range and these BT(R)DFs for each waveband, or band BT(R)DFs, can be pieced together to generate a quasi-spectral radiometric or photometric BT(R)DF like that shown in Figure 6.1.

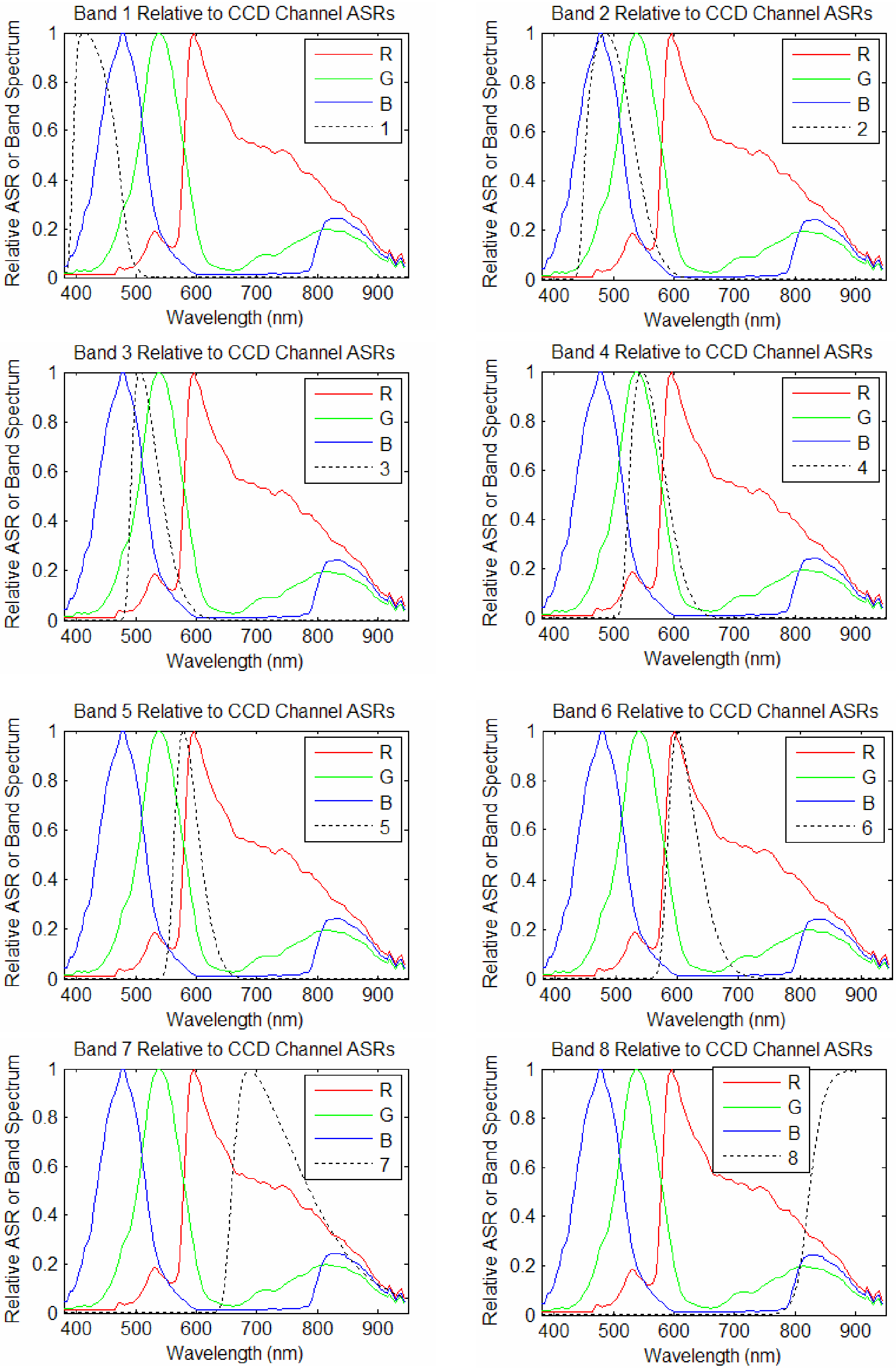

Figure 6.3 Filter Bands Relative to CCD R, G and B ASRs

6.4 Calculating Total Radiometric and Photometric BT(R)DFs

Once each filter set BT(R)DF has been used to estimate the band BT(R)DFs across non-overlapping wavebands spanning the 380 to 1700 nm range, a quasi-spectral BT(R)DF, like that shown in Figure 6.1, is available for further analysis. The following equation can then be used to calculate the total radiometric BT(R)DF across 380 to 1700 nm for an arbitrary source using the quasi-spectral radiometric BT(R)DF:

(6-13)

$$\mathrm{BT(R)DF}_{e,380-1700}(\theta_i,\varphi_i,\theta_{t(r)},\varphi_{t(r)}) = \frac{\sum_{\mathrm{band}=1}^{9}\left[\int_{\mathrm{band}} E_{e,\mathrm{source}}(\lambda)\cos(\theta_i)d\lambda\right]\times \mathrm{BT(R)DF}_{e,\mathrm{band}}(\theta_i,\varphi_i,\theta_{t(r)},\varphi_{t(r)})}{\int_{380}^{1700} E_{e,\mathrm{source}}(\lambda)\cos(\theta_i)d\lambda}$$

- $\mathrm{BT(R)DF}_{e,380-1700}(\theta_i,\varphi_i,\theta_{t(r)},\varphi_{t(r)})$ is the total radiometric BT(R)DF of the sample across the 380 to 1700 nm interval,
- $E_{e,\mathrm{source}}(\lambda)$ is the spectral exitance of the source,
- $\int_{380}^{1700} E_{e,\mathrm{source}}(\lambda)\cos(\theta_i)d\lambda$ is the total irradiance of the sample across the 380 to 1700 nm interval,
- $\mathrm{BT(R)DF}_{e,\mathrm{band}}(\theta_i,\varphi_i,\theta_{t(r)},\varphi_{t(r)})$ is the radiometric band BT(R)DF of the sample as given by equation (6-11), and
- $\sum_{\mathrm{band}=1}^{9}\left[\int_{\mathrm{band}} E_{e,\mathrm{source}}(\theta_i,\varphi_i,\lambda)d\lambda\right]\times \mathrm{BT(R)DF}_{e,\mathrm{band}}(\theta_i,\varphi_i,\theta_{t(r)},\varphi_{t(r)}) = L_e(\theta_i,\varphi_i,\theta_{t(r)},\varphi_{t(r)})$ is the total radiance transmitted or reflected by the sample in direction $(\theta_{t(r)},\varphi_{t(r)})$ for angles of incidence (θ_i,φ_i).

The summation occurs over all wavebands and the integral occurs over each waveband.

The total photometric BT(R)DF can be calculated in one of two ways. First, it could be calculated by using the photometric band BT(R)DFs using an equation similar to (6-13):

(6-14)

$$\mathrm{BT(R)DF}_v(\theta_i,\varphi_i,\theta_{t(r)},\varphi_{t(r)}) = \frac{\sum_{band=1}^{8}\left[\int_{band} E_{v,source}(\lambda)\cos(\theta_i)d\lambda\right]\times \mathrm{BT(R)DF}_{v,band}(\theta_i,\varphi_i,\theta_{t(r)},\varphi_{t(r)})}{\int_{380}^{780} E_{v,source}(\lambda)\cos(\theta_i)d\lambda}$$

Where the spectral irradiance of the sample has been replaced with the illuminance of the sample, the radiometric band BT(R)DF has been replaced by the photometric band BT(R)DF, and the integrals and sums only occur over wavelength intervals and bands that contribute to photometric quantities.

The other approach to calculating the total photometric BT(R)DF involves using the radiometric band BT(R)DFs and the photopic response curve V(λ). The photopic response curve can be inserted into equation (6-11) to find:

(6-15)

$$\mathrm{BT(R)DF}_v(\theta_i,\varphi_i,\theta_{t(r)},\varphi_{t(r)}) = \frac{\sum_{band=1}^{9}\left[\int_{band} E_{e,source}(\theta_i,\varphi_i,\lambda)V(\lambda)d\lambda\right]\times \mathrm{BT(R)DF}_{e,band}(\theta_i,\varphi_i,\theta_{t(r)},\varphi_{t(r)})}{\int_{380}^{1700} E_{e,source}(\theta_i,\varphi_i,\lambda)V(\lambda)d\lambda}$$

Where the only additional term is the photopic response curve V(λ) and the factor of 683 Lumens per Watt cancels out. In this equation, the bi-directional luminance within each band is given by:

(6-16)

$$L_v(\theta_i,\varphi_i,\theta_{t(r)},\varphi_{t(r)}) = \sum_{band=1}^{9}\left[\int_{band} E_{e,source}(\theta_i,\varphi_i,\lambda)V(\lambda)d\lambda\right]\times \mathrm{BT(R)DF}_{e,band}(\theta_i,\varphi_i,\theta_{t(r)},\varphi_{t(r)})$$

Here, because it has been assumed that the sample is neutral across the band, the transmitted or reflected spectrum across the band is assumed to be the same as the source's spectrum across that band but scaled by the estimated radiometric band BT(R)DF.

The difference between these two methods lies in the difference between the wavelength intervals over which the luminous efficacy of the spectrum irradiating a sample is assumed not to change. For the first method, the luminous efficacy of the *filtered radiation* across the filter set wavelength interval has been assumed not to change as described at the end of section 6.3. Then, the filter set photometric BT(R)DFs were calculated using the resulting luminances. These filter set BT(R)DFs were assigned to the wavebands in Table 6.1 to find photometric band BT(R)DFs.

In the second method, the luminous efficacy of the *unfiltered radiation* is assumed not to change over the wavebands, rather than the filter intervals, defined in Table 6.1. The calculation of the radiometric filter set BT(R)DFs include the assumption that the sample is neutral over the filter interval, but by assigning these filter set BT(R)DFs to smaller wavebands, a new assumption is made about the neutrality of the sample over smaller wavelength intervals (the wavebands in Table 6.1).

It has been assumed that the second method, therefore, is more accurate for two reasons. First, the wavebands in Table 6.1 used for the second method are smaller than the corresponding wavelength intervals and provide a finer spectral resolution over the visible wavelengths. Second, this method also allows the use of the unfiltered radiation, and its corresponding luminous efficacies across each waveband, to estimate total photometric BT(R)DFs rather than combining the results from filtered radiation with different luminous efficacies than the original source. The remainder of this analysis assumes that the second method has been chosen to calculate total photometric BT(R)DFs, but the tradeoffs between these two methods should be explored more thoroughly in future work. The resulting accuracy from this method is explored in section 6.5.

Although the total radiometric and photometric BT(R)DF calculations presented above could be performed for a source with an arbitrary spectrum, they are only valid for sources with relative spectra that are similar to that of the HMI lamp across each of the filter set intervals, separately. This is because broad filter intervals are used to calculate *average* BT(R)DFs across each interval for a particular light source, the filtered HMI lamp (including transmission through the hemi-ellipsoid for transmission measurements). A source with a different spectrum may have a different average BT(R)DF across the interval for that source.

This is a similar limitation to that for all non-spectral goniophotometers, except now the relative spectrum must only be the same across each filter interval and not across the entire spectrum, as is the case for all non-spectral goniophotometers. This limitation must be considered when trying to use the quasi-spectral BT(R)DFs to calculate total radiometric BT(R)DFs and photometric BT(R)DFs and in interpreting the meaning of the goniophotometer data. The quasi-spectral BT(R)DFs produced by the goniophotometer are valid only for sources with relative spectra across each filter interval similar to that of the HMI lamp. Because the relative spectrum of the HMI lamp is similar to that of the solar spectrum, it can be used to estimate the sample's BT(R)DFs for the solar spectrum.

6.5 Validating the Quasi-Spectral BT(R)DF Estimation Method

6.5.1 Methods

Because additional components of the goniophotometer must be completed before experiments can be performed, goniophotometer experiments were simulated in order to validate the quasi-spectral BT(R)DF estimation method described above and to estimate the errors in each type of predicted BT(R)DF. The spectral properties of each important component of the goniophotometer, the HMI lamp, the filter combinations for each filter set, and the hemi-ellipsoid are all known for the 380 to 945 nm region. In addition, a model of the camera's digital output for known spectral radiances is available from Chapter 5. By simulating the camera's output for samples with known spectral properties, the quasi-spectral BT(R)DF estimated by the goniophotometer can be compared to the real spectral BT(R)DF of the sample.

The first step in the simulation is to calculate the total irradiance of the sample for each filter set. This is done directly as described in section 6.2. The next step is to calculate the camera's true responsivity to radiation with a relative spectrum produced by the real sample's spectral reflection and transmission coefficients. This can be found using equations (6-4), (6-5) and (6-6). Knowing these responsivities, the digital output of the camera can be simulated using the relation between radiance and digital output described in Chapter 5.

The next step is to determine the total radiance for each filter set that the radiance estimation method for unknown spectra would have guessed based on this digital output. This is done by making the usual assumption that the sample is neutral across the wavelength interval for the filter set. With this filter neutral assumption, as described in section 6.2, the responsivity of the camera is given by equations (6-7) and (6-8).

The relationship between digital output and radiance, equation (5-26), can then be applied using this new, guessed responsivity to estimate the total radiance at each pixel from the digital output for each filter set. These estimated radiances can be compared to the simulated radiances for the real sample properties to determine the radiance and luminance estimation error for each filter set. Knowing the directional irradiance of the sample and both the estimated and simulated bi-directional radiance from the sample for each filter set, the estimated quasi-spectral radiometric BT(R)DF and real spectral radiometric BT(R)DFs can also be compared. Finally, the total radiometric BT(R)DF from 380 to 1700 nm and the total photometric BT(R)DF can be calculated using the estimated quasi-spectral radiometric BT(R)DF. These quantities can then be compared to the calculated total radiometric and photometric BT(R)DFs for the real spectral properties of the sample for the HMI lamp.

6.5.2 Results

A variety of real fenestration materials from the Optics 5 database were simulated to verify the quasi-spectral BT(R)DF estimation method for a variety fenestration systems with a range of spectral properties. They included coatings, applied films, monolithic substrates, and laminate combinations on clear and tinted glazings. Some hypothetical materials were also simulated to investigate the estimation method's success with certain unusual spectral properties. Simulations were only performed across a 380 to 945 nm interval because the HMI spectrum in the NIR region is not yet known. Simulations to estimate the quasi-spectral radiometric BT(R)DF, total radiometric BT(R)DF and photometric BT(R)DF are presented below.

For simplicity, and to estimate the longest exposure times likely to be needed, the samples were assumed to be perfectly diffusing but with the spectral properties of the real material. For each simulation, the errors in estimated radiance for each filter set, the estimated radiance across the 380 to 945 nm wavelength interval for unfiltered radiation, and estimated luminance for unfiltered radiation in a given direction were calculated. The results of the simulations are shown in Figures 6.4 through 6.6.

The predicted and the real spectral reflection coefficients for a given direction are shown. Figure 6.4 shows the results for the BRDFs in one direction for the following six materials found in the Optics 5 database: Solargard @ Silver AG 25 Low-E, Panorama Autumn Bronze 30, Solis Clear on Clear, Pewter Clear, Heat Mirror Twin Coat, and Sea-Storm. Figure 6.5 shows the results for the BTDFs in one direction for the following four samples: Solargard Royal Blue, Armourglass Greylite, Vanceva Sapphire, and Azurelite. Figure 6.6 shows the results for the BRDFs of samples with hypothetical "real" reflection coefficients as shown.

The figures show that the details in spectral properties over small intervals are lost, and only average reflection and transmission over each waveband are captured.

Hypothetical Sample 2, in Figure 6.6 (b), illustrates this well, as the large variations in spectral reflection coefficients are lost because they occur over intervals much smaller than the sampled wavelength intervals. Another observation is that for samples that are neutral across a filter interval, the spectral BT(R)DF can be estimated very accurately. Also, the finer spectral resolution across the visible region does indeed provide better quasi-spectral BT(R)DF estimates over the visible wavelengths, reducing the errors in estimated luminance shown in Tables 6.2 and 6.4 and supporting the use of equation (6-15) for calculating total photometric BT(R)DFs.

The errors in the estimated total reflected radiance or luminance across the 380 to 945 nm interval and total photometric BT(R)DF are shown in Table 6.2. The errors for these quantities are typically less than 3 percent for most of the samples. The samples that show higher errors, such as the Heat Mirror Twin Coat and Solargard Royal Blue in Figures 6.4(e) and 6.5(a), are special cases. The 7 percent error in estimated reflected luminance and 5 percent error in reflected radiance for the Heat Mirror Twin Coat arise mainly because the luminance and radiance are so low. The 5 percent error in estimated reflected luminance for the Solargard Royal Blue sample arises mainly because of the drastically changing spectral transmission coefficients across photometrically significant wavelength intervals.

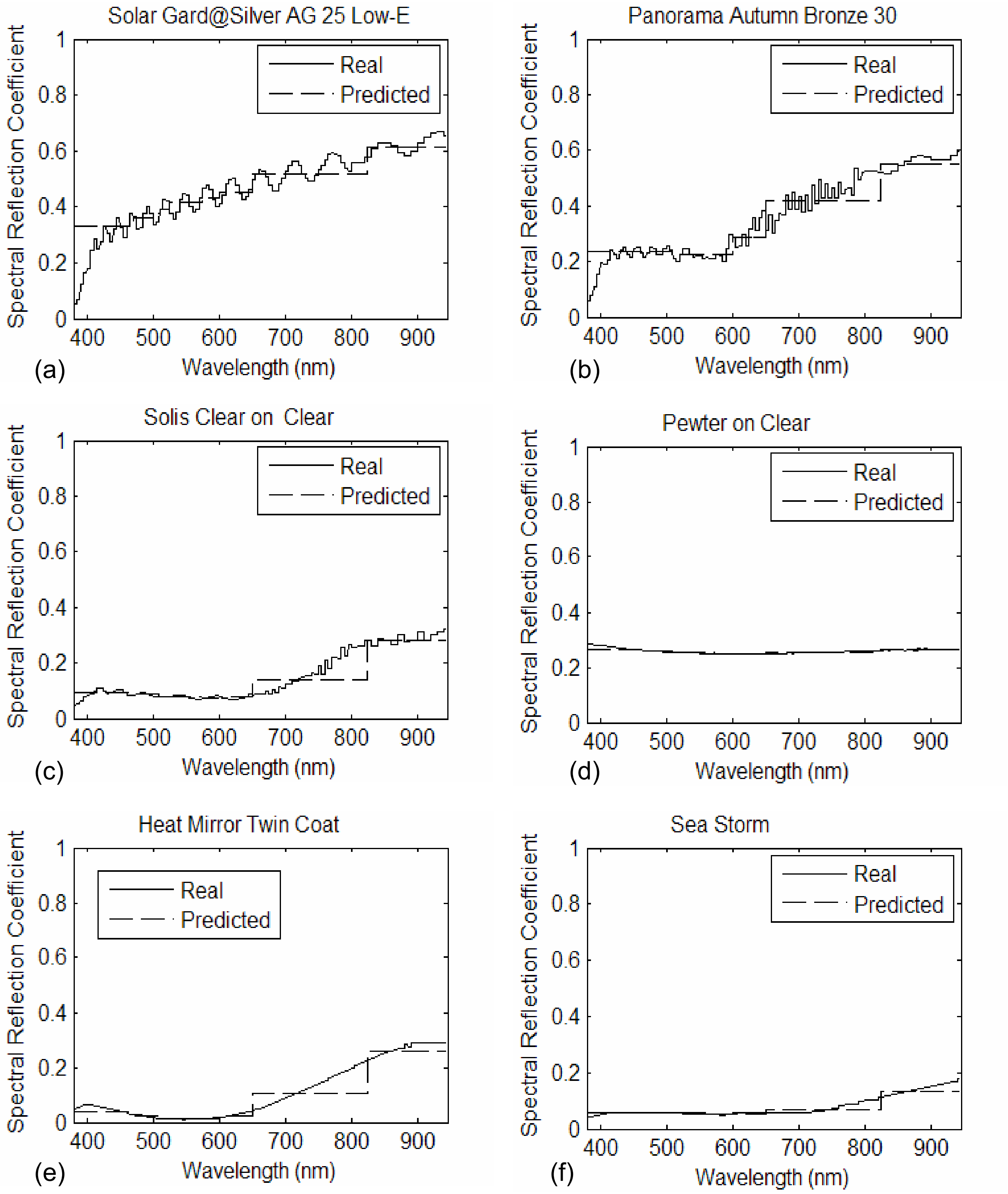

Figure 6.4 Real and predicted spectral or quasi-spectral BRDF in one direction for simulated real samples

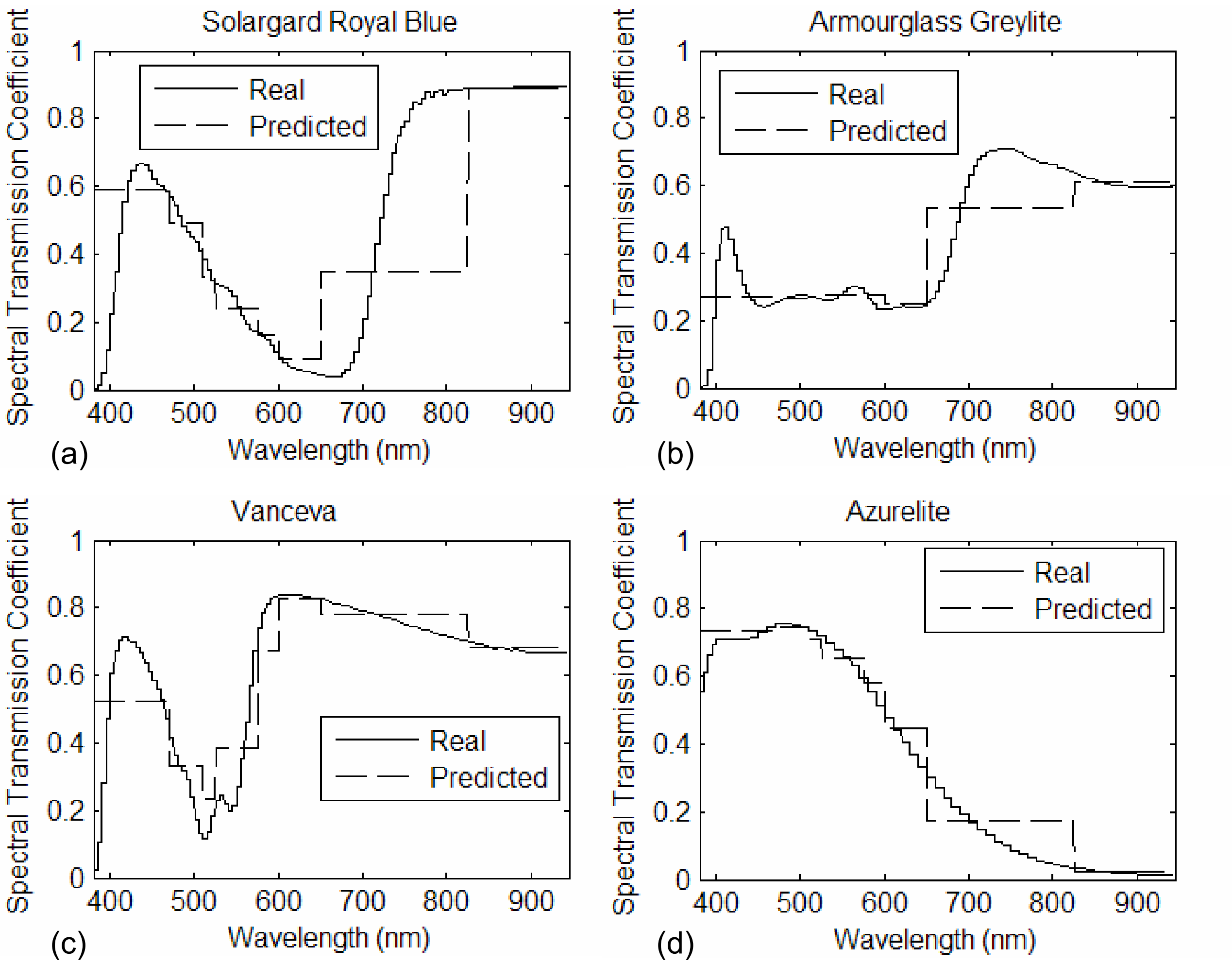

Figure 6.5 Real and predicted spectral or quasi-spectral BTDF in one direction for simulated real samples

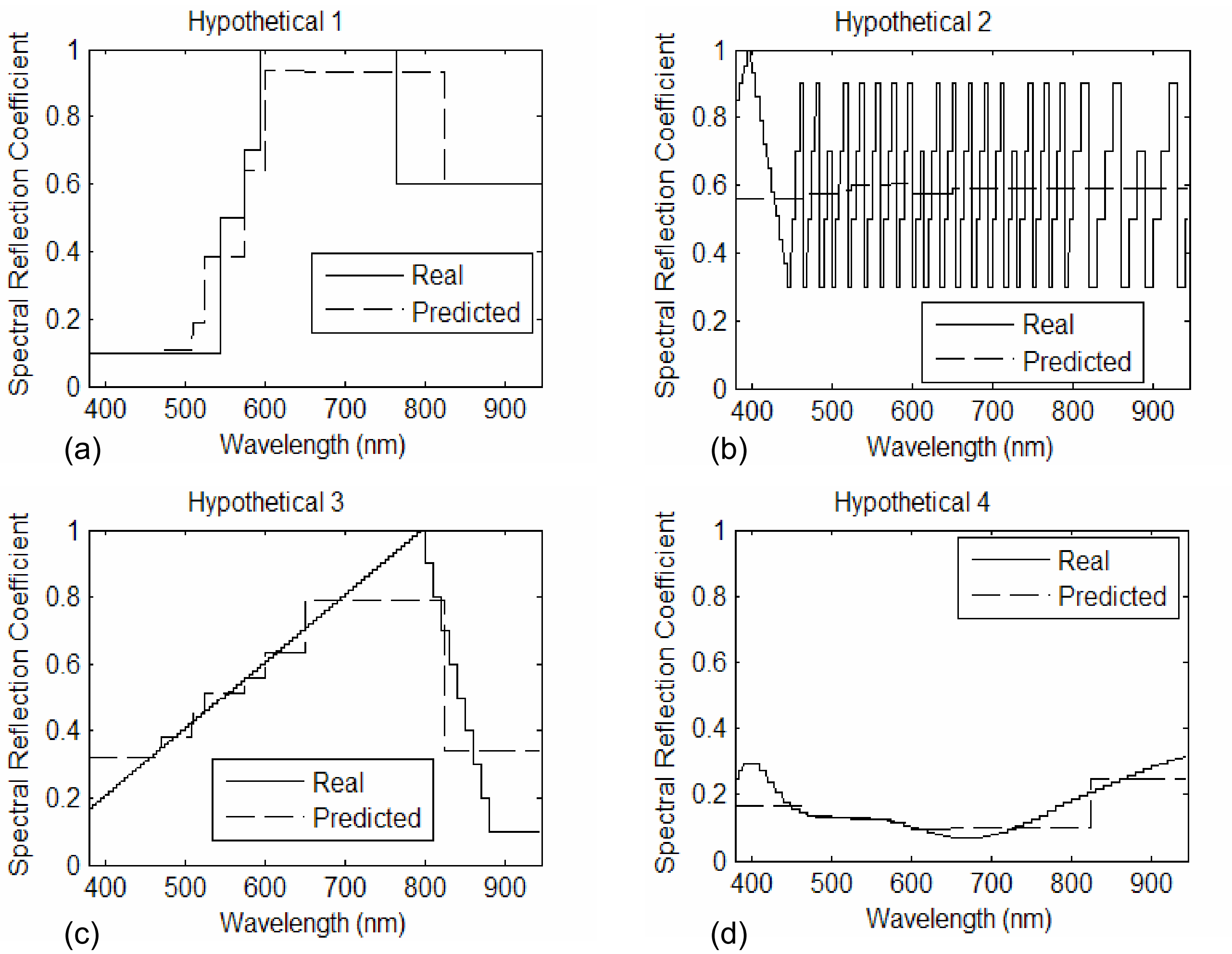

Figure 6.6 Real and predicted spectral or quasi-spectral BRDF in one direction for simulated hypothetical samples

Table 6.2 Total Radiance (380-945) and Luminance Errors for Simulated Samples

Sample	**Total Radiance Error (%)**	**Total Luminance Error (%)**
SolarGard@SilverAG25 LowE	0.19	0.39
Panorama Autumn Bronze 30	1.52	0.31
Solis Clear on Clear	2.21	1.69
Pewter on Clear	0.20	0.08
Heat Mirror Twin Coat	4.98	6.94
Sea Storm	2.06	0.18
Solargard Royal Blue	2.65	5.30
Armourglass Greylight	0.78	2.52
Vanceva	1.10	0.11
Azurelite	2.52	0.31
Hypothetical 1	0.54	3.09
Hypothetical 2	0.24	0.48
Hypothetical 3	0.65	0.52
Hypothetical 4	3.44	1.61

The errors in estimated transmitted or reflected radiance and luminance over each filter set are generally higher than the totals across the full 380 to 945 nm band, as shown in Tables 6.3 and 6.4. In these tables, errors greater than 5 percent are shown in bold. The luminance errors for filter set 8 are irrelevant because it spans a wavelength interval over which there is no luminance. As expected from the analysis in section 5.2.8, much higher errors in estimated radiance for each filter set are found in intervals over which the spectral transmission or reflection coefficients rise sharply and significantly. For example, the sharp rise in spectral transmission coefficients for the Solargard Royal Blue sample, shown in Figure 6.5(a) across filter set seven's wavelength interval lead to over 400 percent error in estimated luminance for that filter set, which is exacerbated by the fact that the luminance is so low. However, this error does not affect the total estimated luminance across the full visible region by much because the luminance within that interval is negligible compared to that over other filter sets. For example, the luminance errors for filter sets 2 and 6 are more significant to the error in total luminance because they contribute more to the total luminance.

Table 6.3 Radiance Errors for simulated samples over each filter set

Sample/Filter Set	**F1**	**F2**	**F3**	**F4**	**F5**	**F6**	**F7**	**F8**	**TOTAL**
SolarGard@SilverAG25 LowE	2.93	3.04	0.69	1.97	1.96	0.72	1.66	0.97	0.19
Panorama Autumn Bronze 30	0.76	0.97	1.04	3.56	**7.93**	1.27	3.17	1.17	1.52
Solis Clear on Clear	1.65	2.21	0.54	1.08	1.28	0.22	**9.74**	1.61	2.21
Pewter on Clear	0.64	0.57	0.18	0.16	0.07	0.02	0.37	0.25	0.20
Heat Mirror Twin Coat	**9.51**	**13.11**	**7.37**	**13.32**	**19.53**	**5.66**	**13.07**	3.34	4.98
Sea Storm	0.26	0.47	0.09	0.88	0.83	0.28	8.22	4.60	2.06
Solargard Royal Blue	0.01	**12.06**	3.92	**16.53**	**22.00**	1.36	**16.32**	0.31	2.65
Armourglass Greylight	**6.82**	0.81	0.12	1.99	**5.61**	1.76	3.03	0.79	0.78
Vanceva	**6.66**	2.04	**7.07**	**22.56**	**9.99**	0.43	1.39	0.65	1.10
Azurelite	0.87	2.40	0.18	**6.44**	**8.99**	1.99	**11.42**	**15.58**	2.52
Hypothetical 1	0.50	**29.04**	2.68	**23.50**	**15.62**	0.17	3.89	0.25	0.54
Hypothetical 2	1.16	0.39	1.87	0.57	1.91	0.22	0.03	1.81	0.24
Hypothetical 3	4.63	**6.48**	1.37	4.41	4.33	0.76	3.66	**27.89**	0.65
Hypothetical 4	**8.90**	1.44	0.49	4.60	**6.98**	1.38	**12.52**	4.65	3.44

Table 6.4 Luminance Errors for simulated samples over each filter set

Sample/Filter Set	**F1**	**F2**	**F3**	**F4**	**F5**	**F6**	**F7**	**F8**	**TOTAL**
SolarGard@SilverAG25 LowE	4.27	**8.16**	1.11	1.31	1.03	1.37	4.97	**45.3**	0.39
Panorama Autumn Bronze 30	0.51	2.97	0.32	1.33	3.85	**6.90**	**18.73**	**129**	0.31
Solis Clear on Clear	3.31	**6.79**	0.65	0.97	0.84	1.00	51.92	**258**	1.69
Pewter on Clear	1.01	1.71	0.17	0.13	0.05	0.02	0.96	4.44	0.08
Heat Mirror Twin Coat	**22.44**	**59.50**	2.36	**6.16**	**9.27**	**23.4**	**96.29**	**1480**	6.94
Sea Storm	0.11	1.22	0.42	0.86	0.12	1.74	**18.10**	**145**	0.18
Solargard Royal Blue	**7.26**	**43.30**	**6.33**	**10.80**	**10.58**	**15.3**	**453**	**301**	**5.30**
Armourglass Greylight	3.19	2.80	0.16	0.71	3.31	1.58	**62**	**128**	2.52
Vanceva	**21.82**	**18.78**	**11.75**	**16.89**	**6.54**	0.98	2.55	**31.6**	0.11
Azurelite	1.13	**5.88**	1.75	3.78	4.26	**8.06**	**39.56**	**95**	0.31
Hypothetical 1	2.36	**49.30**	**17.87**	**17.37**	**9.24**	**5.27**	4.26	**16.8**	3.09
Hypothetical 2	1.44	1.48	0.72	0.21	0.97	0.50	1.44	0.40	0.48
dHypothetical 3	**8.06**	**16.34**	2.39	2.91	2.22	3.53	**8.59**	**35.5**	0.52
Hypothetical 4	**12.61**	4.93	0.71	2.54	3.27	**6.21**	**36.08**	**112**	1.61

In general, it can be seen that when transmitted or reflected radiance is low, errors tend to be higher, such as for the Heat Mirror Twin Coat in Figure 6.4(e). Also, where spectral transmission and reflection coefficients rise or drop sharply over small wavelength intervals, beyond the constraints set in section 5.2.8, errors as high as 20 to 30 percent arise, as can be seen in filter set 5 for Solargard Royal Blue (Figure 6.5(a)), filter set 4 for Vanceva (Figure 6.5(c)), and filter sets 2 and 4 for hypothetical sample 1 (Figure 6.6(a)). However, even with these large errors in the radiance or luminance estimated for each filter set, the total transmitted or reflected radiance and luminance across the entire 380 to 945 nm range is still estimated much more accurately, as shown in Table 6.2, using the estimated quasi-spectral BT(R)DF.

The errors described here only include the additional errors introduced by the quasi-spectral BT(R)DF estimation method. The calibration errors from Chapter 4 and 5 are not included here, such as the errors in ASR calibration for each channel or uncertainties in the properties of the hemi-ellipsoids. The errors addressed here include those introduced by using non-box-like filters, by the assumption that the sample is neutral across each filter's wavelength interval, and by the selection of wavebands with which to estimate band BT(R)DFs from the filter set's BT(R)DFs (which is necessitated by non-box-like filters). This error analysis also does not include the possibility that the spectrum *within* each filter's wavelength interval could be guessed using the output from multiple channels, a possibility for the future which will be described briefly in section 7.2. The influence on errors for all of these additional factors must be measured and quantified before the real error in estimated radiance and luminance or total radiometric or photometric BT(R)DF can be known. This total error calculation will be part of future work on the goniophotometer.

Again, a similar analysis for the NIR camera has yet to be performed, in part because the spectral properties of the hemi-ellipsoid and the spectral exitance of the HMI lamp in the NIR are not yet known and an NIR spectrometer is not yet available. Also, additional validation of the ASR calibration of the NIR camera using an NIR spectrometer is necessary before conclusions can be drawn about the correct filters to use, if any, and the potential errors in BT(R)DF estimation over the NIR.

Although a more detailed experimental analysis of quasi-spectral BT(R)DF estimation errors will be performed once the filters are acquired, the simulations show that, in addition to the calibration error for each channel, total radiometric BT(R)DF across 380 to 945 nm and total photometric BT(R)DF can theoretically be estimated to within about 5 percent for the spectrally and angularly selective fenestrations likely to be studied. The error in each filter set's BT(R)DF will depend on the exact spectral properties under investigation, but many typical samples show errors in radiance and luminance estimation across each filter interval that are less than 10 percent, with many below 5 percent.

These errors are quite low. They suggest that the method presented here can provide very good estimates of the gross amount of radiation transmitted or reflected by fenestrations across wavebands of interest, such as the UV, parts of the visible, or the NIR.

6.5.3 Integration Times

In addition to an understanding of errors, the simulations provide a measure of the integration times likely to be necessary to capture the full luminance or radiance range possible in experiments with the goniophotometer. For each sample, the radiance that would be viewed by the camera can be calculated, and the integration time must be varied until the predicted response of the camera for the appropriate channel lies between the NDLs of 0.05 and 0.85.

The simulations show that for a perfectly diffusing sample that is only 10 percent reflective, the camera would require 4 or 8 second integration times for most filter combinations, except the highest wavelength interval which would require 16 seconds, to “see” radiation reflected off of the least reflective part of the hemi-ellipsoid. This constraint is too strong because it would require too much time for experiments, and typically these conditions will not be encountered. Instead, the integration time could be limited to at most 2 seconds for samples that are known to be highly diffusing or not very transmitting or reflecting. This would provide useable digital outputs for all filter combinations even for 40 percent reflecting, perfectly diffusing samples in the direction of the least reflective part of the hemi-ellipsoid.

Conversely, the simulations also provide the minimum integration time that might be required. If a sample is perfectly transmitting and completely specular (e.g. a hole), in the direction where the hemi-ellipsoid is most reflecting, the camera will encounter the highest radiance possible in experiments. An integration time of about 32 milliseconds would be required for certain filter combinations to avoid saturation and provide useable digital output.

Thus, this analysis also places constraints on the integration times that will be used for experiments with the goniophotometer, with a lower threshold of around 32 milliseconds and an upper threshold around 2 seconds. It is suggested, similar to the approach taken for other goniophotometers such as (Andersen 2004), that the integration time be doubled for each successive image. In addition, the highest integration times should only be used if a sample is known to be highly diffusing or not very transmitting or reflecting.

7. Conclusions

The work presented in this thesis provides innovative new methods for measuring radiance, luminance, and quasi-spectral, bi-directional transmission and reflection properties of materials using digital cameras. The calibrated cameras combined with filters create a novel way for measuring the radiance and luminance of radiation with unknown spectra. The new video-goniophotometer, in which these filters and cameras are integrated, will measure bi-directional properties of fenestration materials more quickly and in more detail than most existing goniophotometers used to study fenestration systems.

7.1 Achievements

The major accomplishments achieved through this research relate to developing the hemi-ellipsoid needed for the new video-goniophotometer, the camera calibration and filtering approach for analyzing radiation with unknown spectra, and methods for estimating quasi-spectral BT(R)DFs of fenestration system samples based on average BT(R)DFs for sub-wavelength intervals using d.

First, the half-mirrored hemi-ellipsoid necessary for the new video-goniophotometer was coated and analyzed. The procedures used to coat the hemi-ellipsoid were developed to accommodate the unusual geometry of the object and the stringent requirements of the goniophotometer. The resulting aluminum-coated hemi-ellipsoid was analyzed to determine its spectral transmission and reflection coefficients across a 380 to 900 nm interval. Further work will be required to extend these results further into the NIR. These spectral properties will be accounted for in experiments with the goniophotometer.

Second, an interesting approach for measuring the radiance and luminance of unknown spectra was developed using calibrated digital cameras and color glass filters. A color CCD camera and an NIR InGaAs camera were calibrated to measure the radiance, or luminance, of polychromatic radiation with unknown spectra. This includes accounting for vignetting for each camera, the angular resolution of the cameras, the non-linear spectroradiometric response of the cameras, and the response of the cameras to polychromatic beams. A spatial calibration was also performed to relate pixel locations in the cameras' images to angular directions emerging on the camera. Finally, Schott color glass filters were selected to filter radiation impinging on the CCD camera. This filtering method allows the conversion of the digital output of the camera to total radiance or luminance "seen" by the camera even when the spectrum being viewed is unknown.

These calibrations and absorption filters enable the camera's to measure the radiance and luminance of a full hemi-sphere of radiation with unknown spectra impinging on the camera. The methods employed draw from a large body of research on using digital cameras as multi-point radiometers and luminance-meters, but it extends this body of work to the use of NIR digital cameras in a similar way and new uses of CCD cameras with absorption filters.

Lastly, a method was developed to determine a quasi-spectral, BT(R)DF of fenestration systems using the new video-goniophotometer. This method exploits radiances estimated by the calibrated cameras for each set of filters and the known irradiance of fenestration samples to determine the average BT(R)DF of the sample across each filter set's wavelength interval. These average filter set BT(R)DFs are then assumed to correspond to the average BT(R)DF across a smaller waveband, for which the average filter set BT(R)DF is most significant and most accurate. This method has been shown, in section 6.5, to accurately recreate the gross spectral properties, in the form of a quasi-spectral BT(R)DF, of a variety of real fenestration systems that are likely to be studied. It has also been shown in section 6.5 that this method very accurately measures the total radiometric BT(R)DF of fenestration samples across the full 380 to

945 nm interval and total photometric BT(R)DFs. It is expected that similar, but somewhat lower accuracies can be achieved for the 945 to 1700 nm wavelength interval.

These BT(R)DFs are useful not only for predicting the angular distribution of luminance and radiance emerging from fenestration systems, typical output for most goniophotometers, but also for determining how much of different parts of the spectrum are transmitted or reflected in each direction. This will enable faster, more detailed studies of fenestrations with spectrally and angularly dependent optical properties, providing more information relevant to color rendering, the distribution of thermal gains and thermal comfort than most existing goniophotometers.

7.2 Errors

There are a few significant types of errors that impact the accuracy of the new video-goniophotometer. These include:

- Errors introduced by estimating the radiance and luminance of unknown spectra across finite wavelength intervals,
- Errors introduced by the estimating the quasi-spectral BT(R)DF of samples and using this to calculate total radiance across a larger interval (380 to 945 or 1700 nm) and total luminance,
- Errors introduced by inaccuracies in the measurement of each camera or channels ASR, and
- Errors introduced by physical components of the goniophotometer.

The analysis shows that with relatively few absorption filters the CCD and InGaAs digital cameras can provide reasonably accurate estimates of radiance and luminance across selected wavelength intervals for radiation with unknown spectra. Sections 5.2.8 and 5.3.7 as well as the analysis presented in Tables 6.2 and 6.3 show that errors introduced by the radiance or luminance estimation methods, in which samples are assumed neutral over certain sub-intervals, remain below 5 percent for a wide variety of unknown spectra. They also show, however, that if the spectrum viewed by the camera is altered significantly from the spectrum the camera is assumed to be viewing, the estimation errors in radiance and luminance over each interval can jump as high as 20 to 30 percent.

On the other hand, much greater accuracies can be achieved for estimating the total radiance or luminance over the 380 to 945 nm range, and similar results are expected for the total over the 380 to 1700 nm range. Table 6.1 shows that for a variety of spectral properties at the limits of those expected to be studied, the errors in the total radiance across 380 to 945 nm or luminance transmitted or reflected by a sample in a given direction due to the estimation method generally remains below 5 percent, and typically even lower. These low errors are the result of a successful method for estimating quasi-spectral BT(R)DF across the 380 to 1700 nm range using the camera's predicted radiances for filtered, sample-altered spectra.

The calibration of the cameras introduces other errors. Currently, the errors in the CCD camera's calibration, including the spectroradiometric response model, the absolute spectral responsivity curve, and the polychromatic responsivity model were measured to be 8.9 percent for the R channel, 4.3 percent for the G channel, and 5.2 percent for the B channel. These errors may be improved upon through minor modifications to the CCD camera's ASR curves using a few more validation experiments, particularly the R channel's ASR. These refinements may be explored in future work.

The errors in the NIR camera calibration have not yet been fully investigated. An NIR spectrometer is needed in order to measure the spectral radiance of polychromatic radiation viewed by the NIR camera. Once this has been performed, the accuracy of the camera's ability to estimate radiance can be assessed and the accuracy of the goniophotometer in measuring average BT(R)DFs over the NIR can be explored.

In addition to camera calibration and radiance estimation errors, there are also errors introduced by the spatial calibration. The correlation between pixel locations and incoming angles to the camera is very accurate. The relationship between pixel location and zenith angle to the camera was found to within 1.25 percent for the CCD camera and Fujinon fisheye lens, and 0.5 percent for the NIR camera and Fujinon fisheye lens.

A spatial calibration error that has not yet been quantified is the effect of the hemi-ellipsoid on the relationship between angles of emergence from a sample and incoming angles to the camera. Theoretically, these angles can be calculated precisely based on the geometry of the hemi-ellipsoid as described in section 5.2.4. However, the hemi-ellipsoid used for experiments is not optically perfect, nor is it perfectly specular. The spatial calibration errors due to imperfections in the geometry and specularity of the hemi-ellipsoid should be measured once the modifications to adjust the focal plane of the hemi-ellipsoid have been made.

The errors in the measurements of the spectral properties of the hemi-ellipsoid have not yet been quantified. As already mentioned, the methods for characterizing the spectral properties of the hemi-ellipsoid have been developed here, but the measurements must be repeated after the hemi-ellipsoid has been modified as described in section 4.5. To quantify the errors introduced by the spectral properties of the hemi-ellipsoid to BT(R)DF estimates, the final spectral transmission and reflection measurements should be repeated multiple times. The standard error in these measurements will provide an estimate in the accuracy with which the spectral properties of the hemi-ellipsoid are known.

Other errors that may be investigated more thoroughly in future work include inaccuracies in the positioning of fenestration samples for different angles of incidence, irregularities in the spectral irradiance of the sample caused by fluctuations in the spectral exitance of the HMI lamp, and the precision of the absorption filters.

Many of the errors presented here are based on calibrations of components, such as the CCD camera, of the goniophotometer. Some, however, are errors based on simulations of the goniophotometer. Validation experiments will be performed with the goniophotometer fully operational to quantify the typical errors in BT(R)DF measurements for a variety of known samples. These experiments will provide a much more direct measure of the errors in the goniophotometer than those presented here.

7.3 Future Enhancements

A number of enhancements could be considered for future improvements to the goniophotometer. The next steps for completing the goniophotometer in its current design are discussed in Appendix A. Presented here, are potential modifications to the design of the goniophotometer that may improve its accuracy and its capabilities.

One important enhancement that could be made to the radiance and luminance estimation methods presented in Chapter 6 is to loosen the assumption that samples are neutral across each band in the radiance estimation method. As previously explained, the camera's real responsivity for each channel is given by equations (6-4), (6-5) and (6-6) where the only unknowns are the spectral, bi-directional properties of the sample being investigated. By assuming non-neutral spectral properties within each filter set interval, different responsivities for each channel can be calculated from those presented in Chapter 6. These new responsivities will predict different radiances. Because there are three CCD channels with which to estimate radiance, three radiance predictions are made for any pixel location. However, the true radiance is only one real value. Modifying the assumed spectral properties of a sample will make these three radiance estimates converge or diverge. If the radiance estimates from each channel predict the same radiance for a given assumption of spectral transmission or reflection coefficients of the sample, it is likely that this assumption about spectral properties within the band is a better approximation than the neutral assumption.

This spectral estimation method may only work when there are multiple predictions of radiance for the same real radiance. For the CCD camera this occurs at every pixel location because there are three digital channels. However, not all channels can be used over every interval because each channel is insensitive at some wavelengths, such as the R channel in band one. For the NIR camera, there are not multiple measurements to compare.

Another way multiple radiance predictions may be compared is to compare the results of different filter sets where their wavelength intervals overlap. Rather than choosing one filter set that best approximates spectral transmission or reflection coefficients, as described in Chapter 6, each of the filter set's estimates could be used where they overlap to modify the estimated spectral transmission or reflection coefficients. The spectral transmission or reflection coefficients in a given direction will be the same regardless of the irradiating spectrum, but the predictions from each filter set will be different because they are predicting an average over different wavelength intervals. These differences could possibly be used to modify estimated quasi-spectral BT(R)DFs where filter sets overlap.

Another enhancement to the goniophotometer that may be explored is purchasing additional filters to enhance the spectral resolution of quasi-spectral BT(R)DF measurements. If the accuracy of the device is found to be unacceptable once validation experiments are performed (rather than simulated), additional filters could be purchased to improve this accuracy. For example, subdividing filter intervals 7 and 8 and the NIR may be necessary to more accurately estimate quasi-spectral BT(R)DFs for samples with unusual, or at least rapidly varying spectral properties over these intervals.

Substitute light sources may also be considered as an enhancement to the goniophotometer. The HMI lamp is meant to simulate the solar spectrum, however, a Xenon lamp, if appropriate collimation and uniformity can be achieved, would be more appropriate for simulating the solar spectrum as described in (Browne 2006). A Xenon lamp is not used here because adequate collimation and uniformity could not be achieved with existing equipment, and an affordable commercial lamp was not found. Additionally, sample BT(R)DFs to other types of spectra may be of interest, such as electric lighting. To study these properties the HMI lamp would have to be replaced with alternative light sources that have the relative spectrum of the radiation of interest.

Finally, modifications to the physical apparatus may be made to enhance the ability of the goniophotometer to measure high zenithal angles of incidence. Currently light is largely obstructed from the sample by the rotating table for very high angles of incidence. Also, the hemi-ellipsoid is not very transmissive at high zenithal angles of incidence. These enhancements would be much more difficult to achieve because they require forming and coating a new hemi-ellipsoid and making mechanical modifications to the rotating table.

7.4 Applications

The MIT quasi-spectral video-goniophotometer and the research performed to develop it have many applications. First, the ability to study spectrally and angularly selective properties of complex fenestration systems will provide new information about potential design and performance of new systems. As described in Chapter 1, innovative fenestration systems that exploit spectrally and angularly dependent optical properties are being developed and integrated into building to optimize performance and comfort, and at times enhance aesthetics. The video-goniophotometer will support the design of these systems by generating data that can be visualized, assessed and then altered through modifications to systems to tailor its optical properties.

It will also support analysis of these systems in buildings by providing detailed BT(R)DF information for use in performance analysis software such as Radiance, Window5 or DELight. This information will be useful lighting and energy modelers, lighting designers, architects and engineers. The hope is that this new information will improve the design of fenestration systems, building facades, and buildings as a whole to achieve better building performance and comfort.

The goniophotometer may also be used to study other materials beyond the realm of fenestration systems for buildings. Bi-directional, spectral properties of materials are important properties in a variety of engineering and related disciplines. The goniophotometer may have unconsidered applications in disciplines such as materials science, computer graphics or radiative heat transfer.

The radiometric calibration of digital cameras presented here is not limited to applications with goniophotometers. The calibrated cameras could be used, for example, to conduct thermal and visual performance assessments of spectrally neutral rooms. For example, if the spectrum of daylight or sunlight entering a room is known and the surfaces within the room are known to be largely spectrally neutral, either of the cameras could be used to measure radiance or luminance impinging on various points in the room based on the calculated polychromatic responsivity of the camera to the spectrum being viewed. This is similar to the use of many digital cameras for studying luminance or radiance distributions in rooms, such as (Inanici 2006), (Beltran and Mogo 2005) or (Debevec and Malik 1997), except that if the relative spectrum of radiation is known the radiance and luminance can be calculated directly.

Another possible application is to filter radiation that the camera is viewing using the filters specified to provide estimates of radiance or luminance impinging on certain points of a room over certain wavelength intervals. In rooms where the spectrally neutral assumption does not hold, the filters could be used to provide more accurate radiance and luminance measurements accounting for the unknown spectra viewed by the camera. This approach might also be applied to study spectral, hemi-spherical-directional or spectral bi-directional transmission or reflection by uniform surfaces. This could be achieved if the surface imaged is large and uniform, such that light entering the fish eye lens from all direction, corresponding to all points on the surface, was the same as light emerging from one point on the surface in all directions. In other words, the surface would need to be large enough to occupy most of the view of the fisheye lens and uniform enough such that its bi-directional properties could be considered the same at every point on the surface.

7.5 Perspectives

The way buildings and building components are designed is rapidly changing, with significant impacts on energy performance, human comfort, aesthetics, and sustainability. Complex fenestration systems and their effective integration into buildings are one of many opportunities to improve buildings in all these respects. Understanding the detailed optical properties of complex fenestration systems can potentially motivate improvements to their design, increase their integration, and enhance building performance.

Complex fenestration systems and advanced control of radiation through spectrally and angularly dependent system components provide an intriguing strategy for making buildings more responsive to the environment in a passive way. It is interesting to consider fenestration and façade elements that respond to sunlight conditions, thermal conditions, and other climatic conditions to adapt building functioning and improve building performance. The spectral bi-directional properties of materials in fenestration systems, and also facades, roofs, and other surfaces, are very basic parameters which can be employed to imbue a building with passive responses to the environment.

For example, cool roofs, or roofs that are highly reflective to solar radiation, are used in predominantly hot climates to reduce thermal loads on buildings, and thus cooling energy demand and cost. This is a very basic example, outside of the fenestration context, where the spectral properties of materials are used to improve building performance. Materials and systems other than fenestrations that have dynamic spectral properties dependent on the angle of the sun could be applied to buildings in many contexts, such as cool roofs with seasonal reflectance properties, to further manage thermal loads.

The most immediate opportunity presented by this work, however, is enhancing our understanding of daylighting and solar control fenestration systems. Daylighting systems that distribute light usefully in spaces are rapidly evolving. Furthermore, fenestration systems that have the additional capability of controlling how, when and where NIR thermal gains are delivered to spaces are also emerging. This work seeks to provide a tool that will help advance the design, integration and performance of these promising elements of better buildings.

Appendix A. Completing the Goniophotometer

There are a number of additional calibrations, modifications, and programming requirements that must be completed before the goniophotometer is operational. This appendix outlines the basic remaining steps necessary to complete the goniophotometer.

A.1 Light Source

First the final aperture settings, power settings, and positioning of the Dedolight must be fixed to ensure the HMI lamp provides approximately constant spectral exitance. Then, the HMI lamp's spectrum across the full 380 to 1700 nm range must be measured with a new NIR spectrometer.

A.2 Mechanical Components

Certain mechanical components necessary for the goniophotometer must be completed or require refurbishing. This work on mechanical components, excluding the hemi-ellipsoid, includes:

- The accuracy of angular positioning of the mechanical table/sample holder, as described in (Osser 2007), must be either accounted for in the estimation of accuracy for goniophotometric measurements or must be improved,
- The beam shaper, developed in (Browne 2006), must be refurbished and retested. The beam shaper mount needs fixing, including a new casing and new legs, and the programming for the beam shaper must be reworked and integrated into the goniophotometer control interface.
- The filter wheel, as developed in (Koch 2007), must be integrated into the experimental setup. The code controlling the filter wheel must be integrated into the goniophotometer control interface.
- The CCD camera mount must be modified once the hemi-ellipsoid has been modified and the experimental spatial calibration has been performed to correctly position the fish eye lens to achieve a predictable relationship between pixel locations and angular directions.
- Finally, it must be determined whether wireless communication will be used and a laptop mounted to the rotating table, or whether wired communication is possible.

A.3 Hemi-ellipsoid

The hemi-ellipsoid requires special attention, as it is critical to the functioning of the goniophotometer. The following modifications or experiments must be performed in order to complete work on the hemi-ellipsoid.

- The focal plane of the hemi-ellipsoid must be located.

- The hemi-ellipsoid must be trimmed down to size to place the base of the hemi-ellipsoid in the focal plane.
- A strong rim must be made and mounted to the hemi-ellipsoid to prevent cracking and bending at its rim and to enable a better mounting method onto the rotating table.
- The spectral transmission of the modified hemi-ellipsoid must be measured for all incidence angles of interest across the full 380 to 1700 nm spectral range.
- The approximate spectral reflection off of the hemi-ellipsoid must be measured for many transmission (or reflection) angles of interest across the full 380 to 1700 nm range, which will then be converted into real spectral reflection coefficients using the relationship between transmission and reflection coefficients at 550 nm.

A.4 Camera Calibrations

There are a few camera calibrations that are yet to be performed or must be validated with additional equipment, specifically an NIR spectrometer. These are listed below.

- Corrections to the RGB absolute spectral responsivity curves of the CCD camera should be considered where the camera is consistently over or under estimating. Particularly, the R channel's ASR curve could be modified for better accuracy.
- The absolute spectral responsivity of the NIR camera must be validated using brighter monochromatic spots and an NIR spectrometer, or through a polychromatic calibration.
- The polychromatic response function of the NIR camera must be validated using polychromatic NIR radiation and an NIR spectrometer.
- The accuracy with which the R, G, B or NIR channels can convert pixel values to radiances for filtered spectra that has been modified within the constraints of sections 5.2.8 and 5.3.7 should be validated.
- Experimental spatial calibrations to correlate angular directions emerging from sample holder to pixel locations in each camera's images must be performed in situ using the modified hemi-ellipsoid.
- A similarity condition must be developed by which samples can be considered "neutral" across 380 to 945 nm or within filter bands. This condition will be based on the similarity of the predicted radiances based on the R, G, and B channels.

A.5 Image Acquisition and Processing

Once the additional modifications and calibrations described above have been performed, the components of the goniophotometer will be ready for use to collect BT(R)DF data. However, there is additional work required to complete the control and automation of the image acquisition and processing functions, these include:

- Improving the speed and processing methods for the Matlab™ codes for pixel to radiance conversion, spatial averaging both by solid unit of angle and polar coordinates, conversion from band radiances to average band reflection and transmission coefficients, combination of band reflection and transmission coefficients to form quasi-spectral reflection and transmission coefficients, and calculation of total radiometric and photometric reflection and transmission.

- Completing the Matlab™ codes for estimating spectra within each filter band, combining images for different integration times to develop a full hemi-sphere, non-saturated radiance map, and generating BT(R)DF files that include photometric BT(R)DF and radiometric BT(R)DF.
- Completing Visual Basic (VB) codes that control the positioning of the rotating sample holder, the positioning of the beam shaper, the positioning of the filter wheel, image capture and changing integration time.
- Determining a method for controlling the NIR camera image capture remotely and programming the digital interface to change integration times remotely using the NIST IMAQ interface and enabling communication between the NIST interface and the VB goniophotometer interface.
- Integrating the positioning, image capture, and image processing routines into one goniophotometer interface which also allows users to select among angular resolution, incidence angle, and spectral range and analysis options.

Appendix B. Calibration and Validation Codes

This appendix identifies and explains the Matlab™ codes used for calibrating the digital cameras and validating the quasi-spectral BT(R)DF estimation method. It outlines the relationships between and functions of these codes. It contains, in this order, codes relevant to the following:

- calibrating the CCD camera,
- calibrating the InGaAs camera,
- the spatial conversion of pixel coordinates to sample emerging directions,
- measuring the transmission and reflection properties of the hemi-ellipsoid, and
- validation codes, including the polychromatic response of the CCD camera, CCD and InGaAs radiance estimation errors, and total BT(R)DF estimation errors.

It concludes with a summary of the important stored variables from these procedures.

B.1 CCD Camera Calibration Codes

Calcamforsens.m: This function calculates the average pixel value across a spot by calling datamean.m with some additional routines to account for potential noise or saturated pixels. This is adapted from code in (Browne 2006).

CalibrateCamera.m: This code calls the functions which perform each step of the calibration process. This is the highest level routine for CCD camera calibration. It takes a calibration type, either logistic, weibull cumulative, sigmoid, asymmetric sigmoid, or guassian cumulative function as an input.

CombineSensitivities.m: This function pieces together the results of the relative sensitivities for each channel calculated over different wavelength intervals by SensitivityAnalaysis.m. It then uses integrating sphere validation experiments to fix the magnitude of the sensitivity curves to determine the final ASR of each channel. This piecewise assembly of the ASRs is necessary because different experiments, such as with the Xenon bulb or the tungsten halogen lamp, had to be performed to accurately measure ASR over different wavelength intervals. The integrating sphere measurements are used to determine absolute magnitudes of the ASR curves because the spectrometer experiments were determined to only provide a good measure of relative sensitivities.

Datamean.m: This function calculates the mean pixel value over a spot in a cropped image input to the function. The lowest pixels are discarded to account for the edges of the spot in the image and the top few pixels are discarded to account for any unaccounted for noisy (e.g. saturated) pixels. Typically, averaging occurs over more than twenty pixels. This is adapted from code in (Browne 2006)

EvaluateLogistic.m: Evaluates the value of the logistic function for at a value supplied to the function with coefficients a, b, c and d also supplied to the function. Similar functions exist for evaluating each of the other function types described under spectroradiometric response.

ExposureAnalysis.m: This function analyzes images taken by the CCD camera at 50 nm intervals from 450 to 950 nm to determine the shape of the non-linear spectroradiometric response of the CCD camera.

FitRelativeSens.m: This function fits the relative sensitivity curves to the measured normalized spectral exposures $h^{0.3}_{R,G,B}(\lambda)$ determined for various wavelengths.

InvLogistic.m: Evaluates the inverse of the logistic function for a supplied value with coefficients a, b, c, and d which are also supplied. Similar routines exist for the other spectroradiometric response function types.

Opentif.m: This function opens a .tif image file as a matrix in a double number format. This code is borrowed from (Browne 2006)

Reflectance.m: This function supplies the reflectance coefficient of a reflectance standard input to the function at a wavelength input to the function.

SensitivityAnalysis.m: This function calculates the relative sensitivities of each of the CCD's channels, R, G and B using images, spectrometer readings and integrating sphere measurements. The sensitivities are calculated only over intervals input to the function, such as 380 to 450 nm, 400 to 900 nm, or 900 to 945 nm, depending on the experiment being analyzed. The results from many experiments are average here. It calls SpectralAnalysisforSensitivity.m.

SetCurveFittingVariables.m: Sets the starting variables for each of the function types described in the spectroradiometric response calibration.

SpectralAnalysisforSensitivity.m: This function returns the average pixel value for the R, G, and B channels for a monochromatic spot and the radiance viewed by the spot using input images of monochromatic radiances and spectrometer and integrating sphere readings.

Spot Analysis**.m: These codes (where ** is a wildcard to signify codes with different names) analyze the digital output of the camera relative to integrating sphere measurements to determine the normalized spectral that leads to an NDL of 0.3 for different monochromatic radiances.

CCD camera calibration flow chart

Calculates spectroradiometric response function and channel ASRs

Inputs:
CCD images of monochromatic radiances
Integrating sphere and spectrometer measurements of irradiance of the reflectance standard

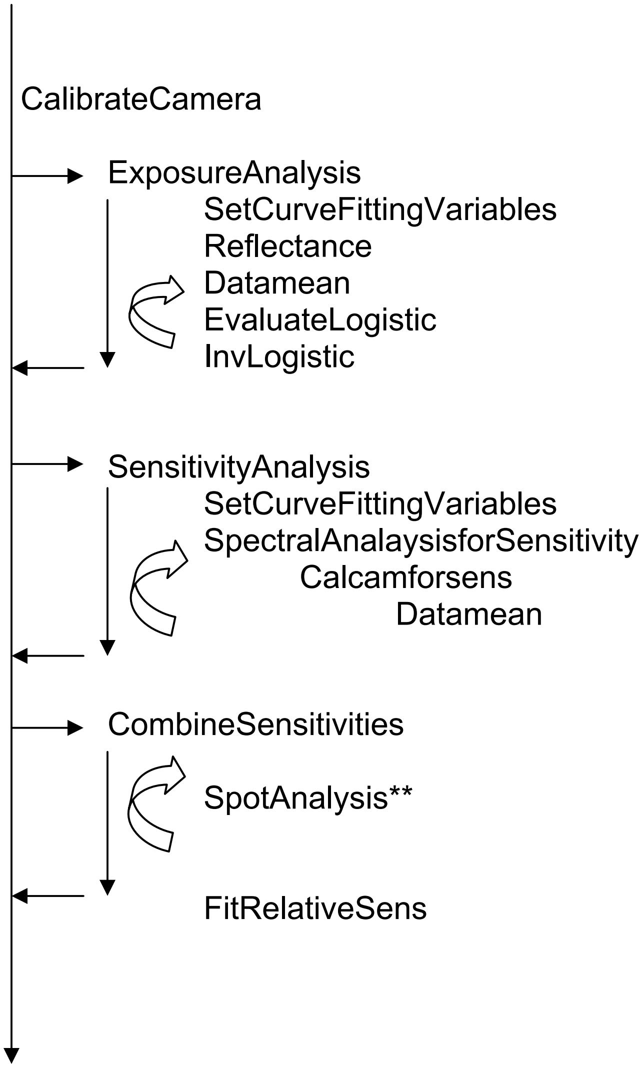

Outputs:
Absolute spectral responsivity (ASR) of R, G and B channels
Logistic dose response function for all CCD camera channels

B.2 InGaAs Camera Calibration Codes

SpectralAnalysisNIR.m: This code calculates the ASR of the NIR camera.

InGaAsExposure.m: This function determines the coefficients for the Gaussian Cumulative response model of the InGaAs camera. Inputs including NIR camera images and integrating sphere fluxes.

EvalGuassCum.m: This function evaluates the guassian cumulative function at a specified value for specified coefficients a,b,c, and d.

InvGaussCum.m: This function evaluate the inverted Gaussian cumulative function at a specified value for specified coefficients a, b, c and d.

InGaAs1480.m: Thus function estimates the normalized spectral exposure of the NIR camera for 1480 nm radiation $h^{0.3}_{NIR}(1480)$.

InGaAs camera calibration flow chart

Calculates spectroradiometric response function and NIR camera ASR

Inputs:
InGaAs camera images of monochromatic radiances
InGaAs camera images of polychromatic radiation (for response calibration only)
Integrating sphere flux readings

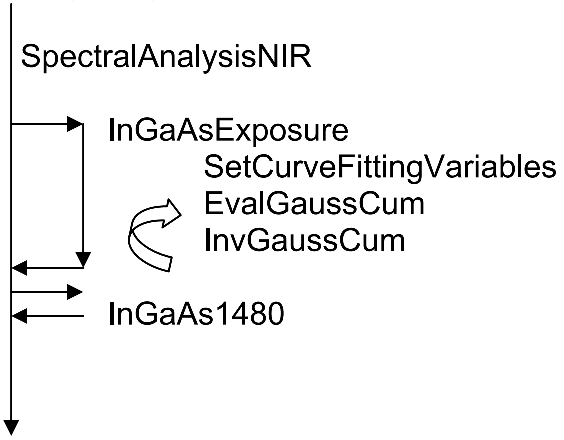

Outputs:
Absolute Spectral Responsivity (ASR) of NIR camera
Gaussian Cumulative response function for NIR camera

B.3 Spatial Calibration Related Code

ConvertToEmerging.m: This function converts the pixel locations in the CCD camera images to emerging directions from a the sample focal point based on the geometry of a perfect hemi-ellipsoid.

B.4 Hemi-Ellipsoid Measurement Codes

EllipsoidTransmission.m: This code takes a baseline spectrometer measurement and transmitted radiation spectrometer measurements for known angular directions relative to the hemi-ellipsoid and calculates the spectral transmission coefficients of the ellipsoid over a 380 to roughly 900 nm interval.

EllipsoidReflection.m: This code takes an approximate baseline, non-reflected spectrometer measurement and reflected radiation spectrometer measurements for known angular directions relative to the hemi-ellipsoid and calculates the approximate spectral reflection coefficients of the ellipsoid over a 380 to roughly 900 nm interval.

ReflectionVTransmission.m: This code takes measurements of the hemi-ellipsoids transmission, reflection and absorption based on integrating sphere measurements and calculates a parabolic fit of the data relating reflection coefficients to transmission coefficients at 550 nm.

CorrectReflection.m: This codes used the relationship between reflection and transmission coefficients determined by ReflectionVTransmission.m to rescale the approximate spectral reflection coefficients of the hemi-ellipsoid determined in EllipsoidReflection.m

Hemi-ellipsoid calibration flow chart

Calculates the spectral transmission and reflection coefficients of the hemi-ellipsoid at any number of angular directions, e.g. 10 altitudes and 8 azimuths

Inputs:
Baseline HMI lamp spectrometer measurement (one for transmission, one for reflection)
Spectrometer readings of transmitted and reflected HMI spectrum
Measured transmission, reflection, and absorption coefficients for 550 nm for many angular directions related to locations on the hemi-ellipsoid

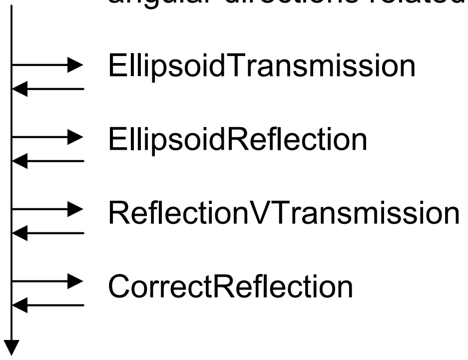

Outputs:
Spectral transmission and reflection coefficients of hemi-ellipsoid from 380 to 900 nm

B.5 Validation Codes

ValidateBTRDF.m: This function simulates the response of the CCD camera to filtered radiances passing through the hemi-ellipsoid, reflecting off of a known sample, reflecting off the ellipsoid, and impinging on the camera. In calculates the errors in estimated radiance and luminance for each filter set, constructs a quasi-spectral BT(R)DF, and calculates the errors in estimated total radiance from 380 to 945 nm and total luminance reflected by the sample using the quasi-spectral BT(R)DF.

CheckPolychromaticResponse.m: This function calculates the error in estimated radiance by the CCD camera for 8 validation spots. Inputs to the code include integratinf sphere measurements and CCD images.

UnknownSpectraCCD.m: This function simulates the CCD camera's response to radiation made up of theoretically possible altered spectra, altered from the HMI lamp's original spectrum. It simulates systematic alterations to the spectrum to estimate the accuracy with which the camera can estimate radiance for each filter set within defined constraints on spectrum alterations.

UnknownSpectraNIR.m; This function simulates the NIR camera's response to alterations to an assumed spectrum of the HMI lamp in the NIR. Alterations to this assumed spectrum are performed systematically to estimate the accuracy with which the camera can estimate within defined constraints on spectrum alterations.

B.6 Important Stored Variables

Responsemodel.mat: This contains the cefficients of the logistic dose response model for the spectroradiometric response of the CCD camera.

InGaAsResponsemodel.mat: This contains the coefficients of the Gaussian cumulative model for the spectroradiometric response of the InGaAs camera.

correctedRGBsens.mat: This contains the final ASR curves for the R, G and B channels of the CCD camera from 380 to 945 nm.

InGaAssens.mat: This contains the current ASR curve for the NIR camera channel, which must be validated in future work.

rhooftau.mat: This contains the three coefficients of the parabolic fit to the reflection versus transmission data points for 550 nm for the hemi-ellipsoid. It can be used to calculate the reflection coefficient of the hemi-ellipsoid for 550 nm radiation at a given location on the hemi-ellipsoid if the transmission coefficient of the hemi-ellipsoid for 550 nm radiation is known at that location.

Taurho.mat: This contains the final spectral transmission and reflection coefficients (rescaled using the reflection vs transmission relation at 550 nm) and the wavelengths at which these coefficients were measured (about every 0.3 nm).

Appendix C. Nomenclature

$a_{\Delta\lambda,\text{filterset}}(\theta_{i},\varphi_{i},\theta_{t(r)},\varphi_{t(r)})$	Fraction of the total radiance viewed by the camera when using a certain filter set over wavelength interval $\Delta\lambda$ for angles of incidence (θ_{i},φ_{i}) and sample angles of emergence $(\theta_{t(r)},\varphi_{t(r)})$
$a_{\Delta\lambda,\text{filterset},\text{neutral}}(\theta_{i},\varphi_{i},\theta_{t(r)},\varphi_{t(r)})$	Fraction of the total radiance viewed by the camera when using a certain filter set over wavelength interval $\Delta\lambda$ for angles of incidence (θ_{i},φ_{i}) and sample angles of emergence $(\theta_{t(r)},\varphi_{t(r)})$ for a neutral sample
a, b, c, d	Camera response function constants
ASR	Absolute spectral responsivity
BS(d)	Beam spread factor as a function of distance from the HMI lamp
BT(R)DF	Bi-directional Transmission (or Reflection) Distribution Function
$BT(R)DF_{e}$	Radiometric BT(R)DF
$BT(R)DF_{v}$	Photometric BT(R)DF
$BT(R)DF_{e(v),\text{band}}$	Average radiometric (or photometric) BT(R)DF of the sample across a given wave band to the HMI lamp or solar radiation, or the "band BT(R)DF"
$BT(R)DF_{e(v),\text{filterset}}$	Average radiometric (or photometric) BT(R)DF of the sample to filtered radiation using a certain filter set, which is a sample of the HMI lamp's spectral irradiance, or the "filter set BT(R)DF"
$BT(R)DF_{e,\lambda1-\lambda2}$	Radiometric BT(R)DF of the sample across wavelength interval λ1 to λ2
CCVT	Constrained centroidal Voronoi tessellation
$DL_{R,G,B}$	Digital level of the R, G, or B channel

E_e	Irradiance
$E_{e,sample,filterset}$	Total irradiance of a sample when using a certain filter set
$E_{e,HMI}(\lambda)$	Spectral exitance of the HMI lamp
$E_{e,source}(\lambda)$	Spectral exitance of an arbitrary source
$E_e(\theta_i)$	Directional total irradiance
$E_{e,sample,filterset}(\theta_i)$	Directional total irradiance on a sample for a certain filter set
$E_e(\theta_i,\lambda)$	Directional spectral irradiance
$E_{e,sample,filterset}\ (\theta_i,\lambda)$	Directional spectral irradiance on a sample for a certain filter set
$E_e(\theta_i,\sigma,\lambda)$	Directional spectral irradiance with polarization dependence
$E_e(\theta_i,\sigma,\lambda)$	Directional spectral irradiance with polarization dependence
E_v	Illuminance
$E_v(\theta_i)$	Directional illuminance
erf	Error function
erfinv	Inverse error function
$H(\lambda)$	True spectral exposure of CCD or InGaAs sensor array
$h(\lambda)$	Measured spectral exposure given by scene radiance multiplied by camera integration time
$h^{0.3}_{R,G,B}(\lambda)$	Spectral exposure leading to an NDL equal to 0.3 for the R, G or B channel
$h^{0.3}_{R,G,B,\Delta\lambda}$	Discretized spectral exposure leading to an NDL equal to 0.3 for the R, G or B channel over a 5 nm wavelength interval $\Delta\lambda$
$h^{0.3}_{R,G,B,beam}$	Effective exposure leading to an NDL equal to 0.3 for the R, G or B channel for a give polychromatic beam
$h^{0.3}_{R,G,B,filter}$	Effective exposure leading to an NDL equal to 0.3 for the any filtered radiation with a known relative spectrum

$h^{0.3}_{R,G,B,\mathrm{filterset}}$	Effective exposure leading to an NDL equal to 0.3 for the R, G or B channel for a polychromatic beam generated by a give filter set
$h_{NIR}(\lambda)$	Spectral exposure of the NIR camera
$h^{0.3}_{NIR}(\lambda)$	Spectral exposure of the NIR camera leading to an NDL equal to 0.3
$h^{0.3}_{NIR,\Delta\lambda}$	Discretized spectral exposure of the NIR camera leading to an NDL equal to 0.3 for the NIR camera over a 25 nm wavelength interval $\Delta\lambda$
$h^{0.3}_{NIR,\mathrm{beam}}$	Spectral exposure, given by scene radiance multiplied by integration time, leading to an NDL equal to 0.3 for the NIR camera for a known polychromatic beam
$h^*_{NIR}(\lambda)$	Surrogate spectral exposure of the NIR camera, given by integrating sphere flux multiplied by camera integration time, used for non-linear response calibration
$h^{*0.3}_{NIR}(\lambda)$	Surrogate spectral exposure of the NIR camera leading to an NDL equal to 0.3 used for non-linear response calibration
$\left[\frac{1}{h^{0.3}_{R,G,B,\mathrm{filterset}}}\right]$	The absolute responsivity of channel R, G or B leading to an NDL equal to 0.3 for radiation using a given filter set
$\left[\frac{1}{h^{0.3}_{R,G,B,\mathrm{filterset}}}\right]_{\mathrm{neutral}}$	The absolute responsivity of channel R, G or B leading to an NDL equal to 0.3 for radiation using a given filter set assuming a sample is neutral across the filter interval
k	Constant of proportionality relating camera spectral exposure to scene radiance

L_e	Radiance
$L_e(\lambda)$	Spectral radiance
$L_{e,\Delta\lambda}$	Total radiance over a wavelength interval $\Delta\lambda$
$L_{e,beam,\lambda1-\lambda2}$	Total radiance in a polychromatic beam in the wavelength interval $\lambda1$ to $\lambda2$.
$L_{e,sample,\ filterset}$	Total radiance emerging from the sample when using a certain filter set
$L_e(\theta_{t(r)},\varphi_{t(r)},\theta_i,\varphi_i)$	Bi-directional total radiance
$L_e(\theta_{t(r)},\varphi_{t(r)},\theta_i,\varphi_i,\lambda)$	Bi-directional spectral radiance
$L_e(\theta_{t(r)},\varphi_{t(r)},\theta_i,\varphi_i,\sigma,\lambda)$	Bi-directional spectral radiance with polarization dependence
L_v	Luminance
$L_v(\theta_{t(r)},\varphi_{t(r)},\theta_i,\varphi_i)$	Bi-directional luminance
N	Numerical aperture
$NDL_{R,G,B}$	Normalized Digital Level (Digital Level divided by 2^8) of the R, G, or B channel
NDL_{NIR}	Normalized Digital Level (Digital Level divided by 2^{12}) of the NIR camera
$p_{\Delta\lambda}$	Fraction of total radiance in wavelength interval $\Delta\lambda$
$p_{\Delta\lambda,HMI}$	Fraction of total radiance of the Dedolight in wavelength interval $\Delta\lambda$
$p_{\Delta\lambda,SpectraCamera}$	Fraction of total radiance viewed by the camera for a known spectrum in wavelength interval $\Delta\lambda$
$r_{R,G,B}(\lambda)$	Absolute spectral responsivity of the R, G or B channel in NDL/(μJ/cm^2–sr)
$r_{\Delta\lambda,R,G,B}$	Discretized absolute spectral responsivity of the R, G or B channel in NDL/(μJ/cm^2–sr) over 5 nm wavelength intervals $\Delta\lambda$
r_{NIR} (λ)	Absolute spectral responsivity of the NIR camera in NDL/(mJ/cm^2–sr)

$r_{\Delta\lambda,NIR}$	Discretized absolute spectral responsivity of the NIR camera in NDL/(mJ/cm^2–sr) over 25 nm wavelength intervals $\Delta\lambda$
t_{int}	Camera integration time
$V(\lambda)$	Photopic response curve
$VC(x,y)$	Vignetting correction factors for pixel location x,y which depend on zenith angle of emergence from a sample, given by $\theta_{t(r)} = \theta_{t(r)}(x,y)$
x	Horizontal pixel location in image
y	Vertical pixel location in image
$\Delta\lambda$	Wavelength interval
θ_c	Zenithal angle of incidence on camera lens
θ_h	Zenithal angle on hemi-ellipsoid relative to apex
θ_i	Zenithal angle of incidence
θ_s	Zenithal angle of emergence from sample
$\theta_{t(r)}$	Zenithal angle of transmission (or reflection)
λ	Wavelength
$\rho\ (\lambda)$	Spectral reflection coefficients
$\rho_{\Delta\lambda}$	Average reflection coefficients over discrete wavelength intervals $\Delta\lambda$
$\rho_{\text{ellipsoid}}(\theta_{t(r)},\varphi_{t(r)},\lambda)$	Spectral reflection coefficients of the hemi-ellipsoid for transmission (or reflection) angles $(\theta_{t(r)},\varphi_{t(r)})$
$\rho_{\Delta\lambda,\text{ellipsoid}}(\theta_{t(r)},\varphi_{t(r)})$	The average bi-directional reflection coefficients of the hemi-ellipsoid for transmission (or reflection) angles $(\theta_{t(r)},\varphi_{t(r)})$ over wavelength interval $\Delta\lambda$
$\rho_{\Delta\lambda,\text{sample}}(\theta_i,\varphi_i,\theta_{t(r)},\varphi_{t(r)})$	The average bi-directional reflection coefficients of a sample over wavelength interval $\Delta\lambda$ for incidence angles (θ_i, φ_i) in reflected direction $(\theta_{t(r)},\varphi_{t(r)})$
σ	Polarization of Radiation
$\tau(\lambda)$	Spectral transmission coefficients

$\tau_{\Delta\lambda}$	Average transmission coefficients over discrete wavelength intervals $\Delta\lambda$
$\tau_{filterset}(\lambda)$	Spectral transmission coefficients of a filter set
$\tau_{\Delta\lambda,filterset}$	Average transmission coefficients of a filter set over discrete wavelength intervals $\Delta\lambda$
$\tau_{ellipsoid}(\theta_i,\varphi_i,\lambda)$	The spectral transmission coefficients of the hemi-ellipsoid for incidence angles (θ_i, φ_i) on the sample
$\tau_{,\Delta\lambda,ellipsoid}(\theta_i,\varphi_i)$	The average transmission coefficients of the hemi-ellipsoid over wavelength interval $\Delta\lambda$ for incidence angles (θ_i, φ_i)
$\tau_{\Delta\lambda,sample}(\theta_i,\varphi_i,\theta_{t(r)},\varphi_{t(r)})$	The average transmission coefficients of a sample over wavelength interval $\Delta\lambda$ for incidence angles (θ_i, φ_i) in reflected direction $(\theta_{t(r)},\varphi_{t(r)})$
φ_c	Azimuthal angle of incidence on camera lens
φ_i	Azimuthal angle on hemi-ellipsoid relative to semi-minor axis
φ_i	Azimuthal angle of incidence
φ_s	Azimuthal angle of emergence from sample
$\varphi_{t(r)}$	Azimuthal angle of transmission (or reflection)

References

[Andersen 2006] Andersen, M. “Validation of the performance of a new bidirectional video-goniophotometer”, *Lighting Res. Technol*. 38, 4 (2006) 295-313.

[Andersen and de Boer 2006] Andersen, M., de Boer, J. “Goniophotometry and assessment of bidirectional photometric properties of complex fenestration systems”, *Energy and Buildings* 38 (2006) 836-848.

[Andersen et al. 2005a] Andersen, M. Roecker, C., Scartezzini, J.-L. “Design of a time-efficient video-goniophotometer combining bidirectional functions assessment for transmission and reflection”, *Solar Energy Materials & Solar Cells* 88 (2005) 97-118.

[Andersen et al. 2005b] Andersen, M., Rubin, M., Powles, R., Scartezzini, J.-L. “Bi-directional transmission properties of Venetian blinds: experimental assessment compared to ray-tracing calculations”, *Solar Energy* 78 (2005) 187-198.

[Andersen et al. 2005c] Andersen, M. Ljubecic, D., Browne, C. Kleindeinst, S., Culpepper, M. “Automated Assessment of Light Redirecting Properties of Materials and Sunlight Penetration within Scale Models: The Heliodome Project”, *Proceedings of the ISES 2005 Solar World Congress. Orlando, Fl*. August 18-12, 2005.

[Andersen and Scartezzini 2005] Andersen, M., Scartezzini, J.-L. “Inclusion of the specular component in the assessment of bidirectional distribution functions based on digital imaging”, *Solar Energy* 79 (2005) 159-167.

[Andersen 2004] Andersen, M. Innovative Bidirectional Video-Goniophotometer for Advanced Fenestration Systems, Swiss Federal Institute of Technology. Ph.D. Thesis. Lausanne, EPFL (2004).

[Andersen et al. 2001] Andersen, M., Michel, L., Roecker, C., Scartezzini, J.-L., “Experimental assessment of bi-directional transmission distribution functions using digital imaging techniques”, *Energy and Buildings* 33 (2001) 417-431.

[Apian-Bennewitz 2007] Apian-Bennewitz, P. “pab Goniophotometer II”, http://www.pab-opto.de/gonio-photometer/ (accessed 5-1-07).

[Apian-Bennewitz and von der Hardt 1998] Apian-Bennewitz, P., von der Hardt, J. “Enhancing and calibrating a goniophotometer”, *Solar Energy Materials and Solar Cells* 54 (1998) 309-322.

[Apian-Bennewitz 1994] Apian-Bennewitz, P. “Designing an apparatus for measuring bidirectional reflection/transmission”, *SPIE Proceedings 2255, “Optical Materials Technology XIII”, Freiburg,* April 18-22 (1994).

[Arasteh et al. 2003] Arasteh, D., Apte, J., Huang, Y.J. “Future Advanced Windows for Zero-Energy Homes”, *ASHRAE Transactions*, Vol. 109 Part 2 (2003).

[ASTM, 2001] American Society for Testing and Materials. “Method E308, Standard Practice for Computing Colors of Objects by Using the CIE System”, *ASTM International, West Conshohocken, PA, astm e308-01 edition* (2001).

[Aydinli 1996] Aydinli, S. “Short description of the spiral goniophotometer for bidirectional measurements (TU Berlin)”, *Report for IEA SHC Task 21, ECBCS Annex 29, Subtask A, Technische Universita¨t Berlin (TUB)*, Berlin, (1996).

[Baker and Steemers 2002] Baker, N. Steemers, K. Daylight Design of Buildings. James and James, London, UK (2002).

[Behnisch 2007] Behnisch Architects, “Genzyme Center Headquarters Building”, http://www.behnisch.com (accessed 5-11-07).

[Bellia et al. 2002] Bellia, L. Cesarano, A., Minichiello, F., Sibilio, S. “Setting up a CCD photometer for lighting research and design”, *Building and Environment* 37 (2002) 1099-1106.

[Berson et al. 2002] Berson, D.M. Dunn, F.A. Takao, M. “Phototransduction by retinal ganglion cells that set the circadian clock”, *Science* 295 (2002) 1070-1073.

[Boyce et al. 2003a] Boyce P.R., Akashi Y., Hunter C.M., Bullough J.D. “The impact of spectral power distribution on the performance of an achromatic visual task*”,* Lighting Res. Technology 35,2 (2003) 141-161.

[Boyce et al 2003b] Boyce, P.R., Hunter, C., Howlett, O. “The Benefits of Daylight”, Lighting Research Center, Rensellear Polytechnic Institute, Troy, NY. Sponsored by Capturing the Daylight Dividend Program. (September 2003).

[Brainard et al. 2001] Brainard, G.C., Hanifin, J.P., Greeson, J.M., Byrne, B., Glickman, G., Gerner, E. Rollag, M. “Action Spectrum for Melatonin Regulation in Humans: Evidence for a Novel Circadian Photoreceptor”, *The Journal of Neuroscience*, 21 (16):6405-6412 (2001).

[Breitenbach et al. 2001] Breitenbach, J., Lart, S., Langle, I., Rosenfeld, J.L.J. “Optical and thermal performance of glazing with integral venetian blinds*”, Energy and Buildings* 33 (2001) 433-442.

[Breitenbach et al. 2000] Breitenbach, J., Rosenfeld, J.L.J. “Goniospectrometer Measurements of the Optical Performance of a Holographic Optical Element”, *Solar Energy* Vol. 68, No. 5 (2000) 427-437.

[Breitenbach and Rosenfeld 1998] Breitenbach J, Rosenfeld JLJ. “Design of a photogoniometer to measure angular dependent optical properties” *Proceedings of International Conference on Renewable Energy Technologies in Cold Climates, Ottawa,Canada*. Solar Energy Society of Canada Inc. (1998) 386_91.

[Browne 2006] Browne, C. Development of a light detection system for bidirectional measurements over the solar spectrum and sun course simulations with scale models, Massachusetts Institute of Technology, Master of Science in Building Technology Thesis. (June, 5 2006).

[Brown et al. 2001] Brown, S., Larason, T., Habauzit, C., Eppeldauer, G. P., Ohno, Y., Lykke, K. “Absolute Radiometric Calibration of Digital Imaging Systems”, *Proceedings of SPIE* Vol. 4306 (2001).

[Brown 1971] Brown, D.C. “Close-range camera calibration”, *Photogrammetric Engineering,* 37(8) (1971) 855-866.

[BYU 2007] Brigham Young University, “Complex Index of Refraction Look-up Utility”, http://www.ece.byu.edu/photonics/opticalconstants.phtml (accessed 5-4-07).

[Carmody et al. 2004] Carmody, J., Selkowitz, S., Lee, E.S., Arasteh, D., Willmert, T. Window Systems for High-Performance Buildings. The Regents of the University of Minnesota, New York, NY (2004).

[Christoffers 1996] Christoffers, D. “Seasonal Shading of Vertical South-Facades with Prismatic Panes*”, Solar Energy* Vol. 57, No. 5 (1996) 339-343.

[Clarke et al. 1998] Clarke, T.A. Fryer, J.F. Wang, X. “The principal point and CCD cameras”, *Photogrammetric Record* 16(92) (1998) 293-312.

[CIE 1977] Commission Internationale de l’Eclairage (CIE). “Radiometric and photometric characteristics of materials and their measurement”. *CIE* 38 (TC-2.3), (1977).

[CEC 1993] Commission of the European Communities. Daylighting in Architecture. Ed. N. Baker, A. Fanchiotti, K. Steemers. James & James, London (1993).

[Cuttle 2002] Cuttle, C. “Identifying the human values associated with windows”, *International Daylighting* 5, 3-6 (2002).

[de Boer 2006] de Boer, J. "Modelling indoor illumination by complex fenestration systems using bidirectional photometric data", *Energy and Buildings* 38 (2006) 849–868.

[Debevec and Malik 1997] "Recovering High Dynamic Range Radiance Maps from Photographs", *Association for Computing Machinery, Inc.* (1997).

[Deniel 2002] Deniel, J.M., Mode´lisation des luminaires et des BRDF: re´alisation, mesure et compression, PhD thesis, Universite´ de Rennes 1, Rennes, April 2002.

[Du et al. 2003] Du, Q., Gunzburger, M.D., Ju, L. "Voronoi-based finite volume methods, optimal Voronoi meshes, and PDEs on the sphere" *Comput. Methods Appl. Mech. Engrg.* 192 (2003) 3933-3957.

[Ducker 2000] Ducker Research Company, Inc. "Study of the U.S. and Canadian Market for Windows and Doors" (2000).

[EIA 2005] Energy Information Administration, U.S. Department of Energy, Annual Energy Outlook 2005, DOE/EIA-0383 (February 2005).

[Frost et al. 1996] Frost, K. Eto, J. Arasteh, D. Yazdanian, M. "The National Energy Requirements of Residential Windows in the U.S.: Today and Tomorrow", *Proceedings the ACEEE 1996 Summer Study on Energy Efficiency in Buildings. Pacific Grove, CA,* (August 25-31, 1996).

[Frose et al. 1993] Frost, K.; Arasteh, D.; Eto, J., Savings from Energy Efficient Windows: Current and Future Savings from New Fenestration Technologies in the Residential Market, Lawrence Berkeley National Laboratory, Sponsored by the U.S. Department of Energy (April 1993).

[HMG 2003] Heschong-Mahone Group, Inc. on behalf of the California Energy Commission. Windows and Classrooms: A Study of Student Performance and the Indoor Environment (October 2003)

[HMG 1999a] Heschong-Mahone Group, Inc. on behalf of the California Board for Energy Efficiency Third Party Program. Daylighting in Schools: An Investigation into the Relationship Between Daylighting and Human Performance. Fair Oaks, CA. (1999).

[HMG 1999b] Heschong-Mahone Group, Inc. on behalf of the California Board for Energy Efficiency Third Party Program. Skylighting and Retail Sales: An Investigation into the Relationship between Daylighting and Human Performance, Fair Oaks, CA. (1999).

[Holst 1998] Holst, G. CCD arrays, cameras and displays, SPIE Optical Engineering (1998).

[IEA 2000] International Energy Agency (IEA). “Daylight in Buildings: A Source Book on Daylighting Systems and Components”, prepared by Ruck, N. Aschehoug, O., Aydinli, S., Christoffersen, J., Courret, G., Edmonds, I., Jakobiak, R., Kischkoweit-Lopin, M., Klinger, M., Lee, E., Michel, L., Scartezzini, J.-L., Selkowitz, S. *A report of the IEA SHC21/ECBCS29* (2000).

[IEA 1999] International Energy Agency (IEA). “Measurement of Luminous Characteristics of Daylighting Materials”, Prepared by Aydinli, S., Kaase, H., *A report of the IEA SHC21/ECBCS29* (1999).

[Inanici 2007] Inanici, M.N. “Re: New Methods for Measuring Spectral, Bi-directional Transmission and Reflection using Digital cameras” Private Communication. University of Washington (2007).

[Inanici 2006] Inanici, M.N. “Evaluation of high dynamic range photography as a luminance data acquisition system*”, Lighting Res. Technol.* 38(2) (2006) 1-14.

[James and Bahaj 2005a] James, P.A.B., Bahaj, A.S. “Smart glazing solutions to glare and solar gain: a ‘sick building’ case study”, *Solar Energy* 37 (2005) 1058-1067

[James and Bahaj 2005b] James, P.A.B., Bahaj, A.S. “Holographic optical elements: various principles for solar control of conservatories and sunrooms”, *Solar Energy* 78 (2005) 441-454.

[Jonsson et al. 2004] Jonsson, J., Karlsson, L., Nostell, P., Niklasson, A., Smith, G. “Angle-dependent light scattering in materials with controlled diffuse solar optical properties*”, Solar Energy Materials & Solar Cells* 84 (2004) 427-439.

[Kischkoweit-Lopin 2002] Kischkoweit-Lopin M. “An overview of daylighting systems”, *Solar Energy* 73: 7782 (2002).

[Koch 2007] Koch, T. Bachelor’s Degree in Mechanical Engineering Thesis, Massachusetts Institute of Technology (2007).

[Köster 2004] Köster, H. Dynamic Daylighting Architecture: Basics, Systems Projects, Birkhauser, Basel, Switzerland (2004).

[Beltran and Mogo 2005] Beltran, L.O., Mogo, B.M. “Assessment of Luminance Distributino Using HDR Photography”, *Proceedings of the 2005 ISES Solar World Congress, Orlando FL* (August 7-12 2005).

[Linton 1999] Linton, H., Color in Architecture. McGraw-Hill. Hong Kong (1999).

[Ljubicic 2006] Ljubicic, D. Automated support for experimental approaches in daylighting performances assessment*,* Massachusetts Institute of Technology. Bachelor’s Degree in Mechanical Engineering Thesis (2006).

[Loftness and Harktopf 2002] Loftness, V. and Harktopf, V. “Building Investment Decision Support (BIDS): Cost-Benefit Tool to Promote High Performance Components, Flexible Infrastructures and Systems Integration for Sustainable Commercial Buildings and Productive Organizations”, *The Austin Papers*, Building Green, Inc. 2002.

[Martinez-Verdu et al. 1999] Martinez-Verdu, F., Pujol, J., Bouzada, A., and Capilla, P. “Spectroradiometric characterization of the spectral linearity of a conventional digital camera”, IS*&T/SPIE Conference on Color Imaging,* International Society for Optical Engineering (January 1999).

[Mitanchey et al. 2002] Mitanchey, R., Escaffre, Le., Marty, C. “From optical performances characterization of a redirecting daylight material to daylighting simulations”, *Proceedings of the 3rd European Conference on Energy Performance and Indoor Climate in Buildings EPIC 2002, Lyon, France* (October 23–26, 2002) 721–726.

[Mbise et al. 1997] Mbise, G.W. Le Bellac, D. Niklasson, G.A. Granquist, C.G. “Angular selective window coatings : theory and experiments”, *J. Phys. D: Appl. Phys.* 30 (1997) 2103-2122.

[Modest 1993] Modest, M. Radiative Heat Transfer. McGraw-Hill Science/Engineering/Math, (January 1993)

[Nicodemus et al. 1977] Nicodemus, F., Richmond, J., Hsia, J., Ginsberg, I., and Limperis, T. “Geometrical Considerations and Nomenclature for Reflectance*”, Nbs monograph 160,* National Bureau of Standards, U.S. Department of Commerce, Washington, D.C. (1977).

[Nicodemus 1970] Nicodemus, F. “Reflectance nomenclature and directional reflectance and emissivity*”, Applied Optics* 9(6) (1970) 1474-1475.

[Ngan et al. 2005] Ngan, A., Durand, F., Matusik, W. “Experimental Analysis of BRDF Models”, *Eurographics Symposium on Rendering* (2005).

[Ojeda and McCown 2004] Ojeda, O.R., McCown, J. Colors: architecture in detail. Rockport Publishers. Gloucester, Massachusetts (2004).

[Palik 1997] Palik, E. Handbook of Optical Constants of Solids. Academic Press (January 1997).

[Palmer et al. 1996] Palmer, S. Mbise, G.W. Niklasson, G.A. Granquist, C.G. “Angular selective optical properties of thin films : Measurement of polar and azimuthal transmittance”, *Solar Energy Materials and Solar Cells* 44 (1996) 397-403.

[Papamichael et al. 1988] Papamichael, K.M. Klems, J., Selkowitz, S., “Determination and application of bidirectional solar-optical properties of fenestration materials”, *Technical report LBL-25124*, Lawrence Berkeley National Laboratory, Berkeley, (1988).

[Phillips 2004] Phillips, D. Daylighting, Natural Light in Architecture. Architectural Press, Burlington, MA (2004).

[Platzer 2000] Platzer, W. “The Altset Project: Measurement of Angular Properties for Complex Glazings” *Proceedings of the 3rd Int. ISES Europe Solar Congress,* Copenhagen, Denmark (June 19-22, 2000).

[Reinhart and Herkel 2000] Reinhart, C.F., Herkel, S. “The simulation of annual daylight illuminance distributions - a state-of-the-art comparison of six RADIANCE-based methods”, *Energy and Buildings* 32 (2) (2000) 167–187.

[Reppel and Edmonds 1998] Reppel, J. Edmonds, I.R. “Angle-Selective Glazing for Radiant Heat Control in Buildings: Theory”, *Solar Energy* Vol. 62 No. 3 245-253 (1998).

[Richter et al. 1998] Richter, F., Kranrich, G., Kuhn, M., Peter, S., Spaeth, Ch. „Cathodic Arc Evaporation – A Versatile Tool for Thin Film Deposition”, *Materials Science Forum* Vols. 287-288 (1998) 193-198.

[Ruck 2006] Ruck, N. “International Energy Agency’s Solar Heating and Cooling Task 31, ‘Daylighting Buildings in the 21st Century”, *Energy and Buildings* 38 (2006) 718-720.

[Schott 2007] Schott, “Glass Filters Catalog”, http://www.us.schott.com/optics_devices/filter/english/us/index.html (accessed 5-22-07).

[Schwalbe 2005] Schwalbe, W. “Geometric modeling and calibration of fisheye lens camera systems”, *Proc. ISPRS*, (February 2005).

[Selkowitz 1999] Selkowitz, S. “High Performance Glazing Systems: Architectural Opportunities for the 21st Century”, *Proceedings from the Glass Processing Days Conference, Tampere, Finland,* (June 13-16, 1999).

[Smith 1999] Smith, G.B. “Photogoniometer at the university of technology”, *Sydney, International Daylighting RD&A,* University of Sydney, Australia, vols. 2–99, no. 8, (September 1999).

[Smith et al. 1998] Smith, G.B., Dligatch, S. Sullivan, R. Hutchins, M.G. “Thin Film Angular Selective Glazing”, *Solar Energy* Vol. 62, No. 3 229-244 (1998).

[Sullivan et al. 1998] Sullivan, R., Beltran, L. Lee, E.S; Rubin, M. and Selkowitz, S.E., Energy and Daylight Performance of Angular Selective Glazings, Lawrence Berkeley National Laboratory, Supported by the U.S. Department of Energy (1998).

[Tanury 2007] Tanury Industries, “Cathodic Arc PVD” http://www.tanury.com/ (accessed on 5-23-07).

[Tremblay et al. 1987] Tremblay, C. Rheault, F. Boulay, R. Tremblay, R. “Passive optical element with selective angular reflection”, *Applied Optics* Vol. 26, No. 3 (1987) 570-577.

[Tripanagnostopoulos et al. 2006] Tripanagnostopoulos, Y. Siabekou, Ch. Tonui, J.K. “The Fresnel lens concept for solar control of buildings”, *Solar Energy* doi:10.1016/j.solener.2006.08.013 (2006).

[Tsuchikawa et al. 2001] Tsuchikawa, S. Torii, M., Tsutsumi, S. “Directional Characterisitics of Near Infrared Light Reflected from Wood”, *Holzforschung* Vol. 55, No. 5 (2001) 534-540.

[USDOE 2006] U.S Department of Energy. “2006 Building Energy Databook” http://buildingsdatabook.eren.doe.gov (accessed 4/30/07).

[USGBC 2003] U.S. Green Building Council, “Building Momentum: National Trends and Prospects for High-Performance Green Buildings”, *Based on the April 2002 Green Building Roundtable, prepared for the U.S. Senate Committee on Environment and Public Works.* (February 2003).

[Voss and Chapin 2004] Voss, K.J., Chapin, A.L., “An Upwelling Radiance Distribution Camera System, NURADS”, Optical Society of America (2004).

[Vyskocil et al. 1992] Vyskocil, J., Musil, J. “Cathodic arc evaporation in thin film technology”, *J. Vac. Sci. Technol. A* 10(4), (Jul/Aug 1992).

[Walze et al. 2005] Walze, G., Nitz, P., Ell, J., Georg, A., Gombert, A., Hossfeld, W. “Combination of microstructures and optically functional coatings for solar control glazing”, *Solar Energy Materials and Solar Cells* Vol. 89 (2-3) (November 2005) 233-248.

[Ward 1992] Ward, G. “Measuring and Modeling Anisotropic Reflection”, *Computer Graphics* Vol. 26, No.2 (1992) 265-272.

[Watts 2005] Watts, M. “Comparing the Energy Conservation Capabilities of Spectrally Selective and Conventional Applied Window Film”, *Energy Engineering* Vol. 102, No. 4 (2005).

[Webb 2006] Webb, A.R. “Considerations for Lighting in the Built Environment: Non-Visual Effects of Light”, *Energy and Buildings* 38 (2006) 721-727.

[Young and Berry 1979] Young, H.H., Berry, G.L. “The impact of environment on the productivity attitudes of intellectually challenged office workers”, *Human Factors* 21, (1979) 399-407.